Experimental and Computational Study of Multiphase Flow in Dry Powder Inhalers

By

Yahia M. Fouda

A Doctoral Thesis

Submitted in partial fulfilment of the requirements for the award of Doctor of Philosophy of Loughborough University

September 2014

Abstract

Dry Powder Inhalers (DPIs) have great potential in pulmonary drug delivery; the granular powder, used as active ingredient in DPIs, is ozone friendly and the operation of DPIs ensures coordination between dose release and patient inhalation. However, the powder fluidisation mechanisms are poorly understood which leads to low efficiency of DPIs with 10-35 % of the dose reaching the site of action. The main aim of this thesis is to study the hydrodynamics of powder fluidisation in DPIs, using experimental and computational approaches.

An experimental test rig was developed to replicate the process of transient powder fluidisation in an impinging air jet configuration. The powder fluidisation chamber was scaled up resulting in a two dimensional particle flow prototype, which encloses 3.85 mm glass beads. Using optical image processing techniques, individual particles were detected and tracked throughout the experimental time and domain. By varying the air flow rate to the test section, two particle fluidisation regimes were studied. In the first fluidisation regime, the particle bed was fully fluidised in less than 0.25 s due to the strong air jet. Particle velocity vectors showed strong convective flow with no evidence of diffusive motion triggered by inter-particle collisions. In the second fluidisation regime, the particle flow experienced two stages. The first stage showed strong convective flow similar to the first fluidisation regime, while the second stage showed more complex particle flow with collisional and convective flow taking place on the same time and length scales.

The continuum Two Fluid Model (TFM) was used to solve the governing equations of the coupled granular and gas phases for the same experimental conditions. Sub-models for particle-gas and particle-particle interactions were used to complete the model description. Inter-particle interactions were resolved using models based on the kinetic theory of granular flow for the rapid flow regime and models based on soil mechanics for the frictional regime. Numerical predictions of the first fluidisation regime showed that the model should incorporate particle-wall friction and minimise diffusion, simultaneously. Ignoring friction resulted in fluidisation timing mismatch, while increasing the

diffusion resulted in homogenous particle fluidisation in contrast to the aggregative convective fluidisation noticed in the experiments. Numerical predictions of the second fluidisation regime agreed well with the experiments for the convection dominated first stage of flow up to 0.3 s. However, later stages of complex particle flow showed qualitative discrepancies between the experimental and the computational approaches suggesting that current continuum granular models need further development.

The findings of the present thesis have contributed towards better understanding of the mechanics of particle fluidisation and dense multiphase flow in DPI in particular, and particle bed fluidisation using impinging air jet in general. The use of TFM for predicting high speed convective granular flows, such as those in DPIs, is promising. Further studies are needed to investigate the form of particle-particle interactions within continuum granular flow models.

Keywords: Dry Powder Inhaler (DPI), Fluidisation, Multiphase Flow, Granular Flow, Multi-scale Flow, Two Fluid Model (TFM).

Acknowledgments

I would like to express my sincere gratitude to my supervisors, Henk Versteeg and Ricky Wildman, for giving me the opportunity to purse this Ph.D. project. Throughout the time of this project, they encouraged me to freely explore the fundamental aspects of the hard science. Their continuous guidance and support contributed towards shaping my research ideas, and gave my scientific judgements new dimensions. Their immediate critical evaluation of my work helped me to navigate my way through this research project, and materialise this thesis.

I am grateful to the Wolfson School of Mechanical and Manufacturing Engineering, Loughborough University, for providing the financial support for this project.

I am thankful to the USA National Energy Technology Laboratory (NETL) for making the MFIX code available as an open source code. The support from the MFIX team during this project has been immensely helpful in understanding the code implementation and usage.

Finally, the support from my family and friends has been crucial to keep me on track during this critical phase of my life. I am speechless with gratitude in acknowledging the role of my parents. Many thanks for their massive effort, continuous care and infinite love.

Table of Contents

List of Figures

List of Tables

List of Symbols

Roman Letters

C_D	Dimensionless drag coefficient
D	Strain rate tensor (1/s)
d_p	Particle diameter (m)
e	Particle-particle coefficient of restitution
e_w	Particle-wall coefficient of restitution
g	Gravity acceleration (m/s²)
$g_{0,s}$	Radial distribution function at contact
I	Identity matrix
I_{gs}	Inter-phase momentum interaction (N/m³)
J_s	Granular temperature dissipation (kg/m.s³)
K_0	Dilute thermal conductivity (kg/m.s)
K_{diss}	Dissipation parameter (kg.m/s³)
K_s	Granular conductivity (kg/m.s)
k_B	Boltzmann constant (kg.m²/K.s²)
m	Particle mass (kg)
N_p	Number of particles in a spatial region
n	Number density (1/m³)
n_1	Exponent which determines the shape of the yield surface
n_2	Unit normal from the boundary wall into the particle assembly
$n_{p,l}$	Number of particles per computational cell
n'	Number of computational cells
n^*	Dimensionless number density

p	Phase Pressure (N/m²)
p_c	Critical state granular pressure (N/m²)
p_f	Frictional granular pressure (N/m²)
Re	Reynolds number
T	Temperature (K)
t	Time (s)
U	Total velocity of particles in a spatial region (m/s)
u	Phase velocity (m/s)
u_p	Individual Particle velocity (m/s)
$u_{s,w}$	Granular phase slip velocity at boundary wall (m/s)
u_{wall}	Boundary wall velocity (m/s)
V	Volume of region (m³)
V_l	Volume of computational cell (m³)
V_p	Volume of solid particle (m³)
v_s	Fluctuating component of particle velocity (m/s)
X_p	Particle horizontal position in experiments (m)
Y_p	Particle vertical position in experiments (m)

Greek Letters

β_{gs}	Drag coefficient (kg/m³.s)
γ	Cooling rate (1/s)
$\gamma^{(0)*}$	Zeroth-order dimensionless cooling rate
$\gamma^{(1)*}$	First-order dimensionless cooling rate
Δp	Air pressure difference across test section (Pa)

Δt	Time increment of the experiment (s)
δ	Angle of friction between the particulate phase and the wall (º)
ε	Volume fraction
${\varepsilon_{sf}}^{max}$	Maximum packing fraction
${\varepsilon_{sf}}^{min}$	Critical packing fraction
ε^*	void fraction at the maximum packing
η_0	Dilute solid viscosity (kg/m.s)
Θ_s	Granular temperature (m²/s²)
λ	Dilatational viscosity (N.s/m²)
μ	Shear viscosity (N.s/m²)
ν_0	Characteristic collision frequency (1/s)
${\nu_k}^*$	Dimensionless collision frequency due to kinetic transport
${\nu_\eta}^*$	Dimensionless collision frequency due to viscous transport
Π_s	Granular temperature source due to gas interaction (kg/m.s³)
ρ	Density (kg/m³)
σ	Phase stress tensor (N/m²)
τ	Viscous stress (N/m²)
Υ	General variable of the experiments (ensemble average)
ϕ	Angle of internal friction of solid particles (º)
ϕ'	Specularity coefficient
Ψ	Standard deviation of the experimental variables

Subscripts

g	Gas phase

i, j	Einstein summation convention indices
k	Particle number index in experiments
l	Index for the computational cell
n	Index for the experiment number within the ensemble
s	Solid phase
x, y	Horizontal and vertical coordinates

Superscripts

k	Kinetic component of the solid phase variables and coefficients
$rapid$	Rapid granular flow regime
$slow$	Slow granular flow regime
$*$	Dimensionless variable

Abbreviations

CFC	Chlorofluorocarbons
DEM	Discrete Element Model
DPI	Dry Powder Inhaler
Exp	Experiment
FSW	Free-Slip Wall
HFC	Hydrofluorocarbons
J&J	Johnson and Jackson
KTGF	Kinetic Theory of Granular Flow
MDI	Metered Dose Inhaler
NSW	No-Slip Wall

PSW	Partial-Slip Wall
pMDI	Pressurised Metered Dose Inhaler
SD	Standard Deviation
TFM	Two Fluid Model

Chapter 1 : Introduction

1.1 Background

1.1.1 Dry Powder Inhalers

Dry powder inhaler (DPI) is a device used for pulmonary drug delivery. It is used mainly for treating asthma and respiratory illness with a potential for delivering drug for other diseases such as insulin for diabetics (Larhrib et al., 2003). The drug used in DPIs is in the form of granular powder. When this powder is inhaled by the patient, it flows through the respiratory tract until it reaches the lungs. Figure 1-1 (Daniher and Zhu, 2008) illustrates the use of dry powder inhaler by a patient.

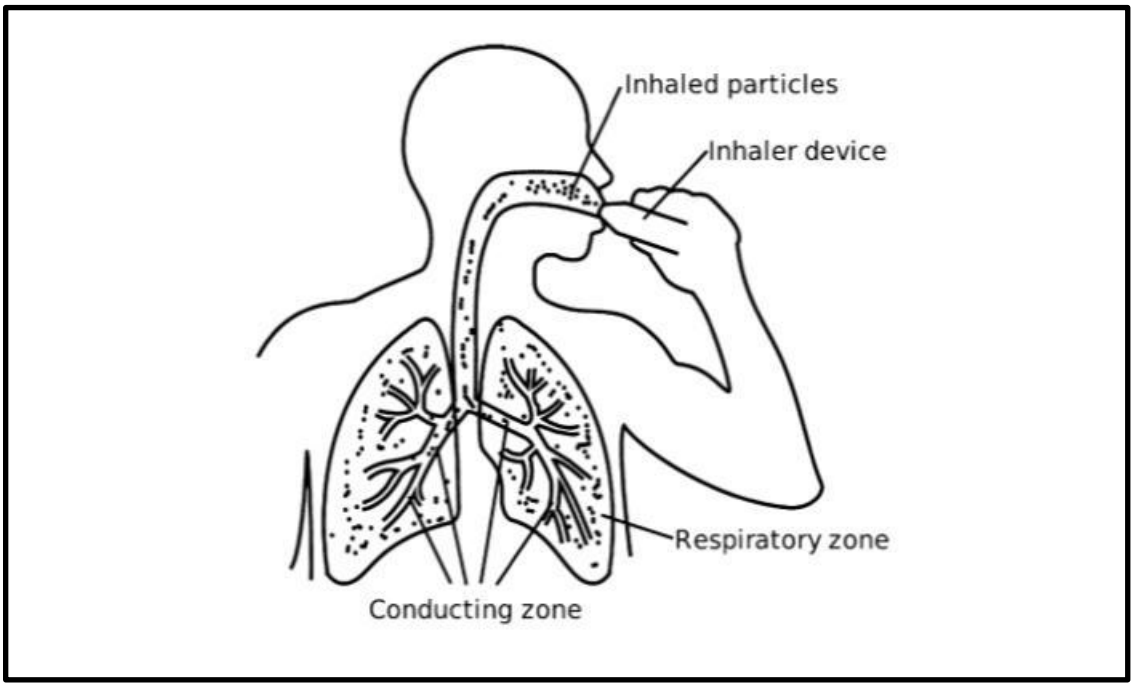

Figure 1-1: Pulmonary drug delivery using DPI (Daniher and Zhu, 2008).

DPIs are one of two types of drug delivery devices for the treatment of asthma; the other being pressurised metered dose inhalers (pMDI). In pMDIs, the drug is contained and delivered in suspension or solution in a liquid. The device atomises the drug liquid to small droplets so that the drug can reach the bronchi

and alveoli. The main problem which moved the pharmaceutical industry to develop a replacement of pMDI is that the atomising liquid is a type of chlorofluorocarbons (CFCs). CFCs have severe impact on the depletion of the ozone layer and the use of these chemicals has been phased out by the Montreal Protocol. The industry has now replaced CFCs by much more ozone-friendly Hydrofluorocarbons (HFCs), but these substances are very strong greenhouse gases. Accordingly, as HFC-based MDIs, DPIs are considered ozone-friendly devices compared to pMDI (Prime et al., 1997). However, a main drawback of DPI is their poor delivery of drug with 10-35 % of the drug reaches the patient lungs (Versteeg, Hargrave and Hind, 2005).

The principle of operation of DPI relies on the air fluidisation of solid particles. The powder in DPI is initially at rest. It is densely packed in the inhaler. The air flow inside the inhaler is triggered by the patient suction power for the case of breath activated inhaler. This causes the fluidisation of the solid particles creating a multiphase flow environment. This flow causes the removal of the particles from the inhaler. The fact that the patient does not need to make a special effort to coordinate the inhalation of air and the release of the drug dose from the device is a key advantage of DPIs compared with pMDIs (Prime et al., 1997). There is very little information about the exact geometry and design of the current commercial models of DPIs. However, in many devices the geometry of the inhaler creates an impinging air jet to fluidise the powder bed. This configuration was used for two commercial models of DPI: Diskus™ (Tuley, 2007) and Clickhaler® (Versteeg, Hargrave and Hind, 2005). Figure 1-2 shows the two commercial models and the configuration of impinging jet. Another application of impinging air jet over granular bed is the process of landing and take-off of rotorcraft and rockets (Haehnel, Dade and Cushman-Roisin, 2008; Metzger et al., 2009).

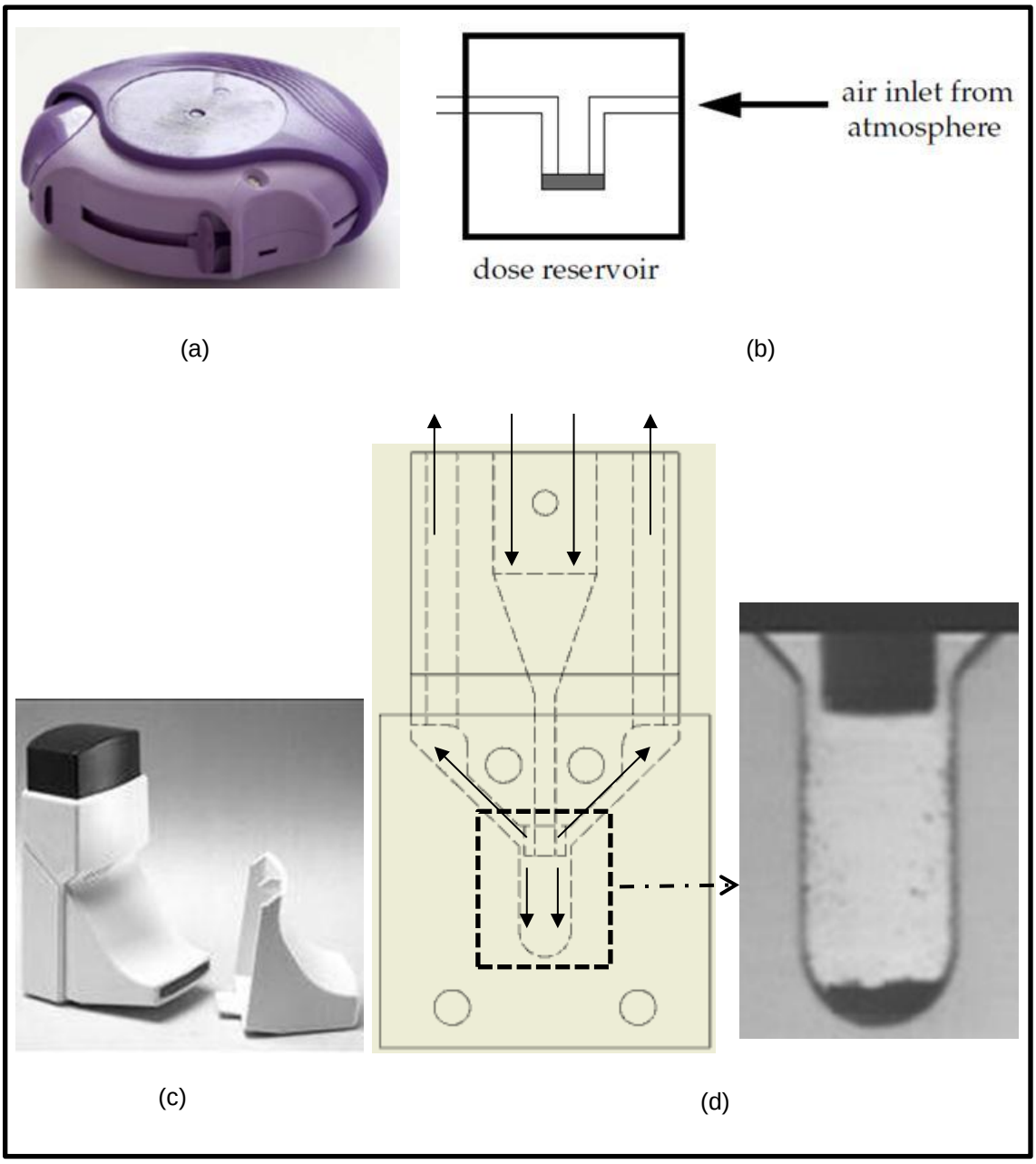

Figure 1-2: Impinging air jet configuration in DPI models: (a) Image of Diskus™, (b) Fluidisation chamber prototype used by (Tuley, 2007), (c) Image of Clickhaler®, (d) Fluidisation chamber prototype used by (Versteeg, Hargrave and Hind, 2005).

The particle size of the drug is made very small (around 5 µm) in order to reach the bronchi and alveoli regions in the lung and have the desired therapeutic effect. Basically, there are two types of formulations for the dose in the inhaler. They are agglomeration-based and carrier-based (Wong et al., 2011). In the former, the dose consists of drug particles only, while in the latter the dose consists of a blend of drug particles and carrier particles. Carrier particles are

made from lactose and they are larger than the drug particles with an average diameter of 50-100 µm. Carrier particles are used to aid the fluidisation and breakup of small drug particles due to the reduction of cohesive forces. These cohesive forces increase significantly as the particle size decreases. Consequently, it is difficult to disperse or fluidise the particles in the agglomeration-based type. In the poly-disperse system of carrier based powders, the process of detachment of drug from the carrier is essential for the delivery of the drug to lungs. Blending the drug with lactose also enhances dosing consistency by making it easier to meter the dose. Furthermore, lactose gives a taste which is felt by the patient and this ensures that the dose is correctly delivered (Prime et al., 1997).

There are many factors that should be taken into account when considering the design of an effective DPI. These factors may be divided into two types; the first type refers to the patient's method of using the inhaler, while the second type refers to the device itself. When considering the patient, the ideal DPI should have the ability to supply the required dose to a wide variety of patients irrespective of their respiratory flow rate. Accordingly, the inhaler should have nearly constant powder flow rate over a wide range of respiratory flow rate which typically exists in different patients and even within one patient. The respiratory flow rate of patients varies due to age and health. It is also affected by the type of the asthma attack and whether it is mild, moderate or severe. Figure 1-3 shows the variation of respiratory flow rate with time (Newman and Busse, 2002).

The device itself should be able to handle two mechanisms of powder flow (Daniher and Zhu, 2008). These mechanisms are:

1- Fluidisation or entrainment of packed particles bed. This also includes the initial dense flow of these particles.
2- Detachment and de-agglomeration of drug particles from the carrier surface.

Both mechanisms include the overcoming of the attraction and cohesive forces between the particles.

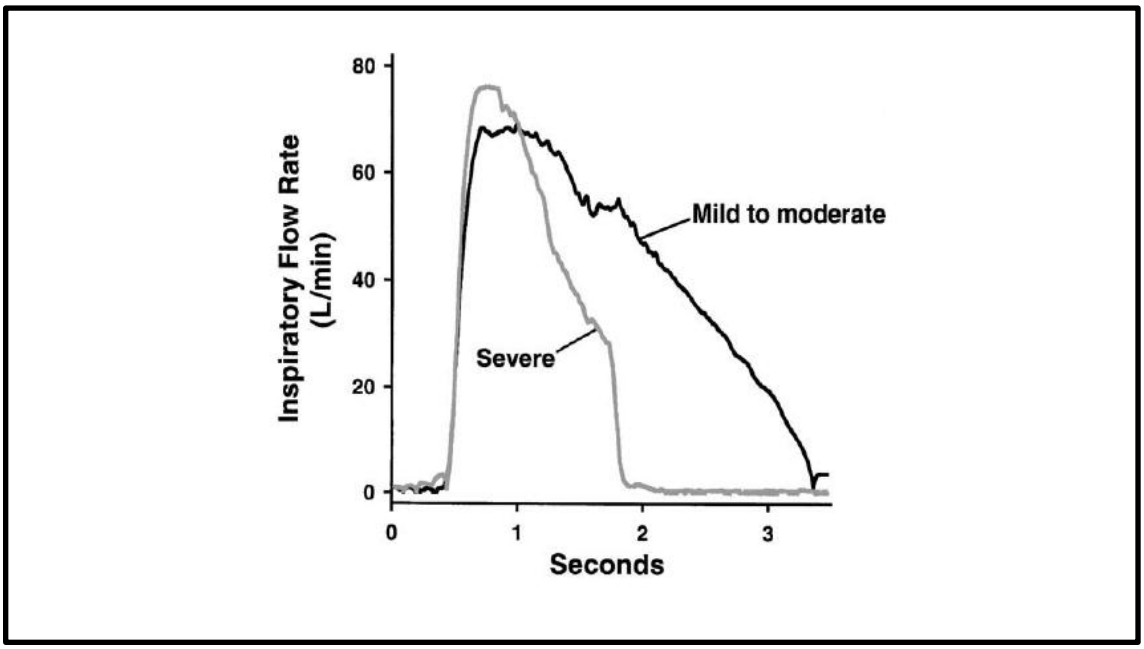

Figure 1-3: Variation of respiratory flow rate with time and with several types of asthma attacks (Newman and Busse, 2002).

There are two approaches to deal with device problems. The first one is the formulation of the drug which means that the particles are formulated in order to reduce the cohesive forces and aid fluidisation. While the other one includes the aerodynamics and flow path design of the device itself. However, the device design has received less attention compared to the formulation (Chan, 2006; Daniher and Zhu, 2008) especially, the process of fluidisation of packed particles and the initial dense powder flow in the inhaler. It has been reported that the turbulence and shear force contribute to the fluidisation and breakup of the particles (Finlay, 2001). However, studies have, thus far, not managed to paint a full picture of the flow in DPI. It is expected that the design of the device affects its performance (Coates et al., 2005b). However, it has been reported that various DPI models have nearly the same performance and they do not have significant advantage over each other (Islam and Gladki, 2008; Haughney et al., 2010). It is also known that the device efficiency in delivering the drug can be as low as 10% (Stevens, 2006; Islam and Gladki, 2008). This low efficiency causes loss of the drug dose which might lead to inconsistent dose.

The complex process of dense bed fluidisation is the first mechanism of powder flow and movement in the inhaler. It is followed by dilute flow of fluidised

particles and the detachment of drug particles from the carrier (Stevens, 2006; Finlay, 2001). Accordingly, it is expected that this initial process controls the whole flow process in the inhaler. Moreover, the flow in the patient's airway depends on the initial fluidisation. Acquiring a concrete understanding of this initial phase of multiphase flow and fluidisation will help in device development. This is mainly by quantifying the effects of aerodynamic and the inter-particle forces during the initial fluidisation. Furthermore, an accurate flow model might be used as a platform for a design protocol with the patient respiratory flow profile as an input parameter.

1.1.2 Dense Multiphase Flow and Fluidisation in DPIs

Based on the previous description of DPI operation, it is clear that the multiphase flow in Dry Powder Inhalers is characterised by three main physical processes. Firstly, the flow is unsteady since the dose is evacuated from the bed which means that the powder concentration changes over time. Secondly, this is a dense flow of solid particles because the particles are packed tightly in the inhaler. Consequently, strong particle-particle interactions are likely to take place in this type of dense flow. These interactions might be collisions, friction or cohesive forces. Thirdly, there is a strong particle-gas interaction. As a matter of fact, this interaction is the main cause for particles fluidisation through the drag exerted by the gas phase on the solid particles which leads to the movement of the particles. Furthermore, the dense solid particles will exert an equal and opposite force on the air flow field and hence, the gas phase is coupled to the particulate phase.

In general, there are two main approaches for modelling a multiphase solid-gas flow problem: the discrete approach and the continuum approach. Both approaches treat the gas phase as continuum and hence their ultimate difference is the way solid particles are modelled. Discrete Element method (DEM) (Cundall and Strack, 1979; Hoomans et al., 1996) relies on solving the detailed flow field of the solid phase. The flow of each individual particle is determined by solving the position and momentum equations for this particle. Although this approach gives details of the solid phase flow field on a micro or particle scale, it requires high computational resources. For the case of dense

flow, these computational resources increase significantly as the number of particles increases. The second approach is the continuum description of both phases. It is usually referred as Euler-Euler or Two Fluid Model (TFM) (Gidaspow, 1994; Jackson, 2000). In this approach, both phases are treated as continua. This means that there is no need to solve the detailed particulate phase interactions. These interactions are computed using physical sub-models. The main advantage of the TFM approach is that it reduces the computational time considerably. This enhances its potential in engineering and industrial applications as an aiding tool for the design of devices and processes. However, the research in this model is not yet complete. The sub-models used in conjunction with TFM are still subject to development.

The validity of a certain modelling approach depends mainly on its ability to predict the real physical process. Accordingly, comparison of modelling results with experiments is vital to understand the model and enhances it in an on-going research process. One of the experimental techniques widely used in studying multiphase flow is the optical technique. This technique provides physical insight into the flow field especially for the particles flow. Optical measurements introduce minimum disturbance to the flow, hence they are considered one of the non-invasive techniques. Furthermore, the output of the measurements can give information for the whole flow field. It can also be used to measure unsteady flow due to its fast response.

1.1.3 Multiphase Flow Devices

In addition to flow in DPI, dense solid-gas multiphase flow is common in many industrial and engineering applications. Figure 1-4 shows some of the devices which handle granular particles. One of those applications is the gas fluidised granular beds. Gas-fluidised granular beds are widely used in Chemical Engineering industry for catalytic cracking, efficient combustion, oil refinery, and many other processes (Candela et al., 2007). Accordingly, there has been extensive research in its application. Mainly, two types of fluidised bed were studied using either TFM or DEM. These types are the bubbling fluidised bed and the circulating fluidised bed. Bubbling fluidised beds are operated so that the velocity of gas phase is higher than the minimum fluidisation velocity yet

relatively small to keep the solid particles inside the bed. This allows air bubbles to develop inside the bed and hence enhances the chemical reactions by promoting mixing between the gas phase and granular particles. There has been a great research interest in modelling bubbling fluidised beds using TFM, DEM and experimental validation (Gidaspow, 1994; Goldschmidt, Beetstra and Kuipers, 2004; Reuge et al., 2008; Xie, Battaglia and Pannala, 2008; Jung, Gidaspow and Gamwo, 2005). On the other hand, circulating fluidised beds use continuous solid particles feeding, for example, particulate cracking agents in catalytic cracking process. This is done by circulating the solid particles in a closed flow loop and feeding them back to the bed. These particles are collected using cyclone separators and re-used in the bed. The hydrodynamics of circulating fluidised beds have attracted attention recently with efforts to model the process using TFM, DEM and experimental validation (Almuttahar and Taghipour, 2008; Benyahia, Syamlal and O'Brien, 2007; Jung, Gidaspow and Gamwo, 2005; Liu, 2001).

The research in fluidised bed technology has enhanced the understanding of multiphase flow models especially TFM. This leads to the potential of applying the TFM to other applications such as the dry powder inhalers. However, there are many differences between these two devices. The size scale of the fluidised beds is many orders of magnitude larger than that of the DPI. The velocity of fluidising air and the particle velocity are higher in the DPI compared to the fluidised beds. On top of this, the flow in DPI is unsteady with strong variations of flow conditions in short period of time. It is not clear whether these differences will restrict applying the TFM to multiphase flow in DPI.

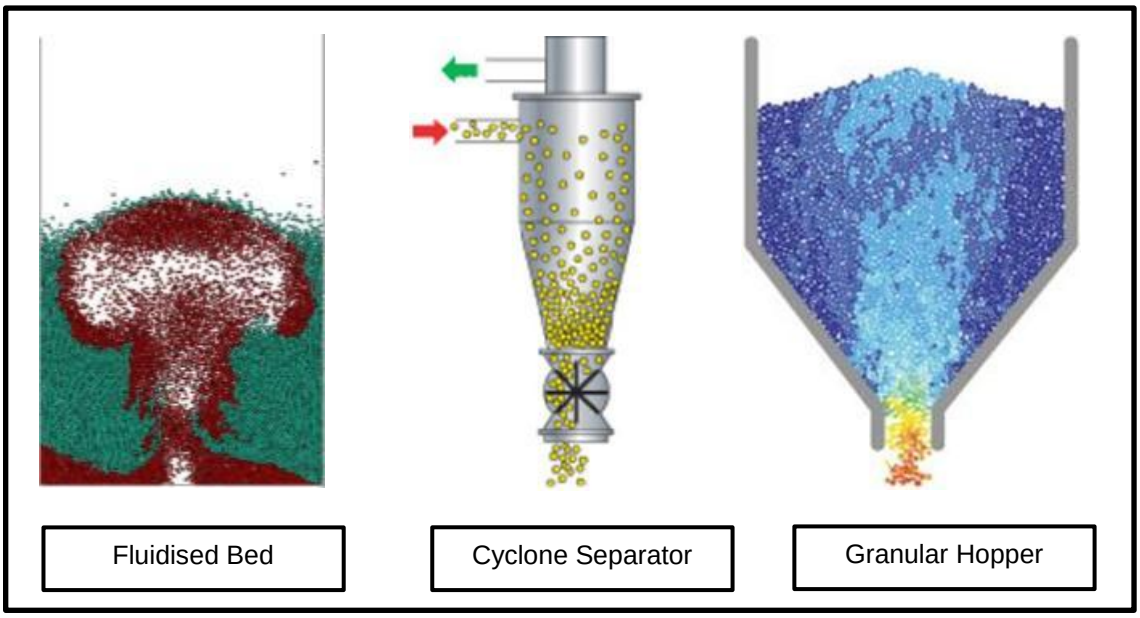

Figure 1-4: Some devices used in handling granular particles.

1.2 Thesis Aims and Objectives

The main aim of this thesis is to develop an understanding of the multiphase flow process in dry powder inhalers. The main focus is on the fluidisation of the packed particles and their initial dense flow. To achieve the main aim of this thesis, the dense multiphase flow is studied using both experimental and numerical approaches. The experimental approach uses an optical technique to capture the unsteady granular flow in a configuration which resembles one of the models of inhaler. This configuration is based on an air jet impinging the particles bed which is similar to some commercially available dry powder inhaler devices such as Diskus™ and Clickhaler® (Versteeg, Hargrave and Hind, 2005; Tuley, 2007). The numerical approach is based on the Two Fluid Model (TFM). Different sub-models are used in conjunction with the TFM to complete the model description. The parameters and the form of these sub-models are investigated as well. The model set up is used to mimic the same conditions of the experiments. Comparison between the experimental results and numerical results for different flow cases is used to assess the validity of the TFM which allows us to test the underlying fundamental physical assumptions of this model.

1.3 Thesis Outline

This thesis is divided into nine Chapters and two appendices. In this chapter the background, the operation of DPI has been presented, the multiphase flow models have been outlined and the aims of the current work have been set. The remainder of the thesis has been organized as follows:

Chapter 2: This chapter presents an extensive review of the relevant literature. The topics included are experimental and computational methods of multiphase flow. It also reviews the studies of multiphase flow in DPI with its wide range of interests. The chapter ends up with a summary and conclusions of the literature.

Chapter 3: This chapter describes the experimental optical technique used in the thesis. It also presents the analysis techniques used to generate the quantitative experimental results.

Chapter 4: This chapter presents the results obtained using the experimental setup for a high air pressure difference. This high pressure difference results in strong impinging air jet which causes full fluidisation of the whole particles bed.

Chapter 5: This chapter presents the results obtained using the experimental setup for two cases of low air pressure difference. This low pressure difference results in weak impinging air jet which causes partial fluidisation of the particles bed.

Chapter 6: This chapter gives the details of the Two Fluid Model (TFM) used in this thesis. This includes the governing equations and constitutive relations. It also describes the model setup for different flow cases. The analysis techniques used in subsequent chapters are presented as well.

Chapter 7: This chapter presents comparisons between the experimental measurements and the numerical predictions for a case of high inlet air velocity which causes full fluidisation of solid particles.

Chapter 8: This chapter presents comparisons between the experimental measurements and the numerical prediction for two cases of low inlet air velocities which cause partial fluidisation of solid particles.

Chapter 9: This chapter presents the main conclusions obtained from the thesis and gives suggestions for directions of future research in the subject.

Appendix A: This appendix presents the CAD design of the multiphase flow test section of Chapter 3.

Appendix B: This appendix presents the Matlab Code used for particle tracking in the experiments.

Publications

YM Fouda, RD Wildman and HK Versteeg "Experimental and Kinetic theory based Numerical Study of Multiphase Solid-gas Flow" 2nd IMA Conference on Dense Granular Flows, Isaac Newton Institute for Mathematical Sciences. (1–4) July 2013, Cambridge, UK.

YM Fouda, RD Wildman and HK Versteeg "Experimental and Numerical Study of Solid bed Fluidisation using Impinging Jet" Gordon Granular and Granular Fluid Flow Conference. (22-27) July 2012, Davidson, NC, USA.

YM Fouda, RD Wildman and HK Versteeg "Modelling of Multiphase Flow in Dry Powder inhalers", UK Particle technology forum. (4-5) April 2012, Loughborough, UK.

Papers manuscript in preparation

YM Fouda, HK Versteeg and RD Wildman "Particle Bed Fluidisation using a High speed Impinging Air Jet. Part A: Experimental study", *Powder Technology*.

YM Fouda, HK Versteeg and RD Wildman "Particle Bed Fluidisation using a High speed Impinging Air Jet. Part B: Computational study", *Powder Technology*.

Chapter 2 : Literature Survey

2.1 Introduction

In this chapter, the literature relevant to the current study is reviewed. It describes the methods used to study the dense multiphase solid-gas flow and its applications to dry powder inhalers. The chapter starts with a review of the experimental approaches containing a detailed description of the optical experimental technique used in this thesis. Then both the continuum or hydrodynamic description and discrete element description are presented and outlined. Special issues related to each method are discussed with special emphasis on the role of particle properties. Then the chapter presents a review of the previous studies concerning the applications of multiphase flow to DPI. The chapter ends with a summary which presents the outcomes of previous research including the gaps in knowledge and possible approaches to bridge these gaps.

2.2 Experimental Approaches

The main problem in measuring the granular flow variables in general and the solid-gas multiphase flow in particular is that the granular media is opaque. The detection process of one particle is affected by the presence of the other particles (Kawaguchi, 2010). This hinders the detection of particles in three-dimensional flow. Nevertheless, the experimental methods studying multiphase solid-gas flow have benefited from recent technological advancements in different areas of science and technology. This made the process of particle detection more feasible. The advanced experimental techniques are shifting towards using non-invasive methods to detect the particles and track them. This ranges from nuclear magnetic resonance imaging (MRI), positron emission particle tracking (PEPT) to optical techniques using high speed photography. However, each of these methods has its advantages and disadvantages. Consequently, it is vital to evaluate each method in order to match it with the relevant multiphase flow application.

MRI is an imaging technique which utilises the Nuclear Magnetic Resonance (NMR) thus; MRI is sometimes referred as NMRI or NMR Imaging (Kawaguchi, 2010). MRI has been used to track granular particles in both dry granular flow and multiphase solid-gas flows (Fennell et al., 2005; Müller et al., 2006; Candela et al., 2007; Mantle et al., 2008; Kawaguchi, 2010; Sheikh, 2011). The working principle of this method is to apply a magnetic field to the flow which detects the particles and tracks them. The granular particles used in this type are hollow spheres filled with liquid to enhance the detection of the magnetic field passing through them. When using MRI systems in granular flow studies, there is a trade-off between the temporal and the spatial resolution. Kawaguchi (2010) used an MRI system which takes between 20 s and 60 s to obtain an image whose spatial resolution is 390 μm. Higher temporal resolution of 1 ms was reported by Müller et al. (2006) and their spatial resolution was 1 mm for a one-dimensional system. Accordingly, MRI systems are inconvenient for the case of highly unsteady or transient flows where a high spatial resolution is needed. In order to obtain high temporal resolution for transient flow, the individual particles are not detected but a volume average is used which results in hydrodynamic fields measurements.

The PEPT technique (Stein et al., 2000; Martin, Huntley and Wildman, 2005; He, Ngoc Cong and Ding, 2006; Wildman and Huntley, 2008) uses radioactive nuclei to label a tracer particle, which is otherwise identical to other granular particles. This tracer particle emits two gamma rays in two opposite directions. Using two position detectors, these gamma rays are detected and hence the position of the tracer particle is known. This technique is capable of detecting the particles in steady granular flow situation. This is because the experiment is run for a long time and the measurements obtained for a single particle are considered to be representative of the whole system for this long period of time. A main disadvantage of this method is that it cannot be applied to flow situations where the particles end up stagnant, because the tracer particle does not move and it cannot provide an image of the whole flow. Accordingly, this method is limited to flow situations where the system keeps moving in a way which enables each particle to circulate or move throughout the whole flow field. It is not convenient for unsteady flows with strongly heterogeneous behaviour,

such as those in a DPI, where the development of the whole flow field should be detected as time passes.

Optical techniques are widely used in multiphase flow applications including granular flows. Their simple method of operation and wide variety of possible measurements make these methods much favoured for the detection of granular particles. Basically, optical methods use a light source, which illuminates the region of interest inside a flow test section or domain. The flow in this region is recorded using a high speed camera. Optical techniques vary with the type of illumination and camera used. The illumination ranges from laser with high illuminating power to ordinary halogen lamps. Certain regions or planes of interest may be illuminated and image processing techniques are used to extract information relating to the most important flow variables within these regions. The accuracy of the optical technique depends on the camera used. The resolution of the camera and the field of view limit the size of particles used in the experiments, i.e. the spatial resolution of the measurements. The frame rate of the camera limits the allowable variations from one frame to another, i.e. the temporal resolution of the measurements.

Optical techniques might be used to obtain qualitative experimental results by using the raw images recorded by the camera to show certain phenomena, flow pattern or configuration. The images may also be processed to obtain quantitative information describing measurable variables. However, optical methods suffer from the opacity of granular particles especially in dense flow situations. When using a three-dimensional test section, the particles closest to the light source block the illuminating light from reaching particles closer to the camera and, hence, making it difficult to detect all the particles within a whole flow field. Increasing the spatial resolution of the camera might lead to detection of the nearest particles layer in three-dimensional flow situations. However, this high spatial resolution comes on the expense of the temporal resolution. Figure 2-1 shows the use of optical technique in three-dimensional fluidised bed (Link et al., 2004). When the particles are moving with low velocity in image (a), the particles are clear and are likely to be detected. However, as soon as the particle velocity increases, it is very difficult to detect those particles as the temporal resolution deteriorates as seen in images (b) and (c). Moreover, the

images show clear interference between different particle layers throughout the bed thickness. These limitations did not prevent the use of optical techniques in three-dimensional granular multiphase flows. Optical techniques have been used to detect the shape of certain regions with strong and clear interface between the granular particles and the gas in the flow field. For example, the bubbles shape and area in bubbling fluidised bed and the average bed height (Yu and Xu, 2003; Goldschmidt et al., 2003; Goldschmidt, Beetstra and Kuipers, 2004; Almendros-Ibáñez et al., 2010). Figure 2-2 shows the measurement of air bubble using optical technique (Almendros-Ibáñez et al., 2010).

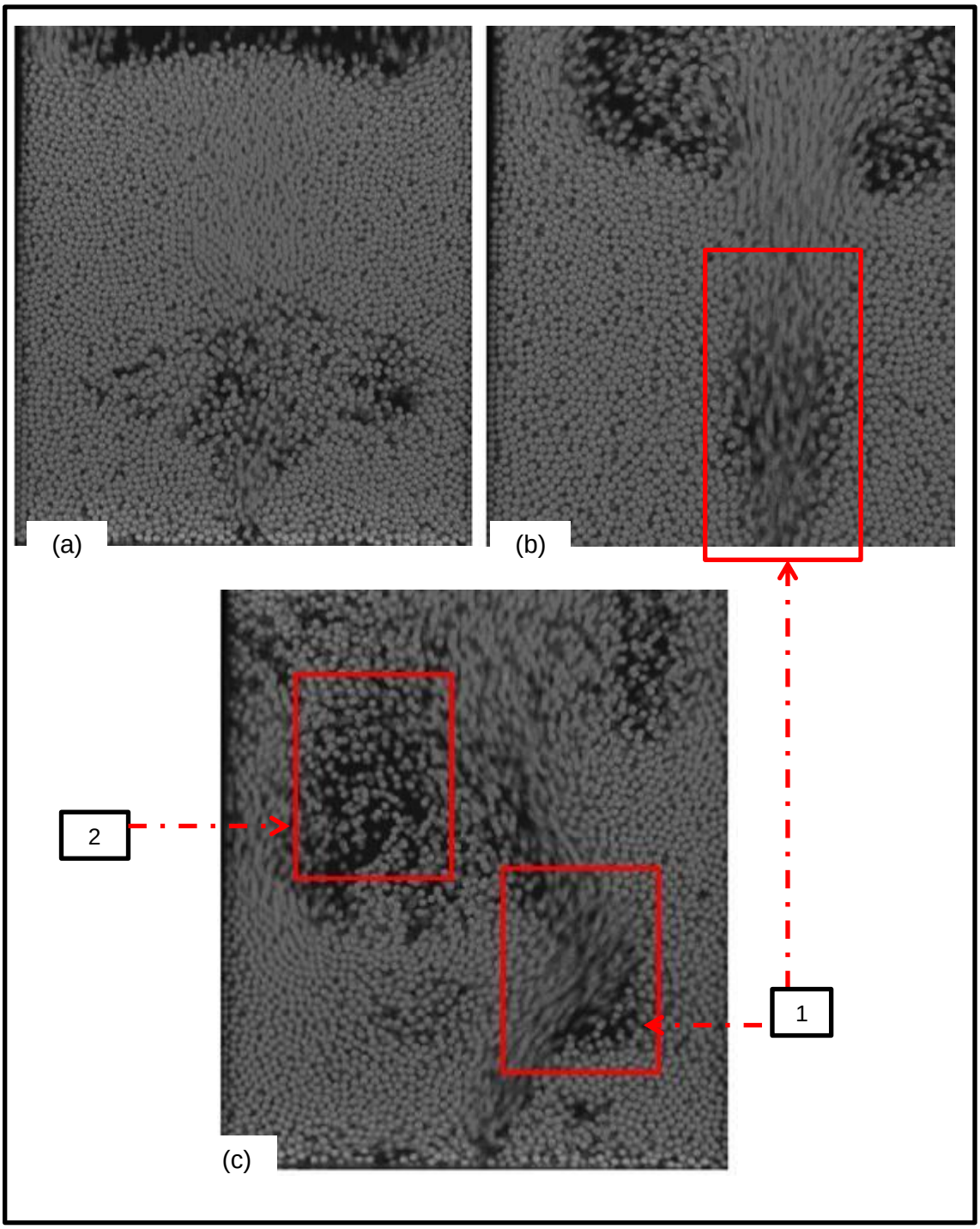

Figure 2-1: Three-dimensional optical images in fluidised bed (Link et al., 2004): (a) Clear image in slow particle flow, (b) Poor temporal resolution due to fast particle flow, and (c) Interference of particle layers in fast particle flow. Regions marked with red boxes show: (1) Low temporal resolution and (2) Interference between particles from different layers throughout the bed thickness.

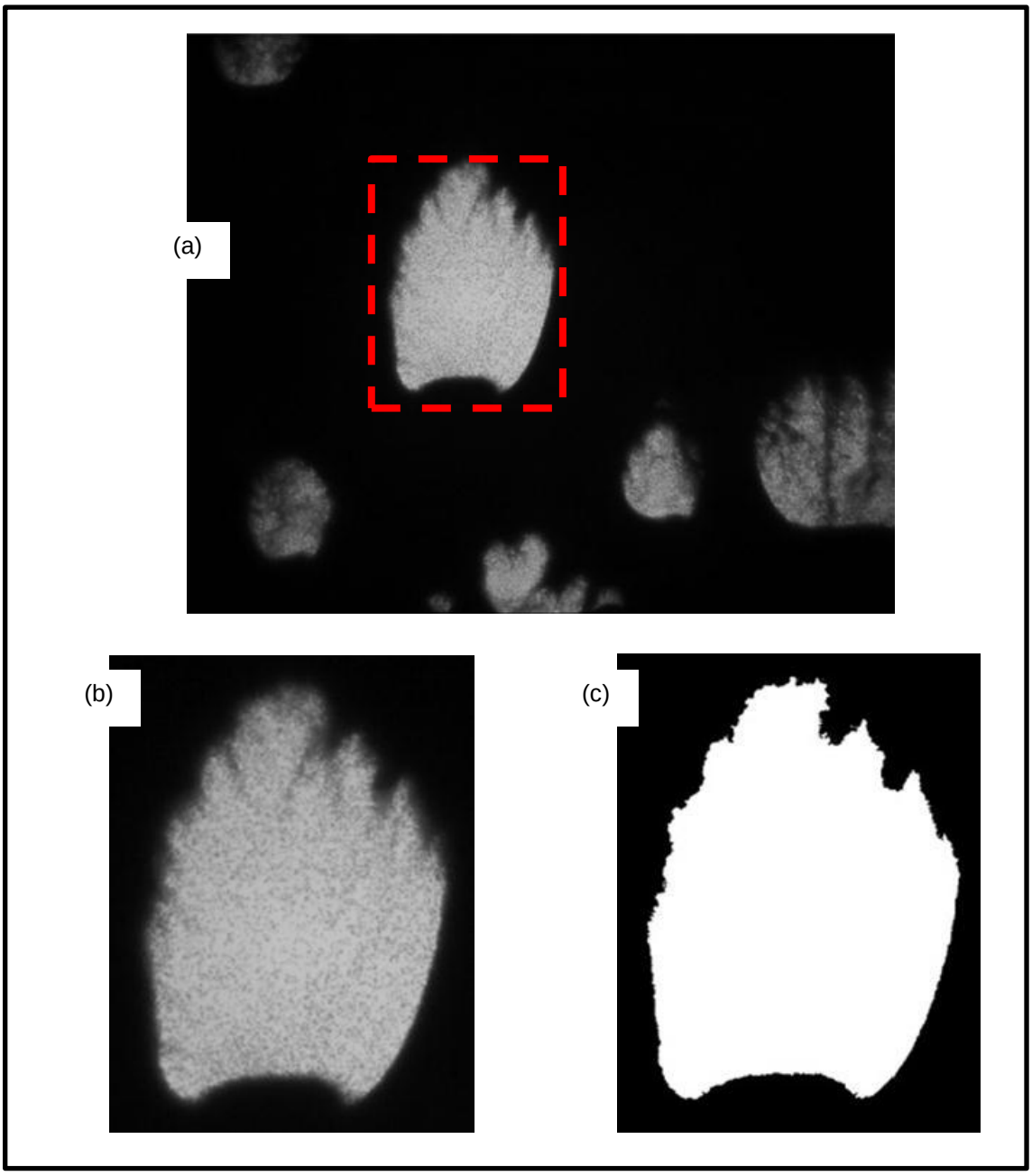

Figure 2-2: Detecting air bubble in opaque three-dimensional fluidised bed (Almendros-Ibáñez et al., 2010): (a) Typical picture captured with the high speed video-camera, (b) Bubble selected, and (c) Bubble contour obtained using a threshold algorithm.

In order to avoid the problem of opacity in three-dimensional flow, Drake (1991) used a pure two-dimensional test section to study dry-granular flow in chute. This two-dimensional test section allows the particles to be restricted in one geometrical plane, which makes it possible to detect the particles in the flow field and, hence, track them. Digital image processing allows all the properties of the particles to be determined, so a full picture of the particulate flow may be

constructed. Detecting and tracking each particle throughout the experimental time and domain allows the study of granular flow on micro or particle scale. This method has been further used to study dry granular flow in vibrofluidised beds (Warr, Jacques and Huntley, 1994; Wildman and Huntley, 2000; Wildman, 2002) and multiphase flow in fluidised beds (Martin et al., 2005). Figure 2-3 shows the optical images produced by using two-dimensional test section. The solid particles are very clear and can be easily detected.

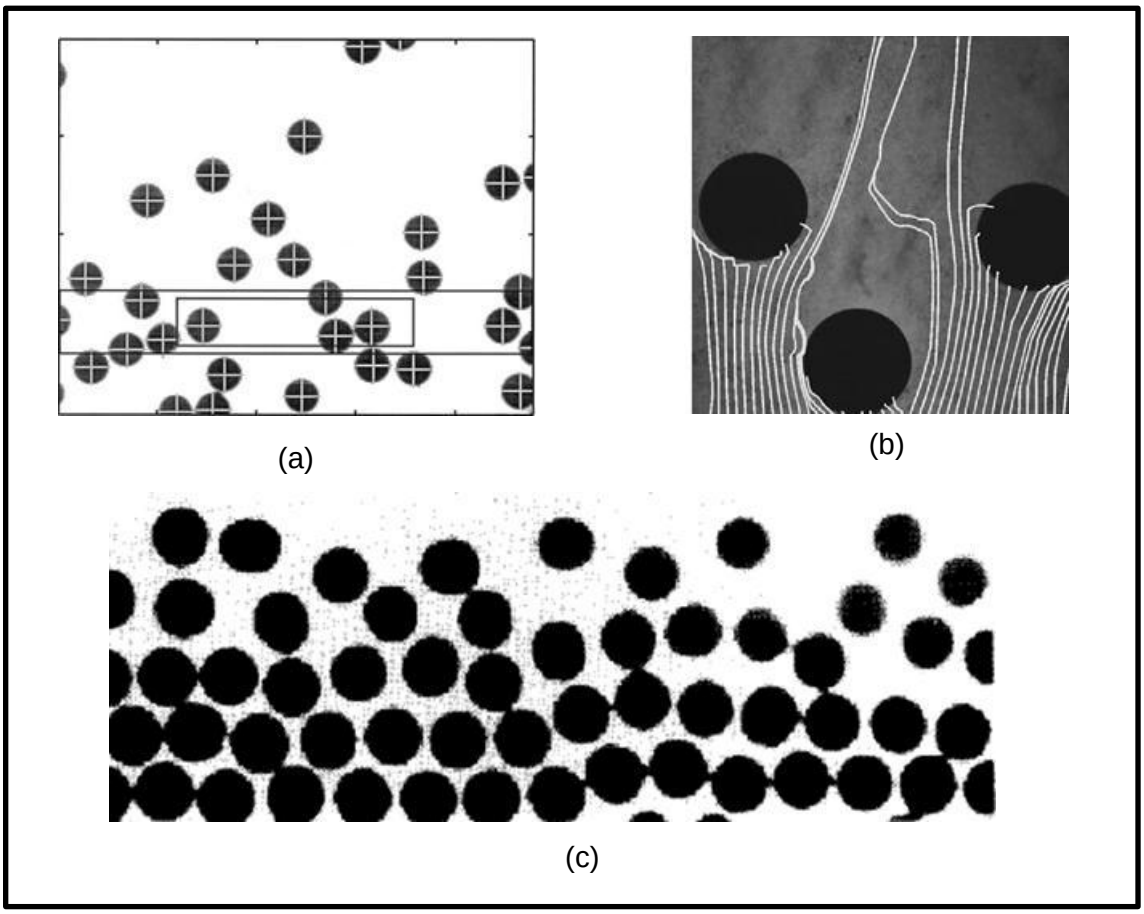

Figure 2-3: Particle flow field images obtained using the two-dimensional optical technique: (a) Wildman and Huntley (2000), (b) Martin et al. (2005), (c) Warr, Jacques and Huntley (1994).

2.3 Continuum Modelling

Two-phase solid-gas flow can be described as interpenetrating continua within the framework known as Euler-Euler Model or Two Fluid Model (TFM). The first version of Euler-Euler method was proposed by Davidson (1961). TFM assumes that each phase exists in every point in the flow domain. The

hydrodynamic equations of each phase are defined using small control volumes similar to those used for the development of single phase flow equations. The concept of volume fraction is introduced to define the proportion of a control volume occupied by one of the phases. Accordingly, the sum of the volume fractions of the two phases at any point is unity.

Based on the previous assumptions, mass and momentum conservation for each phase are represented by a set of flow equations. The coupling between the two phases is achieved through the inter-phase momentum transfer and through the volume fraction fields. The interactions within the gas phase are based on Navier-Stokes equations, which are widely used in other applications of single phase flow. In a similar fashion to the gas phase, the interactions between the particles (i.e. within the solid phase) are modelled using continuum granular flow models. Figure 2-4 shows a schematic diagram outlining the two-phase solid-gas continuum model. In order to complete the TFM, sub-models are used to describe the missing information in the governing equations. These sub-models describe two physical processes: particle-gas interactions and particle-particle interactions. Sub-models for particle-gas interactions are based on evidence from experiments resulting in empirical correlation. Particle-particle interactions are described by continuum granular flow sub-models. In the next two sections, these two categories of sub-models are reviewed.

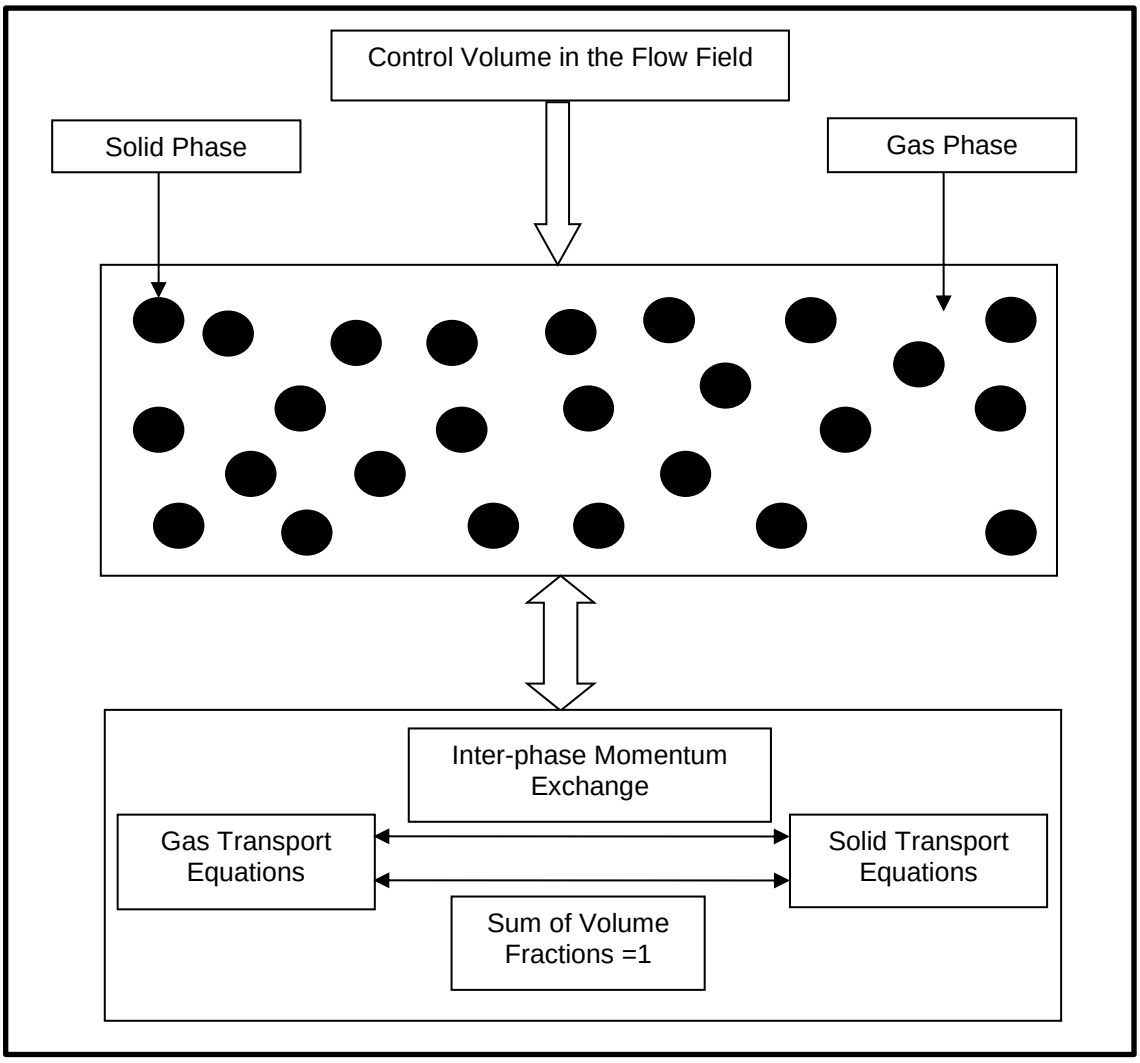

Figure 2-4: Schematic diagram of the Two Fluid Model (TFM) for solid-gas flow.

2.3.1 Particle-gas Interaction

The origin of inter-phase interactions comes from the transfer of mass, momentum, species and energy between the two phases. For isothermal solid-gas flow without chemical reactions, momentum transfer is the only interaction mechanism. These momentum interactions result from the forces exerted from one phase on the other. These forces appear as a source term in the momentum equation for one of the phases, while they appear in the momentum equation of the other phase as a sink term following Newton's third law.

The inter-phase interaction forces can be classified into the following forces:

-Buoyancy force: this force is due to the difference in density between the gas and the solid (solid particles submerged in the gas). When it is applied to the solid phase; its direction is opposite to that of the gravity. The buoyancy force is simply determined using Archimedes' principle. It is usually implemented in the models since it is very easy to represent, though it might be insignificant in gas-solid flow, because the density of solid particles is much higher than that of the gas.

-Drag force: this force is due to the relative velocity between the gas and the particles. The direction of this force is opposite to the direction of the relative velocity between the two phases.

-Lift force (transverse force): a force on the particles in the normal direction to the velocity direction as a consequence of velocity gradients of the gas.

-Virtual (added) mass force: Due to the relative acceleration between the two phases. The accelerating phase must overcome the inertia of the mass that lies in its path.

-Magnus force: this type of force arises due to the rotation and spin of particles.

In general, drag force is the most important force in modelling the momentum exchange between the two phases since the effects of other forces are negligible for most flow cases. Magnus force is usually neglected in flow situations where the transitional motion of particles is very high compared to particle spin. Lift forces are usually small on a single particle because its volume is small and hence the velocity gradient across its volume is small. Accordingly, the inter-phase drag becomes the main force that needs separate sub-models to determine its value at various flow conditions. It is described in terms of a drag coefficient and a function of the relative velocity and the volume fraction. Different forms of drag coefficients have been proposed by several researchers. Some researchers used experiments (Wen and Yu, 1966a), while other researchers (Hill, Koch and Ladd, 2001a; Hill, Koch and Ladd, 2001b) have used the lattice Boltzmann method in order to compute the drag force.

2.3.2 Continuum Description of Granular Flow

The continuum description of granular flow is based on applying the conservation laws to the granular flow field. This results in the definition of average macroscopic flow variables rather than the microscopic description of individual particles. A macroscopic field represents an average over a number of particles occupying a certain volume. The macroscopic fields are mainly the velocity, volume fraction and stresses. However, as in the continuum (hydrodynamic) description of liquid or gas flows, the stresses need to be related to the strain rate, which is a function of the velocity. This means that constitutive relations describing particle-particle interactions are essential to complete the continuum description.

Relating the stress tensors in the continuum granular flow to the strain rate tensor requires a certain level of knowledge of the interactions between the solid particles. The main problem is that the physics of granular flow varies significantly in different flow and packing conditions. Furthermore, unlike fluid molecules, the packing or the density of granular particles might change significantly within a single flow situation. This makes it extremely difficult to construct global constitutive relations describing the granular flow at all flow conditions. It is reported that granular materials can behave like solids, liquids or gases depending on material properties and external forcing conditions (Jaeger, Nagel and Behringer, 1996).

At low packing or dilute granular flow, particles randomly fluctuate and translate between collisions. At moderate packing, the collisions between the particles increase and hence they are the main mechanism of interaction. At high packing, the contacts between the particles become long and enduring. Friction plays the dominant rule in this regime because particles slide over one another. Figure 2-5 shows the three mechanisms of particle-particle interactions (Fan, 2006). Those three types of interactions: kinetic, collisional and frictional, are usually merged into two flow regimes. The first regime is the rapid flow, which consists of the kinetic and collisional interactions. The second regime is the slow (quasi-static) flow, which is characterised by the frictional interactions. There is no clear threshold value of the packing fraction between the two

regimes (Srivastava and Sundaresan, 2003). The rapid flow regime models are usually determined by adopting the kinetic theory of dense gases. In those models, the collisions between particles are assumed to be binary and instantaneous. On the other hand, the quasi-static (slow or frictional) regime models use soil mechanisms rules to model the friction induced by long and enduring inter-particle contacts. Figure 2-6 shows the difference between the two regimes.

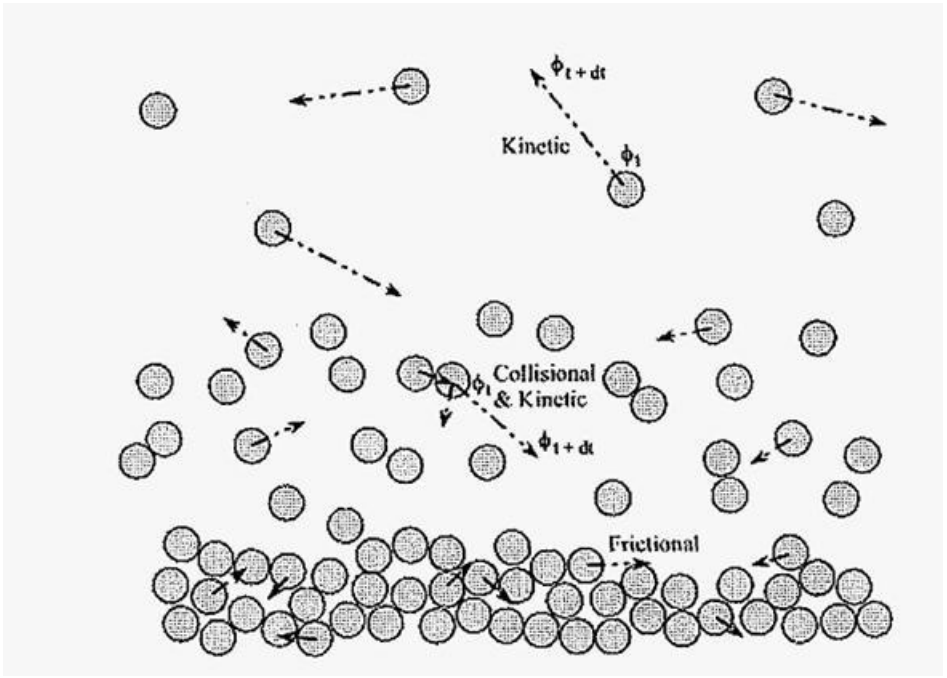

Figure 2-5: The three main mechanisms of particle-particle interactions (Fan, 2006).

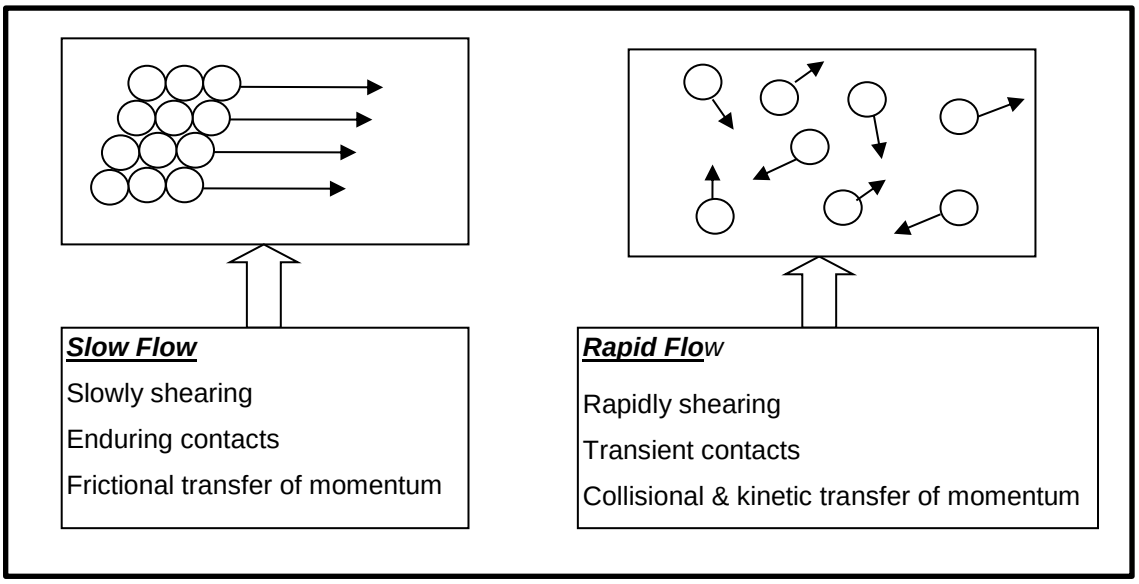

Figure 2-6: Mechanics of particle-particle interactions in slow and rapid flow regimes.

When considering the rapid flow regime, Bagnold (1954) is considered the pioneering work in the development of the kinetic theory of granular flow (KTGF). He used a simple expression for the collision frequency of particles, which resulted in an expression describing the repulsive pressure of particles in the case of uniform shear flow. The repulsive pressure is proportional to the square of the velocity gradient. The kinetic theory of granular flow (KTGF) has subsequently been developed to include more sophisticated physics. This theory (KTGF) treats the solid (granular) particles as the molecules in an analogous fashion to the kinetic theory of gases. The hard sphere approach, employed in KTGF, assumes that the collisions between granular particles are binary and instantaneous. This hard sphere assumption is justified by the fact that the collision time is much smaller than the mean free time. However, an important difference from the gas molecules is that the collisions of the granular particles are inelastic. This leads to including the coefficient of restitution as a parameter in the kinetic theory of granular flow. Now, the transfer of stresses within the flow domain is due to two mechanisms. The first one is the inter-particle collisions, while the second mechanism is due to the motion of the particles between two successive collisions. The relative importance of those two mechanisms depends on the packing fraction. In dilute granular flow, the collision rate between particles is less than the dense case. This means that

the momentum transfer due to particles transitions from one flow plane to another dominates in dilute flows, while the collisional momentum transfer is dominant in dense flows. The dense flow theories include an extra term to account for the increase in the rate of collisional part of the momentum transfer. This term is named radial distribution function.

A key property of rapid granular flow is the granular temperature. The concept of the granular temperature was first introduced by Ogawa, Umemura and Oshima (1980). The granular temperature is a measure of the fluctuations of the solid particles around the mean velocity of the collection of particles in a certain control volume. It is mainly generated by two mechanisms: collisional and streaming (Campbell, 2006). Consequently, it is similar to the molecular temperature of gas. The collisions between granular particles transform the mean particle velocity to random components. The streaming part of granular temperature is due to the motion of the particles relative to the mean velocity of the particle collection. In multiphase flow where the gas phase effect is significant, there is a third mechanism for the granular temperature generation. This mechanism results from the effect of gas turbulence on the particles. Due to the inelastic collisions between the particles, the granular temperature is dissipated with time in absence of external energy source. This dissipative mechanism of granular energy is responsible for particle clustering (Brilliantov and Pöschel, 2010).

Initially, KTGF was derived for identical, smooth, nearly elastic, spherical particles. The form of the velocity distribution function was assumed to be Maxwellian. This assumption simplifies the derivation because there is no need to solve the Boltzmann equation to determine the velocity distribution function. This approach was first applied by Savage and Jeffrey (1981). They derived the collisional contribution of the stress tensor based on the assumption that the random particle velocities followed a Maxwellian distribution. The theory did not include the granular energy equation and the granular stresses were computed in integral forms as functions of particles velocities. Jenkins and Savage (1983) solved the energy balance for granular temperature but neglected the streaming (kinetic) contribution to the stress tensor, when the particles are not in collision. Accordingly, their theory accounted only for the collisional

contribution. Lun et al. (1984) was the first study attempting to compute the streaming contribution to the stress tensor, thus including all the mechanisms of motion in the rapid flow regime. They used a perturbation to the Maxwellian velocity distribution. An accurate prediction of streaming stress was obtained.

Further developments include the solution of Boltzmann-Enskog equations for granular systems. This solution is used for determining the distribution functions using Chapman-Enskog expansion or the method of moments. This approach is based on the assumption (explicit or implicit) that gradients of the mean-flow properties such as velocity, temperature and bulk density are in some sense small (Lun et al., 1984). The small-gradient assumption in this context implies that the energy dissipated during a collision is small, and hence the smooth particles considered here are nearly elastic or the coefficient of restitution is nearly unity (Lun et al., 1984; Savage, 1998). This is done by integrating 'Boltzmann-Enskog' kinetic equation with various weight functions. This method approximates the singlet distribution function (SDF) which appears in the Boltzmann equation on an ad-hoc basis (Lun et al., 1984; Ding and Gidaspow, 1990).

Brey et al. (1998) extended the Chapman-Enskog solution to all values of elasticity for dilute granular systems and hence, the analysis is not limited to weak dissipation or small variables gradients. Kinetic theory models including flows for higher granular densities (packing fraction) were derived based on the Revised Enskog Theory (RET) (Garzó and Dufty, 1999; Brey, Dufty and Santos, 1999). The RET for elastic collisions (Van Beijeren and Ernst, 1973) is known to be an accurate kinetic theory over the entire fluid density domain. In fact it describes the crystal phase as well, which suggests its relevance for granular media undergoing cluster formation (Garzó and Dufty, 1999). Its generalisation to inelastic collisions is straightforward (Brey, Dufty and Santos, 1997) and the Chapman-Enskog method can be applied to obtain the Navier-Stokes hydrodynamic equations and the associated transport coefficients. Garzó and Dufty (1999) extended the analysis of Brey et al. (1998) to the revised Enskog kinetic theory (RET) for a description of the hydrodynamics and transport at higher densities. This model is especially important because its derivation covers the whole domain of particle elasticity values (0,1).

In the slow flow regime, the particle collisions are neither binary nor instantaneous. The quasi-static regime is characterised by high packing fraction and low deformation rates of the granular assembly. The particles typically experience multiple contacts that are long lasting rather than short-term collisions (Savage, 1998). The high packing fraction in addition to the long contact time results in force chains or networks which involve large number of particles, in contrast to the binary contact in the rapid collisional regime. This behaviour was confirmed by experimental studies using photo-elastic disks and two-dimensional computer simulations (Savage, 1998). The behaviour of these force chains connecting the particles through networks keeps changing over time. Some particles are highly loaded and form chains, whereas others in between the chains are subjected to relatively small loads. When the bulk material deforms, particle contacts fade, new ones are generated, and the structure of the force networks has an apparently random transient character (Savage, 1998). Due to this complicated behaviour of inter-particle forces, it is extremely difficult to construct mechanistic models similar to those used in the rapid regime. Accordingly, other approaches using phenomenological models to describe this regime are employed. The stresses in the plastic flow regime are usually described by adopting theories from the study of soil mechanics (Tüzün et al., 1982; Jackson, 1983). During slow or quasi-static flows, the overwhelming interaction between individual particles is considered to be surface friction during which particles slide on top of each other during extended contacts (Tardos, 1997). The soil mechanics theories use the idea of a yield function, which is a relation between the components of the stress tensor for a material about to yield, and a flow rule, which is a set of relations between the components of the stress and the rate of strain tensors.

The division of granular flow to rapid (collisional) and quasi-static (frictional) is somewhat arbitrary (Campbell, 2006). In reality both phenomena occur, with particles both sliding and colliding and energy being dissipated by both mechanisms (Tardos, 1997). However, it is extremely difficult to construct theoretical models capable of capturing both regimes: collisional and frictional. Analyses performed to date have consisted of simple ad hoc patching of results taken from the grain-inertia and the quasi-static regimes (Johnson and Jackson,

1987). The physical basis for such an assumption remains unproven, but it captures the two extreme limits of granular flow; the rapid shear flow regime where kinetic contributions dominate and the quasi-static flow regime where friction dominates. Srivastava and Sundaresan (2003) extended these models to include multiphase solid-gas flow. Their results show that the additive theory captures the qualitative features of such flows.

2.3.3 Challenges in the Continuum Description

The continuum description of granular flow and its closure for particle-particle interactions has received some criticism (Drake, 1991; Campbell, 2006). The justification for a hydrodynamic description and the detailed derivation of the form of the transport coefficients remains a topic of interest and controversy (Garzó and Dufty, 1999). The issues that challenge the applicability of the model to real granular flow are related to both the continuum description and the kinetic theory models, which describe particle-particle interactions.

Modelling the granular particles as continuum rather than discrete entities implies that the field variables, for example, the bulk density and mean velocity, vary continuously in space. Accordingly, the fields generated by solving the continuum models represent collection of particles, which behave in a similar fashion over a prescribed averaged time and space increment. In order to satisfy this assumption, the averaging volume must simultaneously satisfy two criteria: it must contain enough particles so that the variables of interest are statistically meaningful**,** yet be sufficiently small that changes in the variables across it are negligible (Drake, 1991). This is usually represented by the ratio between the averaging volume and the average particle separation distance (molecule in case of molecular gas). This ratio has been reported to be more than 100 (Gad-el-Hak, 1999). This condition might be violated in the granular flow due to two reasons depending on the flow condition. The first one is dilute flow in which the number of particles is very low and consequently their separation distance is high. The second one when the particles are relatively large compared to the domain (gradient) size where their large diameter contributes to the separation distance.

When considering the rapid flow regime, the conditions of the validity of the kinetic theory assumptions are less straight forward when compared to the continuum assumption. This is because the kinetic theory is built on various assumptions: Brownian motion of particles over time, molecular chaos and the separation between the microscopic and macroscopic scales.

In order to apply the kinetic theory to any particulate or molecular system, the micro scale should be completely separated from the macro scale (Reese, Gallis and Lockerby, 2003). This means that the collisions between particles occur on much lower time and length scales compared to the scale of change of macroscopic gradients (i.e. density, velocity). The microscopic length scale is the mean free path. It is defined as the average distance travelled by the particle between two successive collisions. Regarding the macroscopic length scale, it should have two features. It should be much larger than the microscopic length scale and much smaller than the length scale where large changes in the average quantities (i.e. density, velocity) occur. The ratio between this microscopic and the macroscopic length scales is Knudsen number. The microscopic time scale is the mean free time defined as the average time between two successive collisions. It is usually calculated using the velocity scale. The dimensionless number for the velocity scale is Mach number. Mach number represents the ratio between the macroscopic velocity and mean square velocity of fluctuations (temperature). The dimensionless number for the time scale is ‘Knudsen number times Mach number’ (Reese, Gallis and Lockerby, 2003). The diffusion is computed using Chapman-Enskog approximate solution of the Boltzmann equation. This can be regarded as power series expansions in Knudsen number (Chapman and Cowling, 1970).

For the case of molecular gases in normal flow conditions, the separation between the scales usually occurs. This is because the mean free length is of order of few microns and the mean free time is of order of few micro seconds. For a gas flowing in a domain of 1 cm and velocity of 10 m/s, the changes in the mean properties occurs on a length scale which is much higher than the mean free path. The change in the mean velocity also happens over a time scale which is much higher than that of the mean free time.

The continuum approach becomes problematic in some flow situations. We will give three examples of single phase gas flow. The first one is the during high speed flow in boundary layers. The variation of the flow velocity across the boundary layer thickness is high. This is because the flow velocity at the solid boundary is zero and at the boundary layer edge is the free-stream velocity. This means that the continuum approach might be problematic because the macroscopic length scale becomes of order of the mean free path. Furthermore, the well-known no-slip boundary condition at the solid walls might fail because the particles do not have sufficient time to reach equilibrium and also because the gradients are very high (Reese, Gallis and Lockerby, 2003). The relatively high Knudsen number is responsible for this behaviour as shown in Figure 2-7. This is a clear example of the problematic continuum description due to the lack of length scale separation.

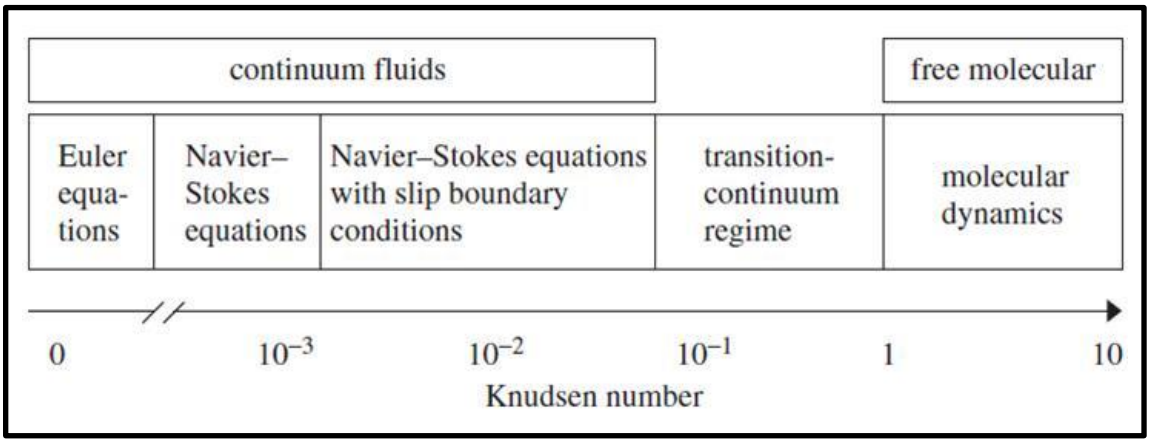

Figure 2-7: Regimes of applicability for various flow models over the range of Knudsen numbers (Reese, Gallis and Lockerby, 2003).

The second example is the rarefied flow. It occurs when the density of the gas is very low (usually at very low pressures). This means that the mean free length and times are relatively high. Accordingly, it is difficult to establish volumes where the variations over the particles' mean variables are larger than the mean free path. The same applies to the time scale where the variables change on a time scale comparable to the time between collisions. This example shows the macro and the micro scales are not separated because the flow is very dilute.

The third example is the supersonic flow. In this kind of flow, the particles move with a mean bulk velocity higher than the oscillating velocity of the particles. This oscillating velocity is a measure of the mean free velocity. Accordingly, the particles are not able to develop sufficient inter-particles collisions. Or the macroscopic movement is faster than the time in which particles reach equilibrium after three or four collisions (Reese, Gallis and Lockerby, 2003). A major result of this phenomenon is that the pressure waves are not transferred downstream the flow. This example shows the problematic continuum description due to the lack of the time scale separation.

Regarding the granular flow, the scale separation is less likely to occur for wider range of flow conditions when compared to molecular gas flow. This is mainly due to the obvious differences between the gas molecules and granular particles. In the kinetic theory of gases, the particles exhibit Brownian motion even if the gas is at rest. On the other hand, granular flows are highly non-linear and random Brownian motion is irrelevant (Müller et al., 2008). Consequently, an inhomogeneity of the mean flow is necessary to force the collisions and to drive the velocity fluctuations for a rapidly deforming granular material (Jenkins and Savage, 1983). This makes the mean free velocity of granular particles much less than that of the molecular particles. For example, the sonic velocity of gas under normal flow conditions is of order 300 m/s, while that of granular flow in fluidised bed is of order 1 m/s (Gidaspow, 1994). In order to satisfy the assumption of the kinetic theory for the hydrodynamic description, the gradients of macroscopic variables should be much lower than the scales of the microscopic motion (Brilliantov and Pöschel, 2010). However, this condition is rarely satisfied in real applications (Campbell, 2006). This low sonic velocity or granular temperature makes the flow supersonic for very small particle velocities. The small granular temperature will make the time scale separation an issue because the convective velocity of particles, which depends on the external forcing, might be comparable or even higher than the collisional velocity. Consequently, we will not be able to distinguish between the diffusive (microscopic) and bulk or macroscopic motion. This even challenges the relevance of granular temperature concept.

Some approaches are used to apply conditions to the granular gases that resemble the gas flow. The experiments using granular particles might be performed in micro gravity or using very light weight or hollow granular particles. Or the experiments are performed using a vibrating fluidised bed to ensure that the energy is supplied to the granular particles like the gas molecules. However, these experimental conditions are far from real applications such as the flow in hoppers, gas-fluidised beds or avalanches. Another difference between the practical granular flow and the gas flow emerges from fluctuations in the density of granular packing. Large changes in the packing fraction occur in granular systems; which are much greater than typical density variations in normal gas flow problems.

2.4 Discrete Element Method (DEM)

The discrete element method (DEM) treats each particle in the granular flow as a separate entity. This is done by solving the equations of motion and computing the trajectories for each particle. Consequently, DEM does not generate macroscopic fields as TFM. Furthermore, there is no need for constitutive equations describing particle-particle interactions as TFM. Accordingly, it overcomes the inherent challenges in the hydrodynamic models such as: regime identification, continuum description and scale separation. However, models for particle-particle interactions are still needed for solving the granular flow problems. Due to the fact that DEM solves the equations for every single particle or a collection of particles, this method needs high computational resources and the computational requirements increase significantly by increasing the number of particles. The number of particles increases when the particle size becomes small or the flow is dense.

The DEM does not require classification of regimes as that of TFM where the granular flow is classified in terms of rapid and slow flow. However, there are some simplifications that might be adequate to one of those regimes. There are two widely used approaches for DEM, which explicitly consider the particulate nature of granular materials and the particulate interactions. They are the hard sphere approach (Hoomans et al., 1996) and the soft sphere approach (Cundall and Strack, 1979). The main difference between those two approaches is by

the way in which particles interactions (contacts) are resolved. The hard sphere method was described in a previous section; however, its use in the DEM will need more details, which are described here.

For hard-sphere systems, these contacts are instantaneous and characterised by impulsive transfers of momentum. Furthermore, collisions occur between two particles only at a given time. The magnitude of the normal component of the post-collisional relative velocity is determined using the coefficient of restitution (i.e., a measure of inelasticity of the particles), whereas the magnitude of the tangential component of the post collisional velocity is based on parameters characterising the frictional interaction (e.g. friction coefficient). As previously mentioned, the hard sphere approach is used in the kinetic theory of granular flow for hydrodynamic models used in TFM.

Soft-sphere simulations treat particle-particle interactions as enduring contacts that generate forces, which change over the duration of the contact. Soft sphere assumption also allows multi-particle contacts at a given time. For soft-sphere systems, a force law is used to determine the magnitude of the force experienced by each particle based on the level of particle deformation during collision. A widely used model for the contact force is the spring-dashpot model (Johnson and Johnson, 1987; Thornton and Yin, 1991; Zhou et al., 1999). In this model, the particle mechanical properties (Young's Modules and Poisson's ratio) are used to determine the forces arising during the collision.

To sum up, the critical difference between these two contact models lies in the instantaneous, binary nature of collisions in the hard-sphere approach versus the enduring, multi-particle contacts utilised in the soft-sphere approach. These differences make the hard-sphere model more computationally efficient, though less robust than its soft sphere counterpart. Soft-sphere simulations can be used to simulate both rapid and slow flow, whereas hard-sphere simulations are only applicable to rapid granular flows.

Cundall and Strack (1979) developed the first DEM that was used to simulate dry granular flow. The coupling of the DEM with a finite volume description of the gas-phase based on the Navier–Stokes equations was developed by Tsuji, Kawaguchi and Tanaka (1993) for the soft-sphere model and Hoomans et al.

(1996) for the hard sphere model. As in the TFM, particle-gas interaction sub-models describing mainly the drag force are required to couple the two phases. The models are usually similar to those of TFM with some modifications to account for the form of equations and microscopic flow fields.

One of the key differences between DEM and TFM is that in TFM the solution of the equations describing the solid phase and the gas phase is performed on the same computational grid. This means that the domain is discretised for the equations of both phases. This approach cannot be applied to DEM modelling, because the position of each particle is not known and the trajectories of the particles are determined within the solution. Another key aspect of DEM is the type of algorithm used to advance particles in time. There are two types of algorithms; event-driven and time-stepped. Event-driven (predictive) algorithms (Allen and Tildesley, 1989) are mainly based on the collisions between particles. In these simulations, every particle is moved along its trajectory for the time needed to reach the next collision. Once that collision is resolved, the time to the next collision is determined, and the process is repeated. In this way, the simulation will proceed at varying time steps from one collision to the next. This type of algorithm is applied exclusively to hard-sphere systems. For time-stepped algorithms, all particles are advanced over a set amount of time. After this particle advancement, a check is performed to determine if any particle overlaps exist. Particle overlaps represent a collision between two or more granular particles. Once the collisions are identified, a contact model is applied and the simulation is then advanced again in time. The time step is set small enough so that numerical inaccuracies are minimised and collisions are detected. Because time-stepped models involve particle overlap, this algorithm is usually applied in conjunction with soft-sphere systems.

The computational time necessary to simulate a given period of real time flow depends on the time step employed in the simulation. For event-driven algorithms, the time step is determined by the time to the next collision, and this value changes for each subsequent collision. In general, dilute systems will result in larger time steps, while dense systems will have smaller time steps. For time-stepped algorithms, the time step is specified by the user. Smaller time steps will result in more accurate results; however, smaller time steps are

computationally expensive. While most time stepped algorithms use a constant time step, some efforts have been made to use variable time steps, for example, via adjustment of the time step based on parameters such as average collision overlap. This ensures that an efficient time step is used throughout the entire simulation (Hopkins and Louge, 1991). In either case, the choice of time step for time-stepped algorithms is always a trade-off between accuracy and computational time.

Search methods (Boyalakuntla, 2003) are used to provide information about neighbouring particles to identify the collisions between the particles. The search algorithm is one of the most computational time consuming during the solution of the equations, which forces the user to make a compromise between the efficiency of the solution and its accuracy. Another aspect of solving the DEM equations for solid phase with the Navier-Stokes equations for the gas phase is the solution of volume fraction of gas phase (void fraction). Integration should be performed over the control volume for the solid particles, so that the volume occupied by these particles is determined and after this the void fraction is determined.

2.5 Particle Properties

As previously discussed; particle-particle interactions play a prominent role in dense flow situations. The granular flow models are mainly concerned with the mechanics of motion of particles and the interaction mechanisms (collisional or frictional). However, the description of any granular flow situation requires certain knowledge of the parameters controlling these interactions. For example, the values of the restitution and the friction coefficients are essential inputs for both TFM and DEM models. The cohesive forces might also have some effects on the flow. The repeatability of experiments of dense granular flow is achieved when the particle parameters are constant.

The particle-particle restitution coefficient is an indication of the elasticity of the collision between particles. It has been reported that this coefficient has a strong effect in the modelling of multiphase systems (Goldschmidt, Kuipers and Van Swaaij, 2001). The restitution coefficient has both normal and tangential components. The restitution coefficient is most commonly measured using the

impact experiments (Foerster et al., 1994; Kharaz, Gorham and Salman, 1999). In this type of experiments, the particles are forced to collide with either other particles or a flat surface. Then the speed of the particle of interest is recorded before and after the impact. This allows the determination of the restitution coefficient. Although this method provides fair measurement of the normal component, measuring the tangential components is difficult with the impact experiments. It is also difficult to ensure that the impact is purely normal. Furthermore, the effect of the flow conditions before the impact on the value of restitution coefficient is not fully understood. For example, it is not clear how the relative velocity between the colliding particles affects the value of the restitution coefficient. The same applies to the particle-wall collisions. All these factors contribute to the consistency of the measured values of the restitution coefficient (Foerster et al., 1994). The friction coefficient is also one of the parameters, which affect the flow conditions. This friction coefficient depends on area of contact between the surface and the time of contact, velocities and probably other parameters.

In hydrodynamic or TFM models, the uncertainties in the particle properties affect the boundary conditions describing the interactions between the granular phase and the bounding walls. For the case of fluid or gas, the wall boundary conditions are assumed to be no-slip. This implies that normal velocity is zero and the tangential velocity equals to that of the bounding wall. However, this is not the case for granular flow. Despite having a zero normal velocity for the granular media at the wall, the tangential velocity is by no means zero (for the case of stagnant wall). The granular particles do not have low inertia as the gas molecules and hence, they are expected to slip at the wall (Stein et al., 2000).

Johnson and Jackson (1987) developed a partial slip boundary condition for hydrodynamic models. This wall boundary condition model has been used in several papers (Armstrong, Luo and Gu, 2010; Li, Grace and Bi, 2010). This model covers the two flow regimes: rapid and slow. In the slow regime, the angle of friction between the wall and the granular particles is used directly to compute the shear stress. For the rapid regime, the model uses two parameters for quantifying the collisions with the wall. The first parameter is the particle-wall restitution coefficient and it represents the normal interactions. The

other parameter is the specularity coefficient. This coefficient quantifies the tangential friction between the wall and the granular phase. It has a value of zero when the collisions are smooth and unity when they are rough. The exact value is usually selected to fit the experimental data (Li and Benyahia, 2012). Typical values used range from 0.1 for fast fluidisation in circulating beds to 0.5 for slow fluidisation in bubbling beds (Li and Benyahia, 2012). Recent efforts for accurately predicting the value of the specularity coefficient include a model developed by Li and Benyahia (2012) to compute the coefficient from first principles. It uses the particle velocity and angle of friction between the wall and the granular phase as inputs. However, this model is still in development and its implementation in CFD MFIX code has been done recently (Li and Benyahia, 2013).

The literature reviewed in this chapter has thus far considered non-cohesive solid particles only. However, it is very difficult to confirm that a collection of particles is non-cohesive for all flow conditions. Accordingly, much uncertainty still exists regarding cohesive behaviour. In general, cohesive forces can be divided into three types: Van der Waals force, liquid bridge force and electrostatic forces. The physical meaning of these forces is described as follows (Seville, Willett and Knight, 2000):

-Van der Waals force: It is an attraction force between the particles due to the electric charge of the molecules within particles (electromagnetic forces between electrons and protons of the molecules). It is a function of the diameter and the surface roughness of the particles.

-Capillary (liquid bridge) force: this force is due to fluid condensation in the gap between the particles. This condensed liquid causes a surface tension force to arise which is the main cause of liquid bridge force. In general, liquid bridge force is due to high humidity in the powder or in the surrounding environment.

-Electrostatic forces: this type of cohesive forces is due to the static electric charge of the particles and the potential difference between the particles. In general, the increase of electrostatic force comes at the expense of the liquid bridge force because increasing water content decreases the electric charge in the particles.

To sum up, the previous uncertainties in the values of particle properties increase the uncertainty in modelling the granular flow. The repeatability of the experiments is affected as well. This is mainly due to the change of particle properties during handling. The variation of surface properties between fresh particles and used particles is a simple example supporting this argument (Drake, 1991). These effects need to be taken into consideration during the interpretation of experimental results.

2.6 Multiphase Flow in DPI

The literature in studying multiphase flow in DPI covered several regimes of the flow in DPI. These regimes might be categorised into three physical processes that happen in the DPI. These processes are:

1- The overall device performance: the whole device is studied either computationally or experimentally.
2- The agglomerate breakup: the effect of fluidising air on the breakup of either poly-disperse or mono-disperse is studied.
3- The dense fluidisation: The fluidisation of the packed particles bed and the initial dense flow is studied. This is the main physical process of interest in this thesis.

2.6.1 Overall Device Performance

Coates and co-workers studied the performance of the Aerolizer® inhaler in a set of papers (Coates et al., 2004; Coates et al., 2005a; Coates et al., 2005b; Coates et al., 2007). The computational model employed in these studies was mainly a single-phase flow simulating the air in the inhaler. The Lagrangian particles are superimposed on the calculated air flow field in the post processing to determine the trajectories of the solid particles. The effect of grid and mouthpiece of the inhaler was studied by Coates et al. (2004). The experiments used to validate the simulations were based on Laser Doppler Velocimetry (LDV) techniques to determine values of the axial and tangential velocities at a large number of measurement points across the exit of the inhaler mouthpiece. The particle outflow from the inhaler was measured using a liquid impinger. Coates et al. (2005b) studied the effect of capsule spinning

using a liquid impinger. High-speed photography was used to get qualitative information of the spinning of the capsule. Coates et al. (2005a) investigated the effect of flow rate on the performance of inhaler. The experimental validation was done using liquid impinger. Coates et al. (2007) studied the effect of the shape of the mouthpiece on the flow in the inhaler.

A major drawback of the modelling approach in these studies is using the dilute Lagrangian approach. This approach is very simple in studying the flow in DPI and it is not applicable to any dense flow regions where the void fraction is higher than 1%. This is mainly because neither the inter-particles interactions, nor the inter-phase momentum exchanges (to gas phase), nor the volumetric effects (void fraction), are taken into account. Accordingly, it cannot be applied to the dense regions inside the inhaler where the inter-particle and inter-phase forces dominate. Regarding the experimental technique, using liquid impinger provides experimental data for the overall behaviour of the flow in the inhaler. However, it does not produce a detailed physical insight of the powder flow. Furthermore, despite using Laser Doppler Velocimetry (LDV) to measure the air flow variables (Coates et al., 2004), the particles flow variables, which are very important, were not measured.

2.6.2 Agglomerate Breakup

Danby (2010) employed a hybrid approach for modelling agglomerate break-up in DPI. This hybrid approach consists of one way coupling between the particles and a pre-determined gas flow field. The particle-particle interactions were modelled using DEM forces models. The study was performed for different cases of air flow field and for different blends of particles sizes. Both mono-disperse and poly-disperse powders were considered. Also different shear flow configurations (simple shear, elongational shear, and pure rotational shear) were studied. Despite the study provides a fundamental insight in the process of the agglomerate breakup, the model does not provide full coupling between the two phases.

2.6.3 Dense Fluidisation

Recently, the process of dense fluidisation in DPIs has received some attention. Versteeg and Wildman (2004) reported an optical technique for the study of powder fluidisation inside a simplified, optically transparent DPI metering chamber geometry. The dimensions of the test section were 250×100×22 mm and the arrangement was of impinging jet as shown in Figure 2-8. They used a system based on digital image analysis of high-speed video recordings of the transient powder-air flow interactions. Black-on-white images of the interaction of frictional, non-cohesive particles with an air jet flow were generated using backlighting. Image-processing techniques were subsequently applied to determine several aspects of the time-dependent properties that describe the development of the bed during the aeration of the powder. The paper concludes by pointing out how the proposed method could be used to improve the understanding of the limitations associated with current DPI metering chamber configurations, and help forward design of improved DPIs. Figure 2-9 shows the qualitative results of images for different types of powder.

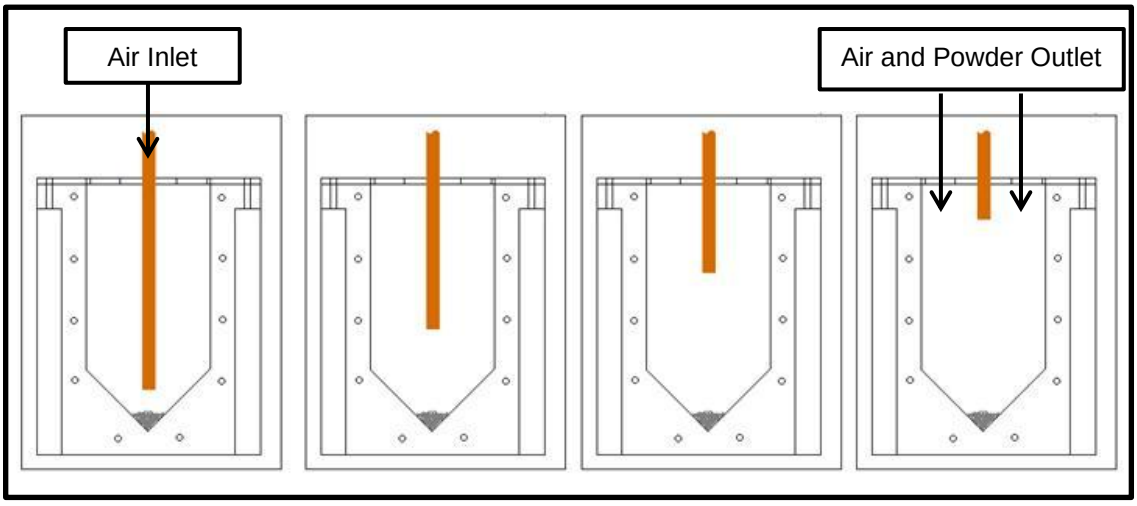

Figure 2-8: Configuration of fluidisation chamber of Versteeg and Wildman (2004).

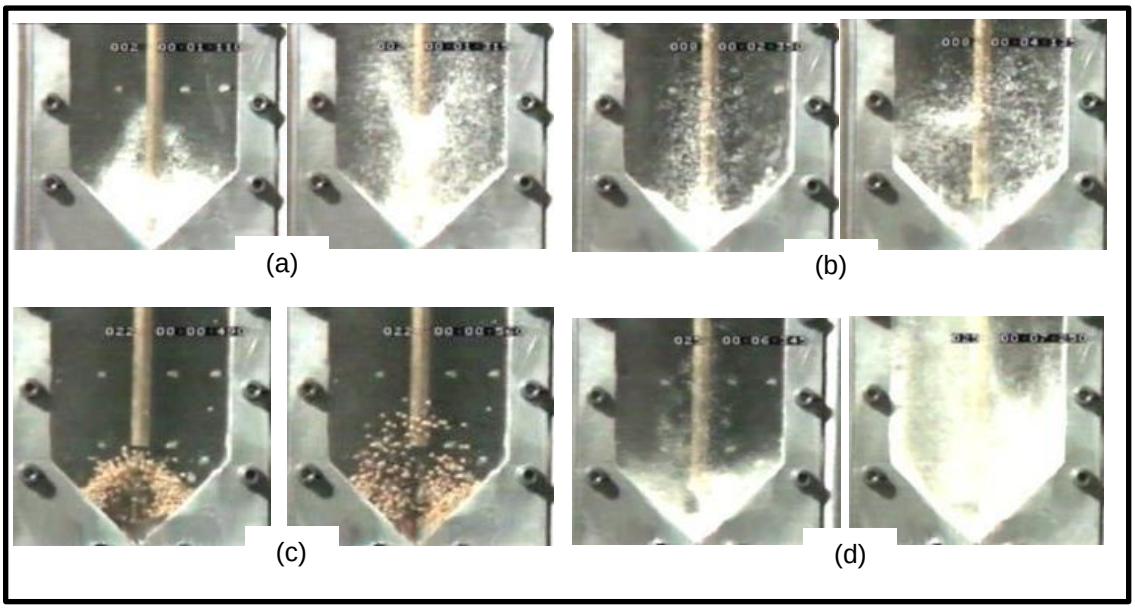

Figure 2-9: Versteeg and Wildman (2004) Images of fluidisation of different types of powder: (a) Milk Powder, (b) Castor sugar,(c) Yellow mustard seeds, and (d) Plain flour.

Subsequently, Versteeg, Hargrave and Hind (2005) used a similar optical technique to study the fluidisation of Lactose powder. The test section dimensions were of similar order of magnitude of Clickhaler®. The fluidisation chamber design and the images of the experiments are shown in Figure 2-10.

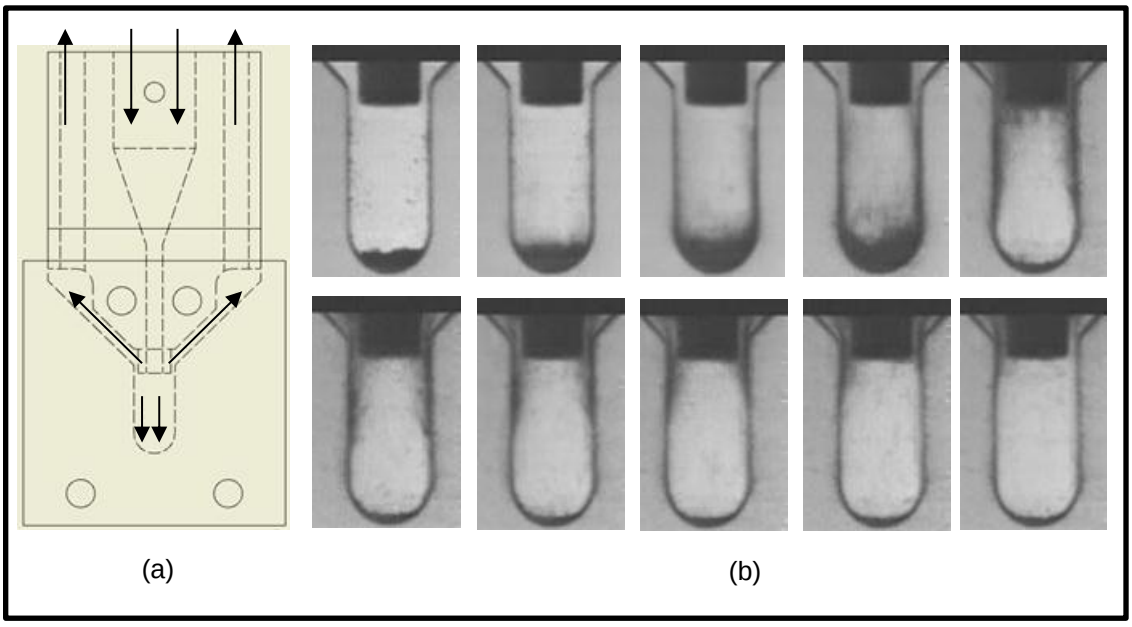

Figure 2-10: Experimental study by Versteeg, Hargrave and Hind (2005): (a) Fluidisation chamber design, (b) Images of the experiments.

Tuley et al. (2008) studied experimentally the process of fluidisation of densely packed solid bed. The experimental technique was based on high speed photography of the fluidisation process. The experiments provided qualitative results describing the entrainment of particles. Four different powder types were tested: spherical glass particles sized 0 to 50 μm, aluminium particle flakes in the range of 0 to 44 μm, lactose '6.0% fines', and lactose '16% fines'. The 'percentage fines' of the lactose refers to the mass fraction of particles smaller than 15 μm in the powder. The fluidisation mechanism for the non-cohesive particles (glass beads and aluminium particle flakes) was erosion, while that of lactose was fracture. The erosion noticed in weak cohesive glass beads means that the fluidisation process happens for the small particles without the entrainment of particles' agglomerate. While the fracture noticed in cohesive lactose means that the packed bed is broken into relatively large particles agglomerates due to the fluidising air. The difference between the fluidisation mechanisms of the two types of particles was mainly due to the cohesive forces in lactose in contrast to the non-cohesive glass beads particles. This type of experimental results provides qualitative information about the fluidisation patterns; however, it lacks the quantitative description of the flow on the particle level.

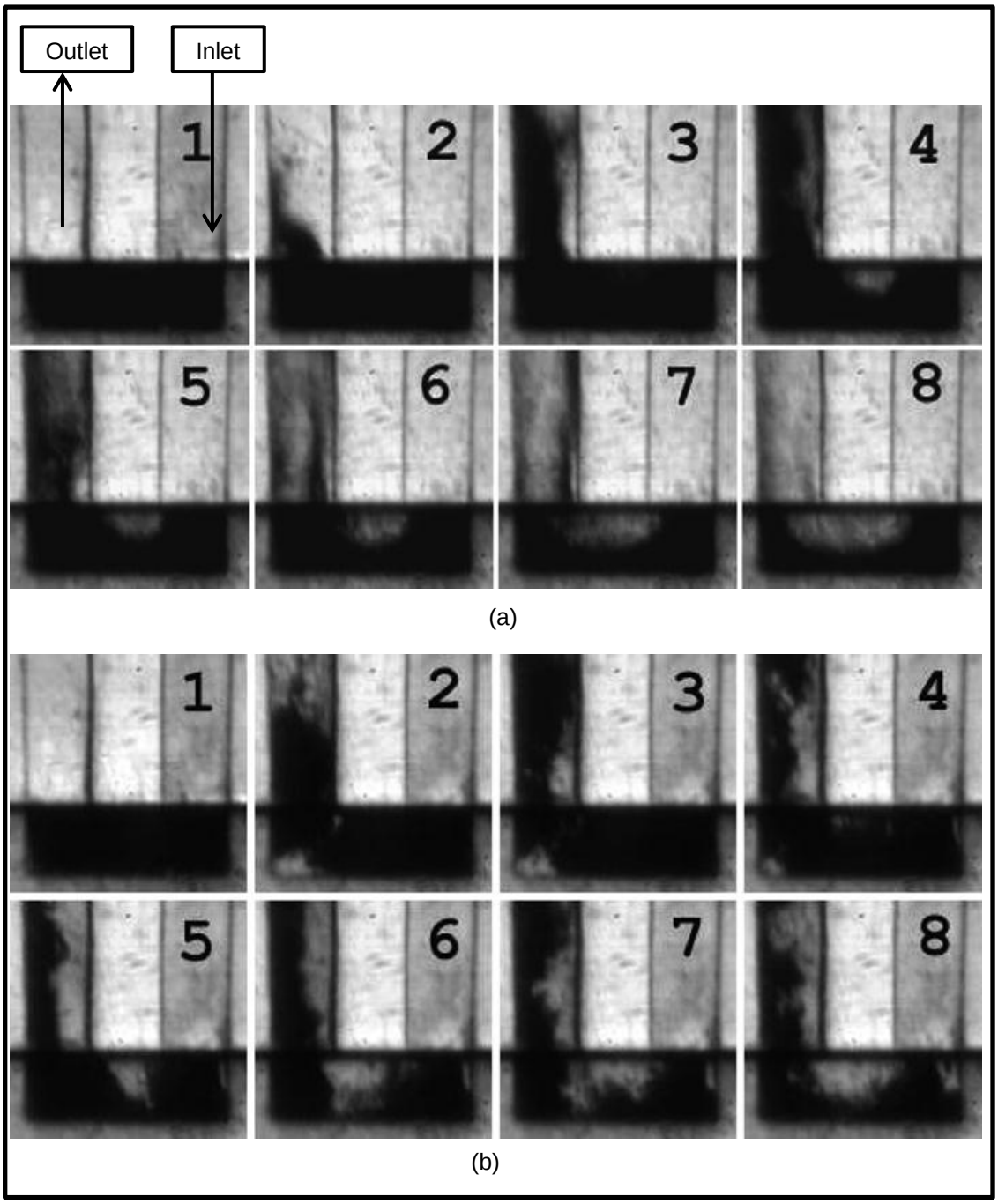

Figure 2-11: Optical images for fluidisation pattern by Tuley et al. (2008): (a) Non-cohesive glass beds, (b) Cohesive '16% fines' Lactose powder.

As shown in the figures in this section, the experimental results using optical technique are not capable of generating quantitative results of three-dimensional powder, due to images opacity in powder flow regions. This hinders the analysis of the images and even the description of the images is vague. Using computational modelling of multiphase flow during the fluidisation

stage provides detailed quantitative flow fields of powder variables. Tuley (2007) used a DEM multiphase flow model to describe the initial dense entrainment of the packed particles bed. The air flow was assumed to be constant with time, and it was assumed to be plug flow in spatial coordinates. This means that the effect of inter-phase interactions on the air flow field is neglected. Tuley (2007) reported that the computational predictions show qualitative agreement with the experimental results regarding the mechanism of particles' fluidisation for even simple one way coupled flow. This was based on snapshots of the particle phase fluidisation. However, those snapshots were not compared directly to the experiments. The computational approach provided quantitative results for the bed void fraction after post-processing. Figure 2-12 and Figure 2-13 show Tuley (2007) DEM predictions of the fluidisation for the mono-disperse glass beds and the Lactose '16% fines', respectively.

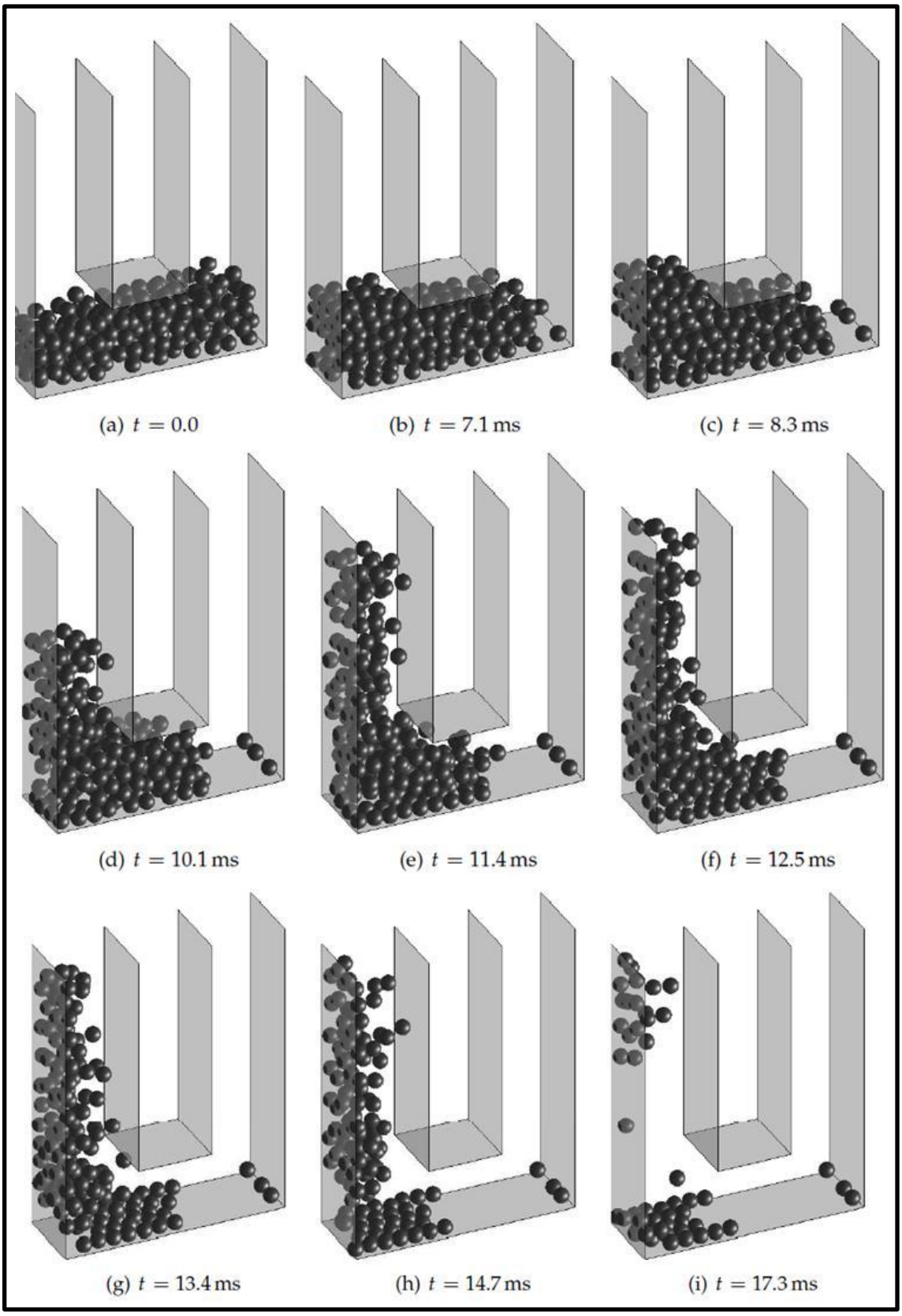

Figure 2-12: Tuley (2007) DEM predictions for the fluidisation behaviour of mono-disperse glass beds.

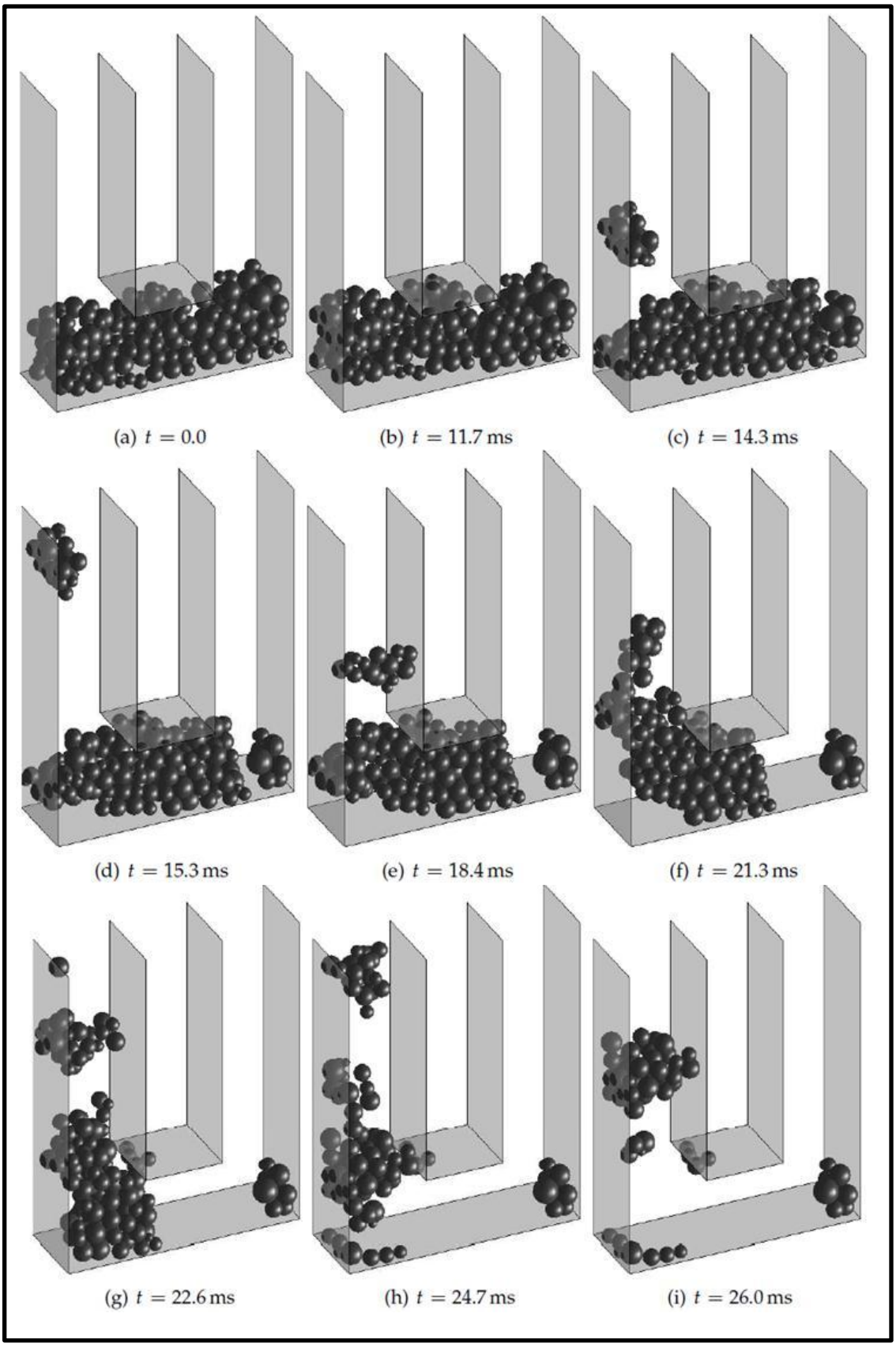

Figure 2-13: Tuley (2007) DEM predictions for the fluidisation behaviour of poly-disperse Lactose.

2.7 Summary

The review presented in this chapter covers the research in both the fundamentals and the applications of multiphase solid-gas flow. The fundamentals work is concerned with the dense multiphase flow. While the applications research is concerned with multiphase flow studies in DPI. Moreover, both computational and experimental approaches for studying multiphase solid-gas flow have been reviewed.

For the fundamental research, the experimental methods in studying multiphase flow are developing with increasing ability to measure individual particles variables. One important advantage for using advanced non-invasive techniques is the ability to study the granular flow on a micro or particle scale. This allows us to test the validity of multiphase flow models in general and the hydrodynamic models in particular. Testing the hydrodynamic models is crucial because its current version suffers from possible causes of physical inconsistency. This ranges from the hydrodynamic continuum averaging and scale separation to the classification of regimes between collisional and frictional. The review shows that high speed photography is considered the most appropriate experimental technique for studying granular flow in DPI.

Regarding the applications research, applying multiphase flow models to study fluidisation and dense flow in DPI has not received great attention. The previous studies tried to assume certain conditions (dilute Lagrangian) which are not applicable to the dense flow and fluidisation. The use of DEM for fluidisation has been reported once (Tuley 2007) with very simplified assumptions such as the one-way coupling and plug air flow. Furthermore, the use of TFM in studying the dense flow in DPI has not been reported in the literature. The experimental validation of the models used is not comprehensive because the experimental methods used do not generate quantitative results on the particle level. We think that one of the main problems in the previous research of multiphase flow in DPI is the lack of framework or context for comprehensive study. This appears in both experimental and computational approaches. An initial step towards developing a framework for studying multiphase flow in DPI would be using one of the multiphase models such as

TFM or CDEM. In this thesis, we decided to use TFM since it requires less computational resources and hence, it might be used initially to explore various flow conditions in DPIs. Furthermore, we decided to use an optical technique with a two-dimensional multiphase flow test section to study the multiphase flow in DPI. This technique is capable of generating high spatial and temporal resolution results. This will allow us to obtain quantitative results on the micro or particle scale. This type of results will have two obvious advantages. The first one is to describe the fluidisation in a very rigorous way by providing the results for the variables such as the instantaneous velocity vectors. The second advantage is to validate the hydrodynamic models on the particle scale, which is considered the smallest scale in granular flows.

Chapter 3 : Experimental Setup

3.1 Introduction

This chapter gives a detailed description of the experimental setup used in this thesis. The main aim of this chapter is to develop an experimental test rig, which is capable of replicating the fluidisation and the initial dense multiphase flow of particles in DPI. In order to overcome the weaknesses of some of the previous studies, the test rig is developed to generate quantitative results describing the particle and air flow. However, this requires some simplifications of the test section compared to the complicated flow configuration and particle type encountered in practical DPI configurations.

Some studies (Versteeg, Hargrave and Hind, 2005; Tuley, 2007) used high speed photography to record images during the granular bed fluidisation. However, the resulting images only provided qualitative information because the particles were neither detected nor tracked during the experiments. In this thesis, we use the two-dimensional test section (Martin et al., 2005) in order to overcome this issue and track all particles throughout the experimental time and test section domain using high speed photography. This will give us a full picture of the solid phase flow. The air pressure at the inlet and outlet of the test section is measured using fast response pressure transducers, since it is difficult to measure the air flow inside the multiphase test section.

The flow in a typical DPI is characterised by rapid fluidisation of the powder dose. The flow is highly transient since the powder pocket should be empty by the end of the patient's suction time (around 3 s). Accordingly, the air flow should be strong enough to cause this rapid fluidisation and entrains all the solid particles. The main focus is to generate an experimental case where the inlet air flow can achieve this condition. However, in order to study different fluidisation patterns of the particle bed, the air flow rate needs to be varied to investigate its effect on the fluidisation regimes. This will generate different flow cases of fluidisation where part of the bed is fluidised and some particles

remain stagnant in the bed. Accordingly, we would be able to draw more general conclusions about the dynamics of particle fluidisation.

Further simplifications are necessary with regard to the type and size of particles and the flow configuration. The drug particles used in DPIs have a size of 5 μm while that of the lactose carrier have a size of 50 μm. Consequently, their size is very small even if the lactose particles are considered and the drug particles are discarded. This small particle size introduces many difficulties in handling and measuring. Firstly, the cohesive forces increase significantly as the size decreases. This complicates the study and diverts the objectives from studying the hydrodynamics to studying the surface forces. Secondly, it is more difficult to manufacture particles of regular shapes (i.e. spherical) when they have small size. Accordingly, we are more likely to lose shape uniformity when we choose smaller particles. This will have two consequences on the flow. It will introduce one more level of uncertainty in the models used in the computational approach. This is because the models for irregular shapes are far less mature compared to those of the spherical regular shapes. Moreover, it is more difficult to track the irregular shapes using image processing. Thirdly, using this small particle size would be challenging in the two dimensional test section proposed for this study.

Based on the previous simplification of using large particles, the domain size should be increased. Its size will be larger than a typical DPI in order to accommodate those large particles. Furthermore, the powder pocket used in this study has a rectangular shape, in order to simplify the flow configuration and minimise the effects of complex geometry. A main challenge is how far this simplified test section from that of the DPI. In the design phase, the flow configuration was chosen to be simple but retains the physics and the configurations of the impinging jet.

The test rig tries to achieve an unsteady flow condition in the effort to replicate the flow conditions induced by a patient’s inhalation. This is achieved using an air pump to drive the air flow. This pump gives a ramp shape of the air flow, which satisfies the transient air flow in the inhaler but without its exact shape.

3.2 Description of the Test Rig

The test rig used here consists of four main components:

1- The multiphase flow test section represents the fluidisation chamber of an inhaler with simplified geometry.
2- The pneumatic rig provides the air flow through the test section in order to approximately replicate the fluidisation regime in a Dry Powder Inhaler (DPI).
3- The optical rig captures the movement of the solid particles during each experiment.
4- The control and acquisition rig controls the experiments and acquires the experimental data.

3.2.1 Multiphase Flow Test Section

The main aim of the multiphase flow test section is to study the flow of an impinging air jet over a packed solid bed. The scale of the experiment is larger than a typical DPI in terms of particles and domain size. The test section consists of a main aluminium body, two Perspex sheets, two rubber sealing gaskets and bolts for assembling. The details and CAD drawing are given in Appendix A. A schematic diagram of the main flow region of the test section is shown in Figure 3-1. The elevation view shows that the test section has a rectangular shape of width 50 mm and height of 90 mm. The thickness (depth) of the test section is 4 mm. The particles are packed at the bottom of the test section throughout its width and with a height of 30 mm.

The test section has an internal design, which creates an impinging air jet flow configuration. At the top left hand side of the test section, there is an inlet port for the air flow. This port has a depth of 4 mm, which is equal to the test section depth. The test section design contains an internal wall with a width of 10 mm. This internal wall forms a passage with a width of 10 mm and height of 60 mm for the inlet air to flow towards the powder bed. This passage ends at the top of the solid particles bed, thus creating an air jet, which strikes the solid particle bed after the air enters the test section.

At a distance of 10 mm from the right hand side of the test section, an air outlet port of 10 mm width is found. A wire mesh is fixed at this outlet port. This wire mesh acts as a semi-permeable membrane, which allows the air to flow through it and prevents the solid particles from escaping from the test section. Furthermore, this wire mesh allows us to focus on studying the fluidisation and dense flow regime by keeping the particles inside the domain, making it easy to repeat experiments without the need to dismantle the test rig and refill it with particles between tests.

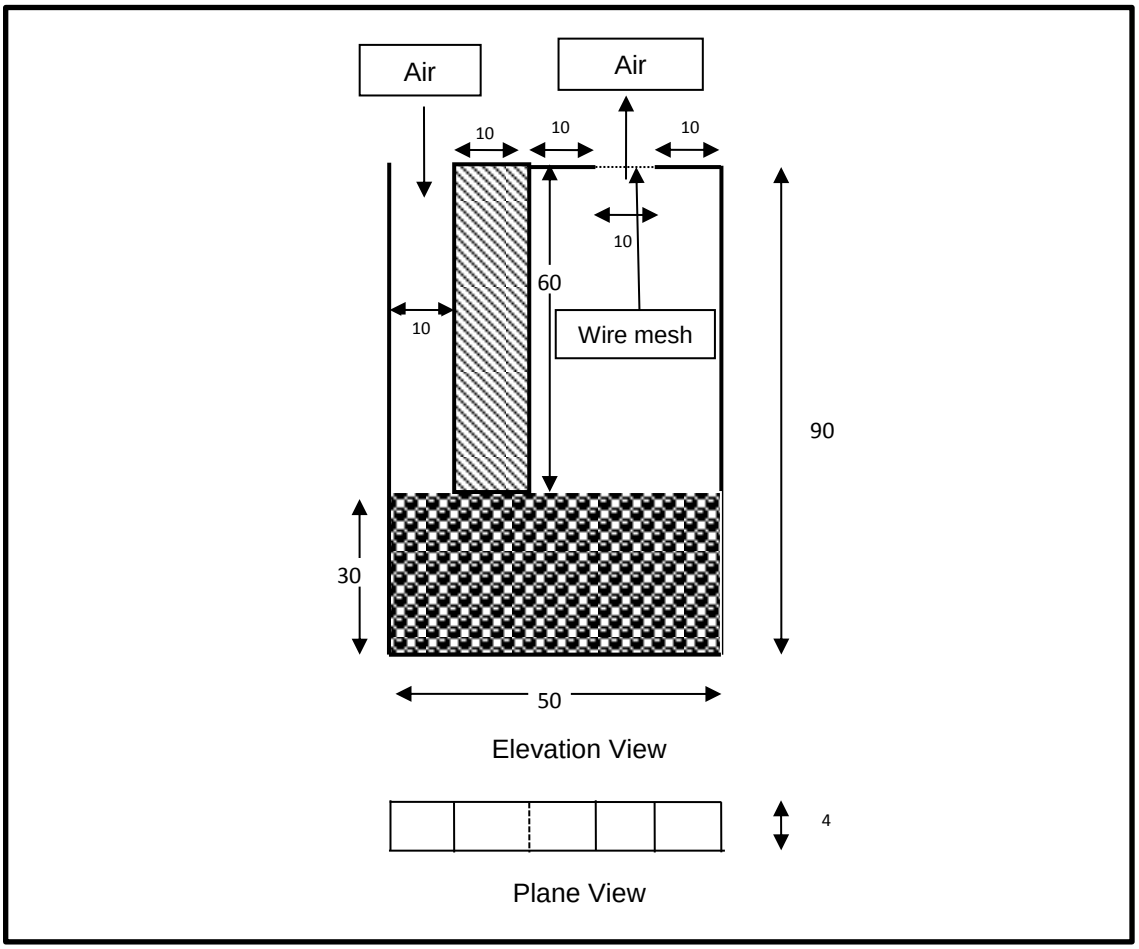

Figure 3-1: Schematic diagram of the multiphase flow test section.

The particles used in this experiment are ballotini (density 2500 kg/m^3) from Cole-Parmer® with a spherical shape and average diameter of 3.85 mm. They can be considered non-cohesive particles due to their large diameter and material properties. Using this type of particles provides a main simplification to the flow in DPI. This simplification allows us to focus on the hydrodynamics of

the dry powder inhalers and avoiding the complex effects resulting from cohesion and non-spherical particle shape. The depth of the test section is 4 mm, i.e. slightly larger than the diameter of the particles, which is around 3.85 mm. Accordingly, a single particle nearly occupies the whole depth of the test section, thus creating a pure two-dimensional test section. This makes it easy to identify every single particle, because each particle stands alone throughout the depth of view. Consequently, light rays are not blocked from any particle by another particle lying behind. The test section dimensions were scaled up to accommodate the larger particles. However, the ratio between the particle diameter and the test section is relatively high or in other words, the number of particles is small. This choice was made so that the test section and particle size fit with the camera resolution (section 3.2.3) and the particles are detected correctly. Figure 3-2 shows an image of the initial condition for one the experiments. It shows the test section with the air flow path and packed solid particles.

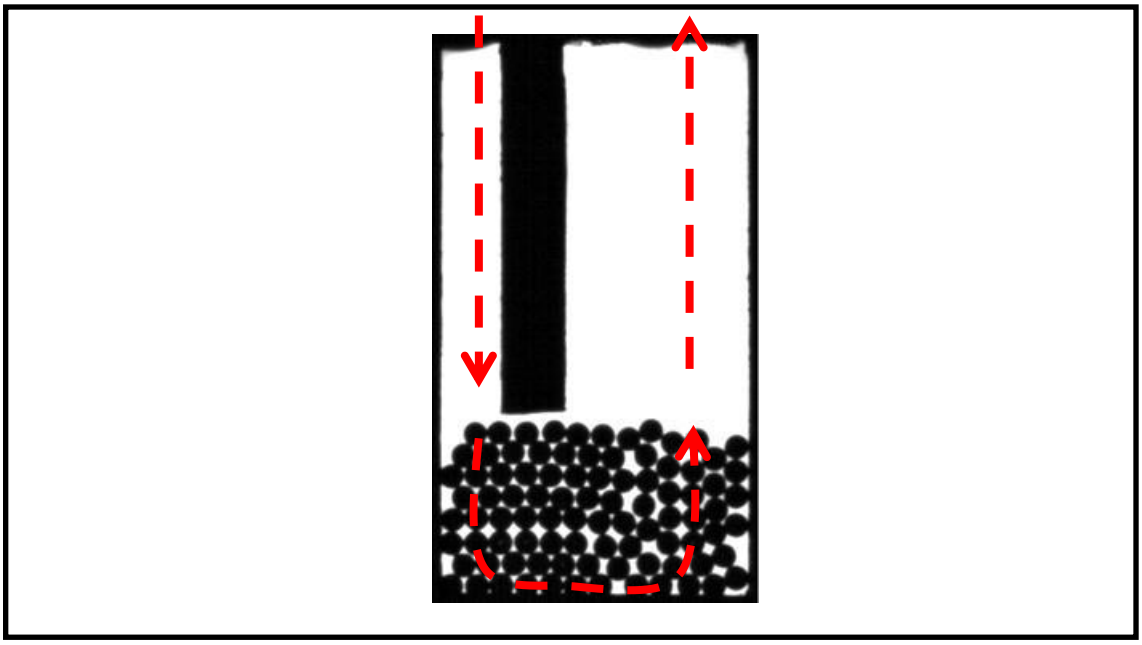

Figure 3-2: Image of the initial condition of the multiphase flow test section.

3.2.2 Pneumatic Rig

The pneumatic rig is used to supply the air to the multiphase flow test section and measure the air inlet and outlet pressures. A schematic diagram of the pneumatic rig is shown in Figure 3-3, while photos of its components are shown in Figure 3-4. Figure 3-3 shows that a vacuum pump (2) is used to drive the system and suck the atmospheric air into the air circuit. Using a vacuum pump creates a negative pressure inside the test section, and hence minimises air leakage. It also replicates the suction process induced by the patient in dry powder inhalers. The pump's model is a Speedvac RB10 from Edwards High Vacuum Ltd. A model 6213 solenoid valve (8), obtained from Christian Bürkert GmbH & Co. KG, is used to turn on and off the air circuit. It is a 2/2-way valve and its default position is normally closed. Its operating voltage is 24 V and power 10 W. A choking nozzle (7) is used to control the amount of air that flows into the circuit. Using different sizes of nozzles allows the air flow rate to be controlled. Three cases of inlet flow rate are studied. Two of them use two nozzles with diameters of 2 and 3 mm. While in the third case the nozzle is not included which provides the highest air flow rate. This allows the generation of three fluidisation cases, which, for the chosen particles and test rig dimensions, depend on the air flow rate. The test section (1) contains the particles, which are fluidised due the effect of the air jet which enters this test section. Two Kistler model 4262A pressure transducers of piezoresistive type (3,4) are used to measure the transient pressure at the inlet and outlet of the test section respectively. A high speed camera (5) is used to capture the images of the fluidisation. These images are saved on a PC (9). The whole rig is controlled using a control unit (6) and a PC (10).

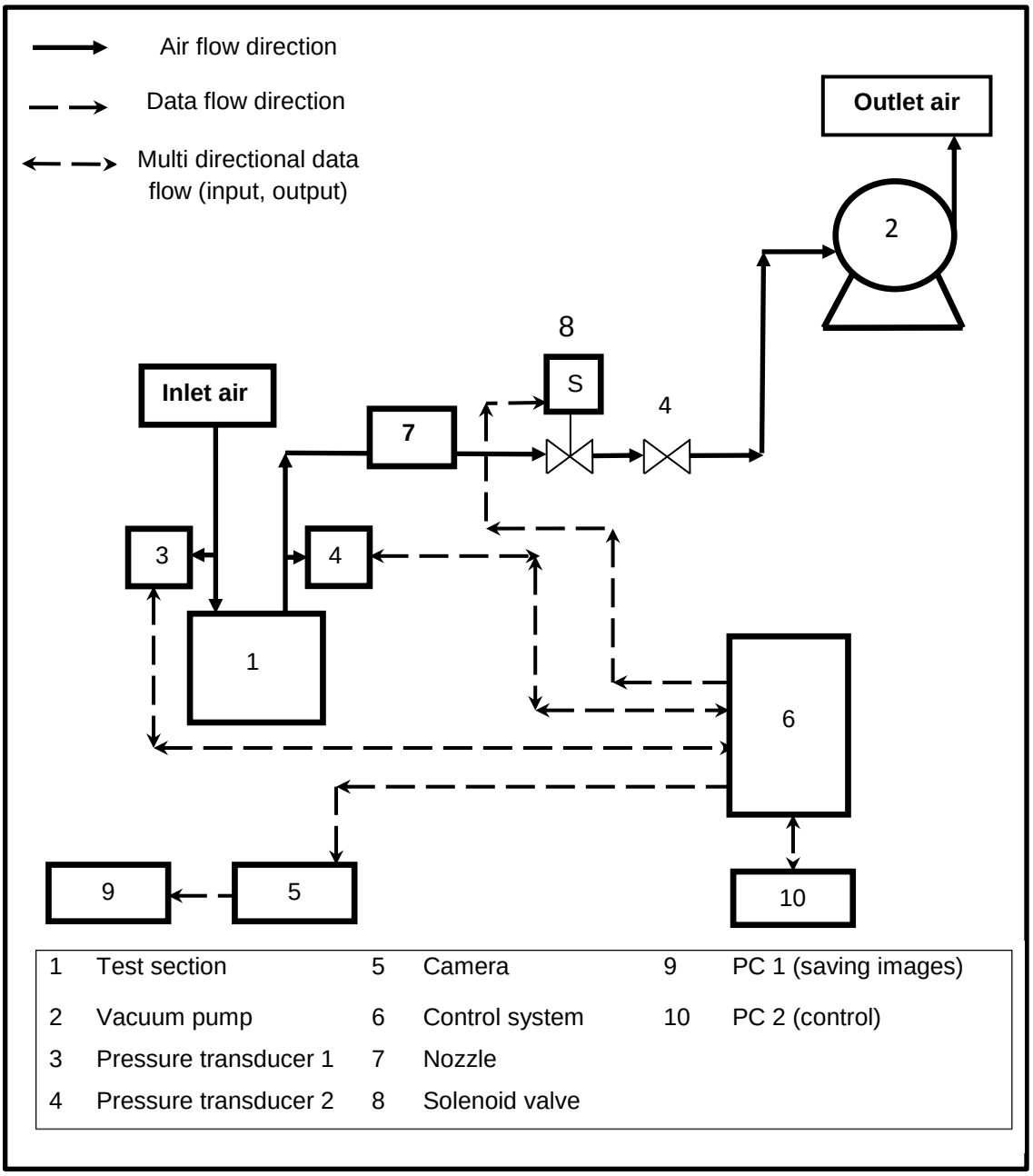

1	Test section	5	Camera	9	PC 1 (saving images)
2	Vacuum pump	6	Control system	10	PC 2 (control)
3	Pressure transducer 1	7	Nozzle		
4	Pressure transducer 2	8	Solenoid valve		

Figure 3-3: Schematic diagram of the pneumatic rig.

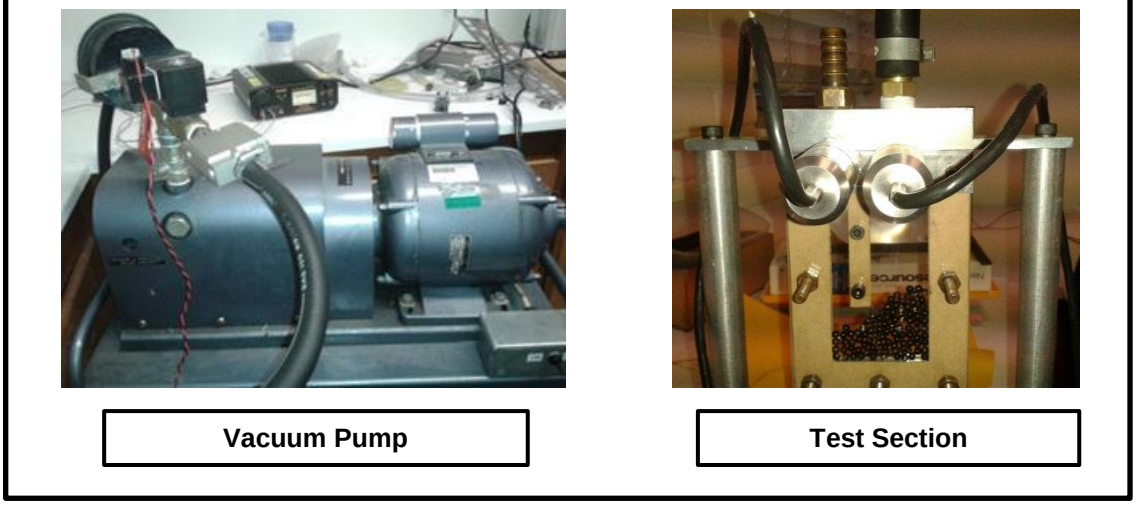

Figure 3-4: Photos of the components of the pneumatic rig.

3.2.3 Optical Rig

The optical rig is used to capture the movement of the solid particles during the time of the experiment. The main aim of capturing these images is to process them and compute transient particles positions and velocities. A schematic diagram of this optical rig is shown in Figure 3-5. The test section (4) is back-lit using a DC lamp (1), glass optical diffuser (2) and a lens (3). The movement of particles within the experimental time is captured using a high speed camera (5). The light source is a Tungsten-halogen spot lamp supplied by Comar Optics Ltd with a DC power supply unit. It has a maximum voltage of 12 V and power of 75 W. Its central intensity is 11200 cd and full beam angle 14º. Adjustment of the DC supply voltage and current provides control of the light intensity. The main motivation for using the DC current is to avoid the fluctuations in the intensity of light between different image frames associated with alternating mains current (AC), whose frequency is 50 Hz. The camera is capable of capturing up to 1000 frames/s, whereas the light intensity fluctuates at 50 Hz. This does not give a constant background of images throughout the experimental frames. The direct current does not suffer from this problem since it has constant supply voltage and current with time.

The optical diffuser (2) has a square shape whose side is 100 mm and thickness of 3 mm, and is used to achieve a uniform illumination throughout the test section. It is made of ground glass which gives a weak diffusion with a diffusion angle of ± 10º. The lens (3), whose diameter is 200 mm, is used to collect the incident light of the lamp and concentrate it on the test section and prevent it from scattering.

The model of the camera (5) is 'HCC-1000 V 1.2' obtained from VDS Vosskühler GmbH. It is a high speed-high resolution camera. Its recording speed varies with the adjusted resolution. It is capable of recording up to 1825 frames/s when the resolution is 1024 × 256. When used with a full resolution of 1024 × 1024, its speed is reduced to 462 frames/s. For the current experimental setup, the resolution is adjusted to 1024 × 512 with a spatial resolution of 100 µm/pixel. The recording speed corresponding to this spatial resolution is 923 frames/s. This trade-off between the spatial and temporal resolution gives the best results for particle detection and tracking and will be discussed in more detail in section 3.4. The camera has an internal memory of 1024 Mbytes at the operating recording speed. This is equivalent to 2000 images, which allows a total experimental time of around 2 s at the selected frame rate. The images captured by the camera are saved in its internal memory then exported to the PC (6) for processing and analysis. Figure 3-6 shows photos of the camera, halogen lamp and diffuser.

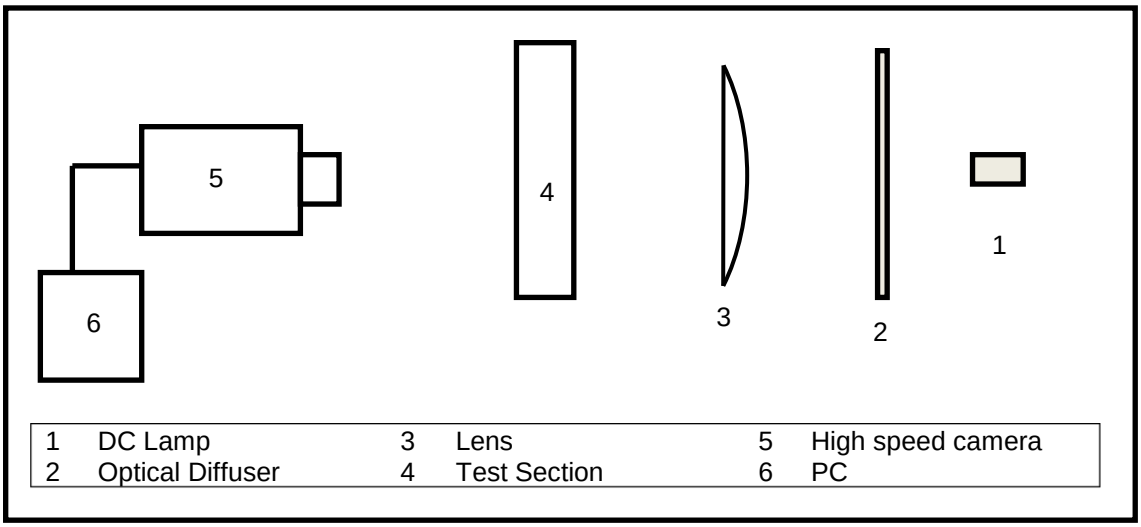

Figure 3-5: Schematic diagram of the optical rig.

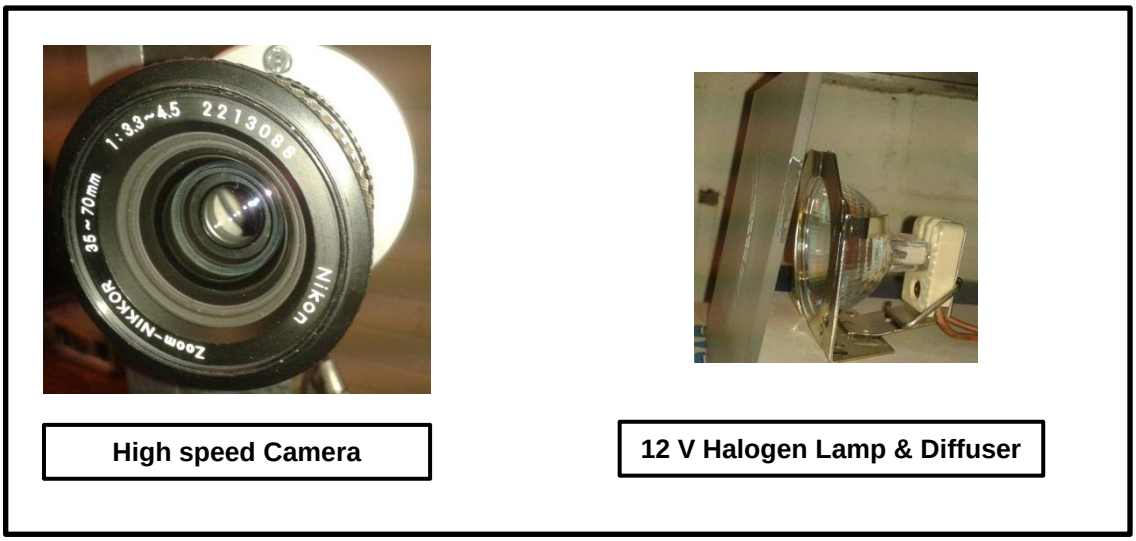

Figure 3-6: Photos of the components of the optical rig.

3.2.4 Control and Acquisition Rig

Since this test rig was mainly developed to study the process of highly transient fluidisation with typical time of inhalation around 3 s and time for fluidisation likely to be even less. Therefore, experimental control and data acquisition are required to a high degree of precision to capture this time varying behaviour. The solenoid valve needs to open as quickly as possible. The camera needs to start capturing images and the pressure transducers should record data as soon as the solenoid is opened. This is achieved by using real-time control and fast response measurement devices. For this purpose, a control and acquisition rig is developed. Figure 3-7 shows the dual instruments control and data acquisition system and arrangement.

The data acquisition and control unit consists mainly of chassis (2) (cDAQ-9174, NI). This chassis hosts several components used in the control process. These components are: analogue voltage input module (3) with a range of ± 10 V (NI 9201), sourcing digital voltage output module (4) (NI 9472), and a DC power supply unit (5) (PS-2, Output: 24 VDC, 0.8 A; Input: UK 240 VAC). The chassis is connected to a PC (1). This PC provides the interface for the control and acquisition of experimental data. The software (interface) used is ‘LabView’ from ‘National Instruments Corporation’.

The power supply unit (5) is used to supply electric power to the digital output unit (4). This output unit is used to supply electric power to the inlet (8) and outlet (9) pressure transducers (24 V), camera trigger (7) (at 24 V, 5 mA) and solenoid valve (6) (at 24 V, 10 W). The output voltage of the transducers (1-6 V), which represents the value of pressure, is extracted via the analogue voltage input module (3). A control and acquisition routine is developed using the program 'LabView'. This routine controls the opening of solenoid valve, hardware triggering of the camera and the excitation of the pressure transducers through passing a digital electrical signal to their terminals. Furthermore, this routine manages the data logging representing the pressures measured by the transducers. Figure 3-8 shows photos of the components of the control and acquisition system.

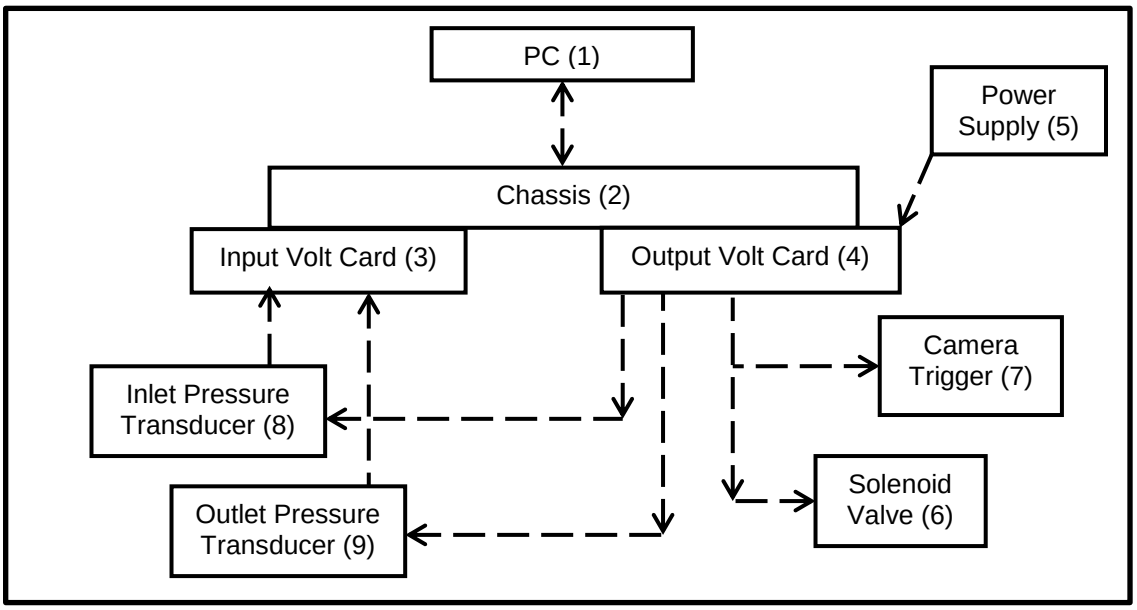

Figure 3-7: Schematic diagram of data acquisition and control rig.

Figure 3-8: Photo of data acquisition and control rig components.

3.3 Experimental Measurements and Procedure

The test rig described in the previous section is used for measurements of gas phase pressure and particulate (solid) phase movement. The gas phase measurements are the inlet and the outlet gauge pressures to the test section. Both pressure transducers record the pressure reading every millisecond. The voltage obtained by the transducer is transformed into pressure using the calibration data of the transducers. Regarding the solid phase, the raw images acquired by the camera are saved and analysed to measure the particulate phase flow.

The following steps summarise the procedure used to run a single experiment.

1- The choking nozzle is checked to achieve the required air flow rate.
2- All electric connections are checked and all devices are turned on.
3- The camera parameters are adjusted, and it is left in the standby mode (state, mode) waiting for the electric signal which triggers the recording process.
4- The vacuum pump is turned on.
5- The ‘LabView’ routine is initiated, this will lead to the execution of the following steps simultaneously:
    - Opening of solenoid valve to initiate the air flow.

- Excitation of pressure transducers for measuring inlet and outlet pressures.
- Hardware triggering of the camera to start recording images.
- Output voltage for both pressure transducers is recorded on the PC.

6- Images are recorded for analysis.
7- The LabView routine is stopped.
8- Images are transferred from the camera memory to the PC.

3.4 Analysis Techniques for Particle Flow

For every experiment performed, the images obtained are analysed in order to measure instantaneous particle variables. These variables are the individual particle positions and velocities in every frame. Once the position and velocity of each individual particle are known in each time frame, macroscopic variables such as the average void fraction and average velocities can be established. An in house 'Matlab' code was used and modified in order to process the images of the particulate phase flow and extract the relevant data.

Figure 3-9 shows the flow diagram of the Matlab code used. A copy of the Matlab Code is presented in Appendix B. The image processing and analysis code consists of two main parts. They are the particle detection part and particle tracking part. The particle detection part is used to detect every solid particle in each frame. This is done by using the Hough transform technique (Warr, Jacques and Huntley, 1994; Wildman and Huntley, 2000). The underlying principle of this technique is to detect the black particles on a white background. Each pixel in a given frame is read by the code and the intensity of light in this pixel is determined. This enables the code to detect the edge (boundary) of each particle when there is a sudden change in the gradient of the intensity of light in the pixel at the interface. Then the centre of each particle is determined based on the known diameter. After each particle is detected, an integer index is assigned to each particle in each frame. This prepares the analysis to be developed to the second part which is particle tracking.

Now the information obtained from the detection part is used in the tracking part. The position of each particle in every time frame is now known. The main

problem is to match the particles in two consecutive frames. This is done by ensuring that every particle is allowed to move a distance less than or equal 90% of the particle diameter. This distance is chosen, because different particles cannot overlap; the minimum separation distance between two different particles equals to the particle diameter in case of contact. Since the distance travelled by a particle for a given air flow rate is not known a priori, the validity of this criterion to track the particles correctly in conjunction with a chosen frame rate must be investigated using a trial and error approach. In experiments, the moving distance between two consecutive frames was varied from 10% to 100% of the particle diameter. It was shown that for the fastest flow all the particles move a distance less than 80% of the particle diameter. Accordingly, using an allowable distance of 90% ensures that all the particles are tracked. This is a simple deterministic approach for particle tracking which is different from the stochastic method used in PIV. The large diameter of particles made it possible to use this approach since they move less than a particle diameter between two consecutive frames.

The individual particle velocity $u_p(t)$ is obtained using direct forward numerical differentiation of its position between two consecutive frames. The following equations describe this operation:

$$u_{p,x,k}(t) = \frac{X_{p,k}(t + \Delta t) - X_{p,k}(t)}{\Delta t} \tag{3.1}$$

$$u_{p,y,k}(t) = \frac{Y_{p,k}(t + \Delta t) - Y_{p,k}(t)}{\Delta t} \tag{3.2}$$

X_p and Y_p are the horizontal and vertical positions of the particle, respectively. t is the time frame of the experiment, and Δt is the time increment between two consecutive frames. x and y are the horizontal and vertical direction, respectively**.** k is an index for the particles

Once the instantaneous velocities of all the particles are determined for all the frames, the positions and velocities are then used to obtain average quantities

describing the packing (volume) fraction and average velocities over spatial regions of interest.

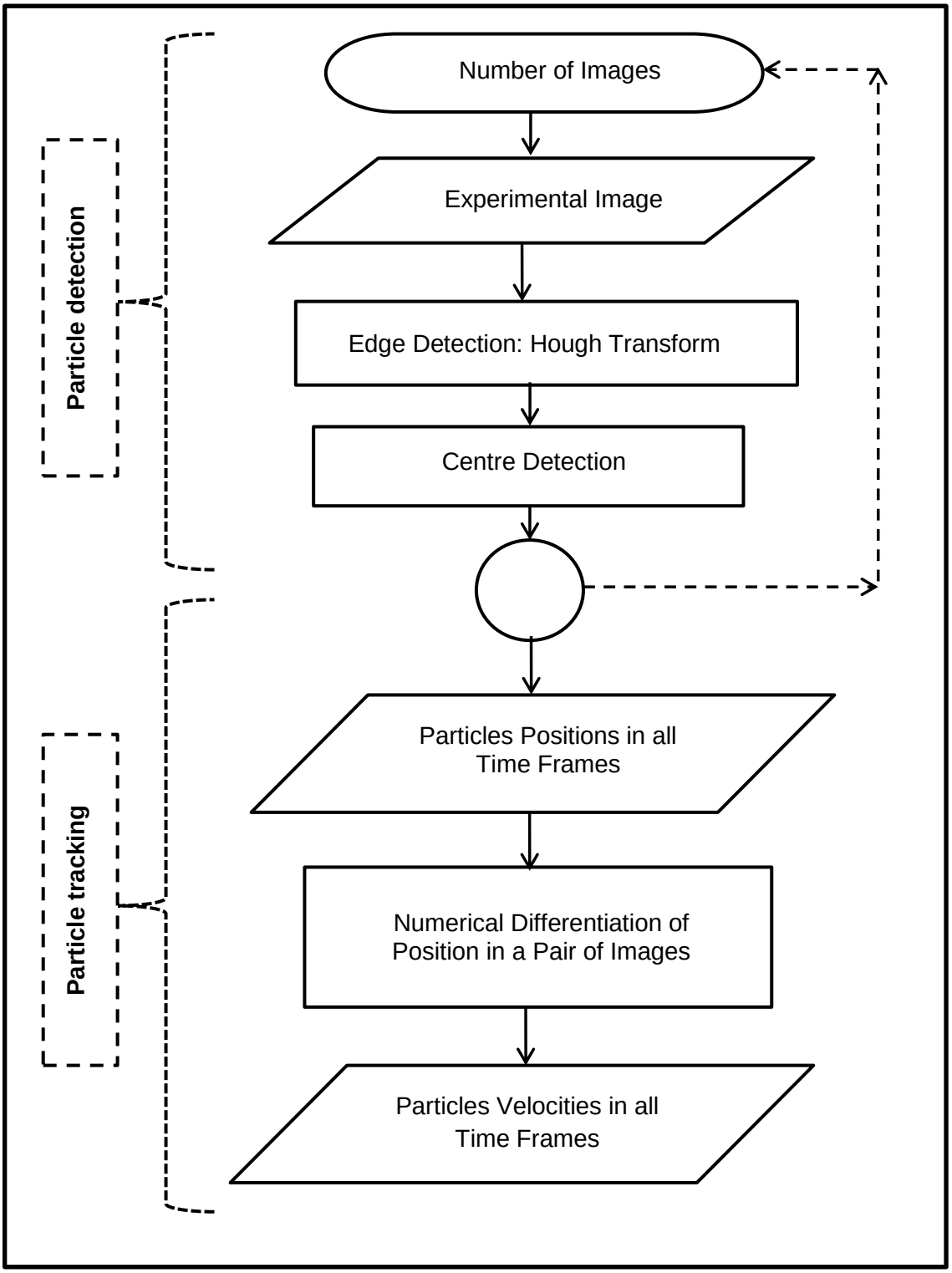

Figure 3-9: Flow diagram of the particle detection and tracking 'Matlab' code.

3.4.1 Average Flow Variables

In order to perform a quantitative analysis of the results, the domain is divided into different regions to compute spatial average properties (e.g. packing or void fraction and granular velocity) over each region. The main aim here is to generate quantities which describe the average particle flow which allows macroscopic representation of the granular phase which also benefits the comparison with simulations. Figure 3-10 shows the regions in the test section. The region ‘ABCD’ is named the ‘bed region’ where all the particles are initially packed. The region ‘IJCE’ is named the ‘freeboard region’ which is occupied by air only at the beginning of the experiment. The region ‘GHFD’ is the inlet jet region. The jet region does not contain any particles at any time during the experiments, and hence it is not included in the analysis. Accordingly, the bed region and the freeboard region are the two regions of interest. These regions are chosen based on the physics of the flow in this configuration. The bed region is the initial fluidisation region where particles start to move. On the other hand, the freeboard region is the region where the flow of particles develops. It is clear that there is a strong connection between the two regions and the flow in the freeboard region depends on that of the bed region.

Next, the area-averaged void fraction and the area-total velocity of the particles are defined. These variables are instantaneous and no time average is performed. A particle is considered to be in a certain region when its centre lies within that region.

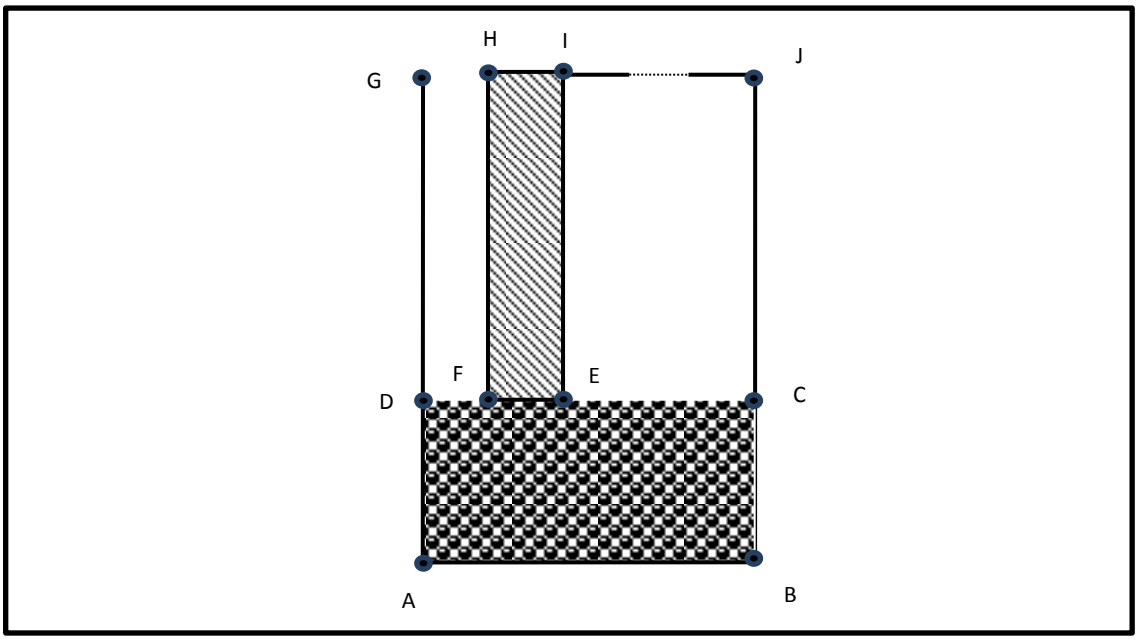

Figure 3-10: Test section sub-regions.

3.4.1.1 Average Void Fraction

Average void fraction $\overline{\varepsilon_g}(t)$ is defined as the total volume of the region minus the total volume occupied by the particles in that region. It can be expressed as:

$$\overline{\varepsilon_g}(t) = V - \frac{\pi {d_p}^3 N_p(t)}{6} \tag{3.3}$$

V is the total volume of the region. d_p is the particle diameter and $N_p(t)$ is the total number of particles in the region of interest.

3.4.1.2 Total Particles Velocity

The particulate phase velocity vector over a certain spatial region is defined as the total velocity of individual particles in this region. This is different from the average particle velocity (Brilliantov and Pöschel, 2010). It should be interpreted as the total momentum of the particles per unit mass for a certain region. Representing the velocity using this definition was found to be more appropriate in our case where the particles move from one region to another and hence the average particle velocity will not be representative of the whole flow situation (dense vs. dilute).

For the case of horizontal component of the total velocity U_x (x-momentum per unit mass) it is computed as follows:

$$U_x(t) = \sum_{k=1}^{N_p(t)} u_{p,x,k}\,(t) \tag{3.4}$$

, and the total vertical velocity U_y (y-momentum per unit mass) is defined as:

$$U_y(t) = \sum_{k=1}^{N_p(t)} u_{p,y,k}\,(t) \tag{3.5}$$

3.5 Test Cases

In this thesis, three flow cases will be presented with different air pressure difference across the multiphase flow test section. The main aim of varying the pressure difference is to study different regimes of fluidisation. This is because the speed and the amount of fluidised particles will change due to the strength of the air jet. This air jet velocity is a direct function of the pressure difference. Figure 3-11 shows the final conditions of the experiments for the three cases.

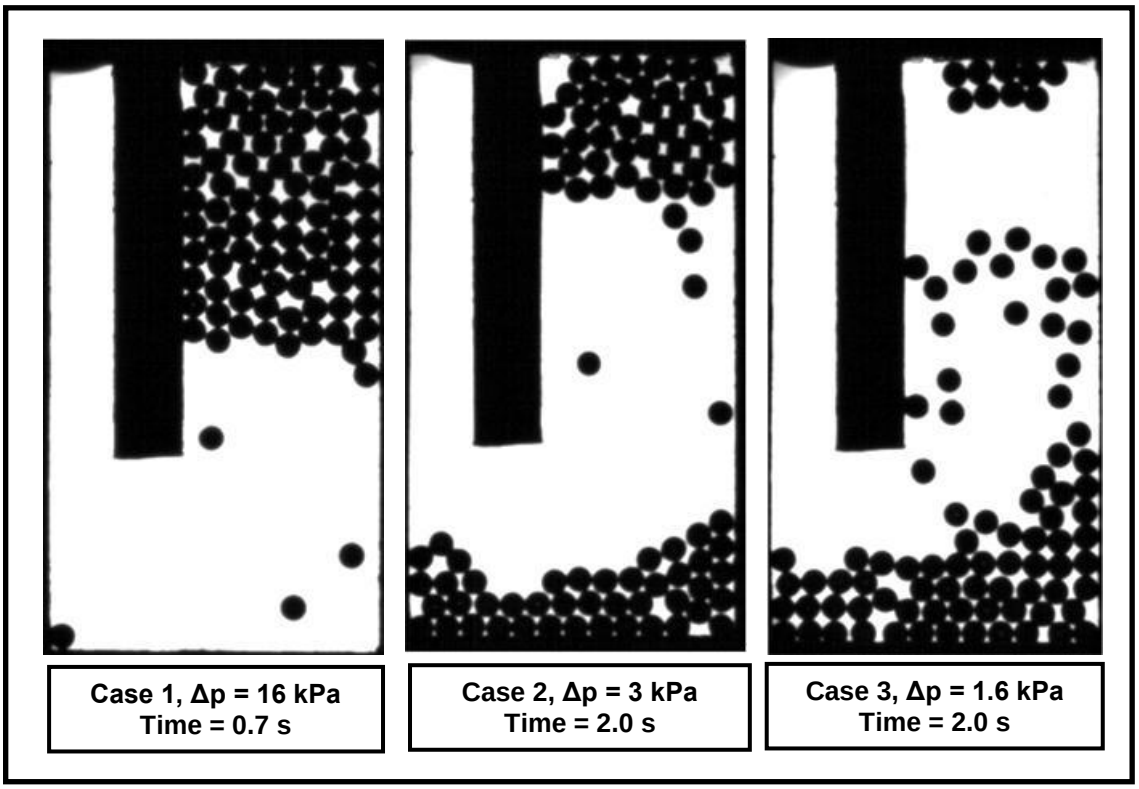

Figure 3-11: Images of test section showing final conditions of the solid phase in different test cases of the experiments.

The experiment for each case is performed five times in order to investigate the repeatability. The variables presented are the pressure difference, average void fraction and total granular velocity. The ensemble average $\overline{\Upsilon}(t)$ of the five experiments for any variable $\Upsilon_n(t)$ is defined as:

$$\overline{\Upsilon}(t) = \frac{\sum_{n=1}^{5} \Upsilon_n(t)}{5} \tag{3.6}$$

The standard $\Psi(t)$ deviation is given by:

$$\Psi(t) = \frac{\sqrt{\sum_{n=1}^{5} |\Upsilon_n(t) - \overline{\Upsilon}(t)|^2 / n}}{\overline{\Upsilon}(t)} \tag{3.7}$$

n is an index for the experiment number within the ensemble.

3.6 Error Analysis

Due to the complications of the experimental technique used in measuring particle variables, the uncertainty analysis of the results is not a straightforward process. The code consists of two parts; particle detection and particle tracking. Some complications are associated with particle detection; occasionally some particles are not detected. Fortunately, this happens only in the densely packed stagnant regions, so this does not affect the velocity results. Velocity vector maps will show a gap where a particle was lost, but the effect on the total velocity (momentum per unit mass) of the relevant region is negligible. The effect on spatially-averaged values of void fraction was also small, again because non-detection errors occur in the densely packed regions. Loss of two or three particles for a total number of particles of order 100 corresponds to an uncertainty of the order of 2%. In the tracking part, the spatial resolution (100 μm/pixel) will have an effect on the value of the particle velocity. For a typical particle movement of 2 mm between two consecutive frames, the spatial resolution gives an estimated average uncertainty of 5%.

3.7 Summary

This chapter has described in detail the experimental setup used in the thesis. The measurements, experimental procedure and the control of each

experiment were outlined and presented. The test rig is automated in order to control the flow and acquire measurements based on images of the particles at each instant in time as function of air pressure difference. The air pressure difference and, hence, the air flow rate is the only independent variable used in this experiment. Three different values of pressure differences (16, 3 and 1.6 kPa) will be considered in order to investigate the effect of inlet air jet on the fluidisation pattern.

The two-dimensional test section is capable of generating images where the individual particles are detected by the image processing algorithms based on the Hough transform. The images obtained during a single experiment are processed in order to determine particle positions and velocities. The macroscopic variables of the granular phase are defined in order to extract the time varying spatial averages over the main regions in the flow domain. These variables are the average void fraction and total velocity.

The results obtained from this experimental setup will be presented in Chapter 4 and Chapter 5. Chapter 4 will present the experimental results in case of 16 kPa pressure difference. Chapter 5 will present the experimental results for 3 kPa and 1.6 kPa pressure differences.

Chapter 4 : Experimental Study of Particle Bed Fluidisation Using Strong Impinging Air Jet

4.1 Introduction

In this chapter, the experimental results for case one (Chapter 3) with high pressure difference (16 kPa) are presented and analysed. This flow causes full fluidisation of the particle bed and hence, this is the desirable regime in DPIs. The results are obtained using the setup presented in Chapter 3. The experimental setup used a two-dimensional multiphase flow test section as a prototype for the inhaler. High-speed photography of the particles was used in the two-dimensional test section described in Chapter 3.

There are two types of results, air flow results and particles (solid phase) flow results. The air flow results consist of the inlet and outlet pressure applied at the boundaries of the test section. They provide boundary conditions for the computations and determine the strength of the air jet by providing the pressure difference across the test section. The particle flow results are those obtained using the particle detection and tracking code presented in Chapter 3. The particle flow results are divided into two types:

1- Whole flow field results which show the images using the high speed camera and instantaneous velocities of each particle. The particle images and velocity vectors are used to describe the flow regime and provide a general picture of the whole flow behaviour.
2- Average void fraction and total particles velocity obtained in bed and freeboard regions of the test section (section 3.4.1). These variables are used to obtain quantitative results for the particulate phase flow in each region, which allows comparison with numerical simulations.

4.2 Initial Conditions

The experiments are repeated for five times in order to investigate their repeatability. Figure 4-1 shows the first frame for the particles for the five experimental runs. It was nearly impossible to replicate the same initial

configuration of particles. However, the average initial packing fraction of particles in the bed was similar for all experimental runs (0.5).

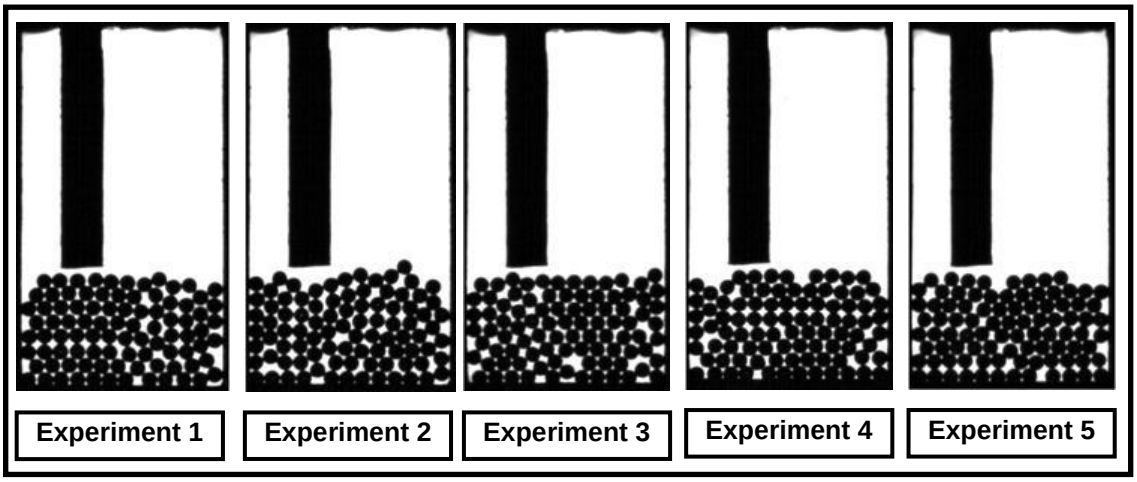

Figure 4-1: Initial frame for different experiments within the ensemble, case one.

4.3 Gas Pressure Difference Boundary Conditions

Figure 4-2 shows the pressure difference between the inlet and the outlet (air boundary conditions), which drives the air flow through the test section. This difference is initially zero until a time of 0.018 s; and when the solenoid is opened, the pressure difference increases rapidly. A pressure difference of around 15000 Pa is reached at a time around 0.04 s. After this, the pressure difference decreases to 13000 Pa until 0.075 s. From this time, the pressure difference undergoes a small increase to reach 16000 Pa at the end of the experiment.

The pressure losses between inlet and outlet come from two main sources. The first source is the losses due to the expansions and contractions in the flow area throughout the test section. The second source of losses is due to the interaction with the solid particles. This includes momentum transfer between the gas phase and the particles due to the drag force exerted by the air on the particles. This drag force leads to losses in the energy of the air and hence its pressure.

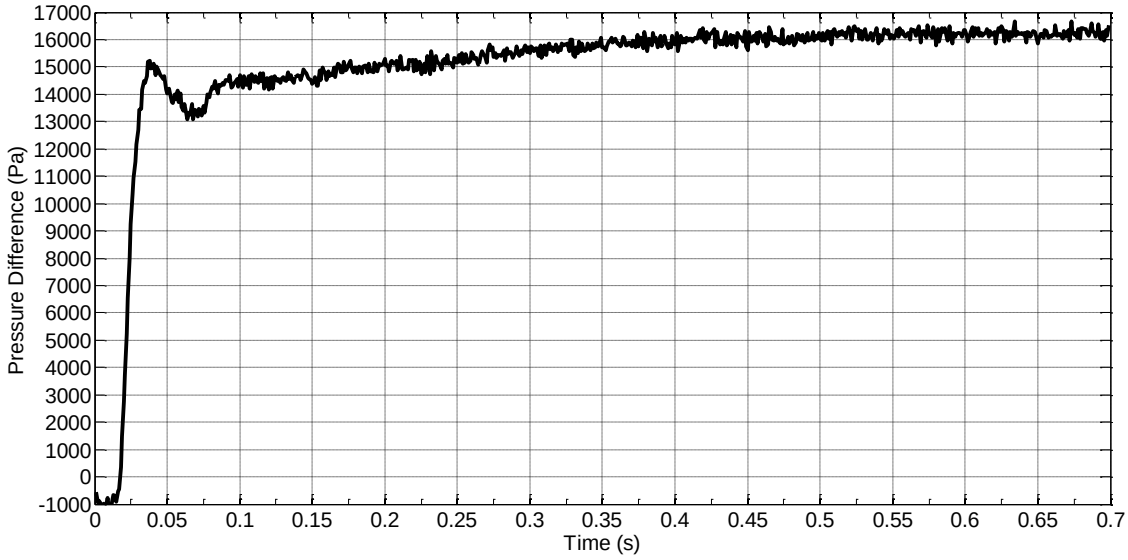

Figure 4-2: Ensemble average of pressure difference versus time, case one.

Figure 4-3 and Figure 4-4 show the relative and absolute standard deviation of the pressure difference respectively (section 3.5). In Figure 4-3 the fluctuations in the pressure, which are obtained in different experiments, are around 3-4% with very few overshoots up to 6%. The absolute standard deviation in pressure difference is between 200 Pa and 800 Pa as shown in Figure 4-4.

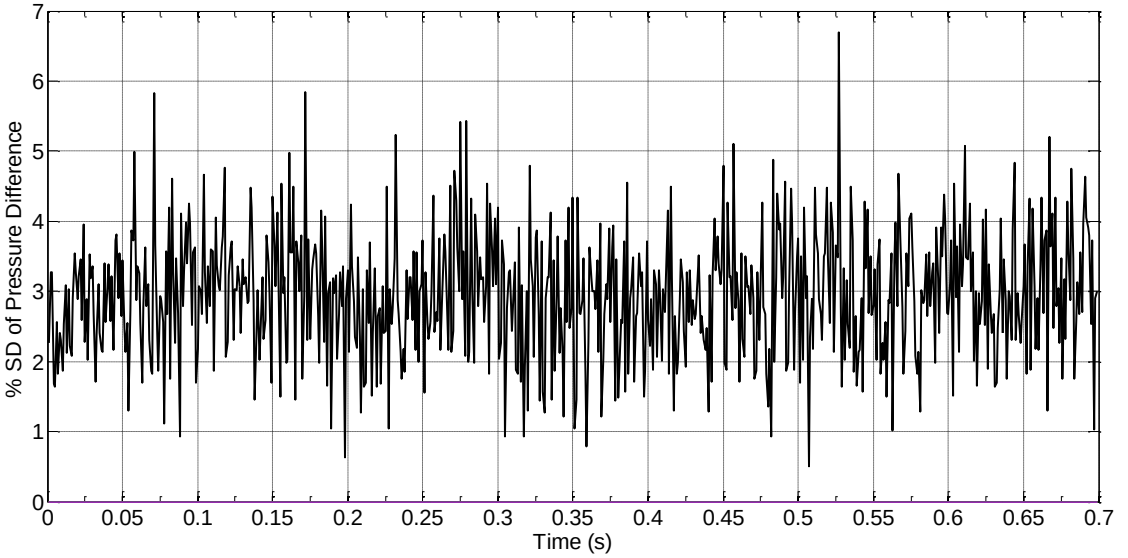

Figure 4-3: Percentage of standard deviation of the pressure difference versus time, case one.

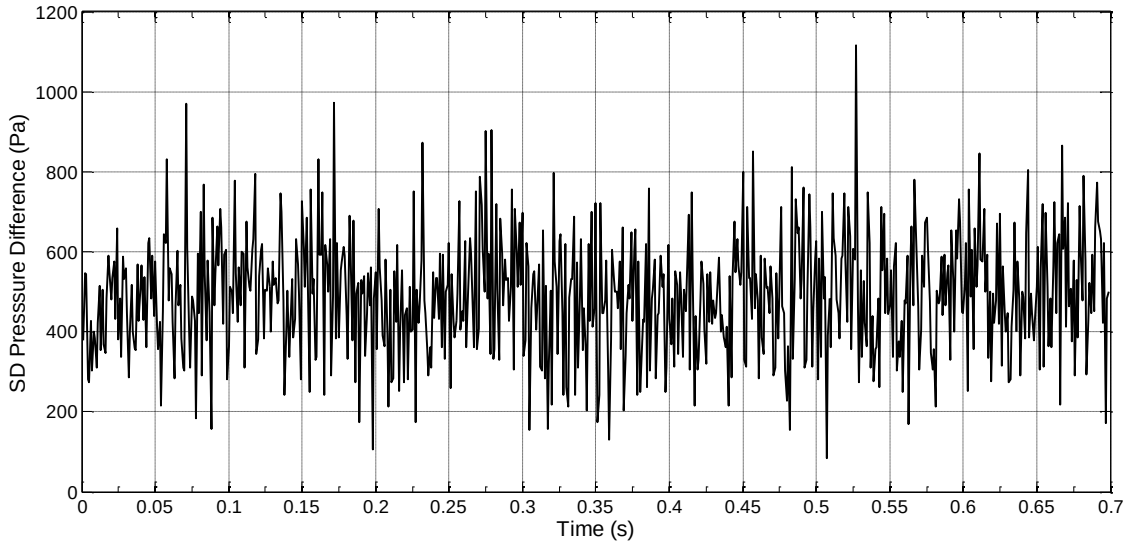

Figure 4-4: Absolute standard deviation of the pressure difference versus time, case one.

Throughout the experimental results of the pressure difference presented in this section, fluctuations around the mean value of the pressure difference are observed. This is noticed in the ensemble average and the standard deviation as well. The main cause of this observation might be due to turbulence, vibrations, flow of the positive displacement vacuum pump, pressure waves, and particle flow. Furthermore, the results suggest that the experiments are highly repeatable for the values of the pressure because of the low percentage (3-4%) of standard deviation within the ensemble.

4.4 Particles Whole Flow Field

In this section we present the flow of particles obtained using images captured by the camera. Figures (4-5 and 4-6) show the images of the particulate phase at different times and the velocity vectors of individual particles corresponding to these times.

In Figure 4-5, the particles are packed in the bed region with no movement until a time of 0.022 s. This is consistent with the pressure difference results presented in the previous section (Figure 4-2). The pressure difference is nearly zero at the beginning of the experiment due to the response time of the solenoid. When the solenoid is opened, the inlet air comes through these

particles and strikes the bed. This triggers the movement of the solid particles due to the drag force exerted by the air. At a time of 0.028 s, there is a slight movement of few particles at the top layers of the bed. These particles are moving horizontally to the right direction and vertically upwards. This indicates that the particles follow the expected air flow direction. At time of 0.047 s, it is clear that the velocity of the particles inside the freeboard becomes higher. Furthermore, some particles leave the bed region and flow to the freeboard region. As soon as these particles leave the bed region and embark into the freeboard, their horizontal component of the velocity decreases and the vertical component increases. This is because the air flow direction is nearly vertical in the freeboard region at time 0.047s. At time 0.072 s, the remaining packed particles in the bed region are fluidised. Furthermore, at this time some of the particles have reached the top of the freeboard region. These particles stay inside the test section because the wire mesh mounted at the top of the test section blocks their potential exit. Between the top and the bottom of the test section, some particles move with nearly vertical velocity component. At time 0.088 s, some of the particles moving in the freeboard region at time 0.072 s are packed against the wire mesh at the top of the freeboard. The fluidisation of the particles in the lower layers continues in a similar mechanism to the top layers.

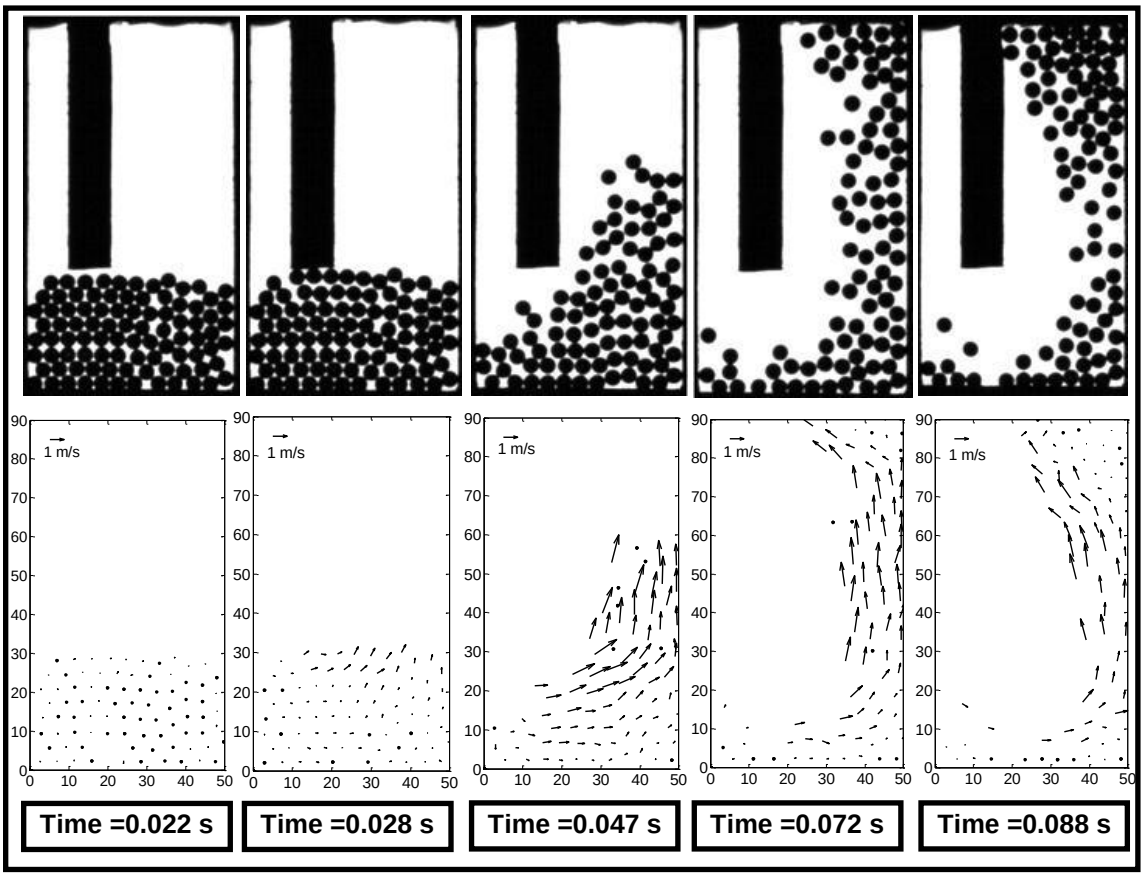

Figure 4-5: Particle flow field and velocity vectors for initial experimental time, case one.

Figure 4-6 shows later frames of the experiment. At time 0.096 s, more particles are packed at the top of the test section. The number of packed particles at the freeboard region keeps increasing as the particles at the bed region are fluidised and move in the test section until they stop. This behaviour is clear by looking at different frames in Figure 4-6. At time 0.222 s very few particles are moving. At time 0.322 s nearly all the particles are stagnant at the top of the freeboard.

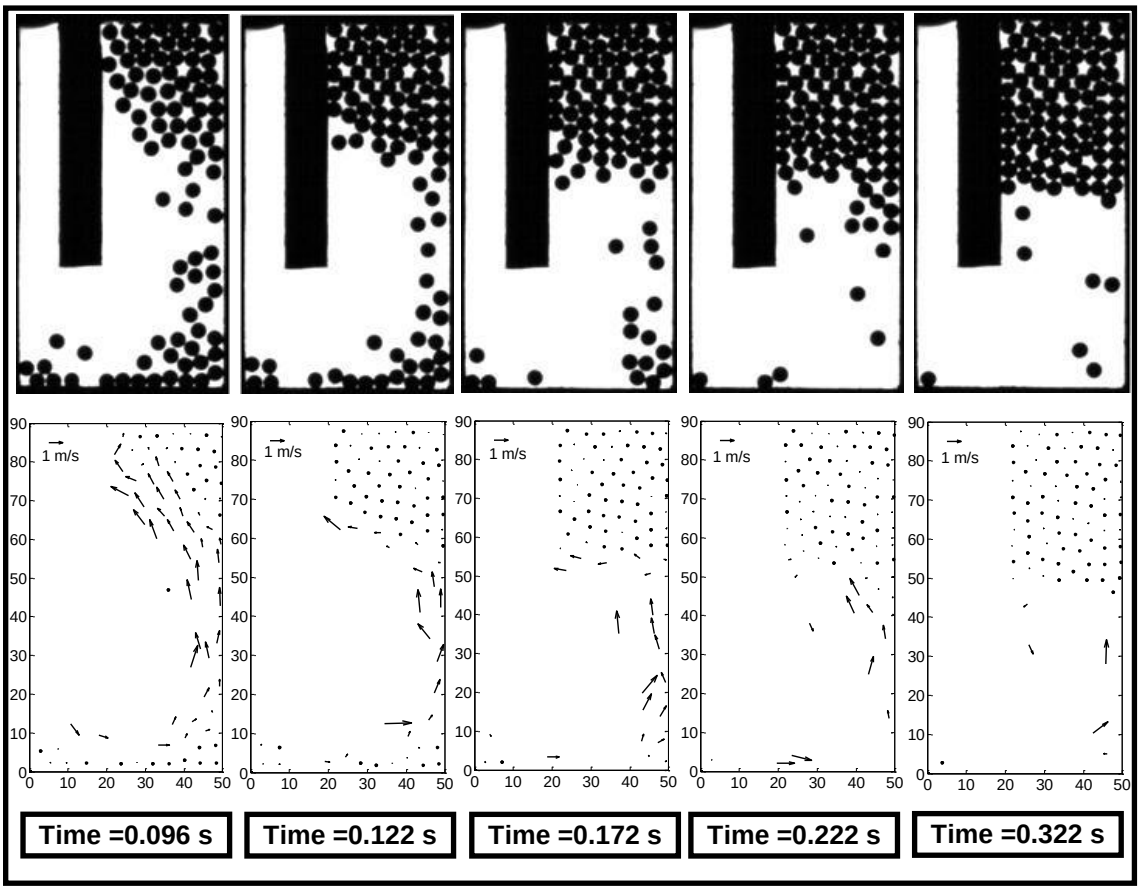

Figure 4-6: Particle flow field and velocity vectors for late experimental time, case one.

By careful examination of Figure 4-6, it is possible to spot an interesting behaviour of particles packing at the top of the freeboard. This appears at time 0.096 s. The fluidised particles moving in the freeboard region have a horizontal velocity component in the left direction. It seems that those particles try to avoid colliding with the particles packed at the top. This is probably due to the direction of the drag force between the particles and the air phase which indicates that the air velocity has a horizontal component. The development of this horizontal component of air velocity is due to the change in the pressure distribution inside the freeboard region due to the change in particles configuration. At the beginning of the experiment, the freeboard region does not contain any particles. Accordingly, it is expected that the vertical air velocity will be much higher than the horizontal component. After the fluidisation of the particles, the geometry of the freeboard region changes. This is because the particles move beside the right wall (Figure 4-5). Then those particles are

packed at the top right corner of the freeboard region. It is expected that the resistance to the air motion is higher in regions where the particles are packed compared to the void regions. Consequently, the air flow is deflected and develops a horizontal component to avoid the highest resistance to the flow. This horizontal air component affects the moving particles by exerting a horizontal drag on them, so the freeboard particles will avoid the stagnant particles at the top of the freeboard region and be transported towards the section of the wire mesh that remains open.

Based on Figure 4-5 and Figure 4-6, the solid phase flow can be divided into three stages. The first stage is fluidisation of the solid particles from the packed bed. The second stage is the flow of these fluidised particles inside the test section. The third stage is packing of the particles at the top of the test section in the freeboard region. These stages are experienced by each particle, but some experience them earlier than others. We shall discuss these three stages in detail by providing the velocity vectors for representative sequences.

Figure 4-7 shows the first stage of fluidisation of the bed region. It represents a sequence of velocity vectors between 0.033 s and 0.044 s. The packed particles in the bed region develop a horizontal velocity initially. This is because the air flow changes its direction from vertical in the jet region to horizontal in the bed region and the particles follow the same direction due to the drag force. Then the air is deflected to the vertical upwards direction when exiting the bed region and moving in the freeboard region. The particles follow this direction and have a vertical upward velocity. It is clear that the particles' velocities do not exhibit fluctuating behaviour with time. A fluctuating behaviour of particle motion, associated with Brownian or vibrating motion means that velocity vectors will change their sign from one frame to another due to the effects of collisions or vibrations. However, this behaviour does not exist in Figure 4-7. This means that the particles flow is dominated by convection with no diffusive motion. This indicates that the effects of inter-particle collisions on particle motion mechanism are negligible during this stage. However, this behaviour does not suggest that particles contacts (collisions and friction) do not exist. It confirms that diffusive motion caused by the collisions is not present.

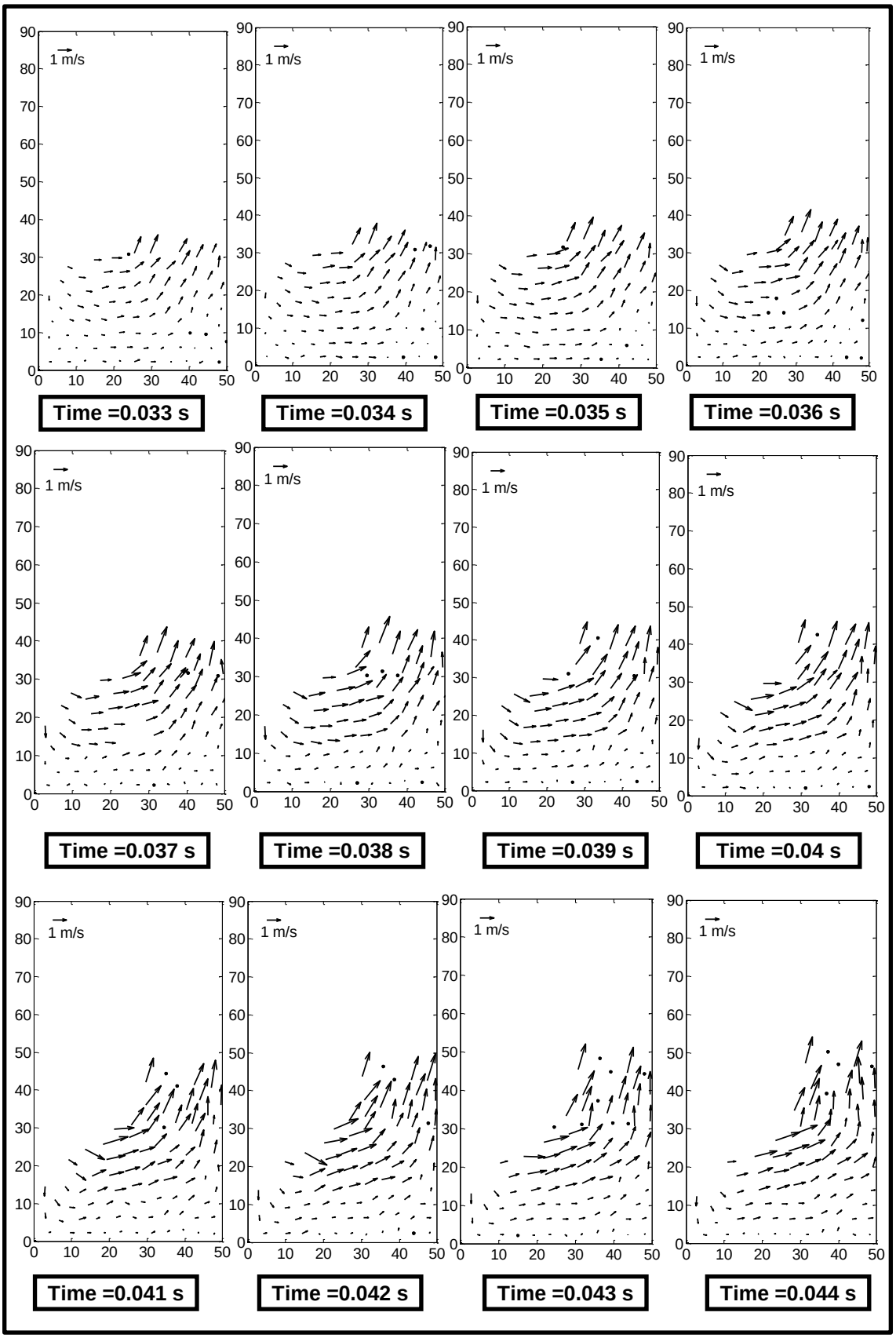

Figure 4-7: Particles velocity vectors in the first stage of flow, bed fluidisation.

Figure 4-8 shows the second stage of flow, which represents the flow of fluidised particles in the test section. The fluidised particles have a nearly vertical flow direction in the freeboard region. Similar to the first stage of the initial fluidisation, particle flow is dominated by convection. The velocity arrows do not show fluctuating behaviour with time. Furthermore, one cannot notice any development of boundary layer in the vicinity of the boundary walls. This is expected because the boundary layer is developed due to collisions, which cause diffusive motion. This indicates that the flow here is dominated by convection due to the external drag forces applied to the particles.

Figures (4-9, 4-10) show the third stage of the fluidisation event, which involves packing of particles at the top of the domain. The particles stop immediately after collisions with the upper wall (Figure 4-9) or with other particles packed at the top of the test section (Figure 4-10). Consequently, the particles do not bounce when they collide with each other and the upper wall. This means that the drag force is much higher than the weight and the inertia.

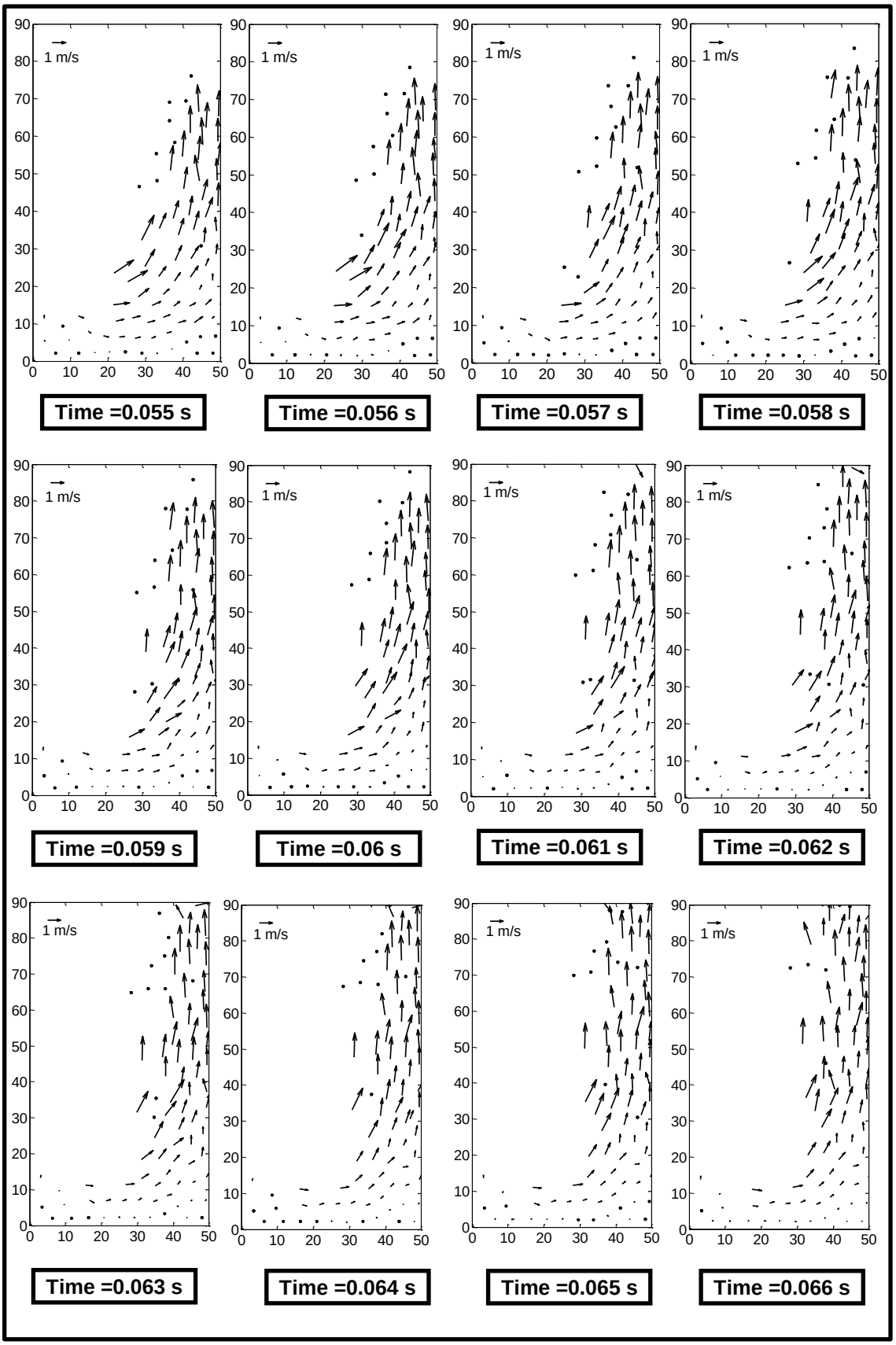

Figure 4-8: Particles velocity vectors in the second stage of flow, particle flow inside the test section.

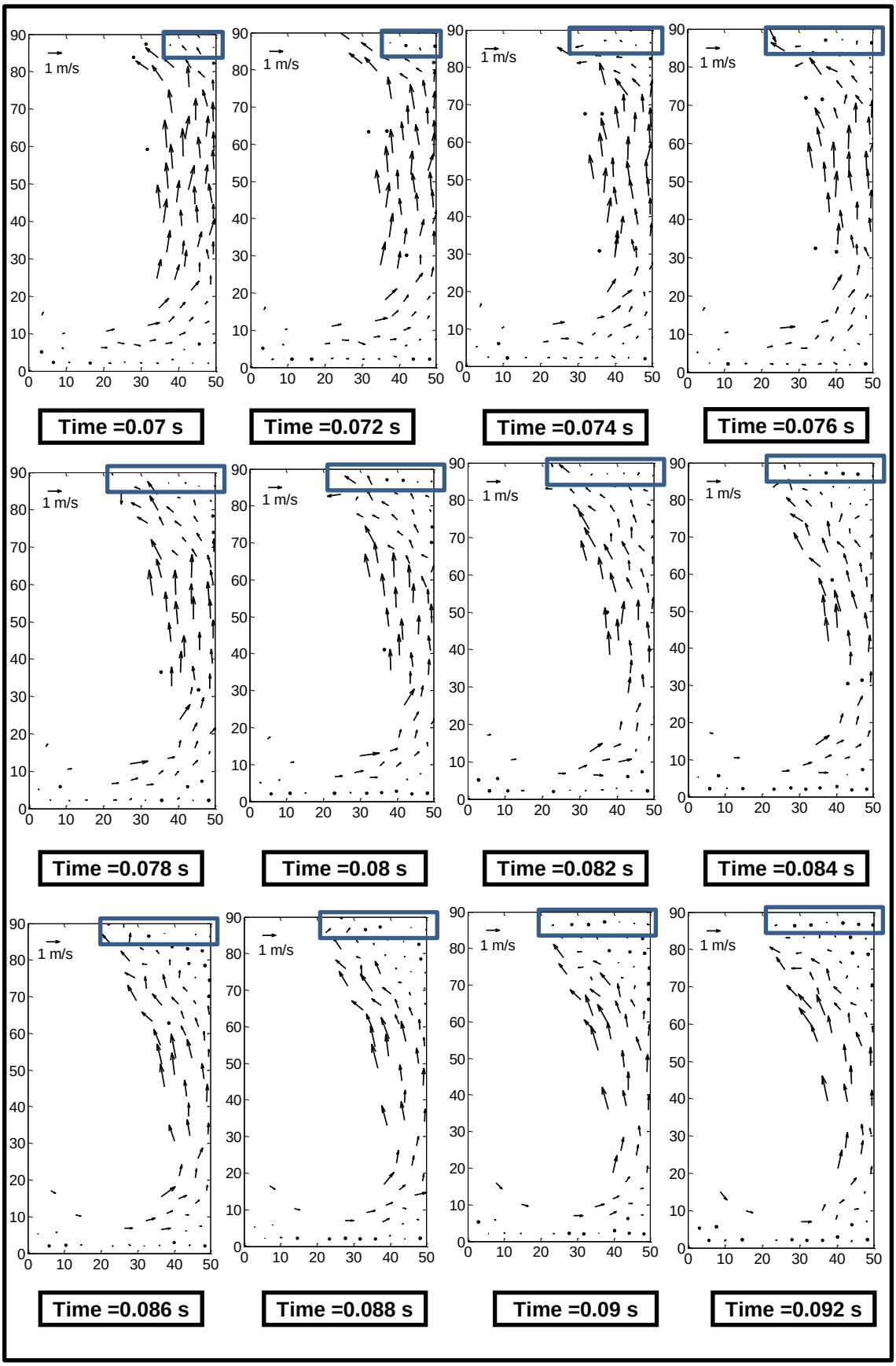

Figure 4-9: Particles velocity vectors in the third stage of flow, particle-wall collisions.

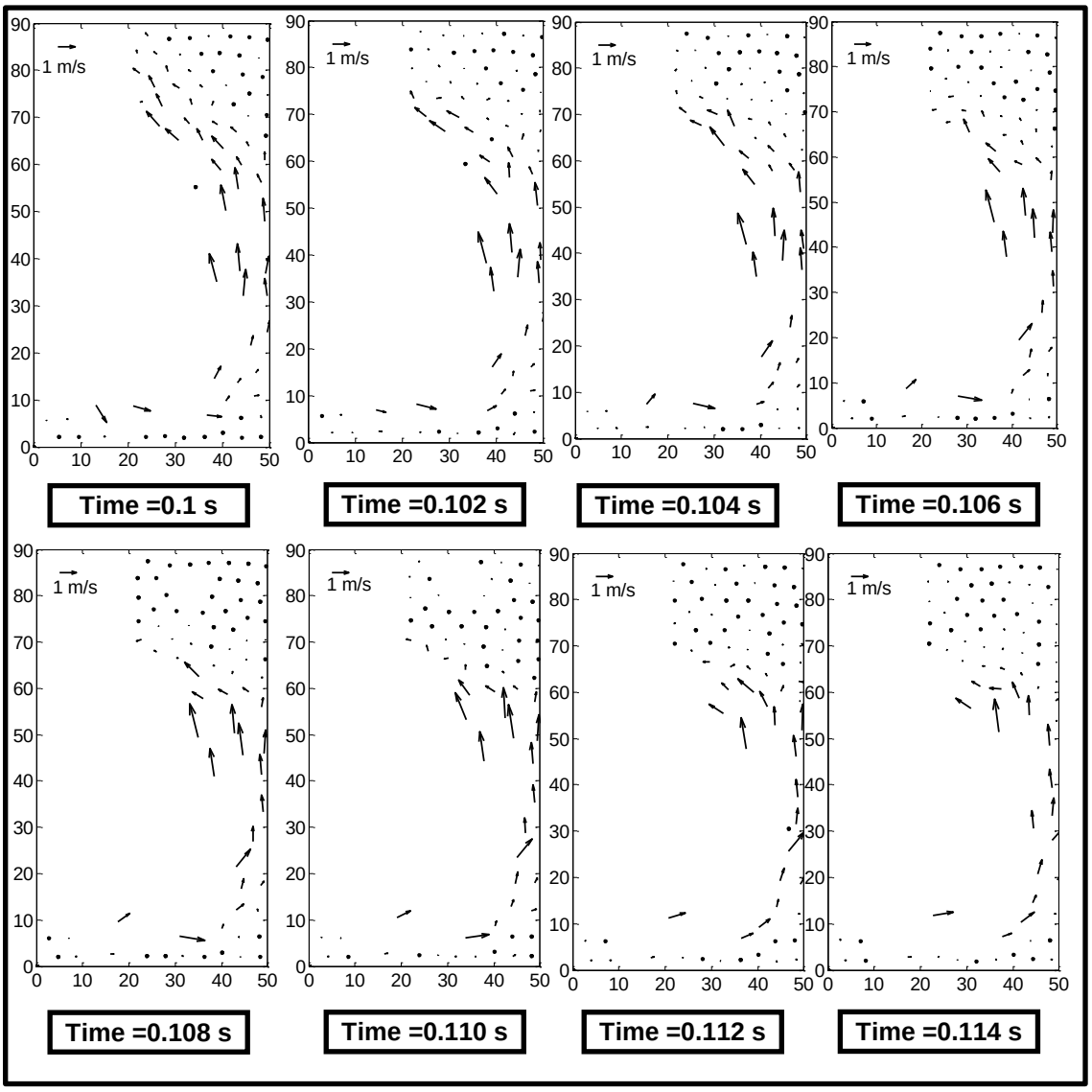

Figure 4-10: Particles velocity vectors in the third stage of flow, particle-particle collisions.

Throughout the motion of the particles in the test section, they might have contacts with the front and back Perspex walls. These contacts might be frictional or collisional. No explicit information about these contacts is recorded using the present experimental technique, because the particles are photographed in one plane only. However, any effects of collisions or friction with those walls will result in reduced particle velocity due to losses. The values of particle velocities, captured using the experimental technique, reflect the overall forces including any possible contacts with the front and back walls.

4.5 Average Particle Variables for the Bed Region

In this section, we show the average void fraction and total velocity components over the bed region. Figure 4-11 shows the temporal variation of the void fraction of the bed region averaged over five experiments. The solid bed has an initial void fraction of 0.5. The void fraction in the bed region starts to increase with time as the air starts to remove the solid particles. The change in the void fraction is very rapid at the start of the air flow and until a time of around 0.07 s. This corresponds to the fluidisation of the top layers in the bed region (Figure 4-7). Those layers are very close to the exit of the air jet. The high air velocity causes high drag force on those layers and hence a large particulate phase acceleration.

For time between 0.07 s and 0.17 s, the change in void fraction becomes less rapid. This corresponds to the fluidisation of the lowest layers of the solid bed (Figure 4-8 and Figure 4-9). Those layers are affected by reduced air velocity compared to the top layers of the bed region due to the divergence of the air jet after exiting the jet region. This reduces the drag force on the lower layers of the bed. The gradient of the void fraction further decreases between 0.17 s and 0.3 s and the void fraction becomes constant at a value of 0.99 from 0.3 s onwards. This means that nearly all the particles are fluidised by this time.

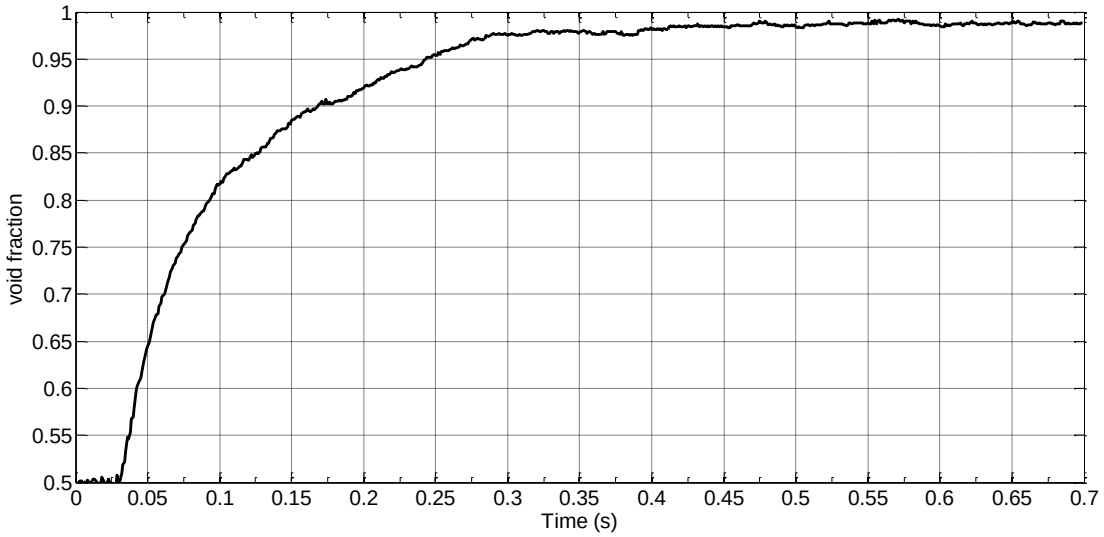

Figure 4-11: Ensemble average of the void fraction of the bed region versus time, case one.

Figure 4-12 shows the percentage of standard deviation of the ensemble-averaged bed void fraction. The value of the standard deviation is less than 3% of the void fraction for the early dense part of the fluidisation event, and is lower during the final part. The low value of standard deviation suggests that the experiments are repeatable for the void fraction of the bed region.

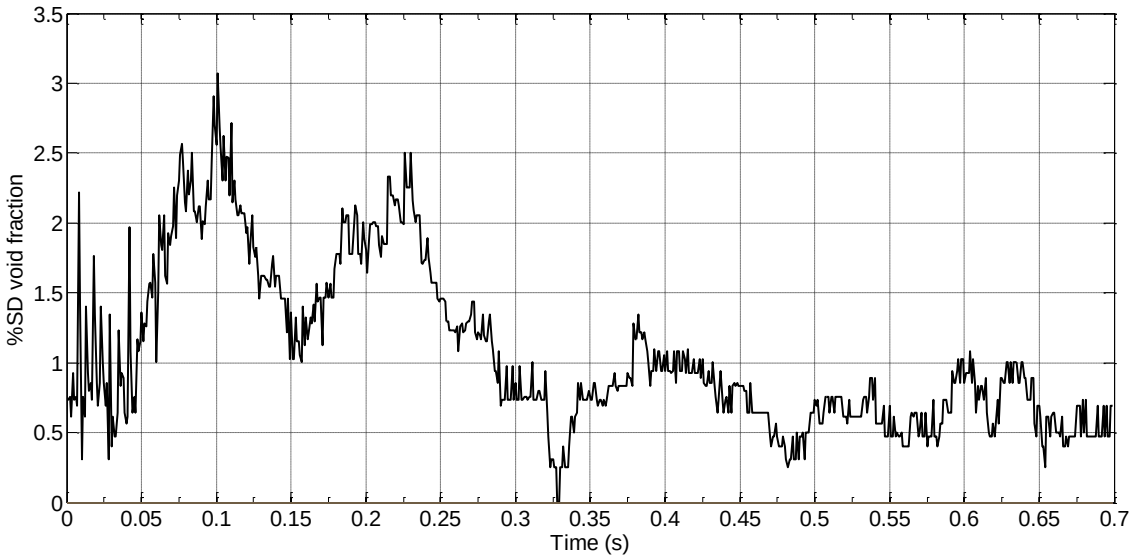

Figure 4-12: Percentage of standard deviation of the void fraction of the bed region versus time, case one.

Figure 4-13 shows the ensemble average of the total horizontal velocity. The total horizontal velocity increases at the beginning of the experiment until a time of around 0.05 s. This corresponds to the initial horizontal movement of the top layers in the packed bed. The horizontal velocity reaches a peak value at this time because the particle velocity is high in the top layers of the bed and many particles are moving horizontally (Figure 4-5). The total horizontal velocity decreases rapidly from 0.05 s to 0.1 s until it reaches a value of 4 m/s. This rapid decrease indicates that the overall movement of all the particles in the bed is slower than the initial phase but the particles are still moving horizontally to the right direction (Figure 4-5 and Figure 4-6). This is because the air jet drags the particles to the direction of the air flow. For time between 0.1 s and 0.25 s, the horizontal velocity keeps decreasing while retaining its positive value. This indicates slower overall movement of particles to the right direction. The value of the total horizontal velocity becomes nearly zero from 0.25 s with

some minor fluctuations. This corresponds to the time when nearly all the particles have left the bed region.

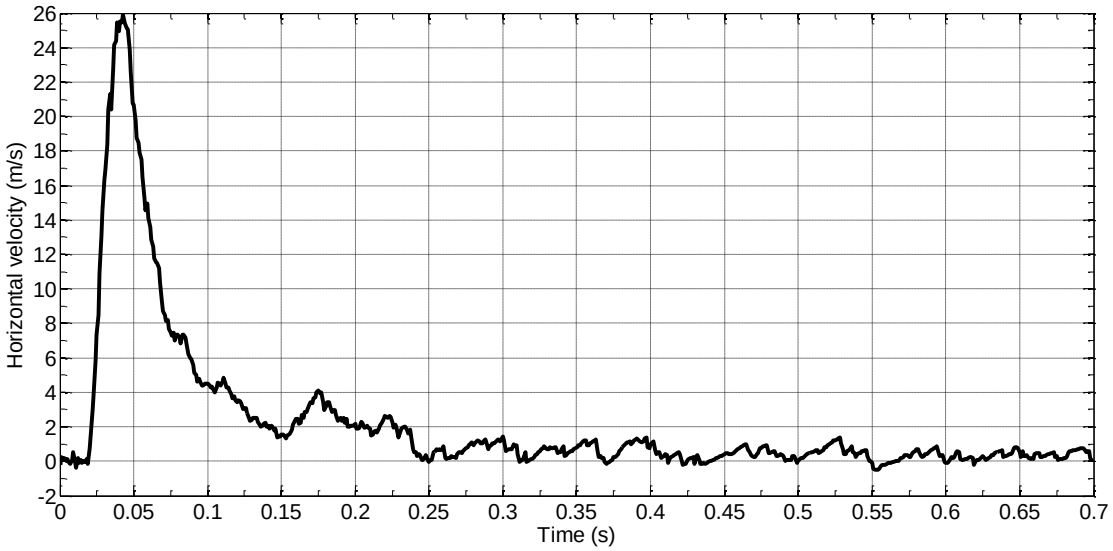

Figure 4-13: Ensemble average of the total horizontal velocity of the bed region versus time, case one.

Figure 4-14 shows the ensemble average of the total vertical velocity with time. The total vertical velocity increases from zero at the beginning of the experiment until it reaches a peak value of around 16 m/s at a time around 0.05 s. This is consistent with the void fraction (Figure 4-11) and total horizontal velocity (Figure 4-13). It corresponds to the fluidisation of the top layers of the bed. The total vertical velocity decreases rapidly from 0.05 s to 0.1 s until it reaches a value of 4 m/s. This corresponds to the relatively weak fluidisation of the lower layers of the bed. From 0.1 s to 0.3 s, the vertical velocity keeps its positive value while retaining less rapid decreasing trend. From 0.3 s onwards, the vertical velocity is nearly zero. This is when nearly all the particles have been removed from the bed region.

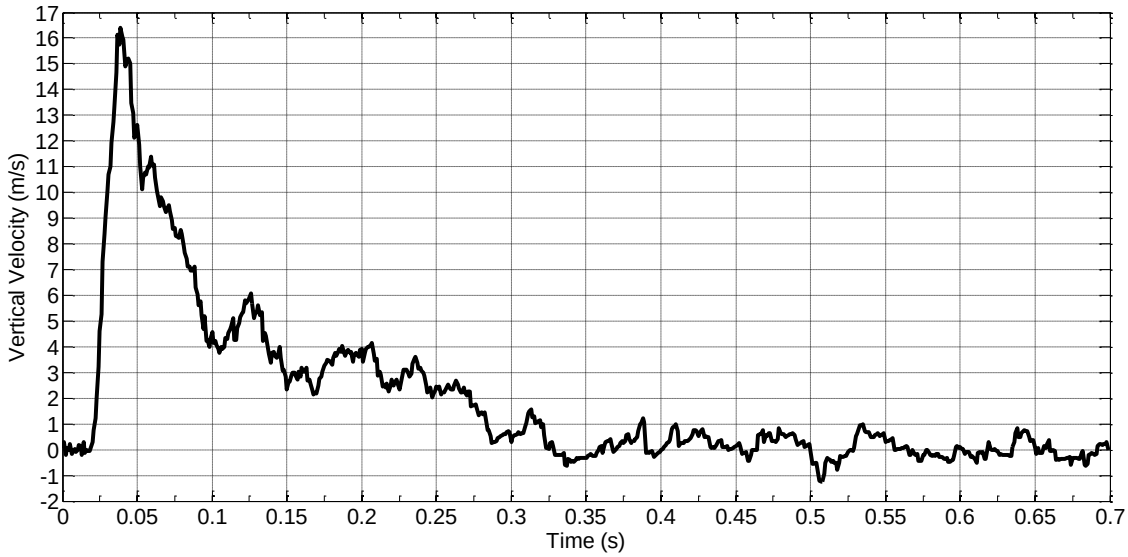

Figure 4-14: Ensemble average of the total vertical velocity of the bed region versus time, case one.

Figures (4-15, 4-16) show the ratio of standard deviation to the ensemble average for the horizontal velocity and vertical velocity, respectively. The standard deviation of the horizontal velocity reaches a maximum value of 35 %. The standard deviation of the vertical velocity reaches a maximum value of 18%. This indicates that the quantitative repeatability of the particle velocity is less than the void fraction (standard deviation 3%).

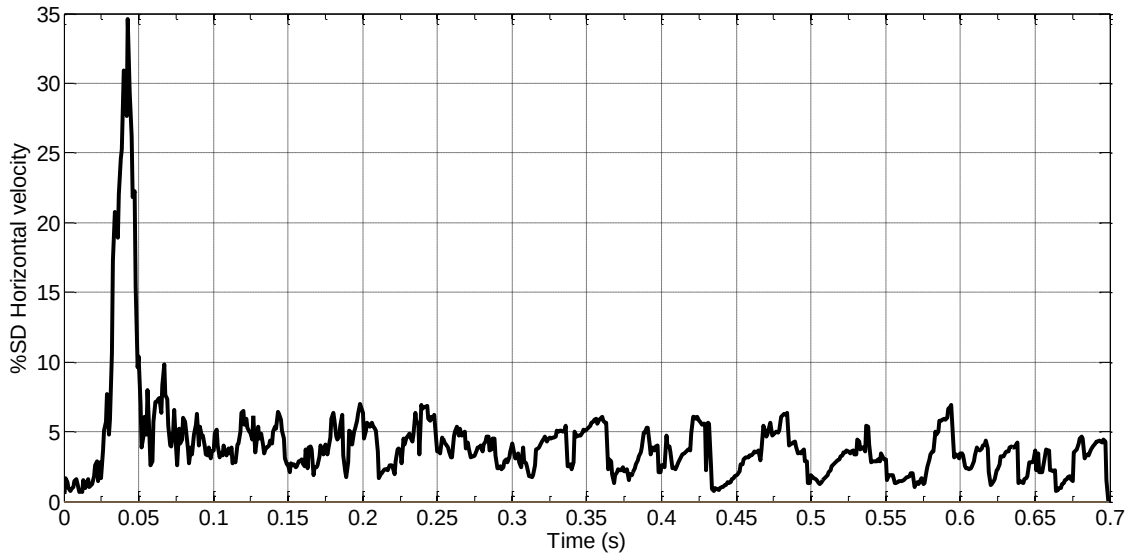

Figure 4-15: Percentage of standard deviation of the ensemble average of the total horizontal velocity for the bed region versus time, case one.

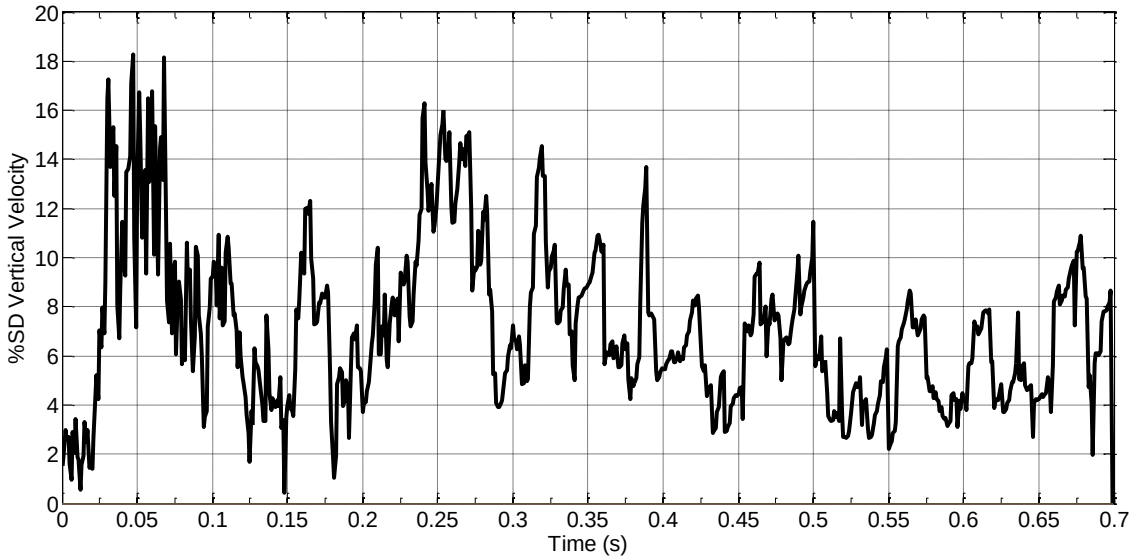

Figure 4-16: Percentage of standard deviation of the ensemble average of the total vertical velocity of bed region versus time, case one.

The relatively high standard deviation of the velocity means that the velocities are not replicated exactly in the experiments. This is in contrast to the void fraction where the standard deviation is around 3%. The next section will present the results of the freeboard region. We will compare the values of the velocities of ensemble average with a single experiment in order to investigate the cause of the standard deviation.

4.6 Average Particle Variables for the Freeboard Region

The variations in different experiments are now compared for the case of the freeboard region. The freeboard region is larger than the bed region, so it is more likely that the particles move longer distances compared to that of the bed region. Consequently, this might increase the uncertainties in the exact movement of the particles within the ensemble of the experiments. This will allow us to examine the repeatability of the experiments at more extreme conditions.

Figure 4-17 shows the freeboard void fraction with time for both the ensemble average and a single experiment. It is clear that the two curves are very similar. The freeboard region has an initial value for the void fraction of 1.0. The void fraction starts to decrease with time as the air starts to remove the solid

particles from the bed region. The change in the void fraction is rapid at the start of the gas flow and until a time of 0.25 s. Then, the void fraction becomes nearly constant until the end of the experiment at a value around 0.6. The freeboard void fraction represents a projection of the bed void fraction. The steady state void fraction of the freeboard (0.6) is higher than that of the bed region. This is because the area of the freeboard region (1800 mm²) is higher than the bed region (1500 mm²) and accordingly, particles fill less percentage of the volume. This gives area ratio of six to five (6/5), which is the same as the steady state void fraction ratio of the two regions.

In Figure 4-18, the standard deviation of the void fraction of the freeboard region is less than 3% which is the same order of magnitude to that of the bed region. These results of mean and standard deviation of void fractions confirm the conclusion that the repeatability of the experiments when measuring the void fraction is high.

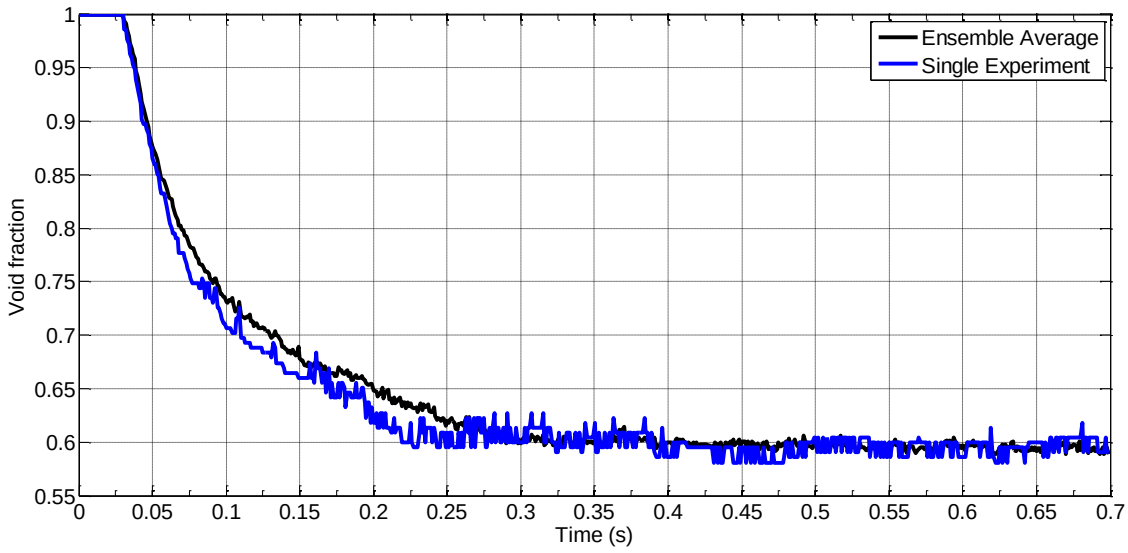

Figure 4-17: Single experiment and ensemble average of the void fraction of the freeboard region versus time, case one.

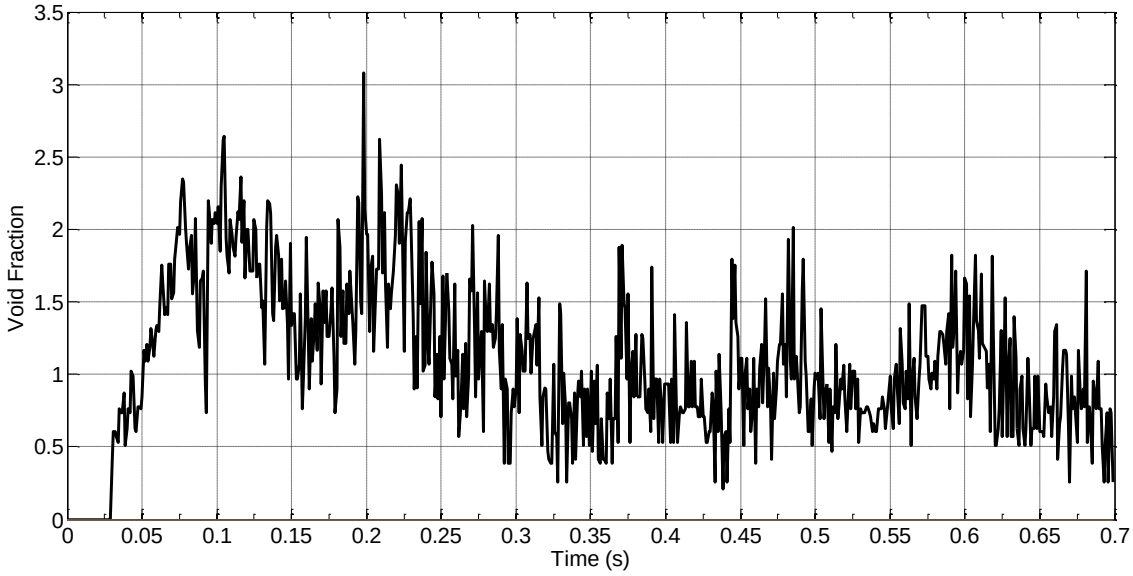

Figure 4-18: Percentage of standard deviation of void fraction of the freeboard region versus time, case one.

Figure 4-19 shows the ensemble average of total horizontal velocity of all experiments with respect to time as well as the total horizontal velocity for a single experiment. The ensemble average total horizontal velocity is zero until 0.03 s and subsequently increases until it reaches a maximum value of around 6 m/s at a time of 0.05 s. This is the stage of initial fluidisation where particles move with a horizontal component to the right direction (Figure 4-5 and Figure 4-7). Then it decreases rapidly until it reaches a value of around -8 m/s at a time of 0.08 s. This corresponds to the stage of where fluidised particles start to move to the left at the top of the freeboard region (Figure 4-6). Then it increases to zero at a time of 0.35 s where it remains constant until the end of the experiment. At this time, most of the particles are fluidised and packed against the top wall of the test section of the freeboard region. For the case of a single experiment, the total horizontal velocity curve follows the same trend of that of the ensemble average. Nevertheless, the values are not the same for all points.

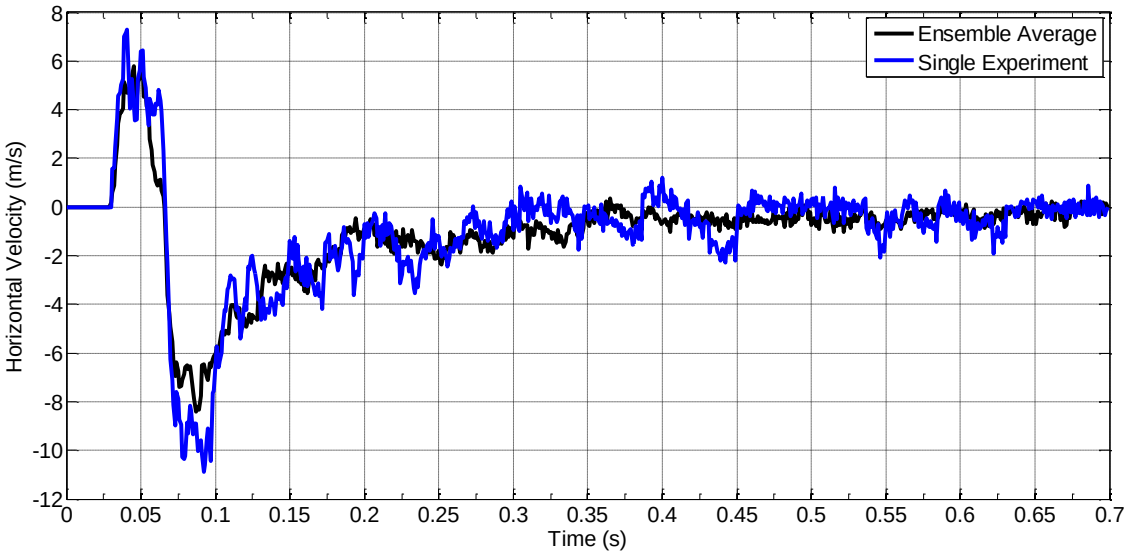

Figure 4-19: Single experiment and ensemble average of the total horizontal velocity for the freeboard region versus time, case one.

The relatively high standard deviation seen in the total horizontal velocity of the bed region appears here with values of around 30% as shown in Figure 4-20. By comparing the individual experiments, it is possible to justify the standard deviation. Figure 4-21 shows this comparison between the total horizontal velocities of the experiments. It is clear that they all have the same trend but with some quantitative differences. These differences cause the relatively high standard deviation of the ensemble average.

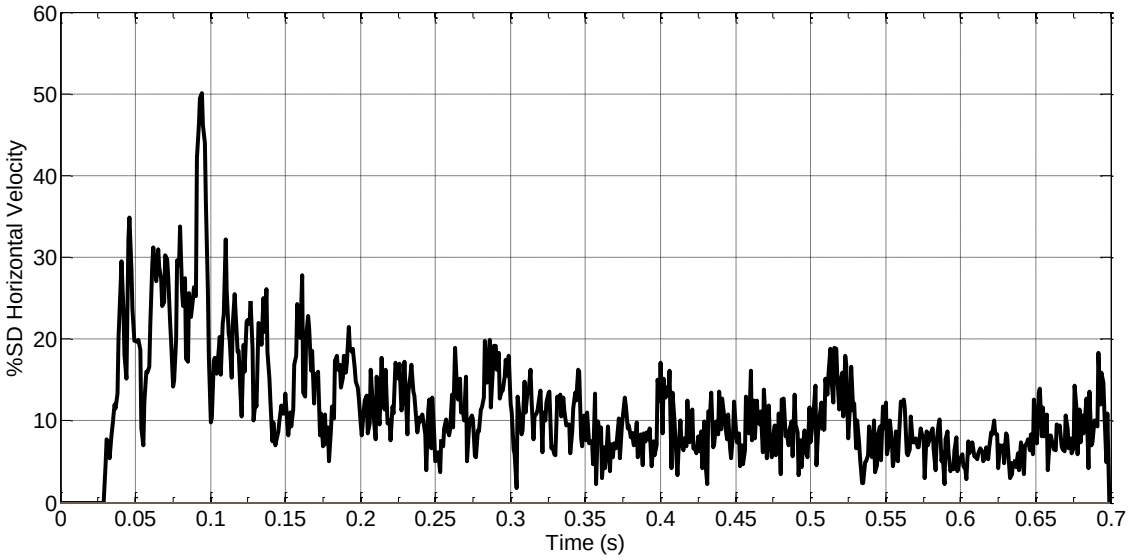

Figure 4-20: Percentage of standard deviation of the total horizontal velocity of the freeboard region versus time, case one

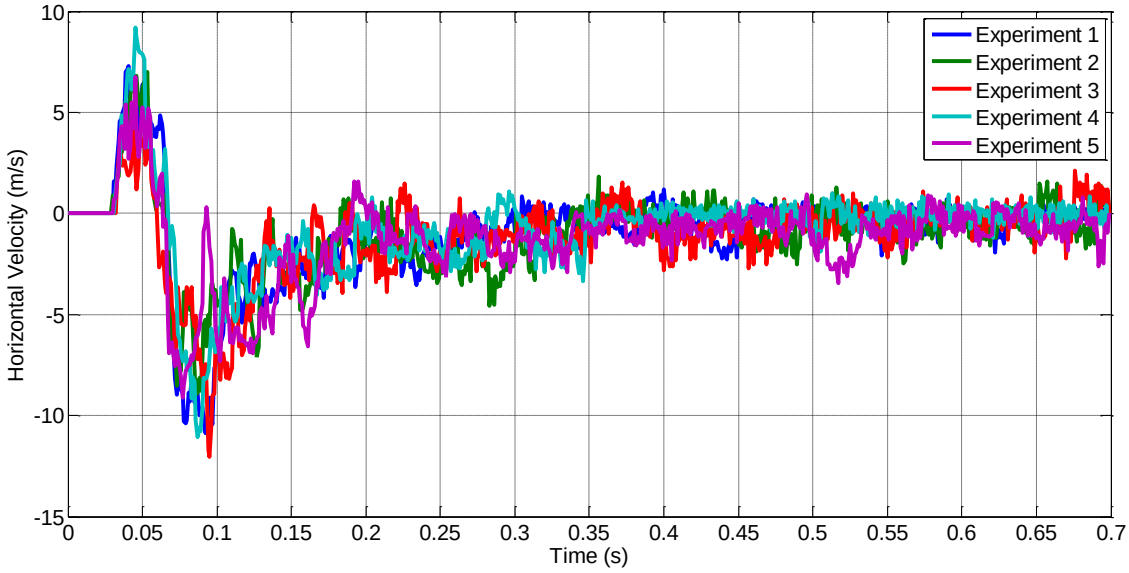

Figure 4-21: Total horizontal velocity of the freeboard region for all the experiments within the ensemble, case one.

Figure 4-22 shows the total vertical velocity for the ensemble average and that of a single experiment with the time on the horizontal axis. As noticed in the bed region, the ensemble averaged total vertical velocity of the freeboard region increases at the beginning to reach a maximum value of 45 m/s. Then the total vertical velocity decreases rapidly from 45 m/s at a time of 0.07 s until

it reaches zero at a time of around 0.3 s. For the case of a single experiment, the curve has the same trend with some quantitative differences.

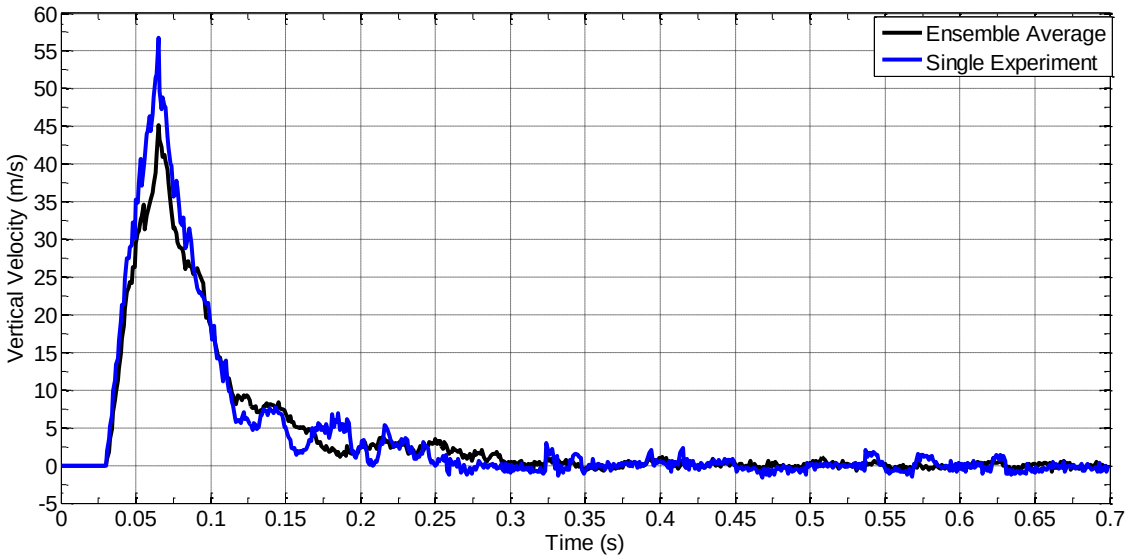

Figure 4-22: Single experiment and ensemble average of the total vertical velocity for the freeboard region versus time, case one.

The standard deviation shown in Figure 4-23 shows that for the case of high total velocity the deviation is high up to 20%. This is similar to the total horizontal velocity. Furthermore, the individual experiments have the same trend as shown in Figure 4-24. The quantitative differences within the ensemble cause the relatively high standard deviation.

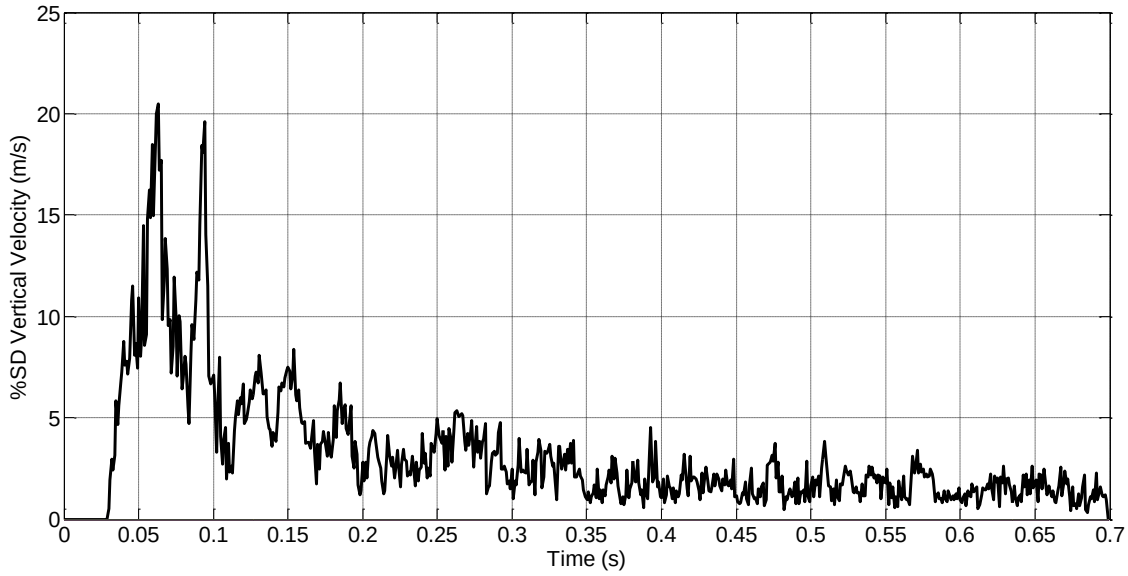

Figure 4-23: Percentage of standard deviation of total vertical velocity of the freeboard region versus time, case one.

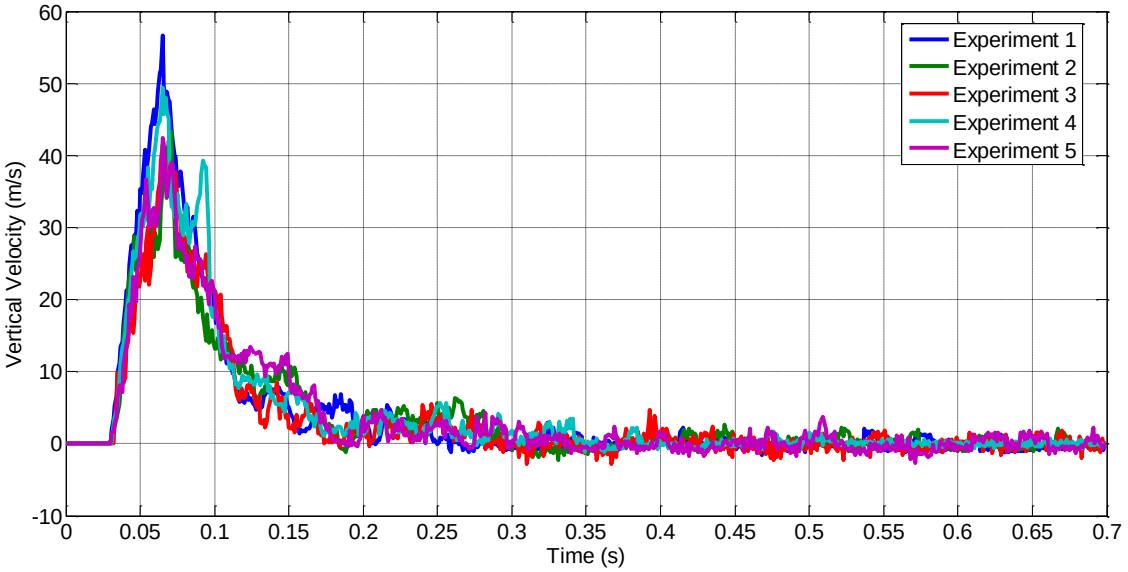

Figure 4-24: Total vertical velocity of the freeboard region for all the experiments in the ensemble, case one.

4.7 Discussion

In this section, we discuss the experimental results presented in this chapter in order to draw the conclusions. There are three main issues identified while

presenting the results. These issues are: experiments repeatability, flow regime and hydrodynamic description.

4.7.1 Experiments Repeatability

The experiments showed good quantitative repeatability regarding the average void fraction. The standard deviation of the mean was less than 3%. For the case of total velocity, the experiments showed less quantitative repeatability, though the qualitative profiles (trends) were similar. The standard deviation was up to 30% of the ensemble average. The high standard deviation in the velocities shows that the experiments are not repeated exactly regarding the values of the particles' velocities. This has been further confirmed by comparing the results of individual experiments to each other and to their ensemble average. These differences can be traced to the variations within the ensemble of the experiments. In order to replicate one experiment exactly, each particle ought to move with the same magnitude and direction at the same time in every experiment. This condition seems to be nearly impossible to achieve, because there are some differences in experiments such as the initial packing configuration (Figure 4-1) and the minor differences in the air pressure boundary conditions (Figure 4-3 and Figure 4-4). Furthermore, the surface properties of both the particles and the boundary walls might change from one experiment to another which affects the particles motion. On the other hand, the repeatability of the void fraction in the experiments requires that the particles are physically inside the freeboard region. There is no need for matching the exact movement in each time frame. Consequently, the variations in the void fraction between the experiments are lower than that of the velocity.

In the literature involving experiments similar to the current experiment, the issue of repeatability was rarely discussed. Many researchers used a single experiment and hence, the issue of repeatability was irrelevant. This observation includes experimental methods such as MRI (Fennell et al., 2005; Candela et al., 2007; Holland et al., 2007), PEPT (Wildman et al., 2008; Sheikh, 2011; Viswanathan et al., 2011) and optical techniques (Drake, 1991; Warr, Jacques and Huntley, 1994; Jung, Gidaspow and Gamwo, 2005). This also includes applications of both dry granular flow (Drake, 1991; Warr, Jacques and

Huntley, 1994; Wildman et al., 2008; Viswanathan et al., 2011) and multiphase flow (Jung, Gidaspow and Gamwo, 2005; Fennell et al., 2005; Candela et al., 2007; Holland et al., 2007).

Experimental studies of applications related to DPI (Versteeg and Wildman, 2004; Versteeg, Hargrave and Hind, 2005; Tuley et al., 2008) were mostly qualitative and hence, they did not provide tangible approach of the investigating the experimental repeatability. However, one of these studies (Tuley et al. 2008) repeated the experiment for three patches of glass beds. Then the experiment using each patch was repeated two times. Figure 4-25, shows Tuley et al. (2008) results for a certain time frame. It is clear that the images are not similar.

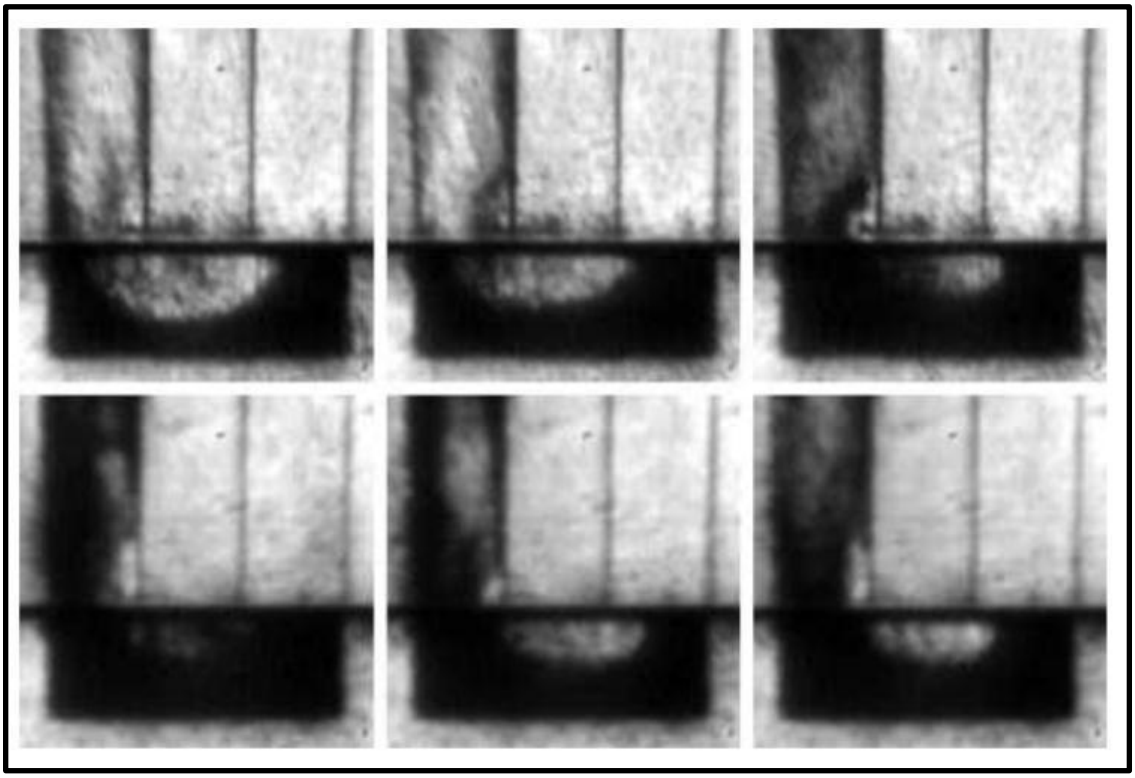

Figure 4-25: Tuley et al. (2008) results for experimental repeatability.

To sum up, the quantitative discrepancies in this chapter should not be an obstacle for using these data for model validation. However, one should not aim for exact quantitative matching in velocities. Using ensemble average as a representative of the experiments might remove some quantitative data.

Moreover, the raw images and velocity vectors are shown by using single experiment and cannot be averaged over the ensemble. Accordingly, we will use a single experiment for comparison with the model.

4.7.2 Flow Regime

The experimental technique based on two-dimensional test section presented in Chapter 3 achieved its objectives in generating quantitative results on the particle level. The raw images of the experiments are very clear and the image processing approach generated velocity vectors for every particle at every time frame. These results allowed us to describe the flow behaviour in a precise way. The results showed that the particulate phase flow depends on the air flow. Due to the dense flow of particles, the air flow is affected by the particulate phase as well. Thus, the two phases are strongly coupled.

The motion of particles showed that they broadly flow the air flow direction. Consequently, the main forces affecting the particles are air drag, inertia and weight. Other forces such as inter-particle and particle-wall contacts were not identified in the first and second stages of particulate phase flow. They were clear in the third stage of the flow where the particles are packed against the top wall of the test section in the freeboard region. The contacts with the front and back wall were not measured explicitly. However, they are expected to affect the velocities due to nature of the two-dimensional test section which increases the area of contact between the granular phase and the walls with respect to the granular phase volume.

4.7.3 Continuum Description

One of the advantages of generating experimental results on the particle scale is to investigate the validity of continuum and kinetic theory of granular flow (KTGF) assumptions, which is one of the main aims of this thesis. In the setup presented in this thesis, the simplifications made in the experimental setup on one hand and the nature of the granular flow in the multiphase test section on the other might challenge the assumptions of the hydrodynamic models. The main simplification made in the experimental setup is the large size of the particles (4 mm) compared to the domain (50 mm width and 90 mm height).

Using large particles constrains the length scale of comparison between the experiments and simulations. While the hydrodynamic simulations result in continuous variables (for the analytical solution), this is not the case for the experiments with large particles where the diameter is the minimum length scale. Using this large particle diameter with respect to domain size forced us to define relatively large averaging volume (bed and freeboard regions) so that each region contains sufficient number of particles and avoid the effects of statistical fluctuations. These statistical fluctuations, associated with the averaging volumes, result from the non-zero value of particle diameter. The whole particle is considered to be in a certain region when its centre lies in this region. Using smaller averaging regions will increase the statistical fluctuations due to the large diameter of the particle and hence its significance to the averaging region.

Regarding the flow condition, the strong convective flow with the lack of diffusive motion suggests that using the kinetic theory models within the frame work of the hydrodynamic model might be problematic. It is well known that applying the kinetic theory within the framework of the continuum description needs full separation between the micro and macro scales of the flow (Chapter 2). This means that the inter-particle collisions happen over smaller time and length scales when compared to the variation in the mean flow of the macroscopic variables (i.e. velocity). This allows the full separation between the diffusive motion and convective motion and hence, kinetic theory models might be applied to compute the diffusive motion. However, the particulate phase flow is dominated by convection with no effect of diffusive motion triggered by inter-particle collisions. The collisions between particles appeared when the particles are stopped at the top of the freeboard region, but this might be regarded as a macroscopic effect because of the force equilibrium between the drag and inertia. However, the absence of the diffusive motion suggests that the issue of scale separation might be irrelevant in this case because there is one scale only which is the convection scale. The most important point is whether the multiphase flow model will be able to replicate this behaviour or not. This also includes the packing of the particles at the top of the freeboard region.

The effect of replacing the large particles (4 mm) with smaller particles on the fluidisation mechanism is unclear. Reducing the particle size will increase the effect of gas turbulence. This effect of turbulence will increase the fluctuations on smaller particles which triggers collisions and diffusive motion. However, these turbulent fluctuations need to be higher than the particle inertia in order to cause the fluctuating motion of the solid particles. Our experimental results do not give quantitative estimation of the ratio between the inertia and turbulent currents.

4.8 Summary and Conclusions

In this chapter, the fluidisation of solid bed using a high speed air jet has been presented. This regime corresponds to flow in DPI where all the particles are fluidised. The fluidisation process occurs very fast and nearly all the particles are entrained from the bed region to the freeboard after 0.25 s. Particles raw images and velocity vectors show that the solid and gas phases are strongly coupled to each other. The results show that the flow of particles might be divided into three stages. The first stage is the initial fluidisation of particles in the bed. The second stage is their flow in the test section. The third stage is their packing at the top of the freeboard. Throughout the three stages of the flow, it is clear that convection is the dominant mechanism of particles motion. There is no evidence that the particles exhibit any kind of diffusive motion triggered by collisions. However, these contacts might have quantitative effects on the particle velocity. For example, the collisions and friction might exert extra force on the particles which reduces their acceleration.

The experiments were performed five times to study the repeatability of the experiments. It was shown that the experiments exhibit the same qualitative trends for the variables with some quantitative discrepancies. Regarding the quantitative repeatability, the standard deviation of the void fraction is less than 3%. The standard deviation is high (up to 30%) when examining the total velocities. This was traced to the differences in movement of particles within the ensemble. The results of single experiment will be used for comparison with numerical simulations.

Chapter 5 : Experimental Study of Particle Bed Fluidisation Using Weak Impinging Air Jet

5.1 Introduction

The case presented in Chapter 4 is similar to the flow in DPI where the pressure difference is high enough (16 kPa) to fluidise the bed. The main aim of the study presented in this chapter is to investigate the particle behaviour at wider flow conditions and examine the behaviour of flow when the pressure difference is low so that it cannot fluidise the whole bed. In this chapter, the results for low pressure difference cases are presented and discussed. There are two cases with two values of pressure difference (3 kPa and 1.6 kPa).

5.2 Case Two: 3 kPa Air Pressure Difference

In this section, the experiments are performed for a case of 3 kPa pressure difference across the test section. The main aim is to study the flow profile when the strength of the air jet is relatively weak so that it cannot fluidise the whole particle bed.

As in Chapter 4, the experiments were performed several times with nearly similar initial conditions. The particles are packed at the bottom of the test section with packing fraction 50% for all the experiments as shown in Figure 5-1. The initial packing configuration is different since it is nearly impossible to replicate the same configuration for every experiment similar to the previous case.

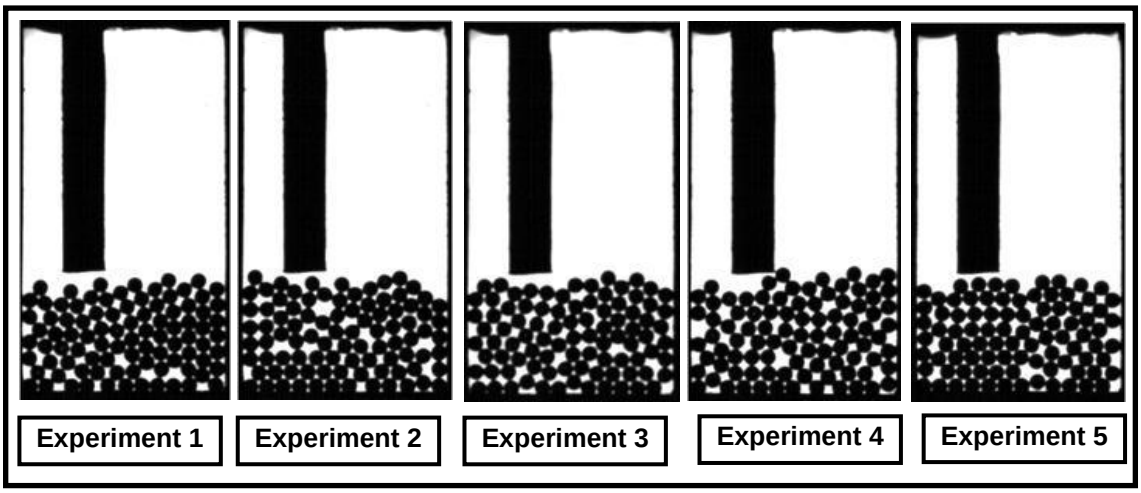

Figure 5-1: Initial frames for different experiments within the ensemble, case two.

5.2.1 Gas Pressure Difference Boundary Conditions

Figure 5-2 shows the ensemble average of the pressure difference between the inlet and the outlet with respect to time. This difference is initially zero; and when the solenoid is opened, the pressure difference increases rapidly. A pressure difference of around 2000 Pa is reached at a time around 0.05 s. After this, the pressure difference decreases to 1000 Pa at 0.1 s and remains constant until 0.2 s. From this time, the pressure difference increases until it reaches the steady state value of 3000 Pa at around 0.7 s.

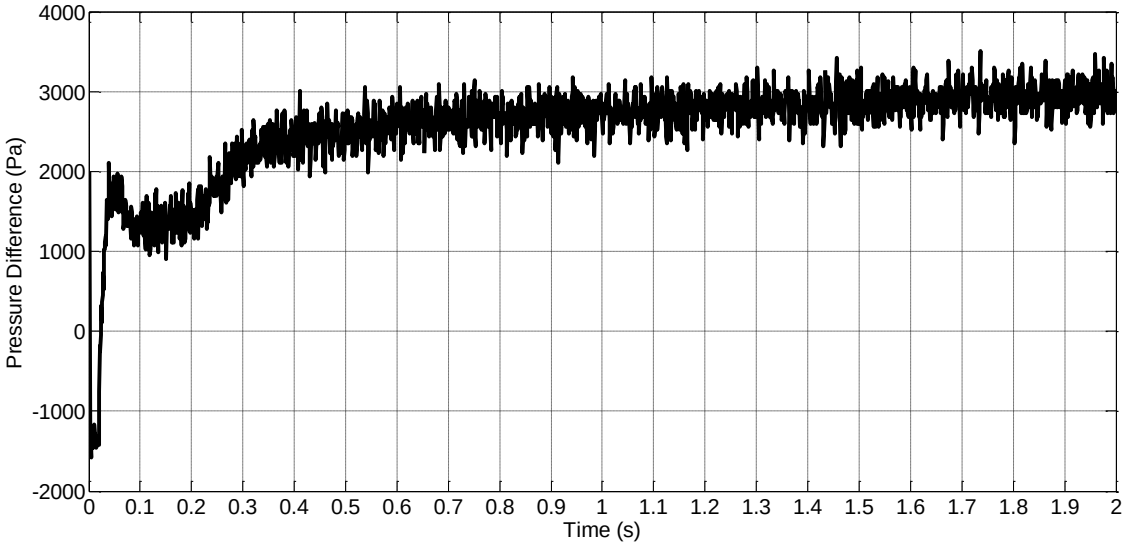

Figure 5-2: Ensemble average of pressure difference versus time, case two.

Figure 5-3 shows the percentage of the standard deviation in the pressure difference with respect to time. This standard deviation results from the different experiments carried out for this case. The standard deviation stays fluctuating around 10 % with overshooting up to 30% and down to 5%. The figure shows that the pressure difference results can be repeated within a range of 10%. Figure 5-4 shows that the absolute standard deviation of the pressure is between 200 Pa and 600 Pa, which is nearly the same order of magnitude of the case of high pressure difference (Figure 4-4).

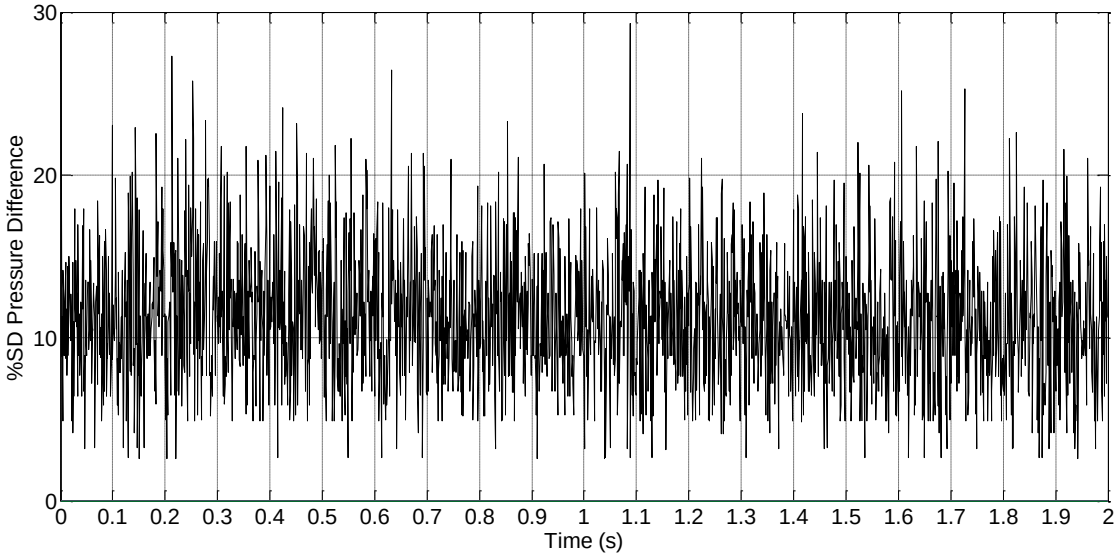

Figure 5-3: Percentage of standard deviation of the pressure difference versus time, case two.

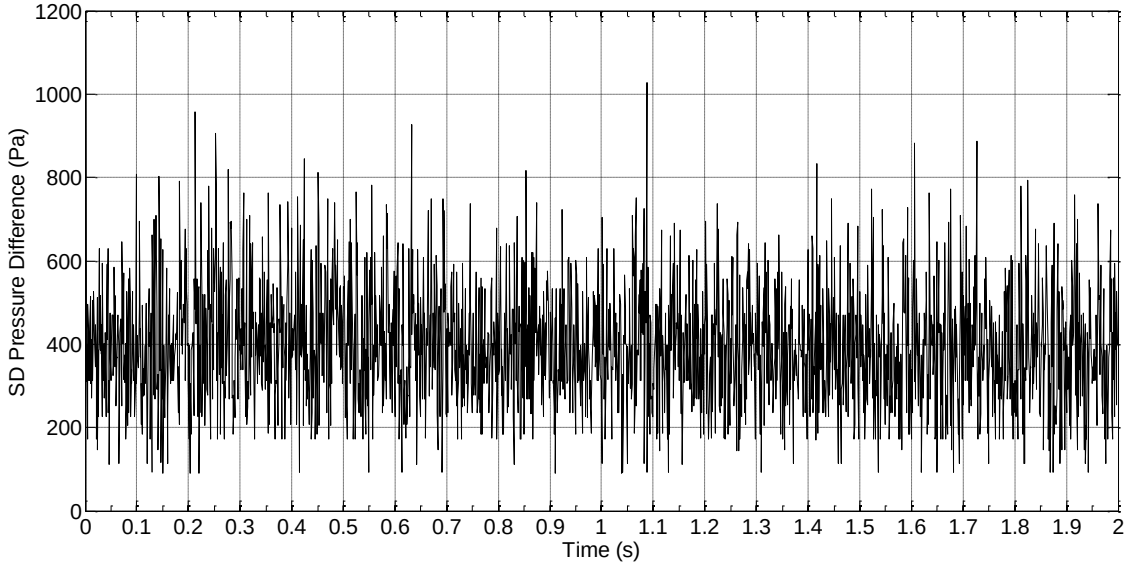

Figure 5-4: Absolute standard deviation of the pressure difference versus time, case two.

5.2.2 Particles Whole Flow Field

Figure 5-5 and Figure 5-6 show the particle flow profiles for different time frames in the upper row and the instantaneous velocity vectors in the lower row.

In Figure 5-5, the particles are packed at time 0.04 s with very few particles moving horizontally to the right (positive x-direction). At time 0.07 s, the fluidisation pattern that was observed in the previous case in Chapter 4 (Figure 4-5) occurs. The particles in the powder bed move to the right and upwards. However, the velocity of particles is lower than that for the higher pressure difference case, because in the current case the velocity of air in the test section is lower than that of the previous case. Accordingly, the drag force is lower than that of the high pressure difference (case one, Chapter 4) which results in lower particle velocity. The particles keep moving in the freeboard region after their entrainment from the bed region. The main driving forces for this upward movement are the inertia gained by the particles and the drag force exerted by the air on the particles. At time 0.2 s, the particle velocity decreases significantly. This is mainly due to the reduction of the drag force exerted on the particles by the gas phase due to the air jet expansion. In the current case, it seems that the air velocity is too low to induce sufficient drag to lift all the particles. At time 0.2 s and 0.3 s, it is clear that the particles have random movement in the freeboard region.

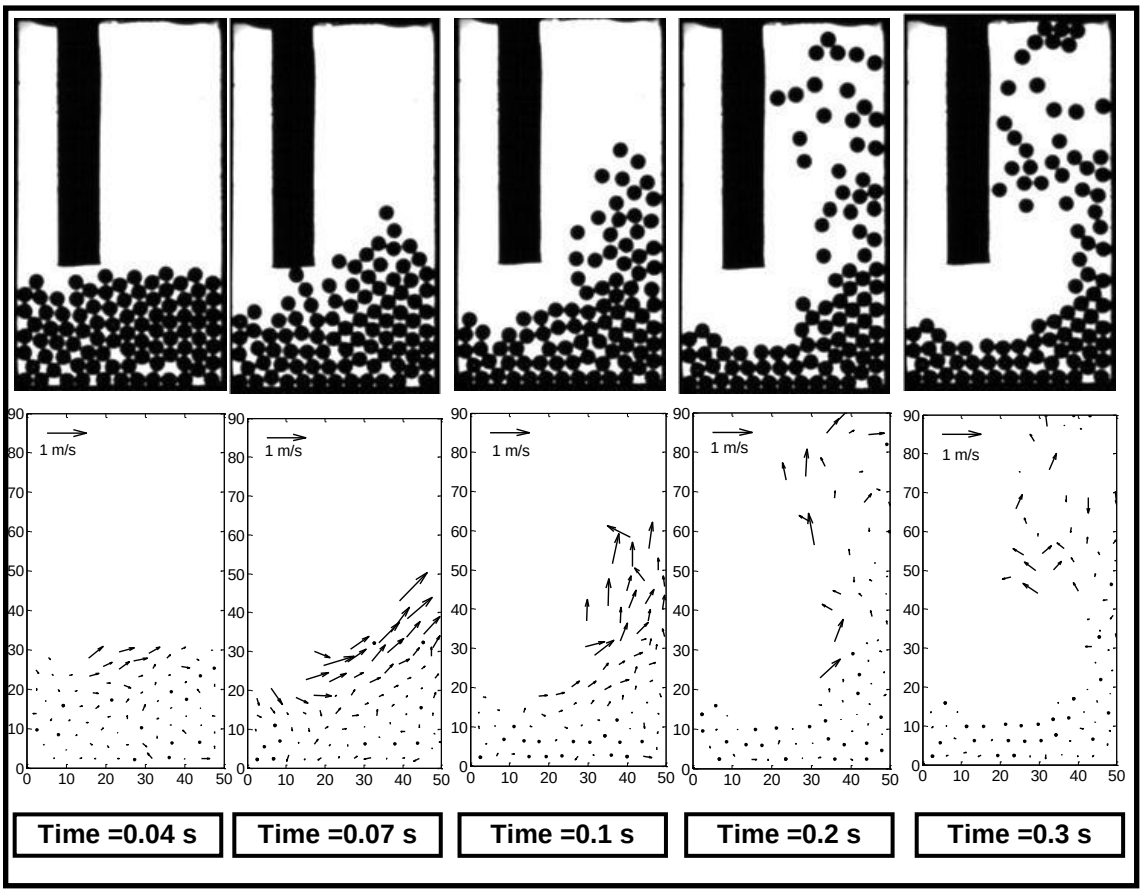

Figure 5-5: Particles flow field and velocity vectors for initial experimental time, case two.

In Figure 5-6, the particles flow is shown for later times of the experiments. It is clear that the rate of removal of particles from the bed region at this range of experimental time is lower than earlier time (Figure 5-5). The particles are moving randomly in the freeboard region. Furthermore, the particles tend to cluster at the top of that region. This clustering increase with time and the phenomena of clustering is very clear at time 1.9 s. The final steady state involves some particles packed at the top of the test section (freeboard region), and the other particles remain packed at the bottom (bed region). Very few particles move from one region to another.

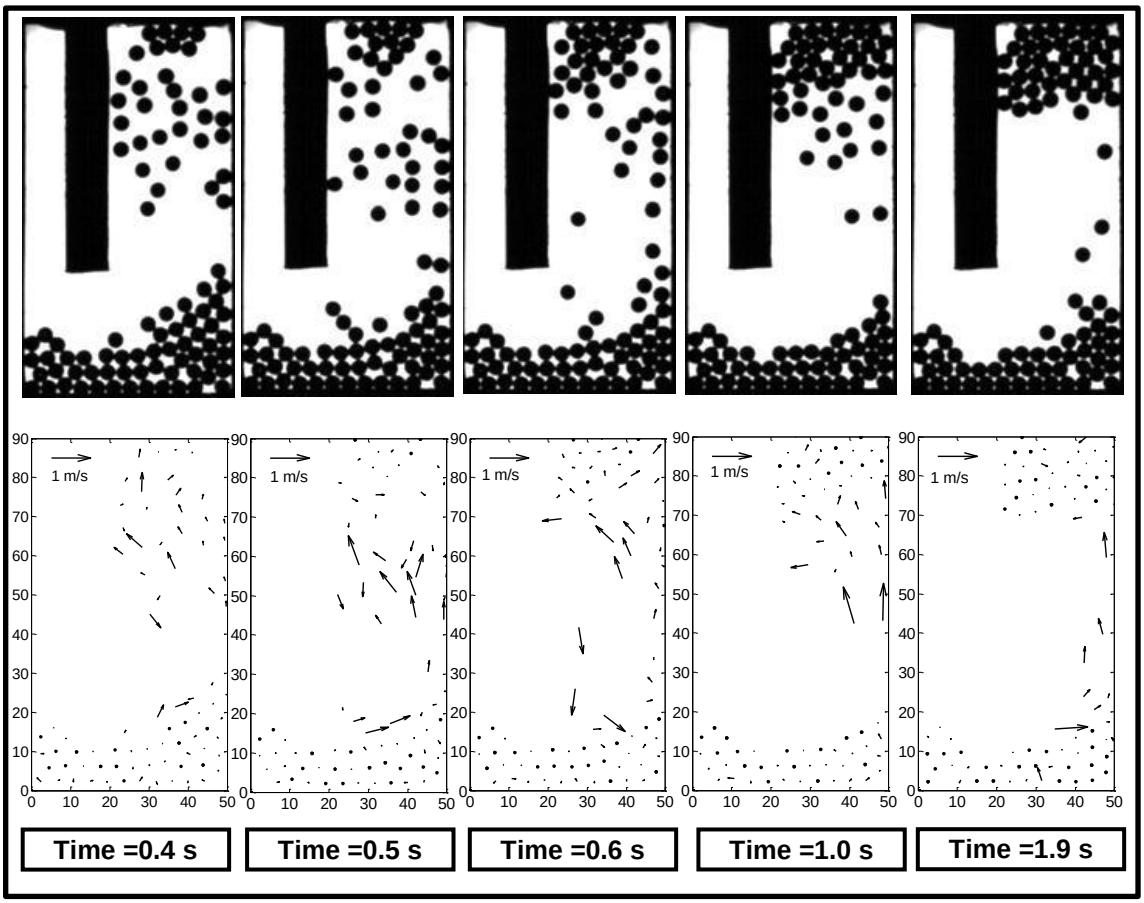

Figure 5-6: Particles flow field and velocity vectors for late experimental time, case two.

Throughout the different time frames in Figure 5-5 and Figure 5-6, it is clear that the air pressure difference (3 kPa) was able to move around half of the particles of the bed. This shows the effect of the reduction of the pressure difference across the test section in this case. The fluidised particles in the freeboard region keep moving until they cluster at the top and become stagnant.

The flow in this case might be divided into two main stages. The first stage is the initial fluidisation of the solid particles in the bed and their entrainment to the freeboard. The second stage is the random motion of the particles after their fluidisation. The transition between the two stages happens gradually at some time between 0.2 s and 0.3 s, and it is not possible to define an exact starting time. The second stage ends with particles clustering at the top of the freeboard region.

Figure 5-7 shows the velocity profiles for the first stage for time range between 0.052 s and 0.063 s. The first stage is similar to the fluidisation of the top layers in case one. The particles develop a horizontal velocity first and then they start to develop vertical velocity. The velocity vectors show that the motion of the bed is dominated by convection, which is similar to case one. This is mainly due to the absence of fluctuations in the velocity vectors within this time range. The velocity vectors show clear and defined motion of particles with no Brownian or vibrating motion. Consequently, the diffusive motion does not exist and convection is the main mechanism for particle motion.

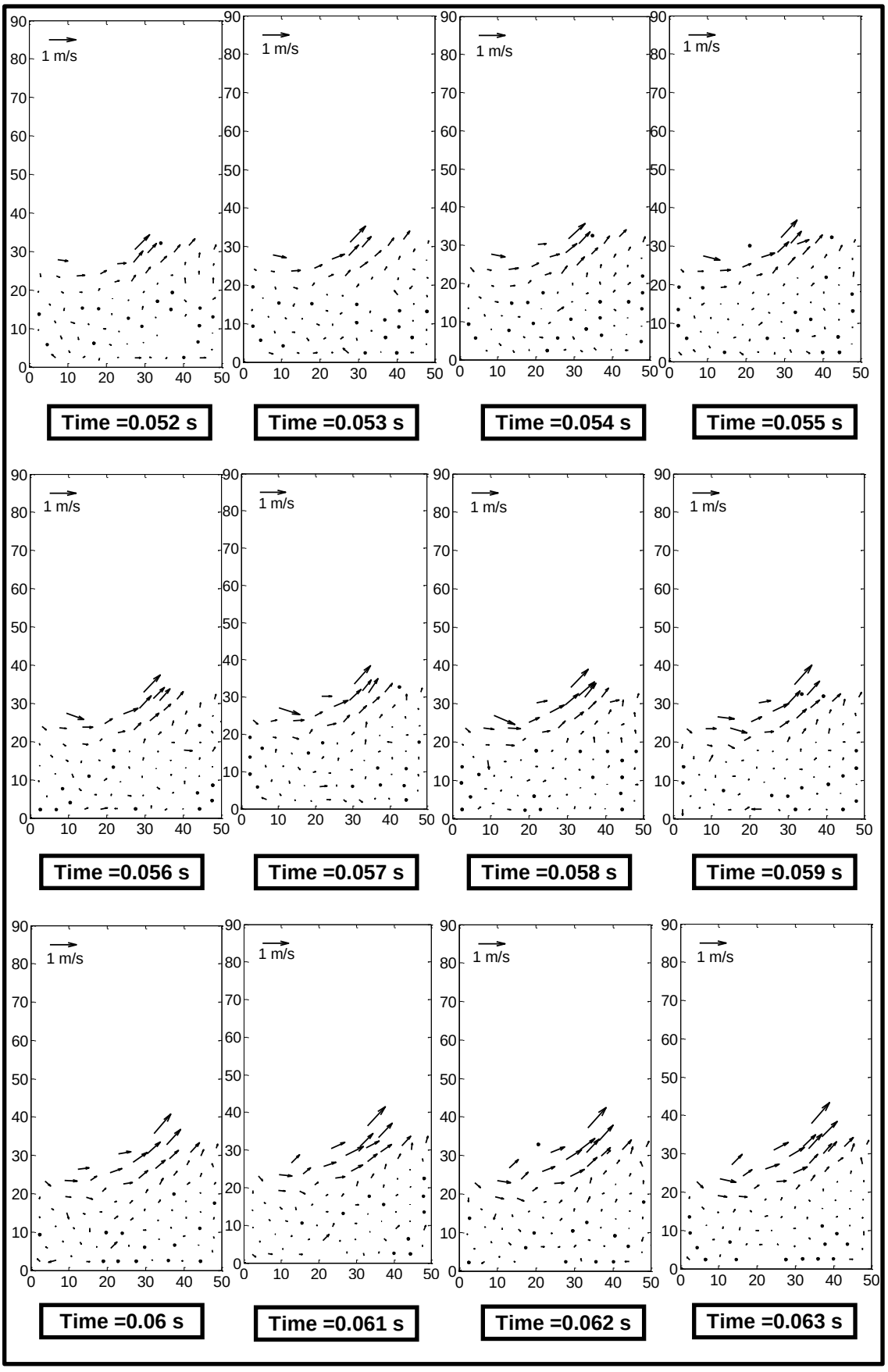

Figure 5-7: Particles velocity vectors in the first stage of flow, initial fluidisation.

The second stage is more complicated. It seems that different types of motion take place in it. The fluidised particles exhibit random motion from 0.3 s until the end of the experiment (Figure 5-5 and Figure 5-6). Another phenomenon that occurs is the clustering of the particles at the freeboard region. Figure 5-8 and Figure 5-9 show the velocity vectors at different time frames within the second stage. In Figure 5-8, it is clear that the particles exhibit different types of motion. Throughout all the time frames presented, the motion between 40 mm and 60 mm of the bed height is characterised by random velocity vectors (enclosed by red boxes). The particles in this sub-region have the potential of collisions at time 0.293 s (enclosed by blue box). By 0.299 s, particles have collided with each other. This is because they change the direction of the velocity vectors from the previous time frames (0.293 s, 0.295 s and 0.297 s). In the sub-region between 60 mm and 80 mm height, the particles have different type of motion (enclosed by green boxes). Their velocity vectors keep their direction and the motion is convective. This indicates that those particles move without being subjected to collisions. This kind of motion is due the effect of macroscopic forces such as inertia, weight and drag.

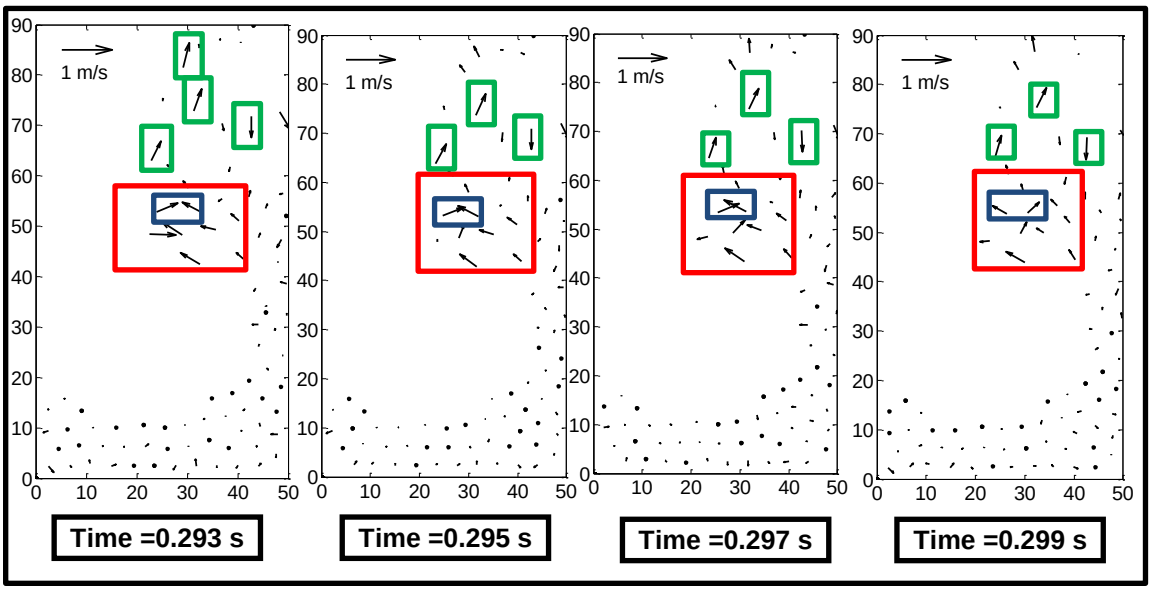

Figure 5-8: Particles velocity vectors in the second stage of flow from 0.293 s to 0.299 s.

For an ideal case of molecular or granular gas, the microscopic motion should take place over a much smaller time and length scales compared to

macroscopic motion. This allows the separation between the two particle flow scales; microscopic and macroscopic. The microscopic motion results from the inter-particle collisions and its consequent kinetic motion, while the macroscopic motion results from the macroscopic forces (weight, aerodynamic forces). In Figure 5-8, the coexistence of these two types of motion on the same time and length scales suggests that that the micro and macro scales are not separated.

Figure 5-9 shows the particles motion between 0.483 s and 0.505 s. It is clear that circulation of particles takes place between the freeboard and the bed region (enclosed by red boxes). This can be confirmed by tracking the motion of particles between 30 mm and 10 mm of the height (enclosed by red boxes). The particles at this range have clear downward direction from 0.483 s to 0.493 s. This downward motion disappears at later time frames. This indicates that those particles have collided with other particles in the packed bed and they have lost their momentum. Other particles start to develop horizontal motion in this sub-region which becomes very clear at time 0.505 s. Their motion might be due to the collisions with falling particles or due to air drag. In addition to the circulating motion, the particles moving behaviour seen in Figure 5-8 takes place. At time 0.483 s, there are two different types of motion between 30 mm and 70 mm on the vertical axis. The first type of motion is between 30 mm and 50 mm (enclosed by blue boxes). In this range, the particles have clear upward convective flow. In the range between 50 mm and 70 mm (enclosed by green boxes), the particles move randomly. These two streams of moving particles approach each other until they interact at 0.491 s. Then they form a single region (enclosed by black boxes) whose particles have a random velocity vectors, and the result of the interaction is clear from 0.493 onwards. Again this indicates that different types of motion exist at this time range. The forces responsible for this motion include macroscopic forces (weight, drag and inertia) and microscopic forces (collisions). Again, the coexistence of these two types of motion on the same time and length scales suggests that that the micro and macro scales are not separated.

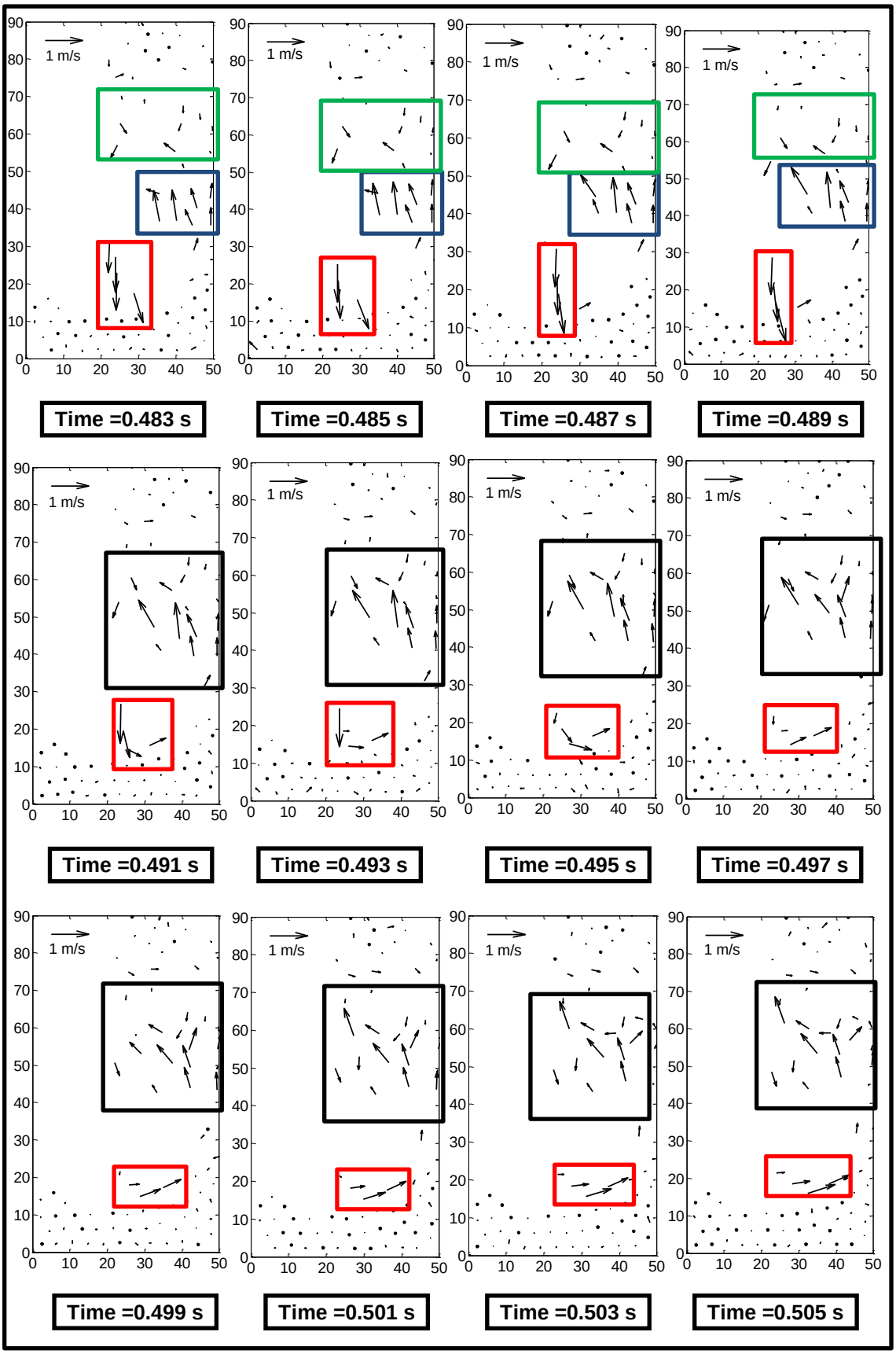

Figure 5-9: Particles velocity vectors in the second stage of flow from 0.483 s to 0.505 s.

The random motion noticed in the second stage indicates that the forces on the particles change with time. It seems that the drag force cannot support the weight of the particles and they fall. Interaction between two different streams of particles moving along converging trajectories triggers collisions. Some particles circulate between the bed region and the freeboard region. Moreover, particle clustering happens at the top of the freeboard.

Particle clustering is common in both dry granular flows and gas-solid flows (Brilliantov and Pöschel, 2010; Mitrano et al., 2014). It happens due to the loss of the fluctuating energy of particles due to different dissipative mechanisms such as inelastic inter-particle collisions in dry granular flows. In addition to inelastic collisions, drag forces play an important role in clustering for gas-solid systems. Furthermore, friction can be regarded as another dissipative mechanism. It is expected that friction will play an important role in the current flow situation due to the two-dimensional configuration. The friction results from the contacts between the particles and the front and the back walls. These contacts also might result in inelastic collisions. Other sources of inelastic collisions are the contacts with other walls and with other particles. The drag force might act as a dissipative force when the particle has a higher velocity than the surrounding air. For the current flow case, it is difficult to quantify the main energy dissipation mechanism. The contacts between the particles and the front and the back walls were not identified using the experimental technique. Furthermore, the random motion of the particles and the geometry used suggest that the value of the drag force changes over time. Probably, the effects of all these dissipative mechanisms and complex particle flow contribute towards the clustering process.

The clustering happening in this case is different from the particle re-packing seen in Chapter 4. The particle re-packing at the top of the freeboard in Chapter 4 is due to the immediate stop of particles and the loss of their bulk velocity or kinetic energy. On the other hand, the granular clustering (collapse) is due to the loss of fluctuating energy of the particles due to dissipative mechanisms such as inelastic collisions.

5.2.3 Average Particle Variables for the Bed Region

As shown in Chapter 4, the average void fraction of the freeboard region is closely connected to that of the bed region, because the constant total number of particles is divided between the two regions throughout the experimental time. Consequently, it is repetitive to present both results. Furthermore, the flow in whole domain was discussed in the previous section. This discussion showed the flow behaviour and regime. It is clear that the most interesting behaviour takes place in the freeboard region where different types of motion exist. Accordingly, we will not present the average results of the bed region and use the freeboard region average results only.

5.2.4 Average Particle Variables for the Freeboard Region

Figure 5-10 shows the instantaneous void fraction with respect to the experimental time. The void fraction is plotted for both the ensemble average of all five experiments and a single experiment. For the mean void fraction, its value is initially unity since there are no particles in the freeboard region. At the beginning of the experiment, there is an initial period of around 0.05 s where the particles are stagnant before the pressure difference reaches a value, which induces an air flow capable of moving the particles. Then the void fraction starts to decrease rapidly to a value of 0.83 until a time of 0.4 s. At this time, the void fraction decreases slowly until a time around 1.2 s. From this time, the void fraction remains nearly constant until the end of the experiment. The value of the void fraction fluctuates with low amplitude from a time of 0.3 s until the end of the experiment while keeping its decreasing trend. This means that particles circulate between the bed region and the freeboard region. However, the net flux of the particles over this period of time is in the upward direction. The single experiment is identical to the ensemble average for time up to 0.2 s which corresponds to the initial convection stage. From this time (0.2 s) to the end of the experiment, the amplitudes of fluctuations in the single experiment are higher than that of the ensemble average. However, the void fraction of the single experiment follows the same trend. The fluctuations in the void fraction of the single experiment indicate that the particles keep circulating between the freeboard and the bed regions. The low amplitude of fluctuations noticed in the

ensemble average suggests that this circulating behaviour is reduced when averaging over the ensemble of the experiments. The standard deviation shown in Figure 5-11 has a maximum value of 3.5%. This suggests a good repeatability for the void fraction between different experiments.

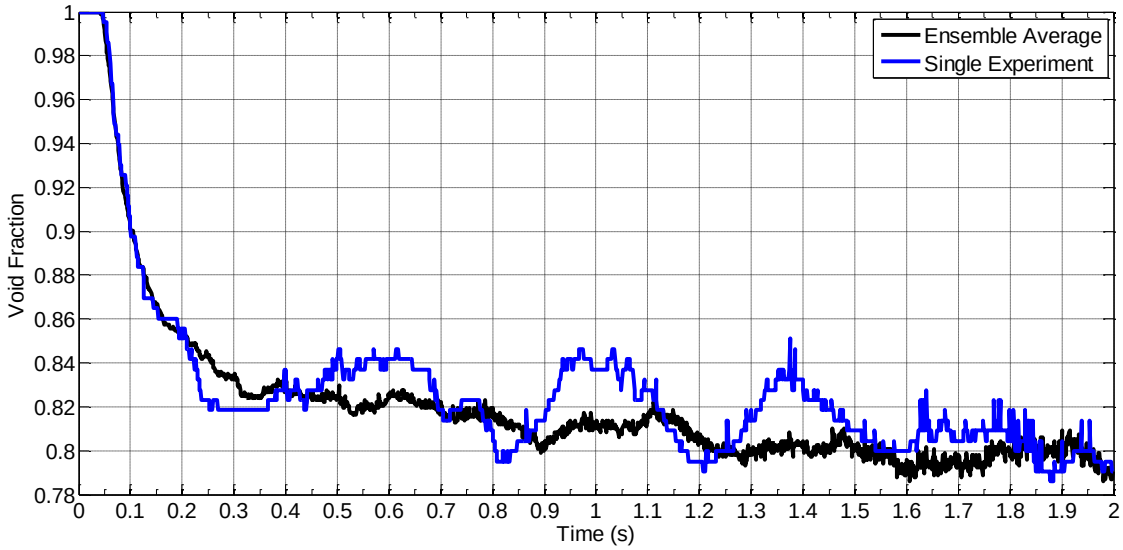

Figure 5-10: Ensemble average and a single experiment of the void fraction of the freeboard region versus time, case two.

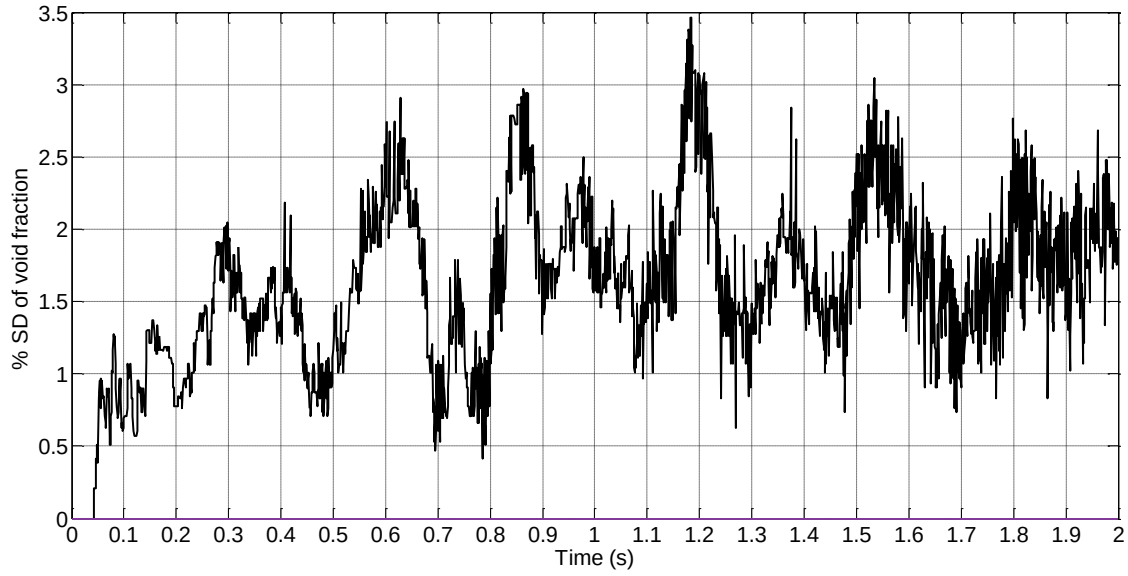

Figure 5-11, Percentage of standard deviation of the void fraction of the freeboard region versus time, case two.

Figure 5-12 shows the total horizontal velocity over the freeboard region versus time. The velocity is plotted for both the ensemble average and a single experiment. The ensemble average of the total velocity shows that after an initial period (up to 0.05 s) of zero velocity, the velocity starts to increase rapidly until it reaches a maximum value of around 3 m/s at a time around 0.075 s. This corresponds to the initial phase of fluidisation (convective flow) noticed in Figure 5-7. The particles move horizontally to the right following the direction of flow of the air jet. This leads to rapid increase in the total horizontal velocity. Then the velocity decreases until it reaches a value of around -1 m/s at a time of 0.2 s. This decrease in the velocity results from two types of flow behaviour as the velocity vectors reveal at 0.2 s in Figure 5-5. The first type is due to the fact that fewer particles are fluidised and acquire horizontal movement in the freeboard region after the top layers of the bed are fluidised. The second type is due to the vertical motion of particles in the freeboard. In general, the negative value of the horizontal velocity means that the particles move to the left direction in the freeboard region. This trend is similar to the one observed in the high pressure difference case (Figure 4-19).

The velocity keeps fluctuating until the end of the experimental time between values of -1 and 0.0 m/s. This indicates that the forces on the particles change with time, which leads to continuous change in the magnitude and direction of the velocity. Furthermore, the particle circulation in the domain (Figure 5-9) contributes towards this fluctuating behaviour of the total velocity. Similar to the void fraction profile, the horizontal velocity of the single experiment is identical to that of the ensemble average for time up to 0.2 s. The fluctuating behaviour seen in void fraction appears again for the horizontal velocity from 0.2 s to the end of the experiment.

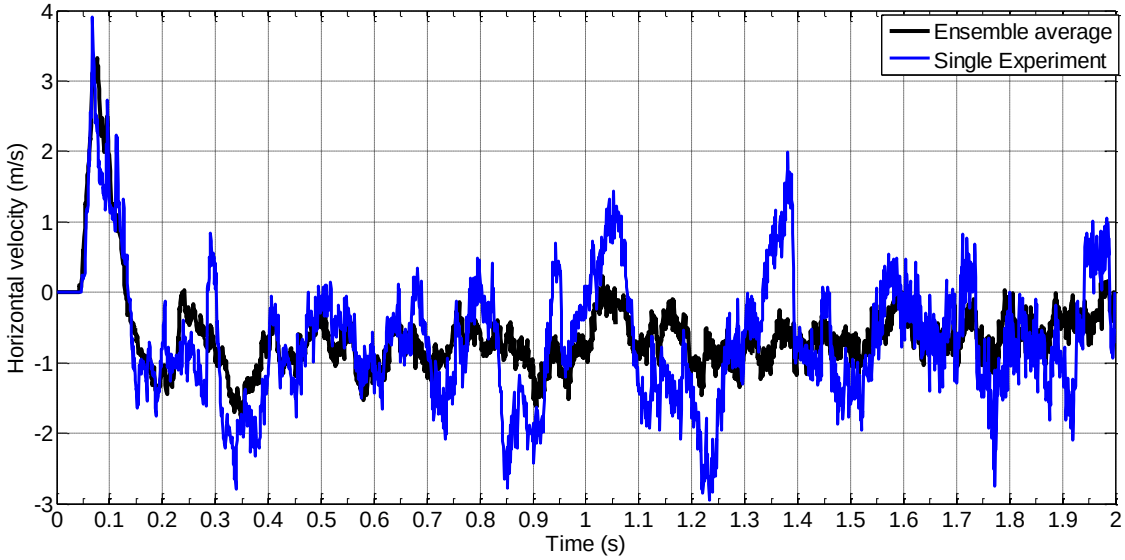

Figure 5-12: Single experiment and ensemble average of the total horizontal velocity of the freeboard region versus time, case two.

Figure 5-13 shows the percentage of standard deviation of the ensemble average of the total horizontal velocity. The standard deviation has a fluctuating nature and its value ranges between 5% and 40%. This shows the degree of repeatability in the experiments. Its value is of the same order of magnitude of case one. The cause of this relatively large standard deviation can be traced to the differences between the experiments in the ensemble as shown in Figure 5-14.

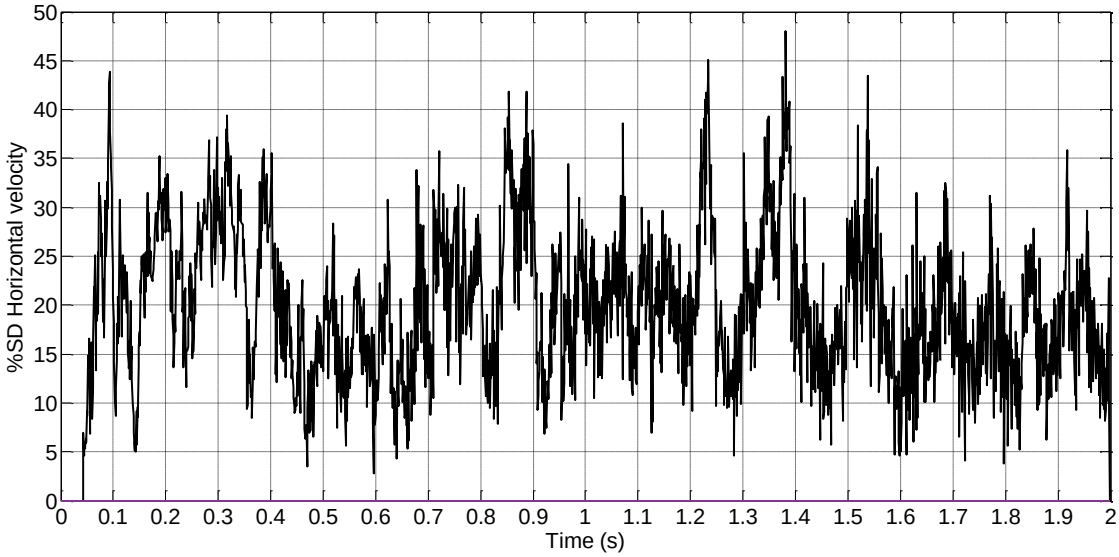

Figure 5-13: Percentage of standard deviation of the total horizontal velocity of the freeboard region versus time, case two.

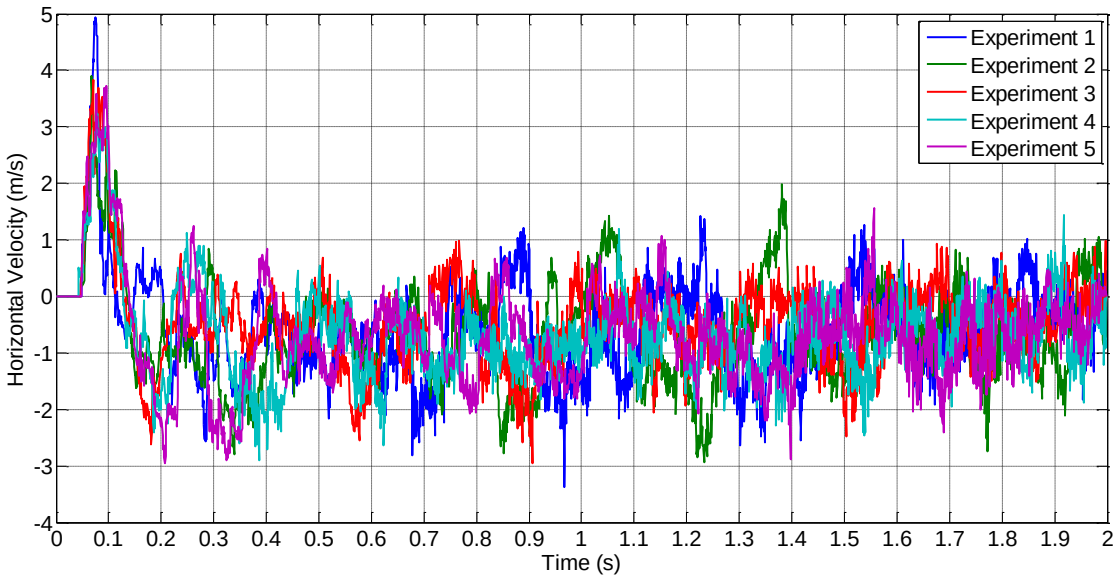

Figure 5-14: Total horizontal velocity of the freeboard region for all the experiments within the ensemble.

Figure 5-15 shows the vertical velocity with respect to time. Initially, the ensemble average velocity has a profile that is similar to the horizontal velocity with the rapid increase from zero to a maximum value. This maximum value is around 9 m/s in the vertical velocity. Then the vertical velocity decreases to zero at time around 0.45 s. The total vertical velocity fluctuates between zero

and 2 m/s until the end of the experiments. For the case of single experiment, the fluctuations in the velocity are much higher than the ensemble average. This confirms that the averaging process reduces the amplitude of fluctuations because the movement events do not happen at the same time within the ensemble.

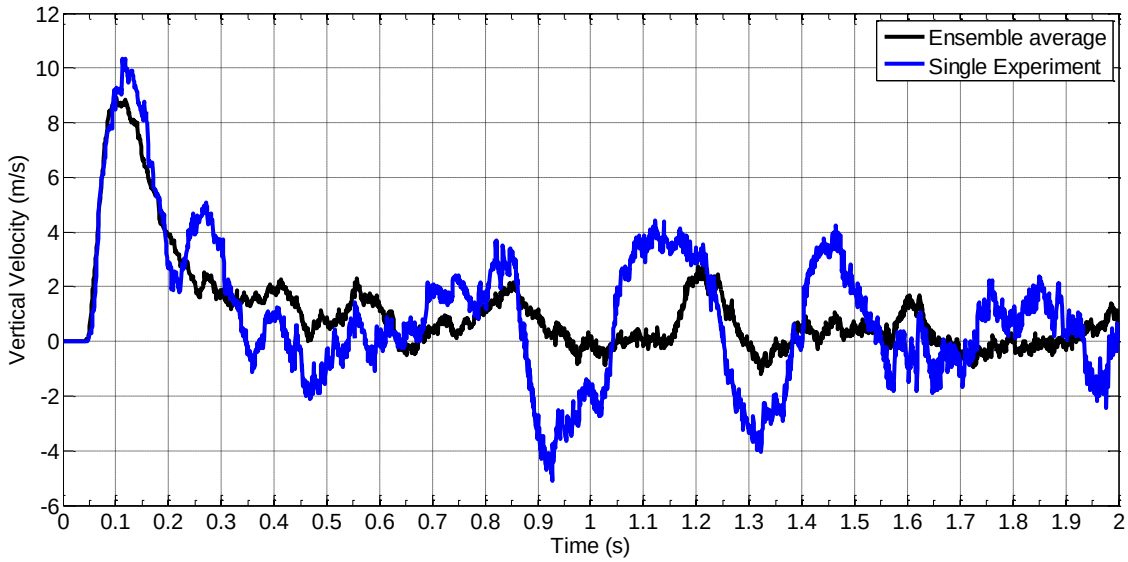

Figure 5-15: Single experiment and ensemble average of the total vertical velocity of the freeboard region versus time, case two.

Figure 5-16 shows the standard deviation of the total vertical velocity. As the total horizontal velocity, the standard deviation has a fluctuating nature and its value is up to 45% of the ensemble average. As in the horizontal velocity, the cause of this relatively large standard deviation can be traced to the differences between the experiments within the ensemble as shown in Figure 5-17.

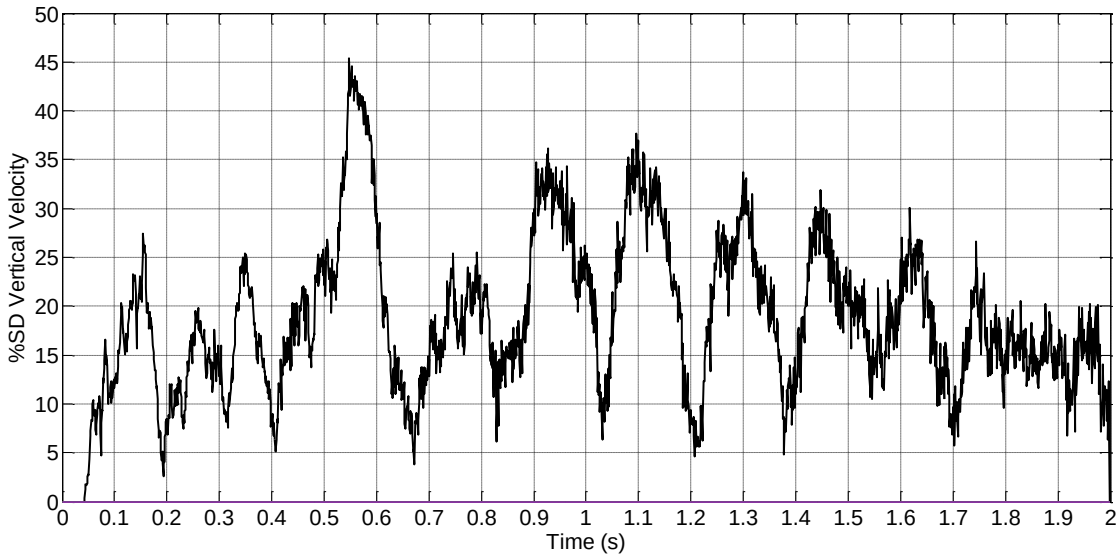

Figure 5-16: Percentage of standard deviation of the vertical velocity of the freeboard region versus time, case two.

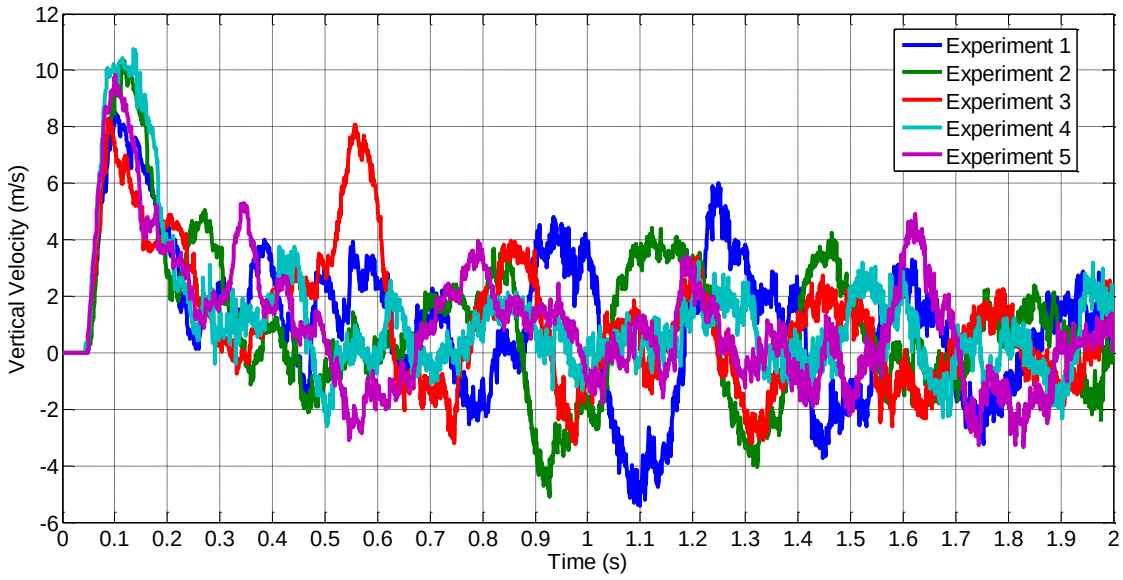

Figure 5-17: Total vertical velocity of the freeboard region for all the experiments within the ensemble.

5.2.5 Discussion

In this section, the fluidisation of solid bed using a low speed air jet with pressure difference of '3 kPa' has been presented. This low pressure difference results in partial fluidisation regime where around half of the solid bed is

fluidised. Although this regime in unlikely to occur in a typical DPI, it is important to study it because it gives physical insight to process and physics that occur in this multiphase flow at different conditions. There are three main discussion issues in this flow case: flow regime, continuum description and repeatability of experiments

5.2.5.1 Flow Regime

The solid flow in this section is divided into two stages. The first stage is the initial fluidisation of some particles in the packed bed. The second stage is their movement in the freeboard region. In the first stage, around half of the particles in the bed are fluidised. The process occurs in a similar fashion to case one (Chapter 4) where the convective flow dominates. This initial fluidisation lasts until an experimental time of around 0.3 s. In the second stage (0.3 s onwards), the fluidised particles move inside the freeboard region with some circulation between the freeboard and the bed. The motion of those particles is random with fluctuating total horizontal and vertical velocity. Different types of motion occur such as convective and collisional motion. It seems that the forces on the particles change their magnitude and direction during this stage. This makes it very difficult to identify quantitatively the cause of this motion. Moreover, the particles tend to cluster at the top of the freeboard at the end of the experiment. This clustering is due to the loss of energy by dissipative mechanisms such as wall friction and inelastic collisions.

5.2.5.2 Continuum Description

As discussed in Chapter 4, one of the main aims of these experiments is to validate the hydrodynamic models. Accordingly, we need to know whether this flow case satisfies the assumption of continuum and kinetic theory or not. This flow case was divided into two stages. The first stage is the initial convection up to time 0.3 s, while the other stage is the fluctuating motion from 0.3 s to 2.0 s. The first stage of convective flow is similar to the high pressure difference case presented in Chapter 4. There is no evidence that diffusion has an effect during this stage. Furthermore, the particles move in a dense aggregate behaviour. Accordingly, one might consider that the main challenge here is the large size

of particles and its consequences on the statistical fluctuations. Regarding the flow regime, the hydrodynamic model is challenged in its ability to minimise the effects of diffusive motion and promote convection.

In the second stage of flow, complex particle motion takes place. Particle velocity vectors present strong evidences that both collisional and convective motion take place. For some time frames, the convective motion is more prominent and no collisions exist while for other frames both types of motion take place. However, for all time frames one cannot say that the collisions happen on a smaller length and time scales than the bulk motion driven by macroscopic forces (inertia, weight and drag). This indicates that there is no scale separation in this stage of flow, and hence the kinetic theory assumptions are not satisfied. Furthermore, the continuum assumption is even more challenged compared to the first stage of convective aggregate flow. This is due to the relatively dilute flow of particles in this stage which increases the statistical fluctuations. Accordingly, the continuum and kinetic theory models might not work for this stage of flow.

5.2.5.3 Experiments Repeatability

The experiments were performed five times to study their repeatability. The void fraction shows very good quantitative repeatability with standard deviation of around 3%. The qualitative repeatability of the void fraction is good where the circulation between the freeboard and the bed regions results in fluctuating regional void fraction from time 0.3 s to the end of the experiment. The ensemble average removes these fluctuations because they do not occur at the same time in different experiments. Regarding the repeatability of the velocity, qualitative agreement is clear because the fluctuations are repeated within the ensemble but with variable timing and amplitude. Regarding the quantitative repeatability of the velocity, the standard deviation exhibits values of around 40%. For experimental time after 0.3 s, the ensemble averaging removes the fluctuations from the experiments.

As discussed in Chapter 4, the high standard deviation in the velocities shows that the experiments are not repeated exactly regarding the values of the particles' velocities. These differences can be traced to the variations within the

ensemble of the experiments. These variations are even higher for this case compared to Chapter 4. This is because the fluctuating motion from time 0.4 s is more likely to mismatch between the experiments within the ensemble. The variations between the experiments are due to the variation in the initial packing configuration (initial conditions), standard deviation in pressure difference (boundary conditions) and the change in the particle and test section surface properties (friction and restitution coefficients) between different experiments. The effect of fluctuations in pressure difference (standard deviation of ensemble average) is more prominent compared to the previous case. This is because the standard deviation in the air pressure difference is relatively high (10-20%). This means that the repeatability of some other particle variables such as void fraction and velocity is more affected.

The fluctuating motion is a main property of this flow case. It is related to some instability in the values of the macroscopic forces. Consequently, we shall use the single experiment for comparisons with the simulation. Using the ensemble average removes this important qualitative behaviour. The Two Fluid Model (TFM) is based on time and space averaging not ensemble average. The time and space average cannot be accomplished here because there is no scale separation.

5.3 Case three: 1.6 kPa Air Pressure Difference

In this section, the experiments are performed for a case of 1.6 kPa pressure difference across the test section. The main aim is to further examine the flow regime noticed in section 5.2. This is a partial fluidisation regime, where the strength of the air jet is relatively weak so that it cannot fluidise the whole particle bed. Figure 5-18 shows the initial conditions for different experiments within the ensemble.

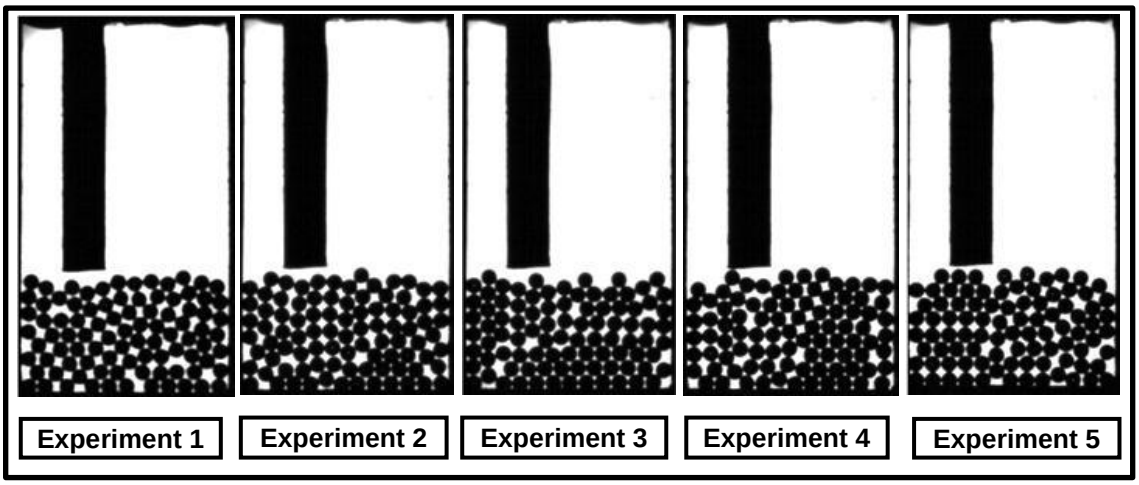

Figure 5-18: Initial frames for different experiments within the ensemble, case three.

5.3.1 Pressure Difference

The ensemble average of the pressure difference between inlet and outlet is shown in Figure 5-19 versus time. The initial increase in the pressure difference is due to the response time of the pneumatic system and mainly the solenoid valve. This was also shown in the previous cases.

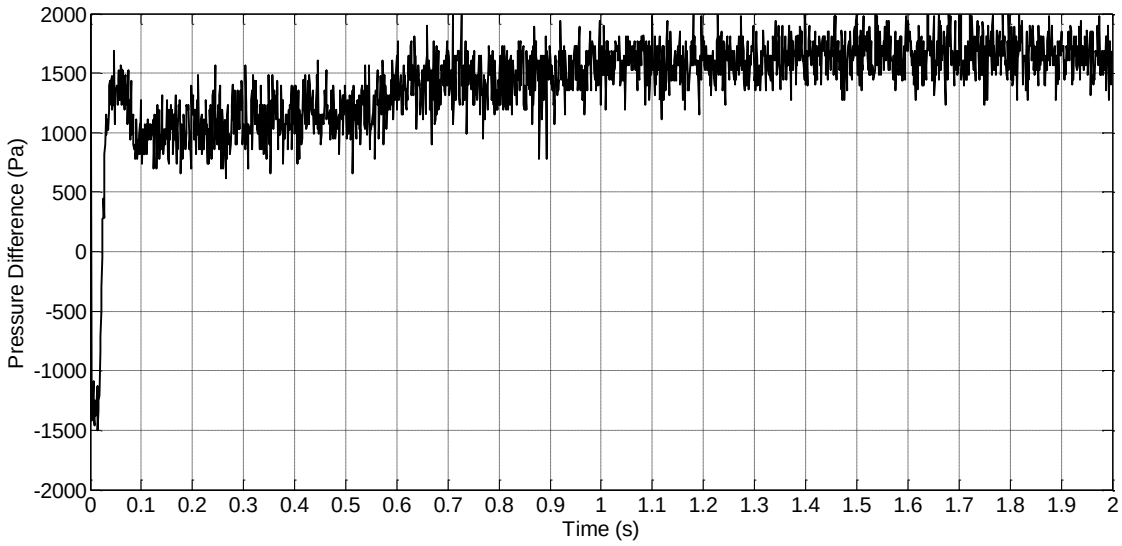

Figure 5-19: Ensemble average of pressure difference versus time, case three.

Figure 5-20 shows the absolute standard deviation in the pressure difference with respect to time. This standard deviation is a result of the different

experiments carried out for this case. The standard deviation has a similar order of magnitude of the previous cases. This confirms that the pressure difference has a similar fluctuating behaviour for all of the three cases.

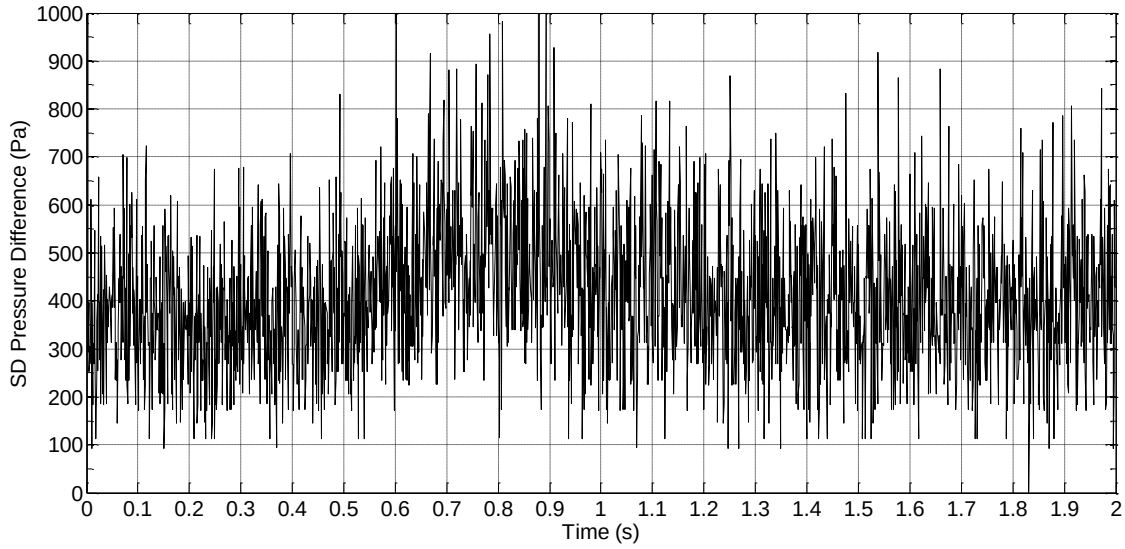

Figure 5-20: Absolute standard deviation of pressure difference versus time, case three.

5.3.2 Particles-whole Flow Field

Figures (5-21 and 5-22) show the images of the particle flow profiles at different time frames. They also show the velocity vectors of individual particles corresponding to these time frames.

In Figure 5-21, it is clear that the particles follow the same fluidisation pattern as the previous case (section 5.2.). Initially, the particles are packed in the bed region. The inlet air comes through these particles and strikes the bed to cause fluidisation. The air jet starts to move the particles due to the drag force. The upper layers of the bed are moved horizontally to the right direction then vertically upwards. Due to the relatively low pressure difference between the inlet and the outlet of the test section, the air velocity of the jet is lower than the previous cases (section 5.2). This results in upward movement of the particles in the bed with lower velocity compared to case two. These fluidised particles move in the freeboard region with few particles reaching the top of this region.

The particles move slowly in the freeboard region at 0.2 s and 0.3 s. The particles at time 0.3 s start to have a random motion.

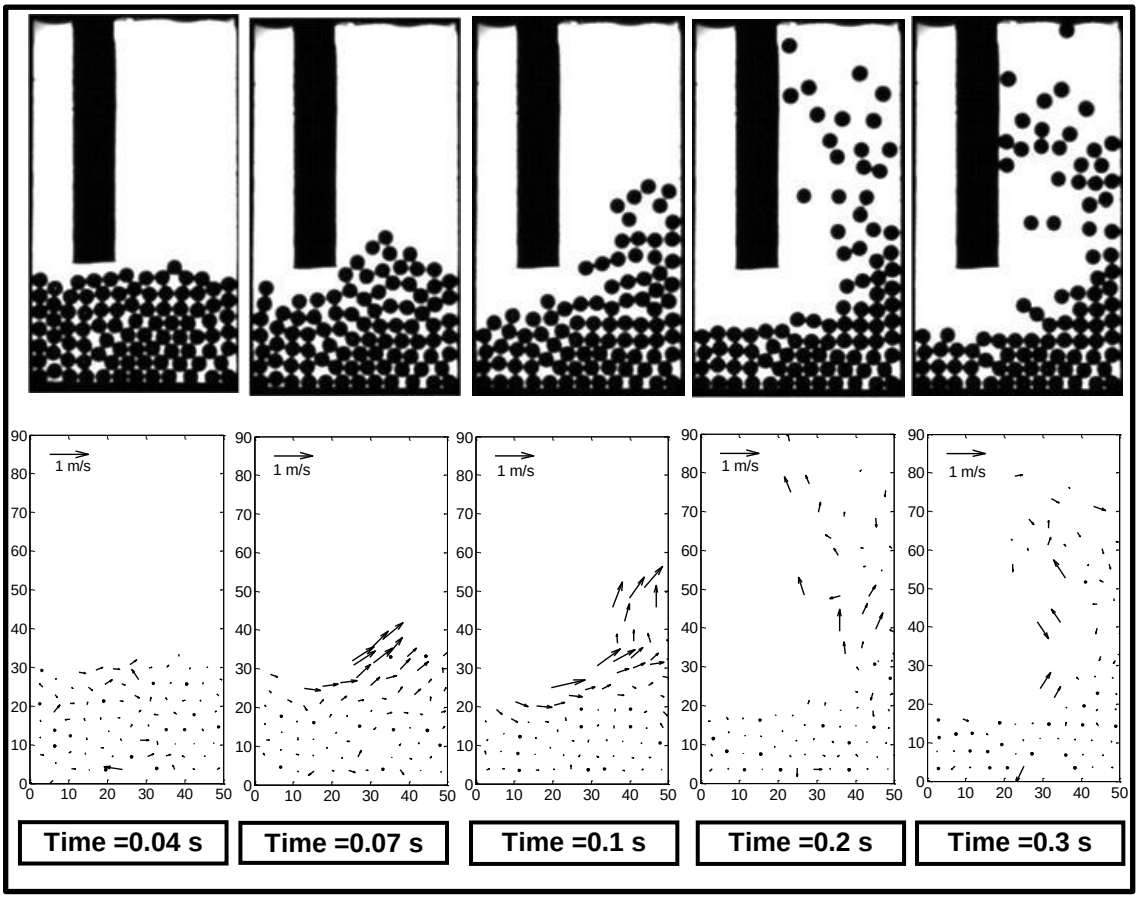

Figure 5-21: Particle flow field and velocity vectors for initial experimental time, case three.

In Figure 5-22, the fluidised particles in freeboard region exhibit random motion as confirmed by the velocity vectors (from 0.4 s to 1.9 s). This random motion was noticed in case two (section 5.2.). Furthermore, circulation of the particles within the test section and between the bed region and freeboard region is clearly observed at 0.6 s and 1.9 s. Despite the random motion and circulation, it is obvious that there is a net upwards motion towards the top of the freeboard region as shown at 1.9 s where the number of stagnant particles at the top of the region increases over time (clustering).

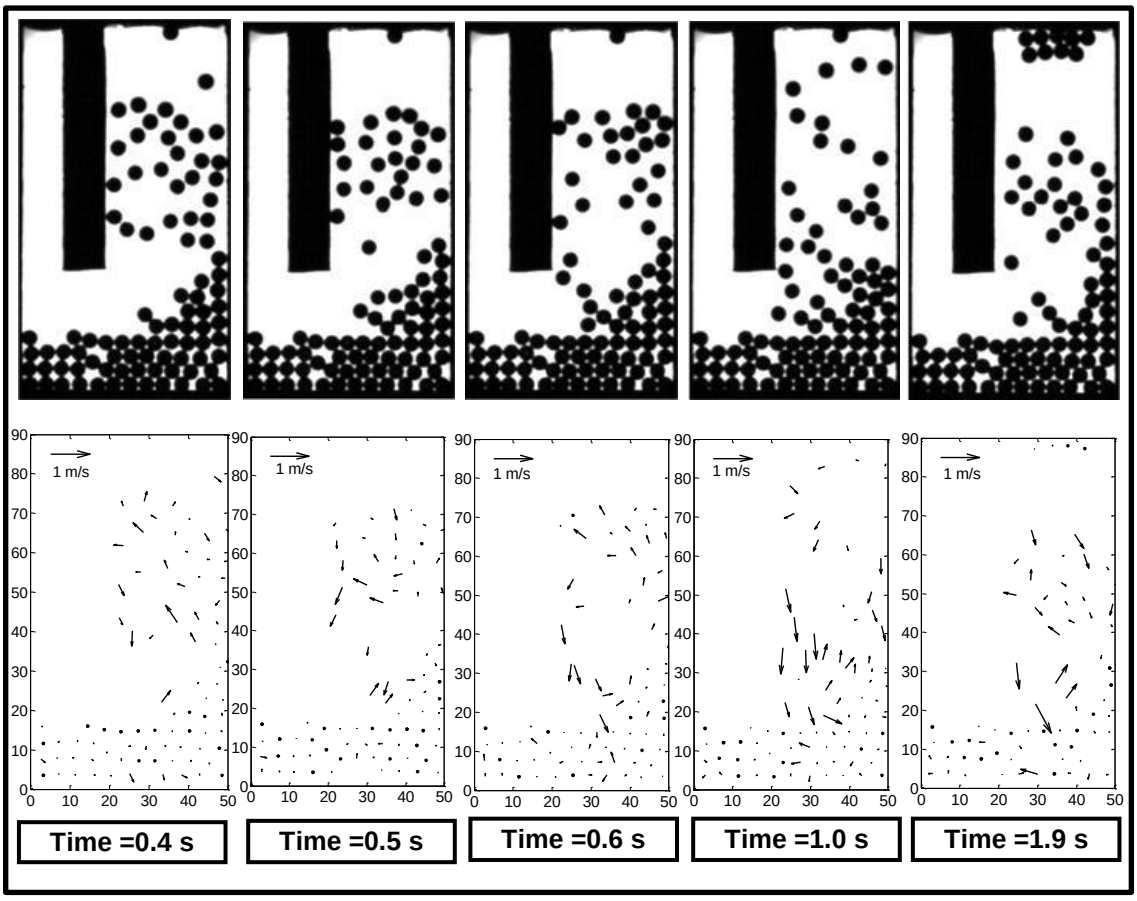

Figure 5-22: Particle flow field and velocity vectors for late experimental time, case three.

5.3.3 Average Particle Variables for the Freeboard Region

Figure 5-23 shows the void fraction of the freeboard region with time of the ensemble of experiments and a single experiment. The void fraction is initially of value of unity which corresponds to no (zero) particles. As soon as the experiment starts and the air flows inside the rig, the void fraction decreases due to the fluidisation of particles in the bed region. The void fraction reaches a minimum value of 0.86 at a time of 0.3 s. At this time, it starts to fluctuate between this minimum value and a maximum value of 0.88. These fluctuations are due to the particles moving between this region (freeboard) and the bed region. The single experiment curve follows the ensemble average with higher amplitude of fluctuations similar to case two (section 5.2.).

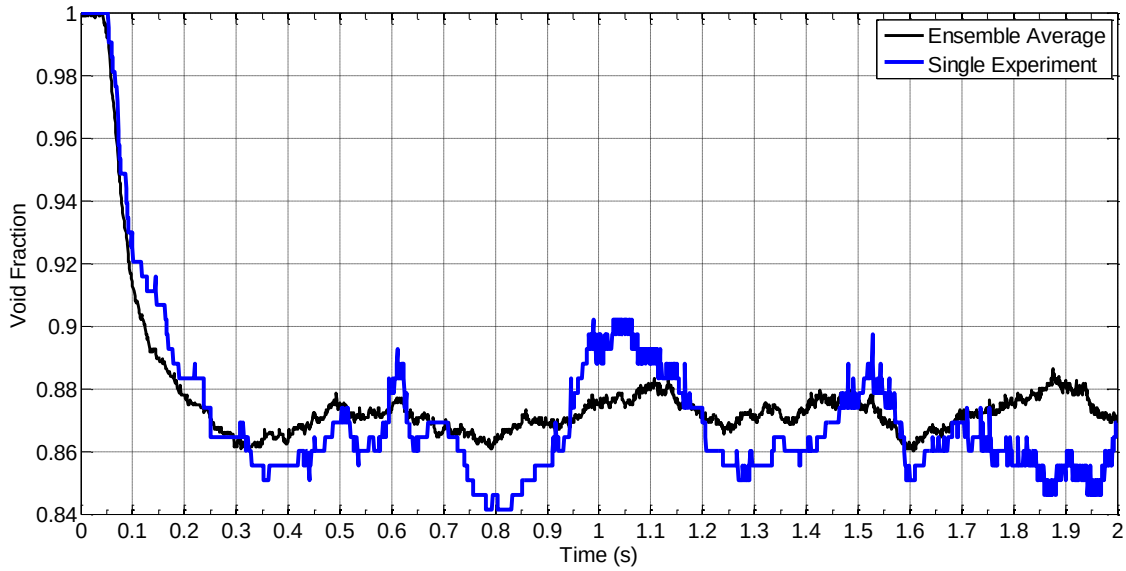

Figure 5-23: Single experiment and ensemble average and of the void fraction of the freeboard region versus time, case three.

Figure 5-24 shows the standard deviation of the void fraction with respect to the ensemble average of the experiments. The standard deviation has a maximum value of 3%. As the previous cases, the low value of standard deviation confirms that the variations within the ensemble have negligible effects on the void fraction.

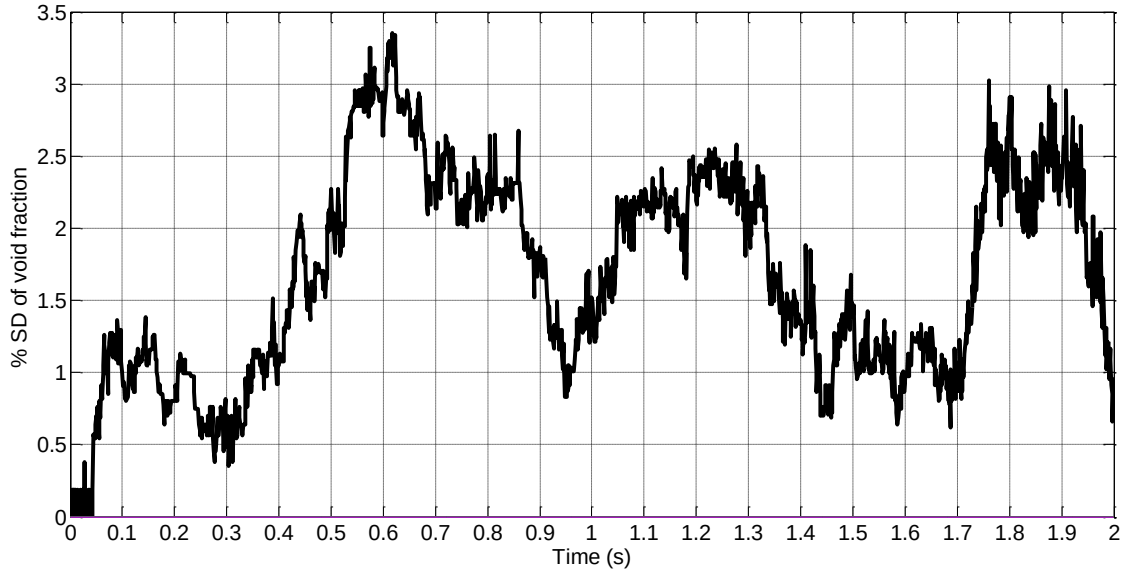

Figure 5-24: Percentage of standard deviation of the void fraction of the freeboard region versus time, case three.

Figure 5-25 shows the total horizontal velocity (single experiment and ensemble average) with time. At the beginning of the experiment, the ensemble average total horizontal velocity increases until it reaches a maximum value of around 4 m/s at a time of 0.1 s. At this time, the total velocity starts to decrease until it reaches a value of -1 m/s at a time of 0.2 s. The velocity of the particles starts to fluctuate at this time between -1 m/s and 0 m/s. The curve for the single experiment follows the same trend of the ensemble average. However, it has higher amplitude of the fluctuations. This has been noticed in the previous case (section 5.2.).

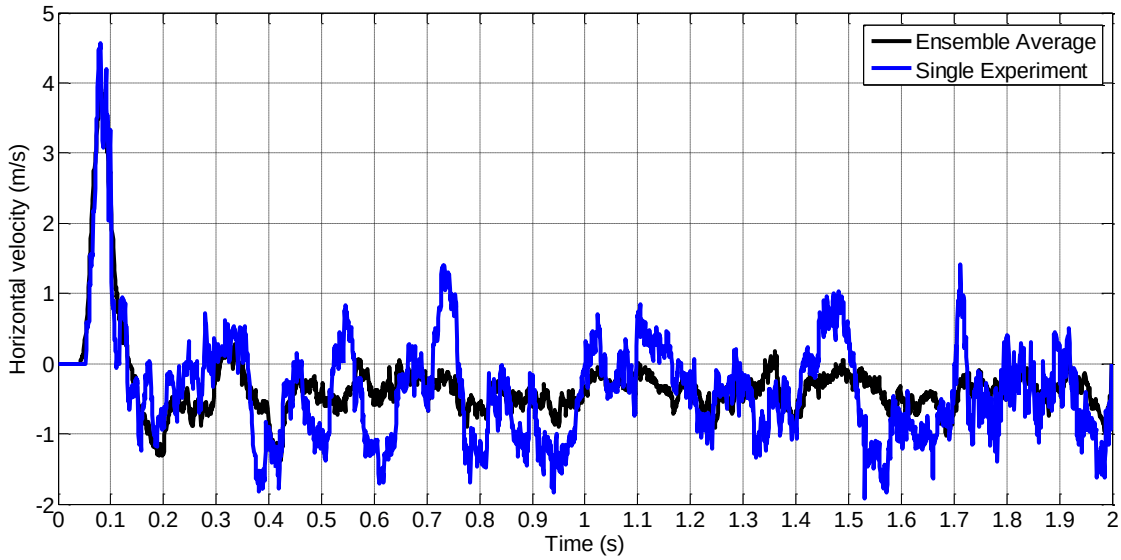

Figure 5-25: Single experiment and ensemble average of the total horizontal velocity of the freeboard region versus time, case three.

Figure 5-26 shows the percentage of standard deviation within the ensemble of the experiments with respect to the ensemble average. The standard deviation fluctuates between a minimum value of 5% and a maximum value of 30%. This shows that the variations in experimental conditions within the ensemble are reflected on the total horizontal velocity. This standard deviation can be traced to the differences within the ensemble of the experiments as shown in Figure 5-27.

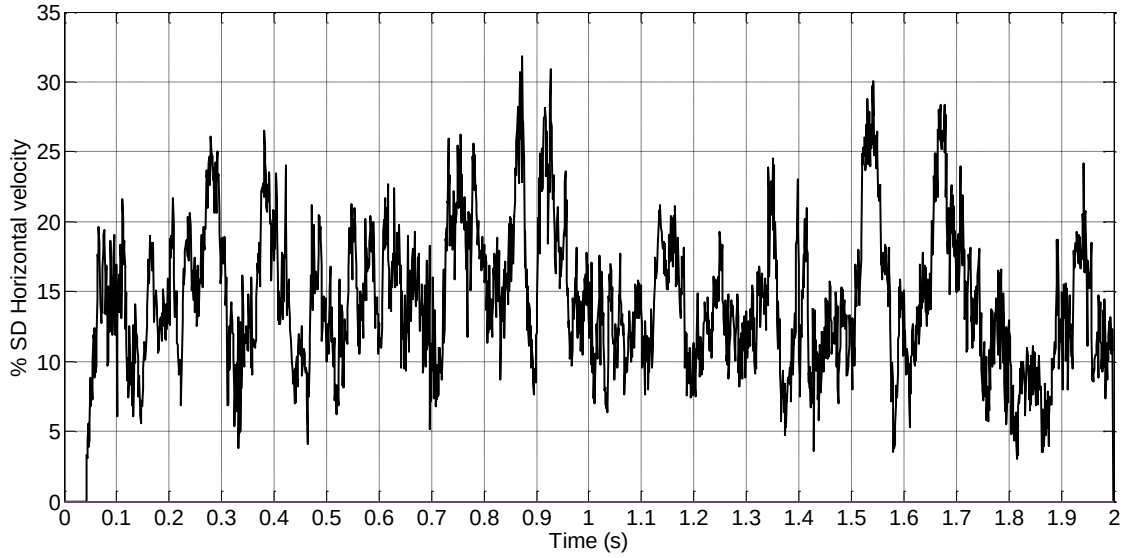

Figure 5-26: Percentage of standard deviation of the total horizontal velocity of the freeboard region versus time, case three.

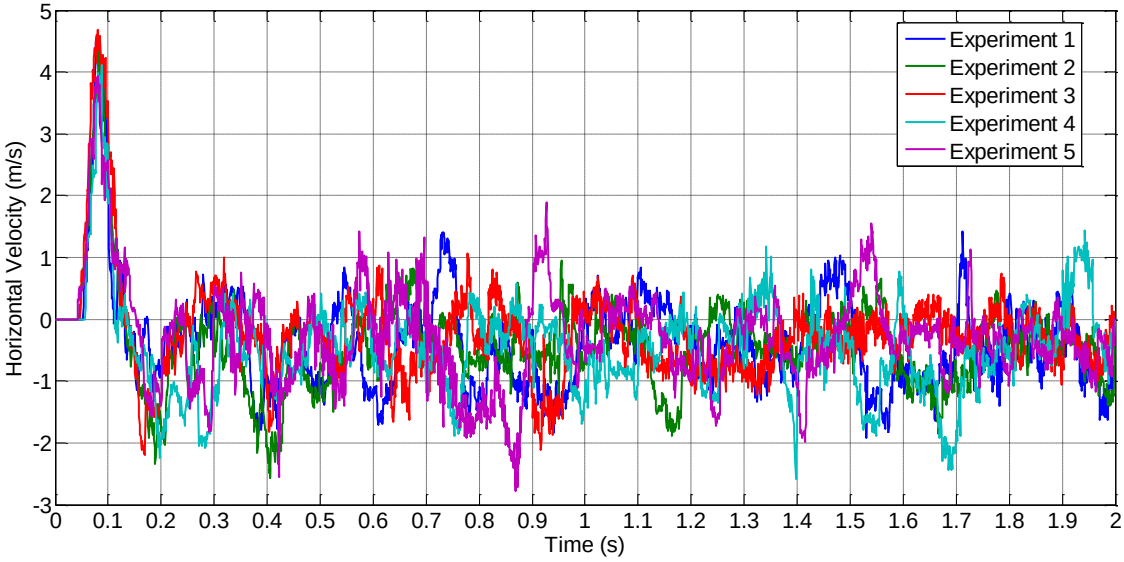

Figure 5-27: Total horizontal velocity of the freeboard region for all the experiments within the ensemble, case three.

Figure 5-28 shows the ensemble average and single experiment results of the total vertical velocity. The total vertical velocity of the ensemble increases at the beginning of the experiment until it reaches a maximum value of 7 m/s. At this time, it starts to decrease rapidly until it reaches a value of -2 m/s. It keeps fluctuating until the end of the experimental time between a minimum value of -2 m/s and a maximum value of 2 m/s. Here, the single experiment shows

relatively high amplitude of the fluctuations. This is very clear between 0.9 s and 1.8 s. The amplitude of the fluctuations is of order of magnitude of the initial convection (up to 0.25 s). This means that the forces exerted on the particles keep changing their magnitude and direction during this experimental time (similar to case two in section 5.2.).

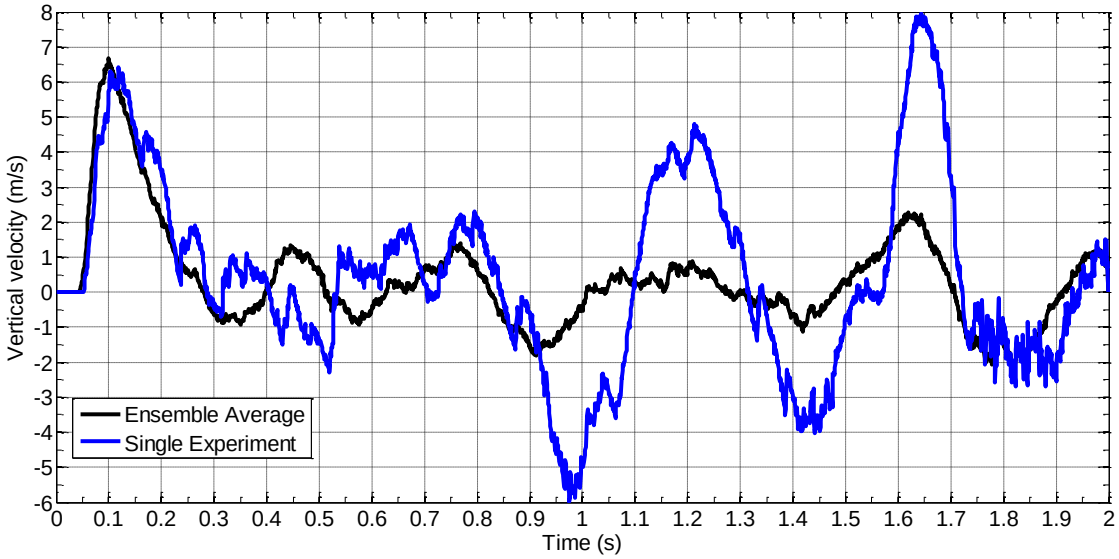

Figure 5-28: Single experiment and ensemble average of the vertical velocity of the freeboard region versus time, case three.

Figure 5-29 shows the standard deviation of the vertical velocity. The standard deviation has a fluctuating value throughout the experimental time. This high standard deviation (up to 60%) can be traced to the differences within the ensemble of the experiments as shown in Figure 5-30.

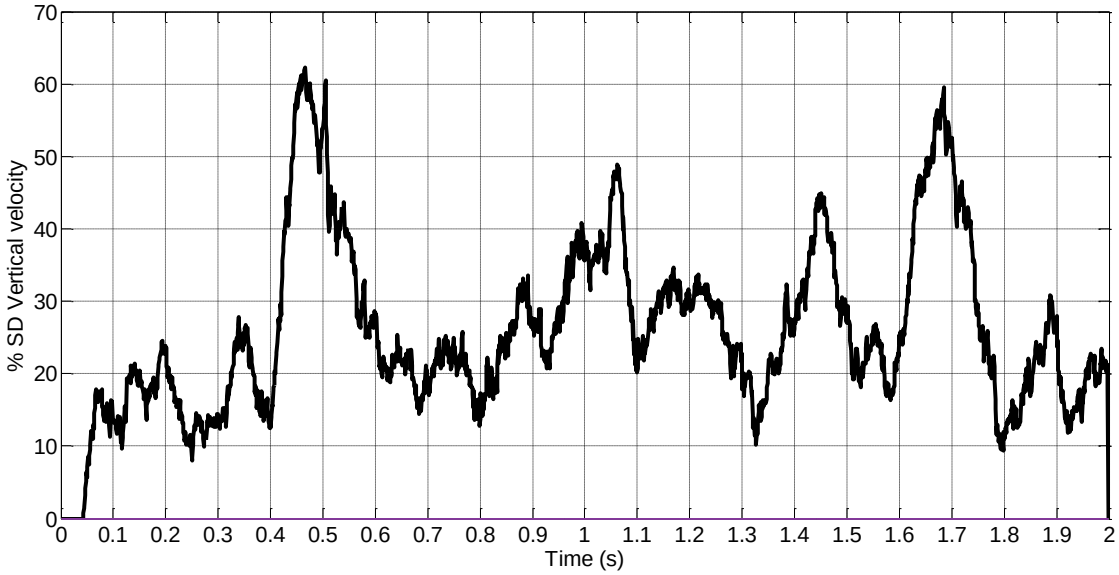

Figure 5-29: Percentage of standard deviation of the vertical velocity of the freeboard region versus time, case three.

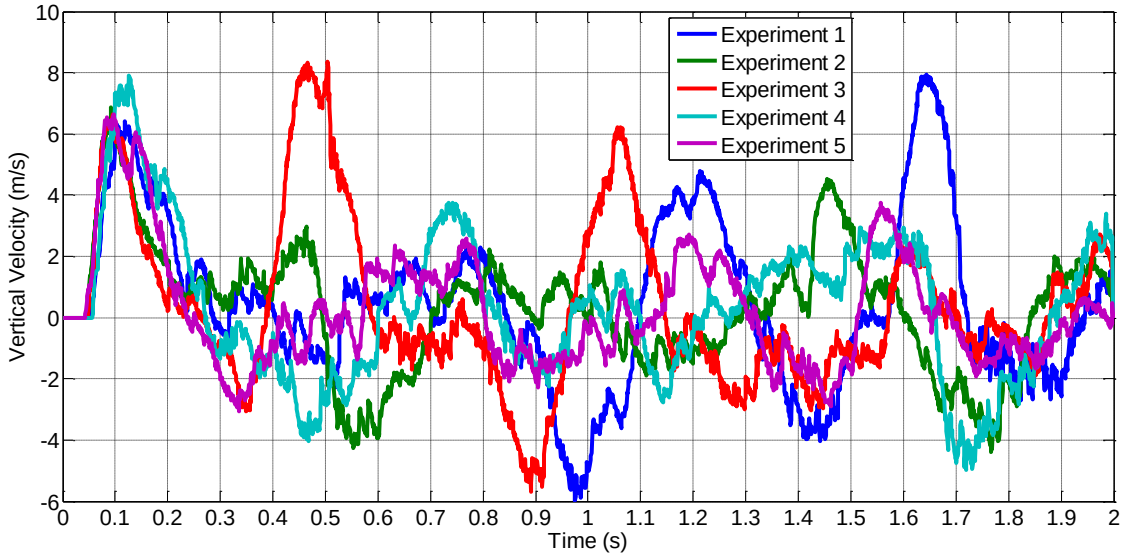

Figure 5-30: Total vertical velocity of the freeboard region for all the experiments within the ensemble.

The repeatability of the experiments exhibits similar trends as those of the previous case. The standard deviation is high for the total velocities.

5.3.4 Discussion

In this section, the results of fluidisation with a pressure difference of 1.6 kPa have been presented. This case has shown similar behaviour to the previous case presented in section 5.2. During the initial stage of fluidisation up to time 0.3 s, the flow is dominated by convection. However, the particle velocity is lower than that of section 5.2. The maximum vertical velocity here is around 7 m/s, while for the previous case was around 10 m/s. Furthermore, the number of fluidised particles is less than the previous case. The void fraction of the freeboard here is around 0.87 while it was around 0.8 for 3 kPa pressure difference in the previous case. The particles clustering noticed in the previous case happens here but with less particles. The average void fraction and velocity have the same trends as the previous case. Fluctuations appear during the second stage of fluidisation (from time 0.3 s). This also indicates that the forces keep changing their magnitude and direction. Furthermore, the random motion indicates that inter-particle collisions take place. These collisions happen on large time scales similar to the previous case. Consequently, the scale separation between the micro and macro flow does not exist.

5.4 Summary

In this chapter, the fluidisation of solid particles using weak impinging air jet has been studied. The experiments were carried out using two values of air pressure differences; 3 and 1.6 kPa. The two cases of partial fluidisation showed similar behaviour. The solid phase flow might be divided into two stages. The first stage is the initial fluidisation stage which is dominated by convection. The second stage is characterised by complex motion where both convective and collisional motion take place. Circulation within the test section and between the bed and the freeboard regions takes place. This indicates that the forces applied to particles change their magnitude and direction throughout the experiment. The results presented for the two cases for the partial fluidisation regime suggest that the model validation might be problematic due to the problems in both continuum and kinetic theory assumptions. This appears in the second stage of random motion of particles. The repeatability of the experiments for the void fraction is high with a standard deviation of 3%.

The standard deviation in the total velocity is high up to 30% for 3 kPa pressure difference and even higher (up to 70%) for 1.6 kPa. This is traced to the mismatching of the motion events of particles within the ensemble. However, the fluctuations in the experiments are qualitatively repeated within the ensemble. This indicates that this fluctuating motion is part of the flow regime. Using the ensemble average to describe this flow regime will be misleading since it removes this fluctuating and circulating motion. Consequently, we will use the results of single experiment to describe the flow behaviour and to compare with numerical prediction in Chapter 8.

Chapter 6 : Two Fluid Model (TFM) Description

6.1 Introduction

One of the main aims of this thesis is to investigate the ability of the hydrodynamic model or TFM to simulate the fluidisation and dense multiphase flow in DPIs. In Chapter 3, an experimental technique was developed to study the flow in DPI using simplified conditions. Subsequently, the experimental results were presented in Chapter 4 and Chapter 5. Those results described in detail the behaviour of solid particles in the experiments. They provided detailed measures of the particles positions and velocities throughout the whole test section and experimental time. These results provide the opportunity for detailed validation of the models. In this chapter, the continuum Euler-Euler or Two Fluid Model (TFM) is described. The basic equations and solution technique of the model are outlined. The time dependent version is used to model the experiments presented in the previous chapters. The TFM is basically a continuum model for each phase. The governing equations are derived based on the assumption that both phases coexist at every point in the domain. The volume fraction occupied by each phase is represented in its set of governing equations. Momentum transfer sub-models are used to account for the interactions between the two phases. Particle-particle interactions are solved using previously derived sub-models. This makes the hydrodynamic model very attractive in terms of computational time.

In order to close the set of governing equations describing a continuum model, the interaction within each phase should be related to other flow variables (e.g. velocity). This description of stresses is introduced for the gas phase by means of standard Navier-Stokes model stress-strain rate relations. On the other hand, the interactions within the solid phase are described by sub-models for continuum granular flow. These sub-models are formulated for two different regimes of granular flow. The rapid regime uses sub-models based on kinetic theory of granular flow (KTGF), while the slow regime uses sub-models based on frictional flow theories. Here, we use MFIX software (Benyahia, Syamlal and

O'Brien, 2012) for the numerical solution of TFM model. MFIX was developed in National Energy Technology Laboratory (NETL) in USA.

6.2 Governing Equations

In the following section, the continuity and momentum equations for each phase are described. The equations used for momentum coupling between the two phases and the KTGF models are introduced.

The continuity equation accounts for the conservation of mass of each phase. For the case of no chemical reactions it is described in mathematical formula for the gas phase as:

$$\frac{\partial}{\partial t}\left(\varepsilon_g \rho_g\right) + \frac{\partial}{\partial x_i}\left(\varepsilon_g \rho_g u_{gi}\right) = 0 \tag{6.1}$$

, and for the solid phase as:

$$\frac{\partial}{\partial t}\left(\varepsilon_s \rho_s\right) + \frac{\partial}{\partial x_i}\left(\varepsilon_s \rho_s u_{si}\right) = 0 \tag{6.2}$$

ε_g, ε_s are the volume fractions of the gas phase and solid phase, respectively. ρ_g, ρ_s are the densities of the gas phase and solid phase, respectively. u_g, u_s are the velocities of the gas phase and solid phase, respectively.

In the continuity equation of both phases, the first term on the left hand side accounts for the unsteady component, and the second term accounts for the spatial variations (mass convection) in the mass flow for the control volume.

The second fundamental law used for describing the fluid equations is Newton's second law of motion. It leads to the momentum equation, which is represented for the gas phase as:

$$\frac{\partial}{\partial t}\left(\varepsilon_g \rho_g u_{gi}\right) + \frac{\partial}{\partial x_j}\left(\varepsilon_g \rho_g u_{gj} u_{gi}\right) = \frac{\partial \sigma_{gij}}{\partial x_j} + \varepsilon_g \rho_g g_i - I_{gsi} \tag{6.3}$$

, and the solid phase as:

$$\frac{\partial}{\partial t}\left(\varepsilon_s \rho_s u_{si}\right) + \frac{\partial}{\partial x_j}\left(\varepsilon_s \rho_s u_{sj} u_{si}\right) = \frac{\partial \sigma_{sij}}{\partial x_j} + \varepsilon_s \rho_s g_i + I_{gsi} \tag{6.4}$$

σ_g, σ_s are the stress tensors of the gas phase and solid phase, respectively. I_{gs} is the interaction term between the two phases. g_i is the acceleration due to gravity.

The first term on the left hand side of the momentum equation of each phase is the momentum generation within the control volume (unsteady term), while the second term accounts for the momentum transfer by convection. The first term on the right hand side is the phase stress tensor, while the second term is the body force due to gravity. The last term accounts for the momentum transfer between the two phases (i.e. the drag force). This inter-phase interaction term appears in the two phases with the same magnitude but different sign following Newton's third law.

The sum of volume fraction for both phases over the control volume should be unity which is described mathematically as:

$$\varepsilon_g + \varepsilon_s = 1 \tag{6.5}$$

The constitutive equations describe the interaction forces (momentum transfer) between the two phases and the stress tensors (interaction within the single phase) in each phase. Gas flow is considered incompressible, because the Mach number of the gas is less than 0.3 (confirmed by air flow measurements in the experiments), so the density of the gas is constant. Accordingly, there is no need for an equation of state for the gas phase since the pressure field is de-coupled from the density.

6.3 Inter-phase Momentum Transfer

Gas-solid momentum transfer is given by:

$$I_{gsi} = -\varepsilon_s \frac{\partial p_g}{\partial x_i} + \beta_{gs}\left(u_{gi} - u_{si}\right) \tag{6.6}$$

p_g is the pressure of the gas phase. β_{gs} is the drag coefficient.

The first term on the right hand side accounts for the forces exerted by the gas on the solid particles, which are immersed in the gas phase, due to the pressure gradient in the gas phase (pressure drag). The second term is the

momentum transfer due to viscous drag exerted by the gas phase on solid particles due the difference of the velocity between the two phases (skin friction).

Evaluation of the viscous drag term requires specification of the drag coefficient β_{gs} . Different sub-models have been developed to describe the drag coefficient. These sub-models are based on different approaches ranging from empirical correlations to lattice Boltzmann modelling of flow over a solid particles arrangement. Different drag models are used in this thesis and they are presented below.

6.3.1 Wen-Yu Drag Correlation

Wen and Yu (1966) derived their drag correlation on the basis of particle fluidisation experiments performed with a wide range of solid-volume fractions and Reynolds numbers. Typically, the range for Reynolds number is from 0.01 to 5000 and void fraction from 0.4 to 1.

The drag coefficient β_{gs} is given by:

$$\beta_{gs} = \frac{3}{4} C_D \frac{\rho_g \varepsilon_g \varepsilon_s |u_g - u_s|}{d_p} \varepsilon_g^{-2.65} \tag{6.7}$$

$$C_D = \begin{cases} \dfrac{24(1 + 0.15Re^{0.687})}{Re}, & Re < 1000 \\ 0.44, & Re \geq 1000 \end{cases} \tag{6.8}$$

Reynolds number Re is given by:

$$Re = \frac{\rho_g \varepsilon_g |u_g - u_s| d_p}{\mu_g} \tag{6.9}$$

where d_p is the particle diameter and μ_g is the gas viscosity.

6.3.2 Gidaspow Drag Correlation

Gidaspow (1994) used a mixture between Wen-Yu correlation for the case of dilute regime (void fraction higher than 0.8) and Ergun equation (Ergun, 1952) for the case of dense regime. The Ergun equation is derived from pressure-drop measurements in closed-packed fixed beds. Furthermore, although Ergun correlation is based on systems with particles in fixed positions, it can be

applied to dynamic systems as well, if the density ratio between the two phases (as generally is the case in gas-solid flow) is large because the gas is moving much faster than the solid phase.

$$\beta_{gs} = \begin{cases} \frac{3}{4} C_D \frac{\rho_g \varepsilon_g \varepsilon_s |u_g - u_s|}{d_p} \varepsilon_g^{-2.65}, & \varepsilon_g \geq 0.8 \\ \frac{150 {\varepsilon_s}^2 \mu_g}{\varepsilon_g d_p^2} + \frac{1.75 \rho_g \varepsilon_g |u_g - u_s|}{d_p}, & \varepsilon_g < 0.8 \end{cases} \quad (6.10)$$

$$C_D = \begin{cases} \frac{24(1 + 0.15 Re^{0.687})}{Re}, & Re < 1000 \\ 0.44, & Re \geq 1000 \end{cases} \quad (6.11)$$

Where Reynolds number Re is given by:

$$Re = \frac{\rho_g \varepsilon_g |u_g - u_s| d_p}{\mu_g} \quad (6.12)$$

6.3.3 Hill-Koch-Ladd Drag Correlation

Hill, Koch and Ladd (2001b) developed their drag correlation based on Lattice-Boltzmann simulations of flow over a packed bed. Benyahia, Syamlal and O'Brien (2006) implemented a modified version of this drag correlation in MFIX. In order to obtain continuous description of the drag force over continuous Reynolds number and void fraction, the modified drag law used natural connectivity between the different functions at intersection points. When the functions did not intersect, a weighting factor was used to obtain a smooth transition.

$$\beta_{gs} = 18 \mu_g (1 - \varepsilon_s)^2 \varepsilon_s \frac{F}{{d_p}^2} \quad (6.13)$$

$$F = 1 + (3/8) Re, \;\; \varepsilon_s \leq 0.01 \; and \; Re \leq \frac{(F_2 - 1)}{\left(\frac{3}{8} - F_3\right)} \quad (6.14)$$

$$F = F_0 + F_1 Re^2, \qquad \varepsilon_s > 0.01 \; and \; Re \leq \frac{F_3 + \sqrt{{F_3}^2 - 4F_1(F_0 - F_2)}}{2F_1} \quad (6.15)$$

$$F = F_2 + F_3 Re \quad \begin{cases} \varepsilon_s \leq 0.01 \; and \; Re > \dfrac{(F_2 - 1)}{\left(\frac{3}{8} - F_3\right)} \\ \varepsilon_s > 0.01 \; and \; Re > \dfrac{F_3 + \sqrt{{F_3}^2 - 4F_1(F_0 - F_2)}}{2F_1} \end{cases} \tag{6.16}$$

$$F_0 = \begin{cases} (1-w)\left[\dfrac{1 + 3\sqrt{\frac{\varepsilon_s}{2}} + \left(\frac{135}{64}\right)\varepsilon_s \ln(\varepsilon_s) + 17.14\varepsilon_s}{1 + 0.681\varepsilon_s - 8.48{\varepsilon_s}^2 + 8.16{\varepsilon_s}^3}\right] \\ \quad +w\left[10\dfrac{\varepsilon_s}{(1-\varepsilon_s)^3}\right] \qquad , 0.01 < \varepsilon_s < 0.4 \\ \quad 10\dfrac{\varepsilon_s}{(1-\varepsilon_s)^3} \qquad \varepsilon_s \geq 0.4 \end{cases} \tag{6.17}$$

$$F_1 = \begin{cases} \dfrac{\sqrt{2/\varepsilon_s}}{40} & 0.01 < \varepsilon_s \leq 0.1 \\ 0.11 + 0.00051\exp(11.6\varepsilon_s) & \varepsilon_s > 0.1 \end{cases} \tag{6.18}$$

$$F_2 = \begin{cases} (1-w)\left[\dfrac{1 + 3\sqrt{\frac{\varepsilon_s}{2}} + \left(\frac{135}{64}\right)\varepsilon_s \ln(\varepsilon_s) + 17.89\varepsilon_s}{1 + 0.681\varepsilon_s - 11.03{\varepsilon_s}^2 + 15.41{\varepsilon_s}^3}\right] \\ \quad +w\left[10\dfrac{\varepsilon_s}{(1-\varepsilon_s)^3}\right] , \varepsilon_s < 0.4 \\ \quad 10\dfrac{\varepsilon_s}{(1-\varepsilon_s)^3} \qquad \varepsilon_s \geq 0.4 \end{cases} \tag{6.19}$$

$$F_3 = \begin{cases} 0.9351\varepsilon_s + 0.03667, & \varepsilon_s < 0.0953 \\ 0.0673 + 0.212\varepsilon_s + 0.0232/(1-\varepsilon_s)^5, & \varepsilon_s \geq 0.0953 \end{cases} \tag{6.20}$$

$$w = e^{(-10(0.4-\varepsilon_s)/\varepsilon_s)} \tag{6.21}$$

where Reynolds number is given by:

$$Re = \frac{\rho_g \varepsilon_g |u_g - u_s| d_p}{2\mu_g} \tag{6.22}$$

6.3.4 Syamlal and O'Brien Drag Correlation

This correlation is implemented in MFIX code and reported by Syamlal, Rogers and O'Brien (1993). It is derived using terminal velocity correlations in fluidised or settling bed. The drag coefficient β_{gs} is given by:

$$\beta_{gs} = \frac{3\varepsilon_s \varepsilon_g \rho_g}{4 V_{rm}^2 d_p} \left(0.63 + 4.8\sqrt{V_{rm}/Re}\right)^2 \left|u_g - u_s\right| \tag{6.23}$$

where V_{rm} is the root mean square dimensionless velocity given by:

$$V_{rm} = 0.5\left(A - 0.06Re + \sqrt{(0.06Re)^2 + 0.12Re(2B - A) + A^2}\right) \tag{6.24}$$

$$A = \varepsilon_g^{4.14} \tag{6.25}$$

$$B = \begin{cases} 0.8\varepsilon_g^{1.28}, & \varepsilon_g \leq 0.85 \\ \varepsilon_g^{2.65}, & \varepsilon_g > 0.85 \end{cases} \tag{6.26}$$

where Reynolds number for this model is given by:

$$Re = \frac{\rho_g \left|u_g - u_s\right| d_p}{\mu_g} \tag{6.27}$$

6.4 Gas phase Stress Tensor

The stress tensor of the gas phase is defined as:

$$\sigma_{gij} = -p_g I + \tau_{gij} \tag{6.28}$$

I is the identity matrix. The first term on the right hand side is the pressure stress. The second term τ_{gij} represents the viscous stress which is given by:

$$\tau_{gij} = 2\varepsilon_g \mu_g D_{gij} + \varepsilon_g \left(\lambda_g - \frac{2}{3}\mu_g\right) tr\left(D_{gij}\right) I \tag{6.29}$$

, and D_{gij} is the strain rate tensor (rate of deformation) defined as:

$$D_{gij} = \frac{1}{2}\left(\frac{\partial u_{gi}}{\partial x_j} + \frac{\partial u_{gj}}{\partial x_i}\right) \tag{6.30}$$

μ_g and λ_g are the shear and dilatational viscosities, respectively. The dilatational viscosity represents the resistance of the fluid to volumetric change. Since the gas is assumed to be incompressible, its value is zero, which yields the following expression for the viscous tensor:

$$\tau_{gij} = 2\varepsilon_g \mu_g D_{gij} - \frac{2}{3}\varepsilon_g \mu_g tr\left(D_{gij}\right) I \tag{6.31}$$

6.5 Solid Phase Stress Tensor

The granular flow model used here divides the granular flow into two distinct regimes:

- Rapid flow regime: the packing fraction is less than the critical packing fraction; kinetic theory is used to provide the expressions for solid phase stress tensor.
- Slow flow or fictional (quasi-static) regime: the particles packing fraction exceeds the critical packing fraction; theories adopted from soil mechanics are used to generate expressions for the solid phase stress tensor. These theories are based on the yield conditions of Coulomb friction.

The stress tensor for the particulate phase is written as a combination of a kinetic part and frictional part (Srivastava and Sundaresan, 2003). They are simply added to each other and it is assumed that each regime acts as if the other does not exist. Accordingly, it can be expressed by the following equation:

$$\sigma_{sij} = {\sigma_{sij}}^{rapid} + {\sigma_{sij}}^{slow} \tag{6.32}$$

where ${\sigma_{sij}}^{rapid}$ is the kinetic stress (rapid flow) and ${\sigma_{sij}}^{slow}$ is the frictional stress (slow flow). The latter is used only when the solid packing fraction exceeds the critical limit. The physical meaning of the critical packing fraction is that the solid volume fraction is sufficiently large for long and enduring particle contacts to become important. In the case of fluidised beds simulations, this value is taken to be equal to the minimum fluidisation velocity. The physical justification for this is that at the minimum fluidisation velocity, the particles are not in contact with each other. However, there is no universal exact value of the packing fraction at which the transition occurs (Tardos, 1997; Srivastava and Sundaresan, 2003).

6.5.1 Rapid Granular Flow

The solid phase stress tensor ${\sigma_{s,ij}}^{rapid}$ is given by:

$$\sigma_{sij}{}^{rapid} = -p_s{}^{rapid} I + \tau_{sij}{}^{rapid} \tag{6.33}$$

, and the viscous stress term is given by:

$$\tau_{sij}{}^{rapid} = 2\mu_s D_{sij} + \left(\lambda_s - \frac{2}{3}\mu_s\right) tr\left(D_{sij}\right) I \tag{6.34}$$

D_{sij} is the strain rate tensor given by:

$$D_{sij} = \frac{1}{2}\left(\frac{\partial u_{si}}{\partial x_j} + \frac{\partial u_{sj}}{\partial x_i}\right) \tag{6.35}$$

The kinetic theory of granular flow gives expressions for the solid phase pressure p_s, the dilatational viscosity λ_s and shear viscosity μ_s in the rapid regime. The relevant expressions for the dilatational viscosity and shear viscosity will be given below, however, they are both functions of the granular temperature Θ_s. The granular temperature is a measure of the fluctuating component in the particles velocity. It is defined as follows:

$$\Theta_s = \frac{1}{3}\langle {v_s}^2 \rangle \tag{6.36}$$

$\langle {v_s}^2 \rangle$ is the fluctuating kinetic energy. It represents the average kinetic energy of particle velocity around the mean velocity of the particles in the control volume. It is represented as:

$$\langle {v_s}^2 \rangle = \langle \left(u_p - u_s\right)^2 \rangle \tag{6.37}$$

, u_p is the particle velocity.

In order to close the set of the equations described by KTGF, the granular temperature field should be obtained. The equation used for solving the granular temperature transport in the flow field is given by:

$$\frac{3}{2}\rho_s\left[\frac{\partial(\varepsilon_s \Theta_s)}{\partial t} + \frac{\partial\left(\varepsilon_s u_{sj} \Theta_s\right)}{\partial x_j}\right] = \frac{\partial}{\partial x_i}\left(K_s \frac{\partial \Theta_s}{\partial x_i}\right) + \sigma_{sij}{}^{rapid}\left(\frac{\partial u_{si}}{\partial x_j}\right) + \Pi_s - J_s \tag{6.38}$$

The pre-factor on the left hand side $\left(\frac{3}{2}\right)$ accounts for transforming the kinetic energy of fluctuation ($\frac{1}{2}\langle {v_s}^2 \rangle$) to granular temperature (equation 6.36).

The first term on the left hand side in the granular temperature transport equation accounts for the unsteady change in granular temperature, while the second term is the convective flux. The first term on the right hand side accounts for the diffusion of the granular temperature. It is represented as a function of the granular conductivity K_s. The second term on the right hand side is the rate of production of granular temperature due to the work done by the hydrodynamic stresses of the rapid flow regime, which implies that the work done by the frictional component of stress is transformed directly into thermal internal energy and does not contribute to the granular temperature production (Johnson and Jackson, 1987; Srivastava and Sundaresan, 2003). The third term (Π_s) accounts for the source of granular temperature due to the exchange between the solid phase and gas phase. It results from the action of the fluctuating force exerted by the gas through the fluctuating velocity of the particles. The last term (J_s) in equation (6.38) is a sink term, which accounts for dissipation of the granular temperature due to inelastic collision between the particles.

In this thesis, two kinetic theory models, which are implemented in MFIX code, are used. They are Lun (Lun et al., 1984) model with a slight modification to account for the effects of gas. The other model is Garzó (Garzó and Dufty, 1999). The superscript '$rapid$' is dropped from the equations describing the kinetic models for the sake of brevity.

6.5.1.1 Lun Kinetic Theory Model

Lun model (Lun et al., 1984) is widely used in multiphase flow applications and is implemented in MFIX code (Benyahia, Syamlal and O'Brien, 2012). This model uses an approach that is close to the established methods of 'Chapman-Enskog' gas theory. To resolve the collisions between particles, the model uses a simple moment method based on the Maxwell transport equation. This is slightly different from using the Chapman and Cowling (1970) method**,** which relies upon the Boltzmann equation. However, it follows the same general approach based on the assumption that gradients of the mean-flow properties such as velocity, temperature and bulk density are in some sense small. This small-gradient assumption implies that the energy dissipated during a collision

is small, and hence the particles considered here are nearly elastic (the coefficient of restitution e is close to unity). This does not mean that the value of elasticity needs to be very close to unity in simulations.

The solid pressure p_s is given by:

$$p_s = \varepsilon_s \rho_s \Theta_s \left[1 + 4\eta \varepsilon_s g_{0,s}\right] \tag{6.37}$$

, where

$$\eta = \frac{(1+e)}{2} \tag{6.38}$$

e is the restitution coefficient . $g_{0,s}$ is the radial distribution function at contact. For Lun model, it is given by:

$$g_{0,s} = \left[1 - \left[\frac{\varepsilon_s}{{\varepsilon_{fs}}^{max}}\right]^{1/3}\right]^{-1} \tag{6.39}$$

${\varepsilon_{fs}}^{max}$ is the maximum solid packing fraction.

The radial distribution function accounts for the increase in collision rate over the predicted by Boltzmann at higher densities due to volume effects.

In equation (6.37), the first component of the solid pressure represents the kinetic contribution and the second part represents the collisional contribution. In general, the kinetic part of the stress tensor represents the momentum transferred through the system by particles moving across imaginary layers in the flow, while the collisional part denotes the momentum transferred by direct collisions between particles.

The dilatational viscosity (λ_s) describes the resistance of the particle suspension against compression (volumetric deformation). Its expression is as follows:

$$\lambda_s = \frac{4}{3}\rho_s d_s {\varepsilon_s}^2 g_{0,s}(1+e)\sqrt{\frac{\Theta_s}{\pi}} \tag{6.40}$$

The shear viscosity (μ_s) accounts for the resistance of the fluid to shear deformation. It is given by:

$$\mu_s = \left(\frac{2+\alpha}{3}\right)\left[\frac{\mu_s'}{g_{0,s}\eta(2-\eta)}\left(1+\frac{8}{5}\eta\varepsilon_s g_{0,s}\right)\left(1+\frac{8}{5}\eta(3\eta-2)\varepsilon_s g_{0,s}\right)+\frac{3}{5}\lambda_s\right] \quad (6.41)$$

The factor $\left(\frac{2+\alpha}{3}\right)$ is a correction for the multiphase effect obtained using experiments. The parameter α is a constant whose value is 1.6.

$$\mu_s' = \frac{\rho_s\varepsilon_s g_{0,s}\Theta_s\mu'}{\rho_s\varepsilon_s g_{0,s}\Theta_s + \left(\frac{2\beta_{gs}\mu'}{\rho_s\varepsilon_s}\right)} \quad (6.42)$$

$$\mu' = \frac{5}{96}\rho_s d_s\sqrt{\pi\Theta_s} \quad (6.43)$$

The solid conductivity K_s is given by:

$$K_s = \left(\frac{K_s'}{g_{0,s}}\right)\left[\left(1+\frac{12}{5}\eta\varepsilon_s g_{0,s}\right)\left(1+\frac{12}{5}\eta^2(4\eta-3)\varepsilon_s g_{0,s}\right) + \frac{64}{25\pi}(41-33\eta)\eta^2\left(\varepsilon_s g_{0,s}\right)^2\right] \quad (6.44)$$

$$K_s' = \frac{\rho_s\varepsilon_s g_{0,s}\Theta_s K'}{\rho_s\varepsilon_s g_{0,s}\Theta_s + \left(\frac{6\beta_{gs}K'}{5\rho_s\varepsilon_s}\right)} \quad (6.45)$$

$$K' = \frac{75\rho_s d_p\sqrt{\pi\Theta_s}}{48\eta(41-33\eta)} \quad (6.46)$$

(Π_s) accounts for the source of granular temperature due to exchange between the solid phase and gas phase and is given by (Agrawal et al., 2001):

$$\Pi_s = -3\beta_{gs}\Theta_s + \frac{81\varepsilon_s\mu_g^2\left|u_g-u_s\right|^2}{g_{0,s}{d_p}^3\rho_s\sqrt{\pi\Theta_s}} \quad (6.47)$$

The expression used in equation 6.47 is not part of Lun kinetic theory because it accounts for the effect of gas phase on the granular temperature and is relevant for multi-phase flow applications. The first term on the right hand side accounts for the production by gas shear, while the second term accounts for the production due to slip between the two phases (Agrawal et al., 2001).

The rate of granular temperature dissipation J_s is given by:

$$J_s = \left(\frac{48}{\sqrt{\pi}}\eta(1-\eta)\frac{\varepsilon_s g_{0,s}}{d_p}\Theta_s^{3/2}\right)\varepsilon_s\rho_s \quad (6.48)$$

6.5.1.2 Garzo Kinetic Theory Model

Garzó and Dufty (1999) used the Revised Enskog kinetic Theory (RET) to describe the hydrodynamics and derive transport coefficients at higher densities. The RET for elastic collisions (Van Beijeren and Ernst, 1973) is known to be an accurate kinetic theory over the entire fluid domain and it describes the crystal phase as well. Consequently, this model covers the entire range of restitution coefficient, while the model developed by Lun et al. (1984) assumes that the particles are nearly elastic. In Chapter 7 and Chapter 8, the predictions of this model are compared with those of Lun's Model.

The changes of 'Garzo' model from 'Lun' model are in the pressure state equation, viscosity and granular conductivity. In addition, a term for the dissipation of the granular energy is introduced in the conduction term in the granular transport equation. This term results from the effect of variables gradients, which were not taken into account in Lun model due to the assumption of small gradients. Also, including the variables gradients change the cooling rate (dissipation of the kinetic energy) from the previous model.

The derivation was established for dimensionless variables. Here, we re-write the equations for the sake of consistency with the governing equations presented. The governing equations were derived using the number density n, which can be expressed as a function of the packing fraction as:

$$nm = \varepsilon_s \rho_s \tag{6.49}$$

, where m is the particle mass.

The dimensionless number density n^* is defined as:

$$n^* = n{d_p}^3 \tag{6.50}$$

$$n^* = \frac{6}{\pi}\varepsilon_s \tag{6.51}$$

The model was derived for general inelastic hard sphere particles and is not limited to granular flows and the temperature defined in the model (T) is in Kelvin units. It is related to the granular temperature used in the current governing equations according to the following equation:

$$m\Theta_s = k_B T \tag{6.52}$$

, where k_B is the Boltzmann constant.

The pressure is given by:

$$p_s = {p_s}^k {p_s}^* \tag{6.53}$$

, where ${p_s}^k$ is the kinetic pressure given by:

$${p_s}^k = \varepsilon_s \rho_s \Theta_s \tag{6.54}$$

, and ${p_s}^*$ is the dimensionless pressure given by:

$${p_s}^* = 1 + \frac{1+e}{3}\pi n^* g_{0,s} \tag{6.55}$$

Here the radial distribution function $g_{0,s}$ is defined as:

$$g_{0,s} = \frac{2-\varepsilon_s}{2(1-\varepsilon_s)^3} \tag{6.56}$$

The dilatational viscosity λ_s is given by:

$$\lambda_s = \eta_0 {\lambda_s}^* \tag{6.57}$$

η_0 is the dilute solid viscosity defined as:

$$\eta_0 = \frac{5m}{16{d_p}^2}\sqrt{\frac{\theta_s}{\pi}} \tag{6.58}$$

The dimensionless dilatational viscosity ${\lambda_s}^*$ is given by:

$${\lambda_s}^* = \frac{32}{45}\pi {n^*}^2 g_{0,s}(1+e)\left(1 - \frac{1}{32}C^*\right) \tag{6.59}$$

$$C^* = 32(1-e)(1-2e^2)[81 - 17e + 30e^2(1-e)]^{-1} \tag{6.60}$$

The shear viscosity μ_s is given by:

$$\mu_s = \eta_0 {\mu_s}^* \tag{6.61}$$

The dimensionless shear viscosity ${\mu_s}^*$ is given by:

$$\mu_s{}^* = \mu_s{}^{k*}\left[1 + \frac{2}{15}\pi n^* g_{0,s}(1+e)\right] + \frac{3}{5}\lambda_s{}^* \tag{6.62}$$

, where the kinetic component of the dimensionless shear viscosity $\mu_s{}^{k*}$ is given by:

$$\mu_s{}^{k*} = \frac{1}{\left(\nu_\eta{}^* - \frac{1}{2}\gamma^{(0)*}\right)}\left[1 - \frac{1}{15}(1+e)(1-3e)\pi n^* g_{0,s}\right] \tag{6.63}$$

$$\nu_\eta{}^* = g_{0,s}\left[1 - \frac{1}{4}(1-e)^2\right]\left[1 - \frac{1}{64}C^*\right] \tag{6.64}$$

$$\gamma^{(0)*} = \frac{5}{12}\, g_{0,s}(1-e^2)\left(1 + \frac{3}{32}C^*\right) \tag{6.65}$$

$\nu_\eta{}^*$is the dimensionless collision frequency due to viscous transport. $\gamma^{(0)*}$is the zero-order dimensionless cooling rate.

The relationship for the diffusion of granular temperature is changed slightly to accommodate the effect of inelasticity on the gradients. This introduces a new term $\left(K_{diss}\frac{\partial \varepsilon_s}{\partial x_i}\right)$ in the conduction component in the granular energy equation. The granular temperature equation is now written as:

$$\begin{aligned}\frac{3}{2}\rho_s\left[\frac{\partial(\varepsilon_s\Theta_s)}{\partial t} + \frac{\partial\left(\varepsilon_s u_{sj}\Theta_s\right)}{\partial x_j}\right] \\ = \frac{\partial}{\partial x_i}\left(K_s\frac{\partial\Theta_s}{\partial x_i} + K_{diss}\frac{\partial\varepsilon_s}{\partial x_i}\right) + \sigma_{sij}\frac{\partial u_{si}}{\partial x_j} + \Pi_s - J_s\end{aligned} \tag{6.66}$$

This new term is a function of the packing (solid volume) fraction gradient and a dissipation coefficient.

The thermal conductivity K_s is given by:

$$K_s = K_s{}^* K_0 \tag{6.67}$$

K_0 is the dilute thermal conductivity given by:

$$K_0 = \frac{15}{4}\eta_0 \tag{6.68}$$

$$K_s{}^* = K_s{}^{k*}\left[1 + \frac{1}{5}\pi n^* g_{0,s}(1+e)\right] + \frac{64}{225}\pi n^{*2} g_{0,s}(1+e)\left(1 + \frac{7}{32}C^*\right) \tag{6.69}$$

$K_s{}^{k*}$ is the kinetic component of the dimensionless thermal conductivity given by:

$$K_s{}^{k*} = \frac{2}{3}\left(\nu_k{}^* - 2\gamma^{(0)*}\right)^{-1}\left\{1 + \frac{1}{2}(1 + p_s{}^*)C^* + \frac{\pi}{10}n^* g_{0,s}(1+e)^2\left[2e - 1 + \left(\frac{1}{2}(1+e) - \frac{5}{3(1+e)}\right)C^*\right]\right\} \quad (6.70)$$

, and $\nu_k{}^*$ is the collision frequency due to kinetic transport given by:

$$\nu_k{}^* = \frac{1}{3}(1+e)g_{0,s}\left[1 + \frac{33}{16}(1-e) + \frac{19-3e}{1024}C^*\right] \quad (6.71)$$

The dissipation coefficient K_{diss} is given by:

$$K_{diss} = \frac{\theta_s K_0 K_{diss}{}^*}{\varepsilon_s} \quad (6.72)$$

The inelastic dimensionless coefficient $K_{diss}{}^*$ is given by:

$$K_{diss}{}^* = K_{diss}{}^{k*}\left[1 + \frac{1}{5}\pi n^* g_{0,s}(1+e)\right] \quad (6.73)$$

The dimensionless kinetic component $K_{diss}{}^{k*}$ is given by:

$$K_{diss}{}^{k*} = 2\left(2\nu_k{}^* - 3\gamma^{(0)*}\right)^{-1}\left\{\begin{array}{c}\left(1 + n\partial_n ln g_{0,s}\right)\gamma^{(0)*}K_s{}^k + \frac{p^*}{3}(1 + n\partial_n ln p_s{}^*)C^* \\ -\frac{2}{15}\pi n^* g_{0,s}\left(1 + \frac{1}{2}n\partial_n ln g_{0,s}\right)(1+e) \\ \left\{e(1-e) + \frac{1}{4}\left[\frac{4}{3} + e(1-e)\right]C^*\right\}\end{array}\right. \quad (6.74)$$

The dissipation due to inelastic collisions J_s is given by:

$$J_s = \frac{3}{2}\varepsilon_s \rho_s \gamma \theta_s \quad (6.75)$$

, where the cooling (γ) rate is related to the dimensionless cooling rate (γ^*) as:

$$\gamma = \nu_0 \gamma^* \quad (6.76)$$

, where ν_0 is the characteristic collision frequency given by:

$$\nu_0 = p_s{}^k/\eta_0 \quad (6.77)$$

The dimensionless cooling rate γ^* is simply the summation of the zero order $\gamma^{(0)*}$ and the first order $\gamma^{(1)*}$ cooling rates as:

$$\gamma^* = \gamma^{(0)*} + \gamma^{(1)*} \tag{6.78}$$

$$\gamma^{(1)*} = \left[-\frac{1}{\nu_0}(1-e)(p^*-1) + \frac{5}{32}(1-e^2)\left(1+\frac{3}{64}C^*\right)g_{0,s}c_D\right]\nabla.u_s \tag{6.79}$$

$$c_D = \frac{1}{\nu_0}\left[\frac{1}{2}\gamma^{(0)*} + {\nu_r}^* + \frac{5C^*}{64}\left(1+\frac{3}{64}C^*\right)g_0(1-e^2)\right]^{-1} \tag{6.80}$$

$${\nu_r}^* = \frac{1+e}{48}g_{0,s}\left[(128-96e+15e^2-15e^3) + \frac{C^*}{64}(15e^3-15e^2+498e-434)\right] \tag{6.81}$$

6.5.2 Friction Stress Model

When the packing fraction of the solid particles exceeds the critical value, the contacts between the particles are long and enduring, and the effect of friction becomes significant. Consequently, an extra component for stresses is superimposed on the stress computed from kinetic theory. The other important value of packing fraction is the maximum packing fraction. It is higher than the critical packing fraction. This is where the packing fraction cannot be increased any more. In order to prevent the particles from exceeding this maximum packing fraction, the stresses are assigned arbitrary large values when the packing fraction is higher than the maximum value. However, these stresses will allow slight compressibility in the granular media. Figure 6-1 shows the critical and maximum packing limits.

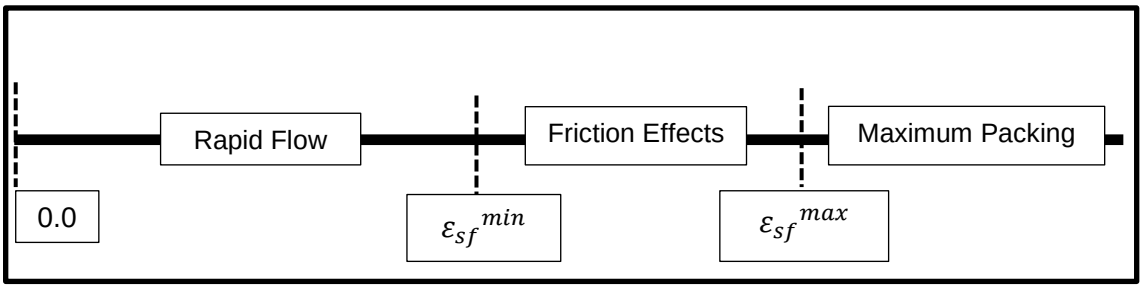

Figure 6-1: Critical and maximum packing limits.

MFIX deals with the frictional regime by combining two models. The first model is Schaeffer (1987) model, which describes the flow when the packing fraction exceeds the maximum packing$\left({\varepsilon_{sf}}^{max}\right)$. The second model is Princeton model (Srivastava and Sundaresan, 2003; Benyahia, Syamlal and O'Brien, 2012), which describes the flow between the two packing fractions: critical $\left({\varepsilon_{sf}}^{min}\right)$ and maximum $\left({\varepsilon_{sf}}^{max}\right)$.

6.5.2.1 Schaeffer Model

This model is used to prevent the granular phase from undergoing unphysical increase in their packing fraction. It uses very high arbitrary values for the granular stresses when the packing fraction approaches the threshold value (maximum packing). This allows the granular phase to be slightly compressible.

Solid phase stress tensor ${\sigma_{s,ij}}^{slow}$ is given by:

$${\sigma_{s,ij}}^{slow} = -{p_s}^{slow} I + {\tau_{s,ij}}^{slow} \tag{6.82}$$

The viscous stress term is given by:

$${\tau_{sij}}^{slow} = 2\mu_s D_{sij} + \left(\lambda_s - \frac{2}{3}\mu_s\right) tr\left(D_{sij}\right) I \tag{6.83}$$

As in the rapid flow models, the superscript $(slow)$ is dropped for the sake of brevity.

The frictional pressure in Pascal units is given by:

$$p_s = 10^{24}\left(\varepsilon^* - \varepsilon_g\right)^{10} \qquad \varepsilon_s > {\varepsilon_{sf}}^{max} \tag{6.84}$$

, ε^* is the void fraction at the maximum packing$\left(1 - {\varepsilon_{sf}}^{max}\right)$.

$$\mu_s = min\left(\frac{p_s \sin(\phi)}{\sqrt{4I_{2D}}}, \mu_s^{max}\right) \tag{6.85}$$

, where

$$\mu_s^{max} = 100\,, \lambda_s = 0 \quad \mathrm{N.s/m^2} \tag{6.86}$$

, and

$$I_{2D} = \frac{1}{6}\left[\left(D_{s,11} - D_{s,22}\right)^2 + \left(D_{s,22} - D_{s,33}\right)^2 + \left(D_{s,33} - D_{s,11}\right)^2\right] + D_{s,12}^2 + D_{s,23}^2 + D_{s,31}^2 \quad (6.87)$$

$$D_{sij} = \frac{1}{2}\left(\frac{\partial u_{si}}{\partial x_j} + \frac{\partial u_{sj}}{\partial x_i}\right) \quad (6.88)$$

ϕ is the angle of internal friction of the solid particles.

6.5.2.2 Princeton Model

Srivastava and Sundaresan (2003) developed this model for expressing the stresses in the case of slow flow. It uses the yield stress rule to express the stress tensor. It assumes that the granular material is non-cohesive and follows a rigid–plastic rheological model of the type proposed by Schaeffer (1987) and Tardos (1997). Furthermore, the model includes the strain rate fluctuation as a function of the granular temperature as proposed by Savage (1998).

The stress is described by:

$${\sigma_{sij}}^{slow} = -p_f I + \sqrt{2} p_f \sin(\phi)\left(n_1 - (n_1 - 1)\left(\frac{p_f}{p_c}\right)^{\frac{1}{n_1 - 1}}\right) \times \frac{S_{ij}}{\sqrt{S_{ij} : S_{ij} + \Theta_s / {d_p}^2}} \quad (6.89)$$

$$S_{ij} = \frac{1}{2}\left(\frac{\partial u_{si}}{\partial x_j} + \frac{\partial u_{sj}}{\partial x_i}\right) - \frac{1}{3}\left(\frac{\partial u_{si}}{\partial x_i}\right) \quad (6.90)$$

The term $\left(\Theta_s / {d_p}^2\right)$ accounts for the strain rate fluctuations, as proposed by (Savage, 1998). p_f is the frictional pressure, which is given as a function of the critical state pressure as:

$$p_f = p_c \left(1 - \frac{\nabla . u_s}{n_1 \sqrt{2} \sin(\phi) \sqrt{S : S + \Theta_s / {d_p}^2}}\right)^{\frac{1}{n_1 - 1}} \quad (6.91)$$

$$p_c = \begin{cases} Fr \dfrac{\left(\varepsilon_s - {\varepsilon_{sf}}^{min}\right)^r}{\left(\varepsilon_g - \varepsilon^*\right)^s} & {\varepsilon_{sf}}^{max} \geq \varepsilon_s > {\varepsilon_{sf}}^{min} \\ 0 & \varepsilon_s \leq {\varepsilon_{sf}}^{min} \end{cases} \quad (6.92)$$

$$Fr = 0.05, r = 2, s = 5 \quad (6.93)$$

It is clear that $(p_f = p_c)$ at the critical state when the assembly undergoes deformation under constant volume ($\nabla . u_s = 0$).

The coefficient n_1 is an exponent, which determines the shape of the yield surface. It is set differently whether the granular assembly undergoes dilation ($\nabla . u_s > 0$) or compression ($\nabla . u_s < 0$).

$$n_1 = \begin{cases} \dfrac{\sqrt{3}}{2\sin(\phi)}, & \nabla . u_s > 0 \\ 1.03, & \nabla . u_s < 0 \end{cases} \tag{6.94}$$

Setting $\left(n_1 = \frac{\sqrt{3}}{2\,sin(\phi)}\right)$ in the dilation branch ensures that the granular assembly is not required to sustain tensile stress anywhere on the yield surface. On the compaction side, n_1 can assume any value greater than unity; however, it appears from literature data that n_1 is only marginally larger than unity (Jyotsna and Rao, 1991; Jyotsna, 1993). The value of n_1 is thus set to 1.03, which is the value determined by Jyotsna (1993) for Leighton–Buzzard sand (Srivastava and Sundaresan, 2003). The intermediate packing fraction ${\varepsilon_{sf}}^{min}$ is usually taken to be around 0.5.

6.6 Initial and Boundary Conditions

In order to close the description of the model, the geometry, initial and boundary conditions should be defined. The geometry is the same as that of the experimental work. The initial conditions for both phases are defined throughout the geometry. Figure 6-2 shows the initial conditions and the geometry for the experimental test section and the corresponding simulations. The solid particles are stationary and packed with the same packing fraction as the experiment (0.5) in the bed region at the bottom of the domain. The thickness of the computational domain is 4 mm, and in all simulations there is one computational cell in this direction; thus the simulation is three-dimensional. The rest of the domain is occupied by the gas at rest (freeboard region). Since the particles are initially at rest, their initial granular temperature should be zero. However, the granular temperature is assigned a very small value ($10^{-6}\, m^2/s$) everywhere in the particle bed; in order to avoid singularity and aid simulations convergence.

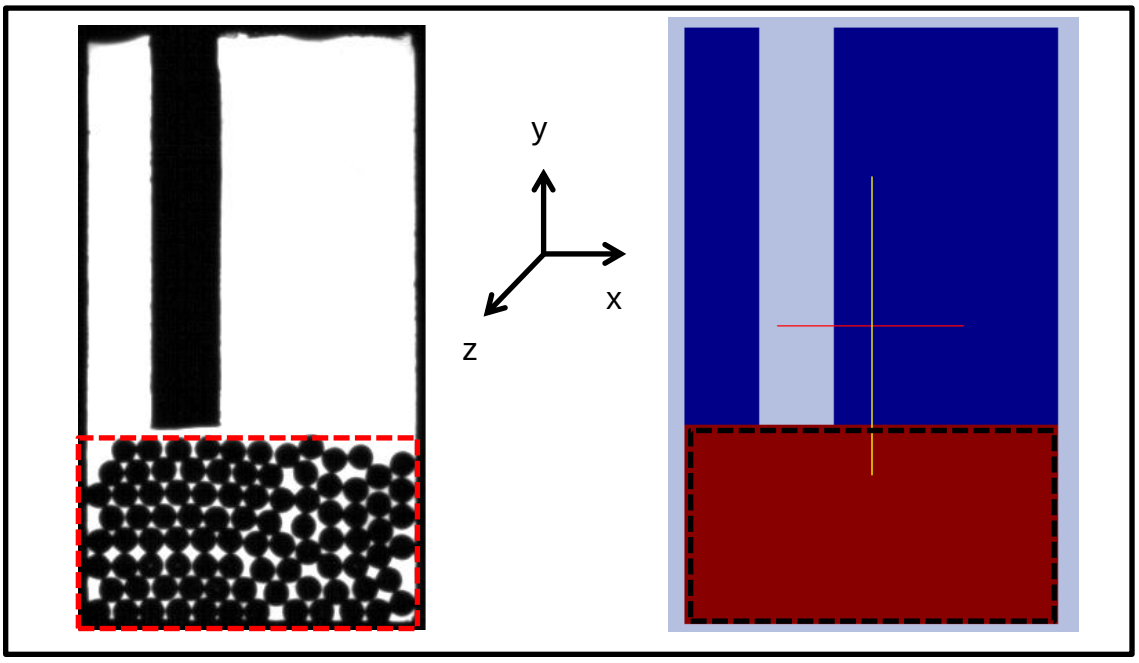

Figure 6-2: Initial conditions for the experiments and the simulation.

The inflow and outflow boundary conditions are needed at the inlet and outlet of the domain, respectively. As seen in the experimental results, the inlet and outlet gas pressures control the flow inside the test section. In order to mimic the experimental results in the computations, the inflow and outflow pressures are taken from the corresponding experiments. Linear interpolation is carried out for the values of the boundary pressures where the computational time step is smaller than the experimental time step for data acquisition (1 ms).

The wire mesh used in the experiments to prevent the particles from leaving the test section is replicated in the simulations. This is done by using a semi-permeable membrane boundary wall at the exit. The normal solid velocity vanishes at this boundary wall. The void fraction boundary conditions at the walls and exit are not needed due to the hyperbolic nature of its transport equation and the void fraction of the inlet air is unity.

Due to the diffusion terms, the momentum equations for both phases and the granular temperature equation for the solid phase are of elliptic nature in spatial coordinates. Consequently, the boundary conditions for velocities and granular temperature need to be specified at all the boundary walls. For the gas phase,

the wall boundary conditions are no-slip (i.e. normal velocity is zero and tangential velocity equal to the velocity of the wall, which is zero). Regarding the solid phase, different types of wall boundary conditions have been reported in the literature. These boundary conditions are used to determine the granular temperature and solid phase velocity at the walls. They include no-slip wall (NSW), free slip wall (FSW) and partial slip wall (PSW). The NSW boundary condition assumes that the velocity at the wall is zero. This is done by assigning the velocity of the ghost cell with the same magnitude but opposite direction to the value of the cell adjacent to the wall. On the other hand, the FSW boundary condition assumes that the gradient of the velocity vanishes at the wall. The granular temperature flux is assumed to be zero for both types of boundary walls: NSW and FSW.

One of the mostly used wall boundary conditions is the Johnson and Jackson (1987) partial slip wall (J&J PSW). This boundary condition covers both regimes of granular flow: rapid and slow. The condition for the tangential velocity at the wall is defined using the following scalar equation:

$$\frac{\overrightarrow{u_{s,w}} \cdot \left(\overline{\overline{\sigma_{sIJ}}}\right) \cdot \overrightarrow{n_2}}{\left|\overrightarrow{u_{s,w}}\right|} + \frac{\pi}{2\sqrt{3}\varepsilon_{sf}{}^{max}} \phi' \rho_s \varepsilon_s g_{0,s} \theta_s{}^{1/2} \left|\overrightarrow{u_{s,w}}\right| + p_f \tan\delta = 0 \qquad (6.95)$$

$\overrightarrow{n_2}$ is the unit normal from the particle assembly into the boundary wall. δ is the angle of friction between the particulate phase and the wall. ϕ' is the specularity coefficient, defined as the average fraction of relative tangential momentum transferred in a particle-boundary collision. It represents the friction between the granular phase and the wall due to collisions in the rapid flow regime. Its value depends on the large scale surface roughness and ranges from zero to unity. It is zero for perfectly specular (smooth) collisions, and unity for perfectly diffusive (rough) collisions. It has been reported that its value is selected to fit the experimental data; several values have been proposed for this coefficient ranging from 0.1 to 0.5 depending on the flow application (Li and Benyahia, 2012).

The slip velocity $\left(u_{s,w}\right)$ with the tangential direction at the wall adjacent to the boundary is given by:

$$u_{s,w} = u_s - u_{wall} \tag{6.96}$$

u_{wall} is the boundary wall velocity.

The bulk granular stress σ_{sij} is given by:

$$\sigma_{sij} = {\sigma_{s,ij}}^{rapid} + {\sigma_{s,ij}}^{slow} \tag{6.97}$$

The first term on equation (6.95) is the tangential component of the solid phase stress. The second term accounts for the rapid flow regime. It represents the rate of collisional momentum transfer at the boundary. The third term ($p_f \tan\delta$) accounts for the slow flow regime contribution. It represents the sliding friction force per unit area at the boundary (Coulomb's law of friction). Accordingly, this boundary condition equates the bulk stress to the sum of the frictional and collisional components at the wall. All the units of stresses are in Pa (kg/m.s²). For the case of packing fraction less than the critical value, the granular flow is in rapid flow regime and hence the last term vanishes (Figure 6-1).

The wall boundary condition for the granular temperature is given by:

$$\overrightarrow{n_2} \cdot \left(K_s \frac{\partial \Theta_s}{\partial x_i}\right) = \frac{\pi\sqrt{3}}{6{\varepsilon_{sf}}^{max}} \phi' \rho_s \varepsilon_s g_{0,s} {\theta_s}^{1/2} |u_{sl}|^2 - \frac{\pi\sqrt{3}}{4{\varepsilon_{sf}}^{max}} (1 - {e_w}^2) \rho_s \varepsilon_s g_{0,s} {\theta_s}^{3/2} \tag{6.98}$$

e_w is the wall particle restitution coefficient. The first term on equation (6.98) represents the conductive flux of the granular temperature normal to the wall. The second term represents the work done by the granular phase at the boundary wall. The third term represents the rate of dissipation of fluctuation energy due to particle-wall inelastic collisions.

In this thesis, the effect of the different types of wall boundary condition for the granular phase will be investigated.

6.7 Method of Solution

The previous governing equations for TFM combined with the sub-models, boundary and initial conditions are solved using 'Multiphase Flow with Interphase eXchange' (MFIX) software (Benyahia, Syamlal and O'Brien, 2012). MFIX is an open source code. It has been developed by National Energy

Technology Laboratory (NETL) in USA. It is mainly used to simulate solid-gas or solid-liquid multiphase flow systems. In this section, a summary of the solution technique employed in MFIX is presented.

The differential equations are discretised over a given spatial and temporal flow domain using the finite volume method. The spatial computational grid in which the pressure is discretised is different from that of the velocity (staggered grid), in order to avoid the unphysical pressure checkerboard distribution. Second order discretisation schemes for convection terms are used, to avoid numerical diffusion. In the case of non-convergence at the beginning of the simulation while using second order schemes, the code gives an option for starting with a first order discretisation scheme and then updates the scheme to a second order one. The code also has an option for automatic time step adjustment to ensure that the run is executed in the lowest possible time.

The equations of the two phases are solved simultaneously on the same computational grid. The gas equations are discretised to solve for the velocity and gas pressure. Since the gas is incompressible, there is no explicit equation for the transport of the pressure. Consequently, the gas phase equations are solved using the pressure correction algorithm SIMPLE (Patankar, 1980). While the solid phase governing equations solve for the solid volume fraction, velocities and granular temperature. The solid phase governing equations use a correction for the solid volume fraction to estimate the flow field variables. The solid volume fraction is connected to the solid pressure using the state equations. The solid particles are allowed to compress slightly beyond their maximum packing fraction.

The coupling between the two phases during the solution is accomplished through the void fraction and the momentum transfer due to the drag exerted on the particles by the gas. In order to solve the equations algebraically, the inter-phase momentum exchange terms need to be de-coupled. Decoupling of the equations by calculating the interphase transfer terms from the previous iteration values will make the iterations unstable or force the time step to be very small. The other extreme of solving all the discretised equations for a certain component together will lead to a larger, nonstandard matrix. An

effective alternative, that maintains a higher degree of coupling between the equations while giving the standard septa-diagonal matrix, is the Partial Elimination Algorithm of Spalding (1980), which is used in MFIX. Detailed description of the numerical technique is given in Syamlal (1998).

In order to run any simulation, some parameters and sub-models need to be prescribed. These input parameters might be categorised into four types: computational parameters, mesh size, material properties and physical sub-models. The computational parameters are: the convergence tolerance and maximum number of iterations. Their values are determined based on preliminary simulations and MFIX documentation recommendations. The dominant term in the continuity equation from the first non-linear iteration is used to determine the residual. The convergence tolerance of the residual is '1E-03' for the continuity and momentum equation, while it is '1E-04' for granular temperature equation. The maximum number of non-linear iterations is 500, while the maximum number of linear iterations is set to 3000. The mesh size is determined in the spatial and temporal coordinates. MFIX uses an adaptive time step, which is variable; in order to speed up the calculation. The spatial grid is uniform and its effect will be discussed with the corresponding computational results. The values of the material properties parameters are shown in Table 6-1 and they are constant for all relevant computational runs. The physical sub-models options are shown in Table 6-2.

Table 6-1: Material Properties values used in simulations

Air density (ρ_g)	1.2 kg/m³
Air dynamic viscosity (μ_g)	1.8×10^{-5}
Particle density (ρ_s)	2500 kg/m³
Particle diameter (d_p)	3.85 mm
Inter-particle restitution coefficient (e)	0.833
Particle-wall restitution coefficient (e_w)	0.72
Inter-particle angle of internal friction (ϕ)	30º
Particle-wall angle of internal friction (δ)	11º

Table 6-2: Physical sub-models used in simulations

Drag Models	Wen-Yu, Sylamal-O'Brien ,Gidaspow, Koch-Hill-Ladd
Kinetic theory Models	Lun, Garzo
Wall BCs for solid phase	NSW, FSW, J&J PSW

As discussed in Chapter 2, the choice of the critical $\left({\varepsilon_{sf}}^{min}\right)$and the maximum $\left(\varepsilon_{s,max}\right)$ packing fractions is arbitrary, because there is no definite threshold value for the transition between the rapid and the slow regimes. Consequently, the choice is made based on previous studies and the physics of the granular flow in the specific problem. The value of the critical packing fraction was assumed 0.5 by Johnson and Jackson (1987); Srivastava and Sundaresan (2003). However, this value is the same as the initial packing fraction in the current experiments. Consequently, the critical packing is reduced slightly to 0.49 because the stagnant particles bed cannot be considered in the rapid regime. Regarding the maximum packing fraction, its theoretical limit for organised granular assembly of spheres is 0.5238. However, the large particles used in the experiments will reduce this limit; because they do not fill all their assigned space. Consequently, the maximum packing fraction is assumed 0.51. Higher values of this maximum packing fraction resulted in non-convergence of the simulations.

6.8 Average and Total Variables

In order to compare the computational results with the experiments, average and total variables across sub-regions should be defined. Figure 6-3 shows the computational domain used for averaging different regions in the flow.

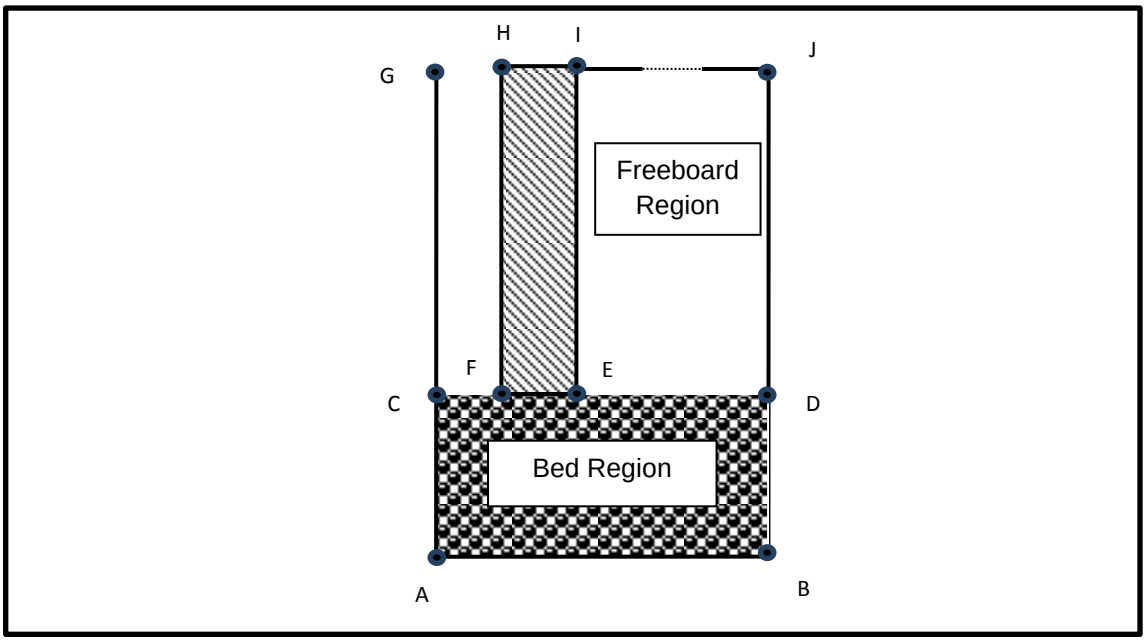

Figure 6-3: Sub-regions of the computational domain.

The average void fraction over a certain region is defined as:

$$\bar{\varepsilon_g}(t) = \frac{\sum_{l=1}^{n'} V_l \varepsilon_{g,l}(t)}{\sum_{l=1}^{n'} V_l} \tag{6.99}$$

l is an index for the computational cell. n' is the total number of computational cells in a spatial region of the domain. V_l is the volume of the computational cell. Since a uniform spatial mesh is used, the average void fraction is:

$$\bar{\varepsilon_g}(t) = \frac{\sum_{l=1}^{n'} \varepsilon_{g,l}(t)}{n'} \tag{6.100}$$

The velocity obtained by solving the model equations represents the average value of the computational cell. However, a consistent comparison between the simulations and the experiments requires that the velocities of the total number of particles are obtained over the region of interest. Changing the field equations from Eulerian coordinates to Lagrangian coordinates requires the multiplication of the number of particles per computational cell $(n_{p,l})$ which is defined as:

$$n_{p,l} = \frac{\varepsilon_{s,l} V_l}{V_p} \tag{6.101}$$

, where V_l and V_p are the volumes of the computational cell and particle respectively.

The total velocity of the region for the horizontal direction is defined as:

$$U_x(t) = \frac{\sum_{l=1}^{n'} V_l \varepsilon_{s,l}(t) u_{x,l}(t)}{V_p} \tag{6.102}$$

And for the vertical direction as:

$$U_y(t) = \frac{\sum_{l=1}^{n'} V_l \varepsilon_{s,l}(t) u_{y,l}(t)}{V_p} \tag{6.103}$$

6.9 Summary

In this chapter, the Two Fluid Model (TFM) used in this thesis has been presented and discussed. This includes the governing equations for each phase and the sub-models for both particle-gas interactions and particle-particle interactions. The boundary and initial conditions have been specified. The solution approach has been outlined. Analysis techniques for obtaining average and total variables have been detailed. In the next two chapters, the model predictions will be compared with the experimental results.

Chapter 7 : Computational Study of Particle Bed Fluidisation Using Strong Impinging Air Jet

7.1 Introduction

In this chapter, the computational results obtained from the model presented in Chapter 6 are presented and discussed. Comparisons between these computational results and the experimental results presented in Chapter 4 are used to investigate the validity of the computational model. This is done for the full fluidisation regime, which has a high air pressure difference (16 kPa) between the inlet and the outlet. This full fluidisation regime corresponds to flow in DPI where all the powder is fluidised.

As seen in the experimental results shown in Chapter 4, the fluidisation process happens very fast; nearly all the granular particles are fluidised after time of 0.222 s. Furthermore, the flow of this high pressure difference case is dominated by convection. This was confirmed by the velocity vectors of particles at different stages of the experiments. Any effects of collisions between the particles in inducing fluctuating diffusive motion do not exist. The minor effects of collisions in experiments challenge the ability of the kinetic theory models in replicating the experimental flow condition. This is because the kinetic theory models assume that collisions take place in this type of flow. However, these collisions are expressed in viscous forces. Accordingly, the model is expected to be accurate if the values of viscous forces in the granular phase are much lower than other forces which cause convection (weight, inertia and aerodynamics forces).

Chapter 6 showed that there are different computational sub-models used in conjunction with the TFM. These sub-models might affect the flow predictions. Accordingly, a study of the effects of these sub-models is crucial in order to validate the TFM for a certain flow situation. The effect of the wall boundary conditions, computational mesh size, kinetic theory models and drag models are presented in sections 7.2., 7.3., 7.4., and 7.5., respectively. The main aim of these sections is to compare the predictions of these sub-models with the

experimental results. The experiment chosen for the validation in this chapter is experiment number one (Chapter 4). The analysis technique used in this chapter starts by comparing the predicted void fraction with the particle flow images presented in Chapter 4. Then the average void fraction and total velocities are used to validate the model quantitatively.

7.2 Effect of Granular Phase Wall Boundary Conditions

The wall boundary condition determines the interactions between the granular phase and the walls. A boundary wall can exert two types of forces on granular particles moving relative to it. These forces are frictional and collisional. However, determining these forces is difficult because they are related to the micro mechanics of the impact between the particles and the wall. Consequently, the wall boundary condition models are usually based on simplified assumptions. There are three types of wall boundary conditions for the granular flow (Chapter 6). They are free-slip wall (FSW), no slip wall (NSW) and partial slip wall (PSW). These three types of wall boundary conditions differ in their physical form. The free-slip wall is implemented by assuming that the shear stress on the layer adjacent to the wall is zero. The no-slip wall exerts the highest possible shear stress on the fluid layer adjacent to the wall. This is done by assigning an equal magnitude and opposite direction velocity at the imaginary wall so that the velocity at the interface is zero. The partial slip wall exerts a medium value of stress on the wall. Accordingly, its value of the slip velocity is between the two extremes: NSW and FSW. In this thesis, Johnson and Jackson (1987) (J&J) partial-slip wall presented in Chapter 6 will be used.

Both the no-slip wall (NSW) and the free-slip wall (FSW) do not need any parameters for their activation. On the other hand, when J&J partial-slip wall boundary condition is used, some parameters related to particle-wall interactions are needed. The parameters used in J&J boundary conditions are angle of internal friction between the wall and the solid phase(δ), the particle-wall restitution coefficient (e_w) and the specularity coefficient(ϕ'). The angle of internal friction appears only during the slow flow regime, which happens for very narrow range of void fraction (0.48-0.51) because the particles are loosely packed in our experiments. Figure 7-1 shows that the predictions are nearly

similar for values ranging from 0.0º to 80º. Consequently, the friction coefficient between the wall and the particles is kept constant with an angle of internal friction of 11º (the default value in MFIX) in all simulations.

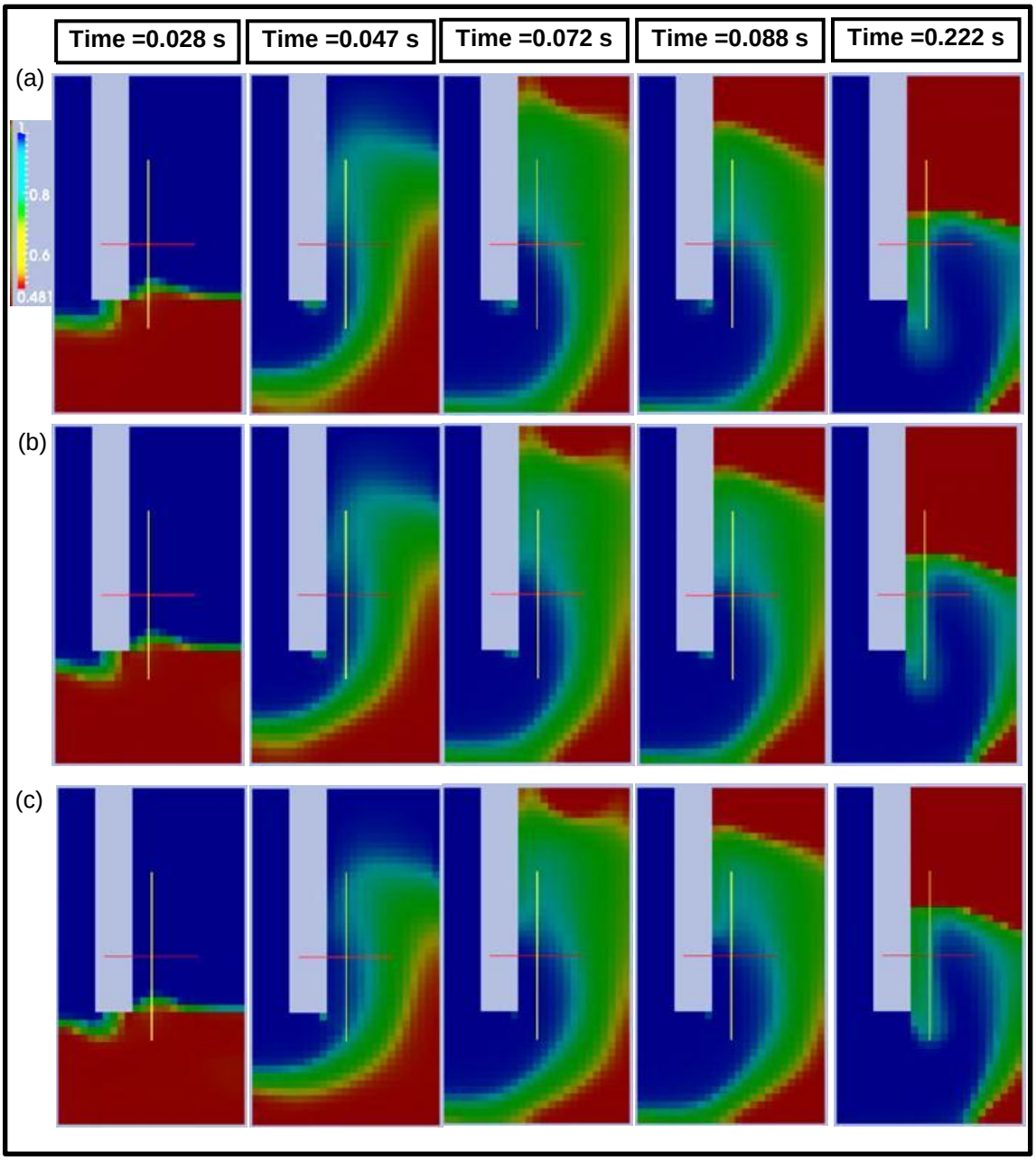

Figure 7-1: Void fraction profiles for the effect of angle of internal friction in J&J PSW for ϕ'=0.1: (a) δ = 0.0º, (b) δ = 11.0º, and (c) δ = 80.0º. Other simulation parameters are shown in Table 6-1. Wen-Yu drag model and Lun kinetic model are used in this simulation.

The particle-wall restitution coefficient was measured using the impact experiments and its value is '0.72' (Table 6-1) though it is reported in the literature (Li and Benyahia, 2013) as having no effect on the simulations and the most important parameter in J&J partial-slip boundary condition is the specularity coefficient (Li and Benyahia, 2013). It accounts for the friction between the walls and the granular phase. It is different from the angle of internal friction because the specularity coefficient (ϕ') is used in the rapid flow regime. It is reported that the value of the specularity coefficient is selected to fit the experimental results (Li and Benyahia, 2013). Typical values reported in the literature (Li and Benyahia, 2013) include ϕ' = 0.5 for bubbling bed where the particles move very slowly. Lower values around ϕ'= 0.1 were reported for higher velocities in circulating bed (Li and Benyahia, 2013). These values will guide us in the initial selection of the value of specularity coefficient since the flow here is different from the applications mentioned above.

In the two-dimensional test section used in the experiments, the friction between the particles and the front and rear walls is expected to play a prominent rule. This is because all the particles are exposed to these walls in contrast to other walls.

7.2.1 Effect of Wall Boundary Conditions

Now we will use the three boundary conditions to compare the predictions to the experiments. For J&J PSW, the value of the specularity coefficient is assumed ϕ' = 0.1. This is an initial choice made to compare the three types of boundary conditions. The effect of this coefficient will be investigated in the next section. We use Wen-Yu drag model and Lun kinetic theory model (Chapter 6). All other simulation parameters are kept constant and reported in Table 6-1. The mesh used in all simulations is uniform with a size of 2 mm.

Figure 7-2 shows comparison between experimental images (solid phase) and predicted void fraction profiles for the three wall boundary conditions. In all time frames, it is clear that the no-slip wall under-predicts the movement of particles. Throughout all time frames, the solid phase mass in the freeboard region is less

than the experiments. This is due to the high shear stress exerted by the front and rear boundary walls on the particles.

The free-slip wall over-predicts the movement of the solid particles. This is very clear at time 0.047 s, 0.072 s and 0.088 s where the solid phase mass in the freeboard region is much higher than the experiments. This is because the walls do not exert any shear stresses on the granular phase. However, the discrepancy between the FSW predictions and the experiments is reduced significantly at time 0.222 s. By careful scanning of the predictions using FSW and the experiments throughout all time frames, one might spot interesting behaviour. The experimental particle flow profiles lag behind the FSW void fraction predictions. For example, the predictions using FSW at 0.047 s are nearly similar to the experiments at time 0.072 s. On the other hand, the match of event timing between the predictions and the experiments is enhanced significantly by using J&J partial-slip wall (PSW). This is clear throughout the time frames of the experiment. For example, the mass of the predicted solid phase in the freeboard is similar to the experiments at 0.047 s, 0072 s, 0.088 s and 0.222 s. Its predictions of fluidisation times are between the two other extremes: NSW and FSW. However, one can spot qualitative difference between the flow behaviour in PSW and the experiments. The solid phase dispersion during fluidisation in PSW is higher when compared to the experiments. This is clear at time 0.072 s and 0.088 s. The predicted fluidisation is more homogenous when compared to the experimental images. This behaviour is not noticed in the FSW predictions.

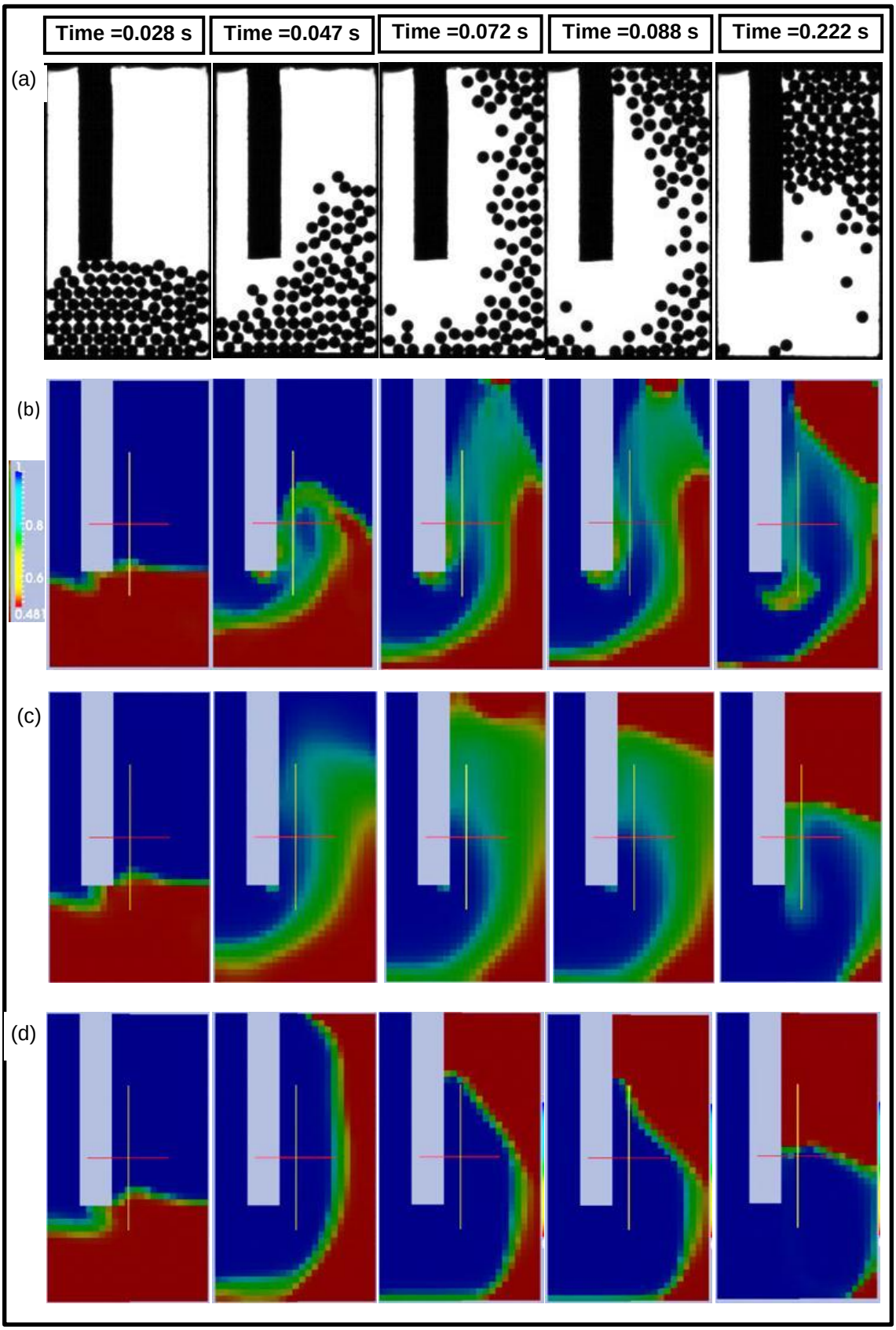

Figure 7-2: Comparison of experimental particles images at different instants in time with numerical void fraction predictions for the wall boundary conditions: (a) Experiments, (b) NSW, (c) J&J PSW with $\phi' = 0.1$, and (d) FSW.

The dispersion of the computed solid phase in the freeboard for J&J PSW can be traced to the effect of diffusion. The predicted diffusion using J&J PSW is higher than that of the FSW due to the higher shear force exerted on the solid phase by the boundary walls. This shear stress transforms the bulk velocity to fluctuating velocity (granular temperature) in the mechanism known as viscous dissipation. The increase in the granular temperature increases the viscosity and hence increases the diffusion contribution. This is confirmed by Figure 7-3 where the average granular temperature in the freeboard is compared for the two boundary conditions: FSW and PSW with $\phi' = 0.1$. The granular temperature of the FSW is much lower than that of J&J PSW suggesting that the viscous dissipation is much lower in the FSW. Moreover, Figure 7-4 shows the average Mach number in the freeboard region for the two boundary conditions: FSW and J&J PSW. The Mach number represents the ratio between the bulk velocity and the granular temperature (fluctuating velocity). It is a measure of the convection to diffusion (Chapter 2). It is clear that the PSW transforms higher portion of the bulk velocity to granular temperature.

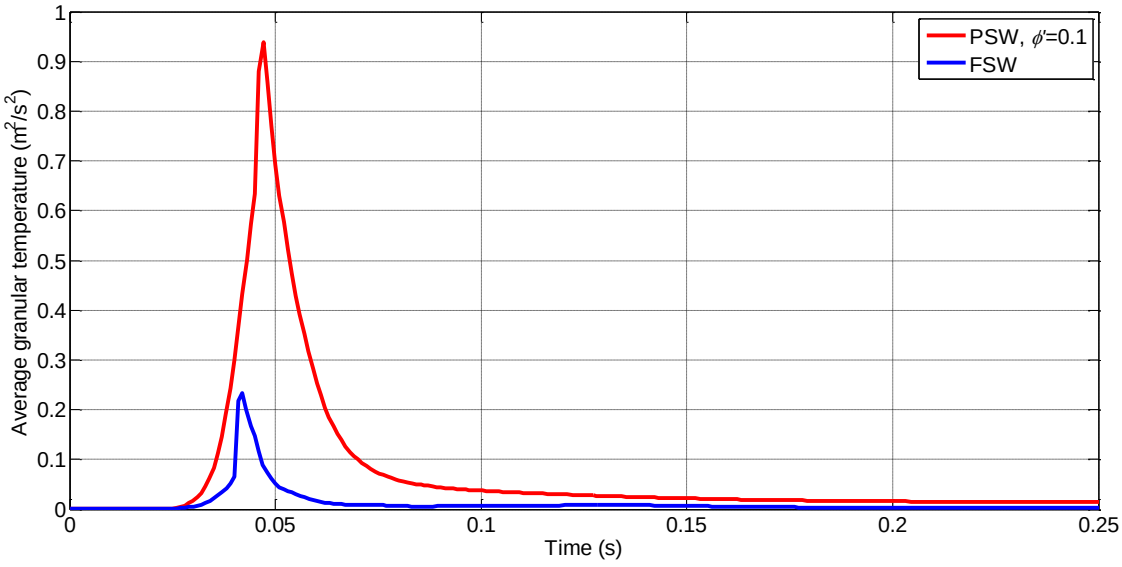

Figure 7-3: Comparison of the freeboard average granular temperature for the wall boundary conditions.

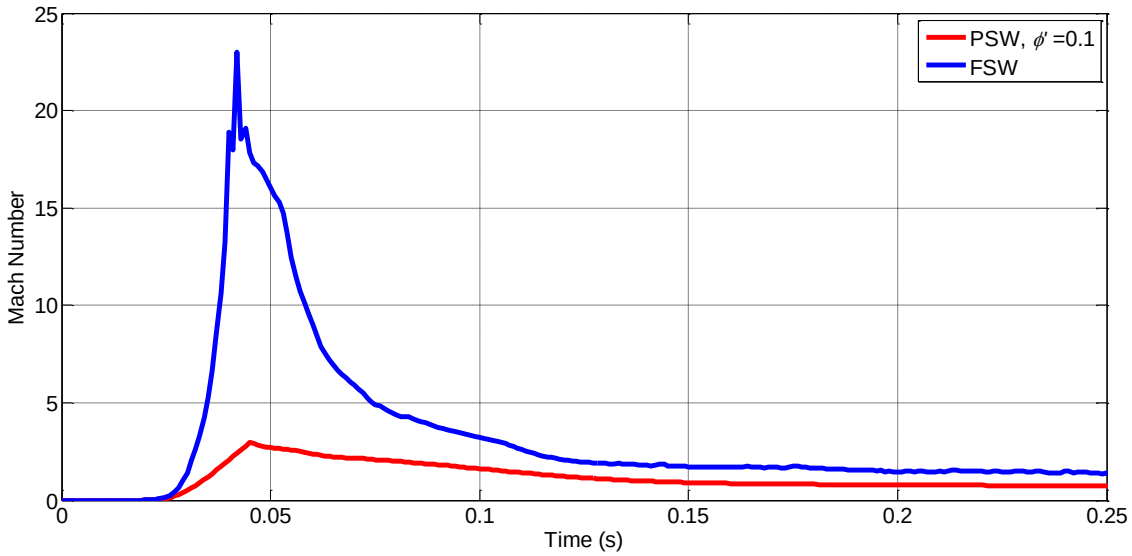

Figure 7-4: Comparison of the freeboard average Mach number for the wall boundary conditions.

The effect of particles-walls interactions can be quantified by looking at average and total flow fields in the freeboard region. This is shown in Figure 7-5, Figure 7-6 and Figure 7-7 which show comparison between the measured and the numerical predictions of the void fraction, total horizontal velocity and total vertical velocity, respectively.

The poor agreement with experimental void fraction profiles shown in Figure 7-5 confirms that the NSW is not suitable for the current flow case. The FSW over-predicts the initial fluidisation up to a time of 0.2 s (same as Figure 7-2). However, its prediction of the steady state yields the best agreement with the experiments. J&J PSW predicts the initial fluidisation up to 0.2 s exactly with minor discrepancy for the steady state. However, the results for the void fraction are averaged over the entire freeboard region, so the dispersion shown in Figure 7-2 does not appear in the average void fraction.

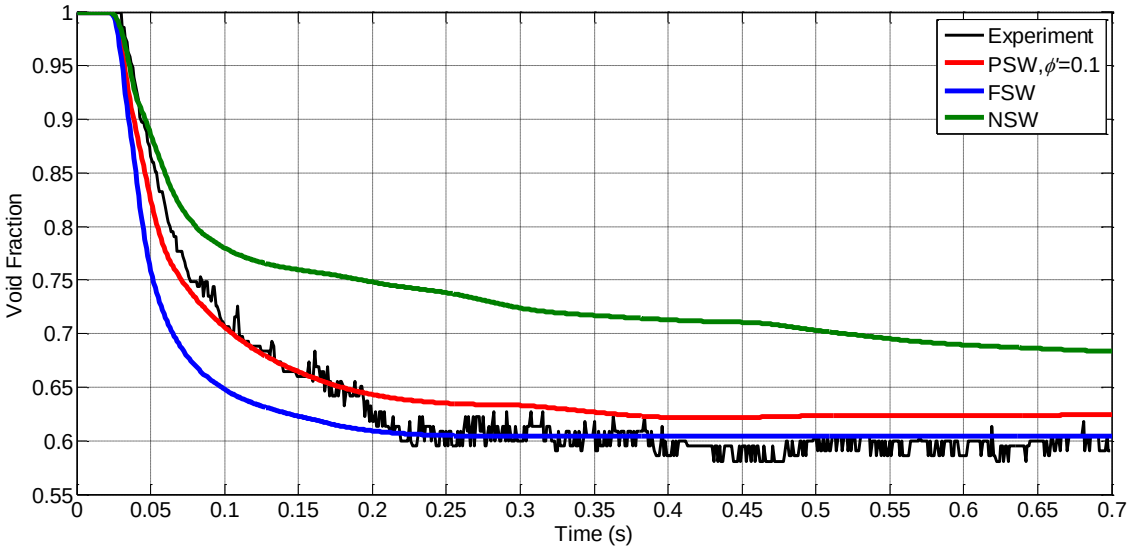

Figure 7-5: Comparison between experiments and numerical predictions of the freeboard average void fraction for the wall boundary conditions.

Figure 7-6 shows the freeboard total horizontal velocity. It is clear that the NSW prediction does not replicate the trend of the experiment. The predicted velocity using the NSW keeps its positive value from 0.02 s until 0.07 s. Then it becomes zero until the end of the experiment. This is different from the experiment where the velocity drops to negative value at 0.07 s. This confirms that the NSW is not appropriate.

The FSW has a similar trend to the experiments. However, the values of both the maximum and the minimum velocities are over-predicted. Furthermore, the timing of the velocity is different from the experiments. The predicted velocity curve is narrow and steep for both the positive and negative parts. One can say that the trend of the curve is similar to the experiments but compacted in less time. As discussed in the void fraction distribution (Figure 7-2), this is due to the lack of frictional forces between the granular phase and the walls. This makes the predicted velocity using FSW higher than the measured.

J&J PSW gives the best results compared to the experiments and retains the same trend of the horizontal velocity. However, it does not match the experiments quantitatively. This is probably due to the extra dispersion seen in Figure 7-2. Furthermore, the high value of standard deviation in the

experiments (Chapter 4) restricts the exact quantitative matching with the simulations.

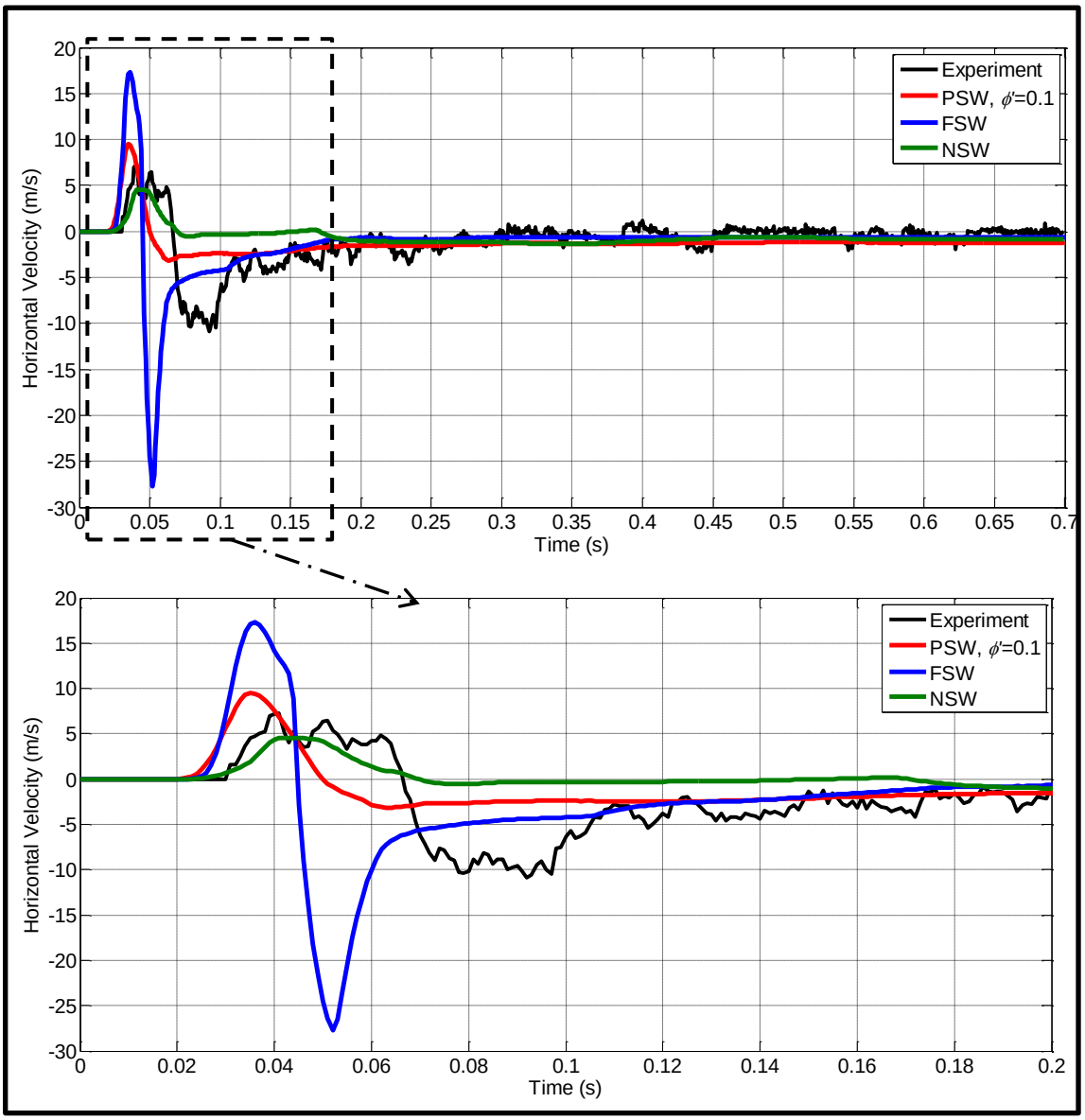

Figure 7-6: Comparison between experiments and numerical predictions of the freeboard total horizontal velocity for the wall boundary conditions.

The total vertical velocity comparison shown in Figure 7-7 confirms the behaviour seen in the void fraction and total horizontal velocity. All the predictions have the same trend of the experiments with various quantitative differences. The PSW predictions are in the best agreement with the experiments.

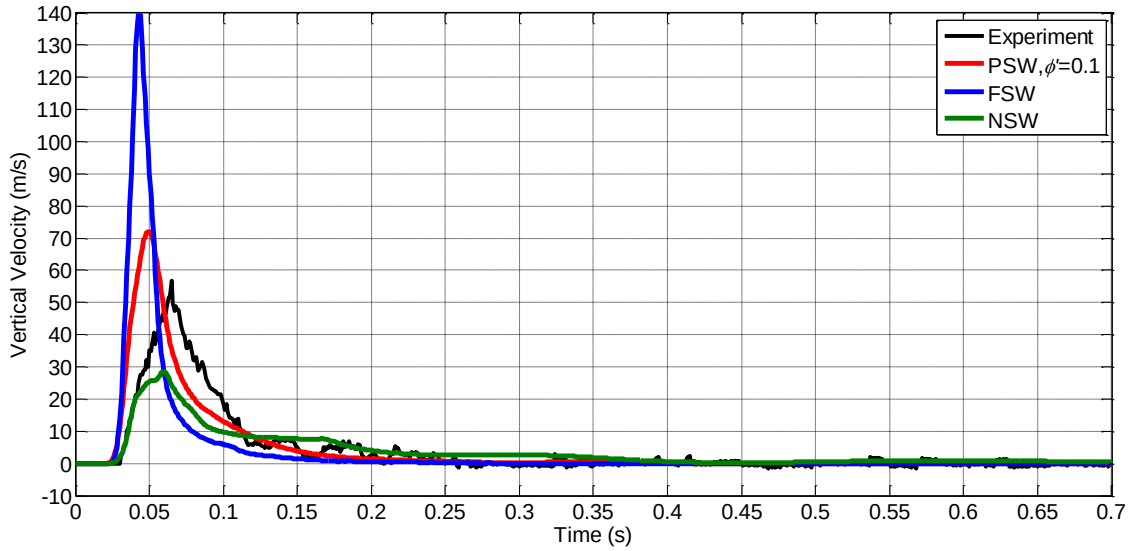

Figure 7-7: Comparison between experiments and numerical predictions of the freeboard total vertical velocity for the wall boundary conditions.

The results shown in this section suggest that model predictions can replicate the experiments when the wall boundary conditions are implemented properly. The NSW is inappropriate due to the high shear stress exerted on the granular phase. This causes the under-prediction of the granular phase fluidisation. In the FSW predictions, the granular phase is entrained in the freeboard region more quickly than the experiments. This is due to neglecting the interactions with the wall. However, the trends of the average void fraction and total velocities of the freeboard are similar to the experiments.

J&J PSW predictions replicate the measured average void fraction over the freeboard. However, the model increases the dispersion of the solid phase in the freeboard region in contrast to the fluidisation behaviour noticed in the experiments and FSW predictions. This is because the shear stress exerted by the walls on the granular phase dissipates the mean solid phase kinetic energy (bulk velocity) and converts it to granular temperature. The correspondingly higher granular temperature increases the diffusion and causes the dispersion of particles. This qualitative difference in the fluidisation behaviour manifests itself in quantitative differences between the predicted and the measured velocity. However, the PSW predictions of the velocity are considered the best compared to FSW and NSW. This suggests that the friction between the

granular phase and the boundary walls is the main mechanism of interaction. The value of the specularity coefficient in J&J PSW quantifies this interaction. Consequently, the effect of the value of this coefficient is studied in the next section.

7.2.2 Effect of Specularity Coefficient

In this section, the sensitivity of the predictions to changes of the value of the specularity coefficient in J&J PSW is studied. Three values of this coefficient (ϕ') are used: 0.1, 0.2 and 0.3. The choice is arbitrary since this coefficient is selected to fit the experimental data. We use Wen-Yu drag model and Lun kinetic theory model (Chapter 6). All other simulation parameters are kept constant and reported in Table 6-1. The mesh used in all simulations is uniform with a size of 2 mm.

Figure 7-8 shows a comparison between the experimental images of the particle flow and the void fraction predictions for the effect of specularity coefficient. It is clear that a value of 0.1 gives the best agreement with the experiments. As the specularity coefficient increases, the simulation under-predicts the motion of the solid phase. This is clear at time 0.072 s and 0.088 s. Furthermore, the dispersion of the solid phase increases during the fluidisation process as the specularity coefficient increases. This is due to the increase in diffusion of the solid phase. As the specularity coefficient increases, the shear stress exerted on the solid phase increases. This increases the viscous dissipation which increases the granular temperature and granular viscosity and leads to increase in diffusion of the solid particles. This is confirmed by the Mach number profiles shown in Figure 7-9. The average void fraction shown in Figure 7-10 further confirms that ϕ' = 0.1 gives the best agreement with the experiments.

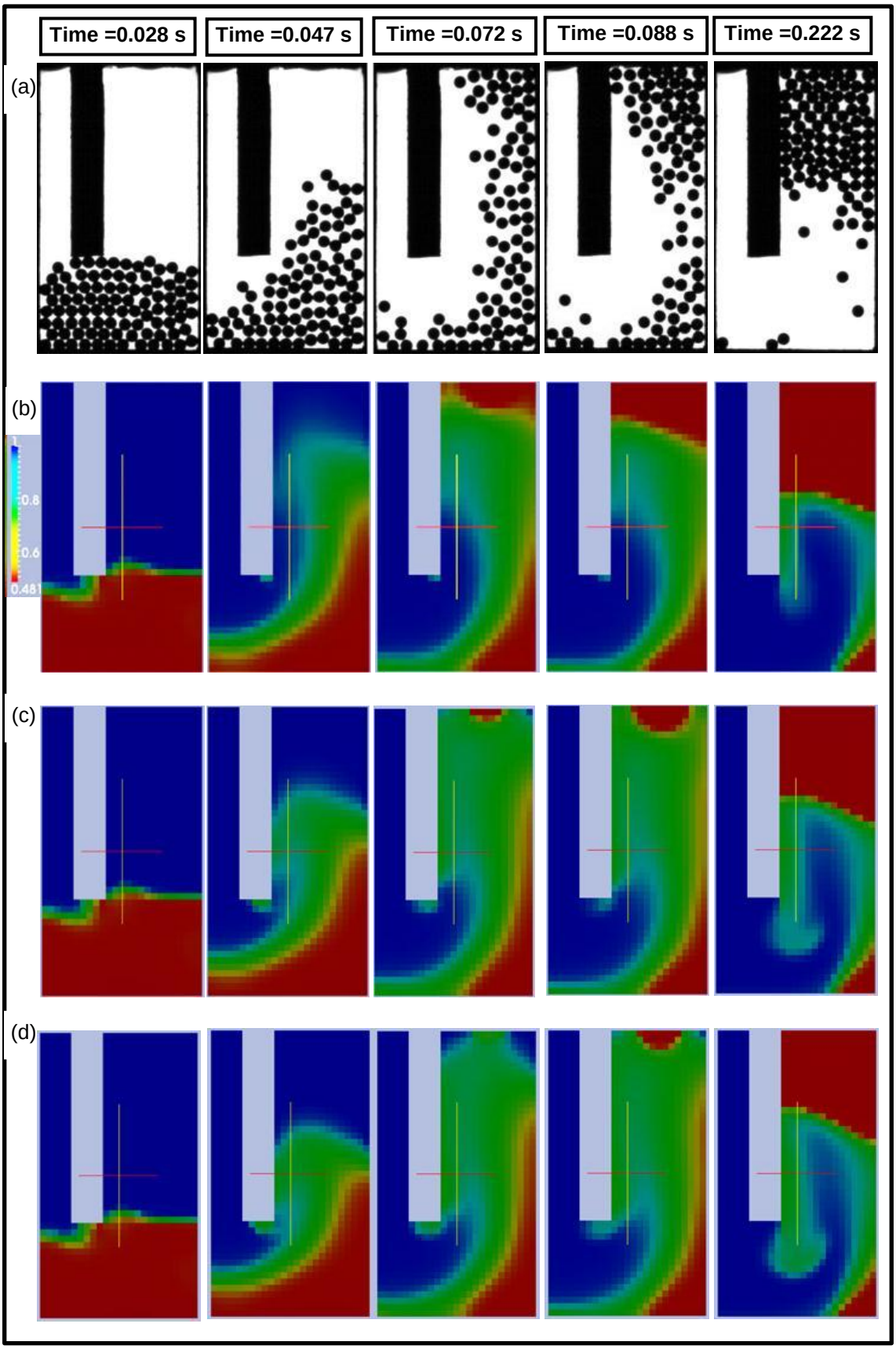

Figure 7-8: Comparison of experimental particles images at different instants in time with numerical void fraction predictions for the specularity coefficient: (a) Experiments, (b) ϕ'=0.1, (c) ϕ'= 0.2, and (d) ϕ'=0.3.

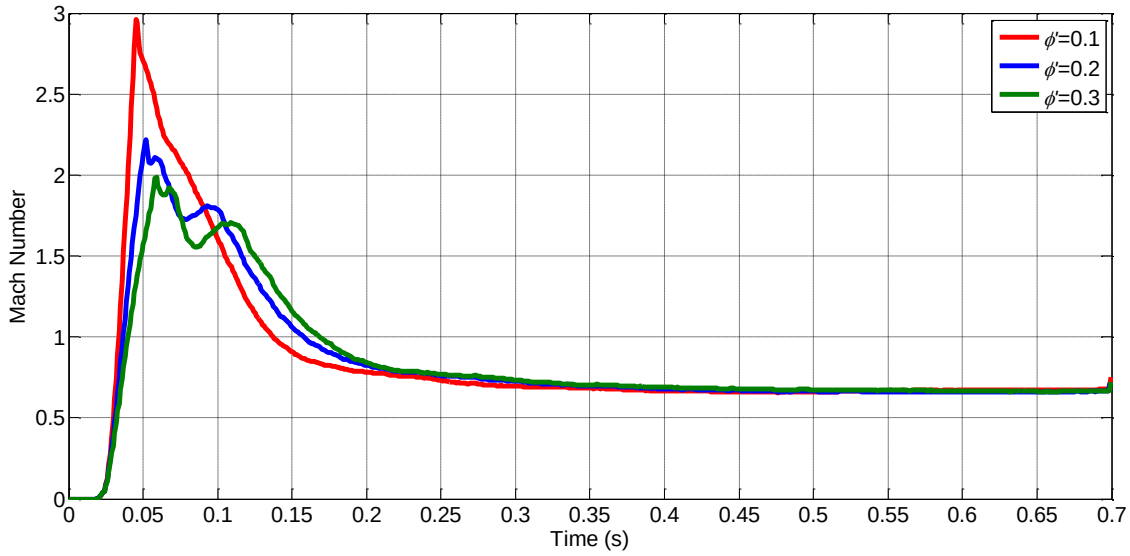

Figure 7-9: Comparison of the freeboard average Mach number for the specularity coefficient.

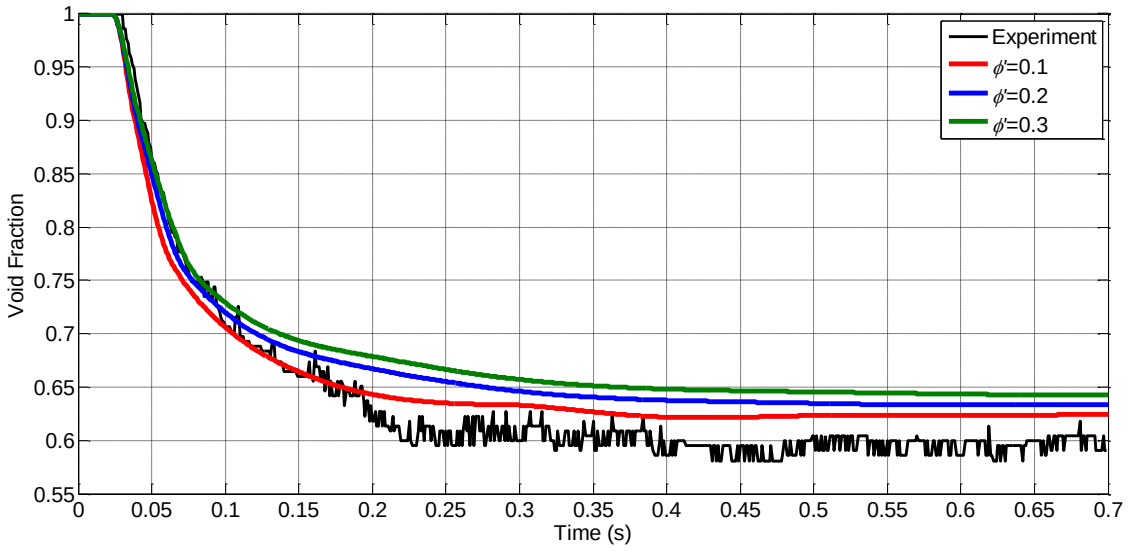

Figure 7-10: Comparison between experiments and numerical predictions of the freeboard average void fraction for the specularity coefficient.

Figure 7-11 and Figure 7-12 show the comparison between the predictions and the experimental total velocities. For the total horizontal velocity, it is difficult to judge which value of specularity coefficient is better. All the values have roughly the same trend. For the vertical velocity it seems that a value of $\phi' = 0.2$ specularity coefficient gives the best agreement. However, we should not rely

on perfect quantitative matching of the velocity because the standard deviation within the ensemble is high. Accordingly, we will use a value of $\phi' = 0.1$ which gives the best overall agreement.

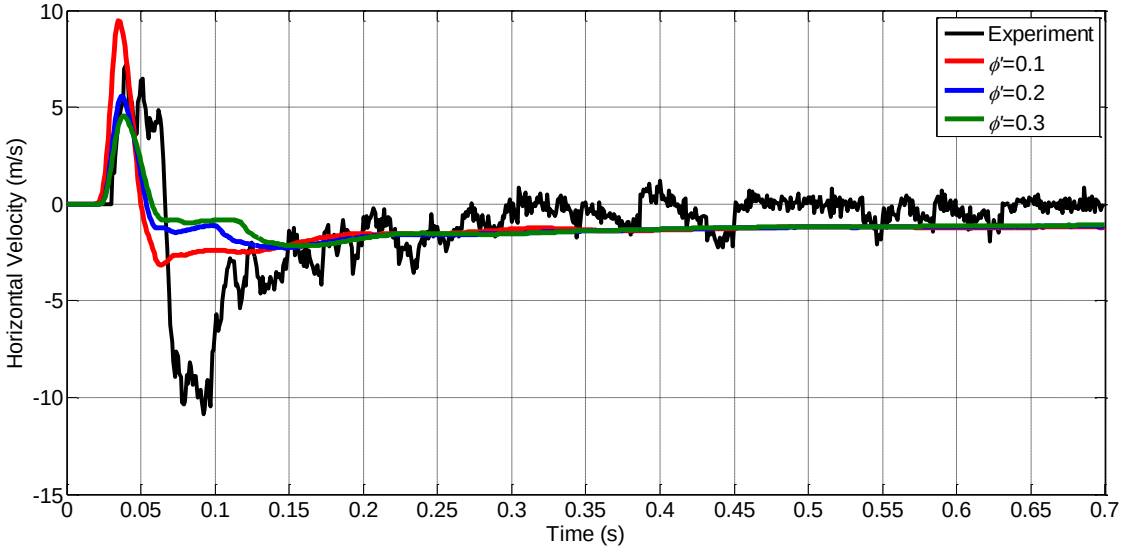

Figure 7-11: Comparison between experiments and numerical predictions of the freeboard total horizontal velocity for the specularity coefficient.

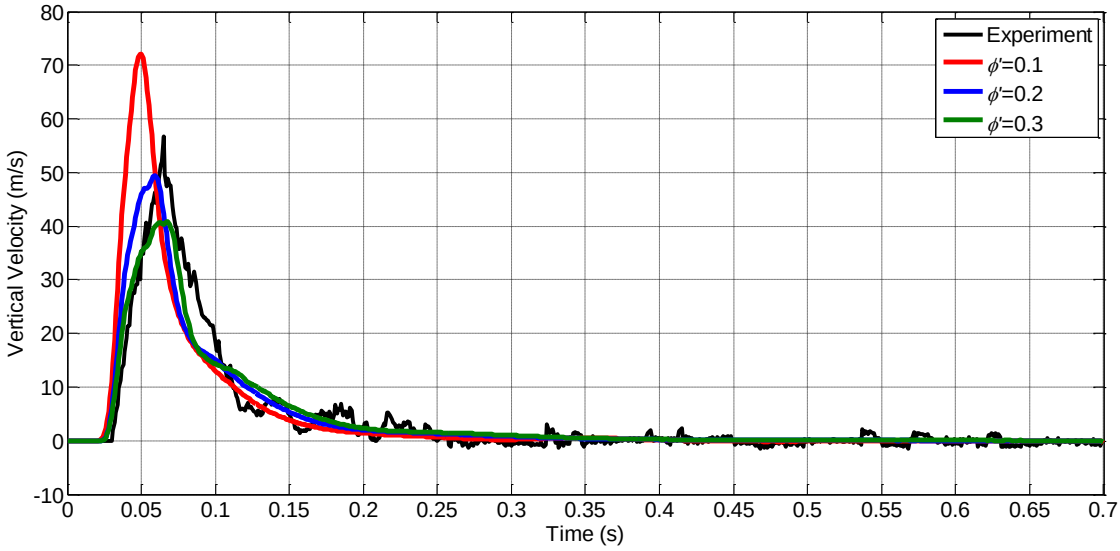

Figure 7-12: Comparison between experiments and numerical predictions of the freeboard total vertical velocity for the specularity coefficient.

7.2.3 Summary and Discussion

In this section, the effect of wall boundary condition for the granular phase has been studied. Three types of boundary conditions were used: the FSW, NSW and J&J PSW. The comparison between the particle images and the void fraction profiles shows that the J&J PSW gives the best agreement of the experimental fluidisation time. This is confirmed by the average void fraction over the freeboard and the total velocities. However, the partial slip wall causes the solid phase to disperse in a diffusive way. This is because the shear stress increases which leads to higher viscous dissipation and higher granular temperature. This diffusion is not seen in the experiments and in FSW simulations. Using J&J PSW increases the importance of the kinetic theory effects (diffusion). This is done by transforming the velocity to granular temperature due to friction. It is inevitable to include friction effects without invoking the granular heating while using current boundary conditions.

Three values of specularity coefficient were used to examine the J&J partial slip wall. This coefficient accounts for the friction between the granular phase and the walls. It has been shown that a value of 0.1 gives the best agreement for the fluidisation pattern and the average void fraction. Using higher values of '0.2' gives better predictions for the vertical velocity. However, this enhancement in vertical velocity deteriorates the fluidisation profile by promoting dispersion caused by diffusion. Furthermore, the prediction of the exact value of the velocity is difficult because of the high standard deviation seen in Chapter 4.

The results suggest that particle-wall friction is an important mechanism of interaction and it can change the predictions significantly. When including the friction in PSW via the specularity coefficient, the diffusion increases compared with the experiments. This suggests that a different wall boundary condition where the friction acts as a sink term in the momentum equations without including granular heating might be appropriate.

7.3 Computational Mesh

In this section, the effect of the computational mesh on the model predictions is investigated. It is a common practice in CFD studies to investigate the mesh independency by examining different mesh sizes. The common approach is to start with a coarse mesh and refine it further. Then the results for different variables obtained using those two mesh sizes are compared. If the results are within a certain tolerance range, the process is deemed to be mesh-independent. Then the coarser of the last two meshes is chosen since further refinement of the mesh does not introduce any differences. The mesh independency test is employed to eliminate the discretisation errors. These errors appear when the governing differential equations are discretised to algebraic equations using Taylor expansion. In this discretisation process, some terms which are functions of the variables gradients and mesh size are removed. Accordingly, as the mesh size decreases, these errors decrease.

For the case of granular flow the equations have the same hydrodynamic form and hence, the same approach can be taken. It has been reported in the literature (Guenther and Syamlal, 2001) that a mesh size of around five particle diameter is appropriate for the computations. However, this choice is not feasible in the present study. This is because we have relatively large particles (4 mm) compared to the domain (50 mm width and 90 mm height). Using the above mesh size (five particle diameter) will lead to unphysical computational mesh where the variations in air and particle flow are not captured. Our initial simulations showed that we need a mesh whose size is at least 2 mm or half particle diameter. Choosing a mesh size which is smaller than particle diameter does not violate any physical rule since we are solving for continuum equations. However, the flow equations cannot give physically meaningful results on a scale which is less than the particle diameter. Accordingly, making the mesh finer reduces the discretisation errors only.

In this section, we use Wen-Yu drag model, Lun kinetic theory model (Chapter 6) and J&J PSW with $\phi' = 0.1$. All other simulation parameters are kept constant and reported in Table 6-1. The two grids used here are (25×45) and (50×90), with uniform mesh size of 2 and 1 mm respectively. Figure 7-13 shows the

effect of mesh size on the transient void fraction profiles, while Figure 7-14, Figure 7-15 and Figure 7-16 show the differences between these grids for average void fraction and total velocity components over the freeboard region. It is clear that the results are nearly identical for both grids and hence any of them might be chosen. However, the coarse grid reduces the computational time considerably. Accordingly, all the computations in this chapter use this grid (25×45).

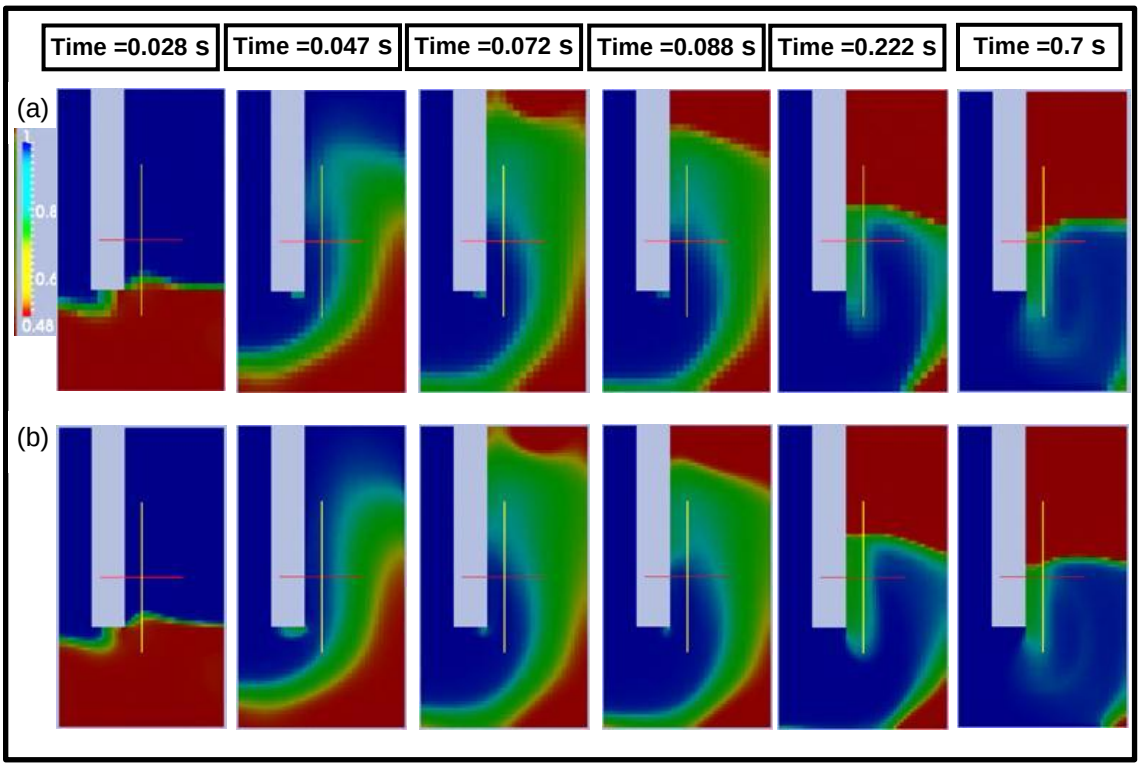

Figure 7-13: Effect of mesh size on void fraction profiles: (a) Coarse mesh with 2 mm size, and (b) Fine mesh with 1 mm size.

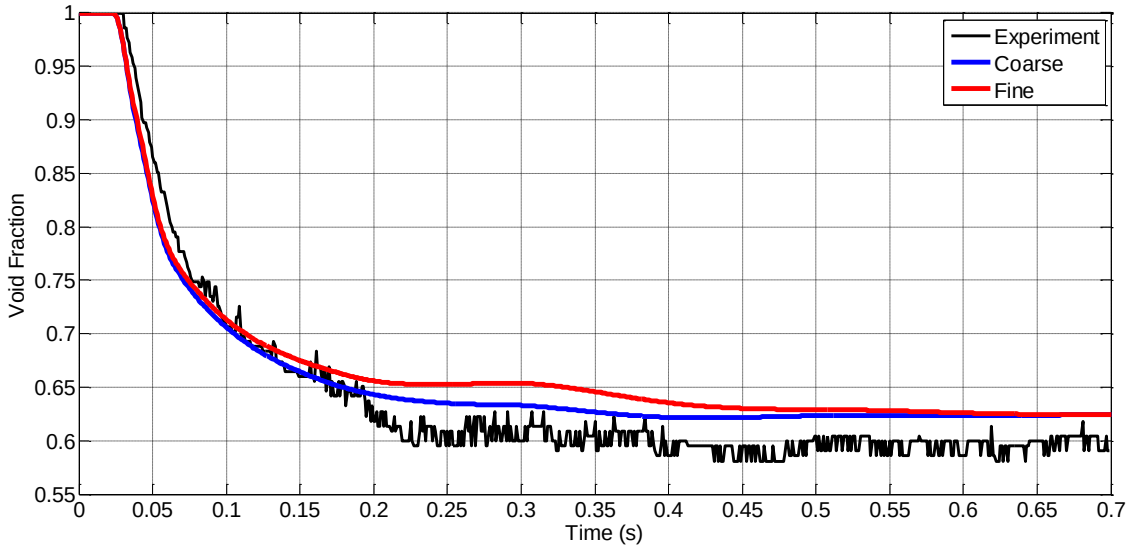

Figure 7-14: Comparison between experiments and numerical predictions of the freeboard average void fraction for the computational mesh size.

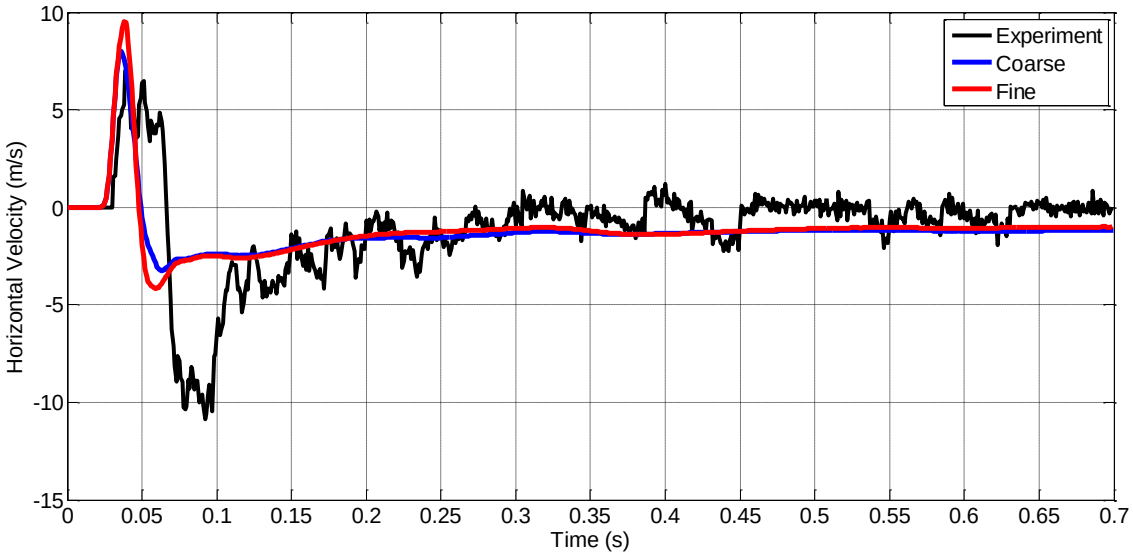

Figure 7-15: Comparison between experiments and numerical predictions of the freeboard total horizontal velocity for the computational mesh size.

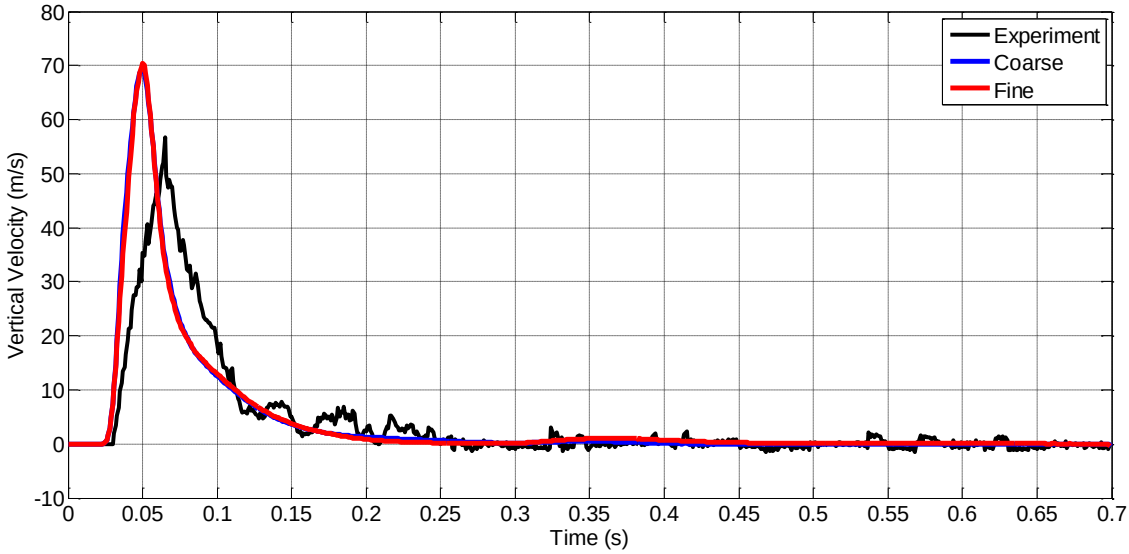

Figure 7-16: Comparison between experiments and numerical predictions of the freeboard total vertical velocity for the computational mesh size.

7.4 Effect of Kinetic Theory Models

The two kinetic theory models used here are 'Lun' (Lun et al., 1984) and 'Garzo' (Garzó and Dufty, 1999). Garzo model is based on the Revised Enskog theory (RET) which is claimed to be valid over the entire fluid domain including all the values of particle-elasticity (Garzó and Dufty, 1999). 'Lun 1984' model is based on the assumption of small variable gradients which implies that the elasticity is nearly unity (0.99). However, there is no restriction for implementing any value of particle-elasticity in 'Lun' model. Full details of these models are given in Chapter 2 and Chapter 6. In this section, we use Wen-Yu drag model and J&J PSW with $\phi' = 0.1$. All other simulation parameters are kept constant and reported in Table 6-1. The mesh used in all simulations is uniform with a size of 2 mm.

Figure 7-17 and Figure 7-18 show a comparison between the void fraction predictions at different time frames using the two kinetic models with the corresponding experimental images. It is clear that there are some differences in the flow behaviour between the predictions of the two kinetic theory models. Despite the two models have similar fluidisation timing; the way the particles are entrained differs between the two models. In 'Lun' Model, the particles are

dispersed throughout the freeboard region showing a more homogenous dispersion. On the other hand, the behaviour for Garzo model is quite different. The fluidisation process takes place in less diffusive behaviour which is in a better qualitative agreement with the experiments. This qualitative behaviour of the aggregate fluidisation was noticed in the FSW predictions (Figure 7-2). This was due to the reduced shear stress which resulted in lower granular temperature which reduces the diffusion. For the effect of the kinetic theory model, the difference in the fluidisation mechanisms (aggregate vs. dispersion) might be caused by a similar mechanism.

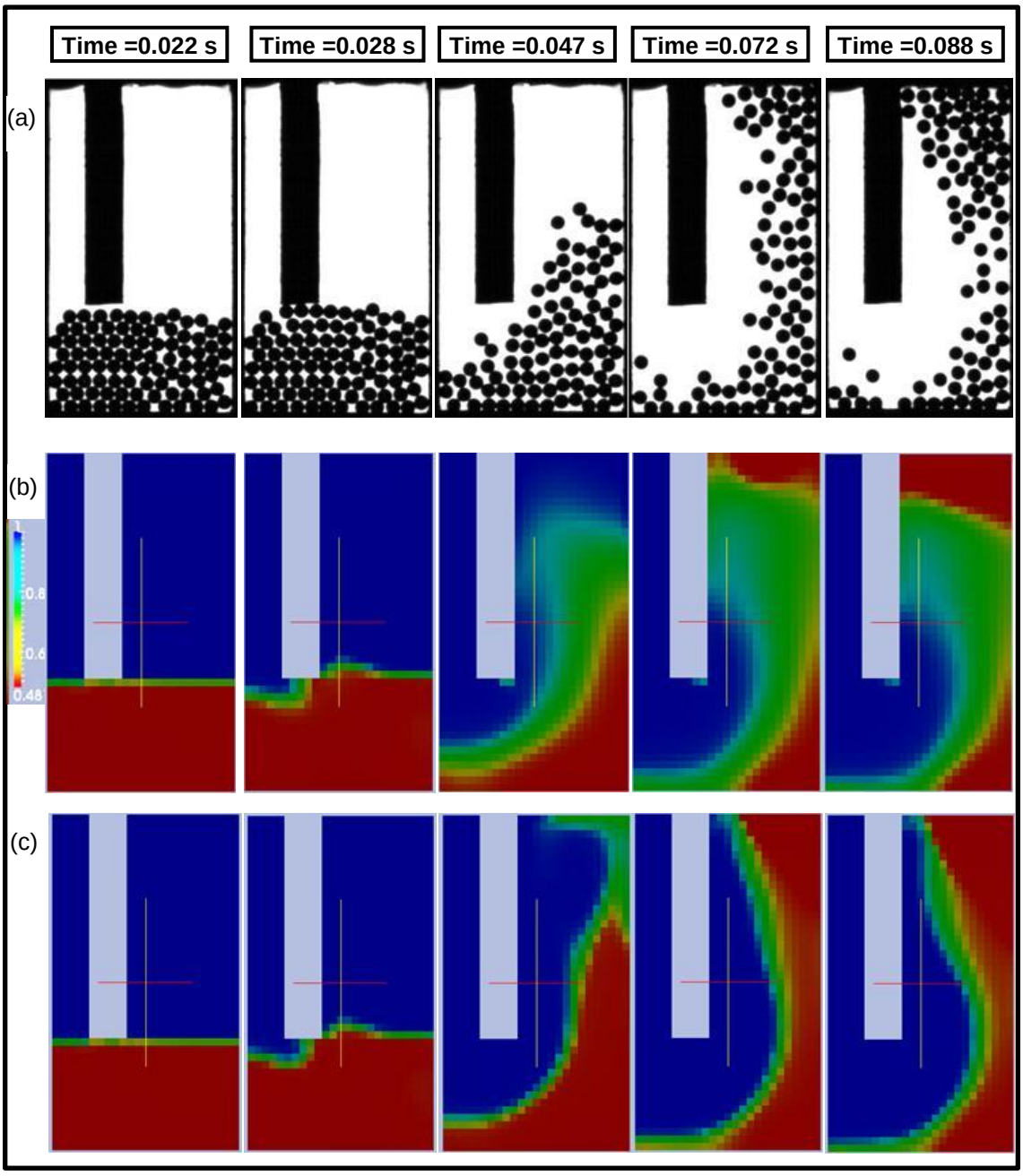

Figure 7-17: Comparison of experimental particles images at different instants in time with numerical void fraction predictions for kinetic theory models: (a) Experiments, (b) Lun, and (c) Garzo.

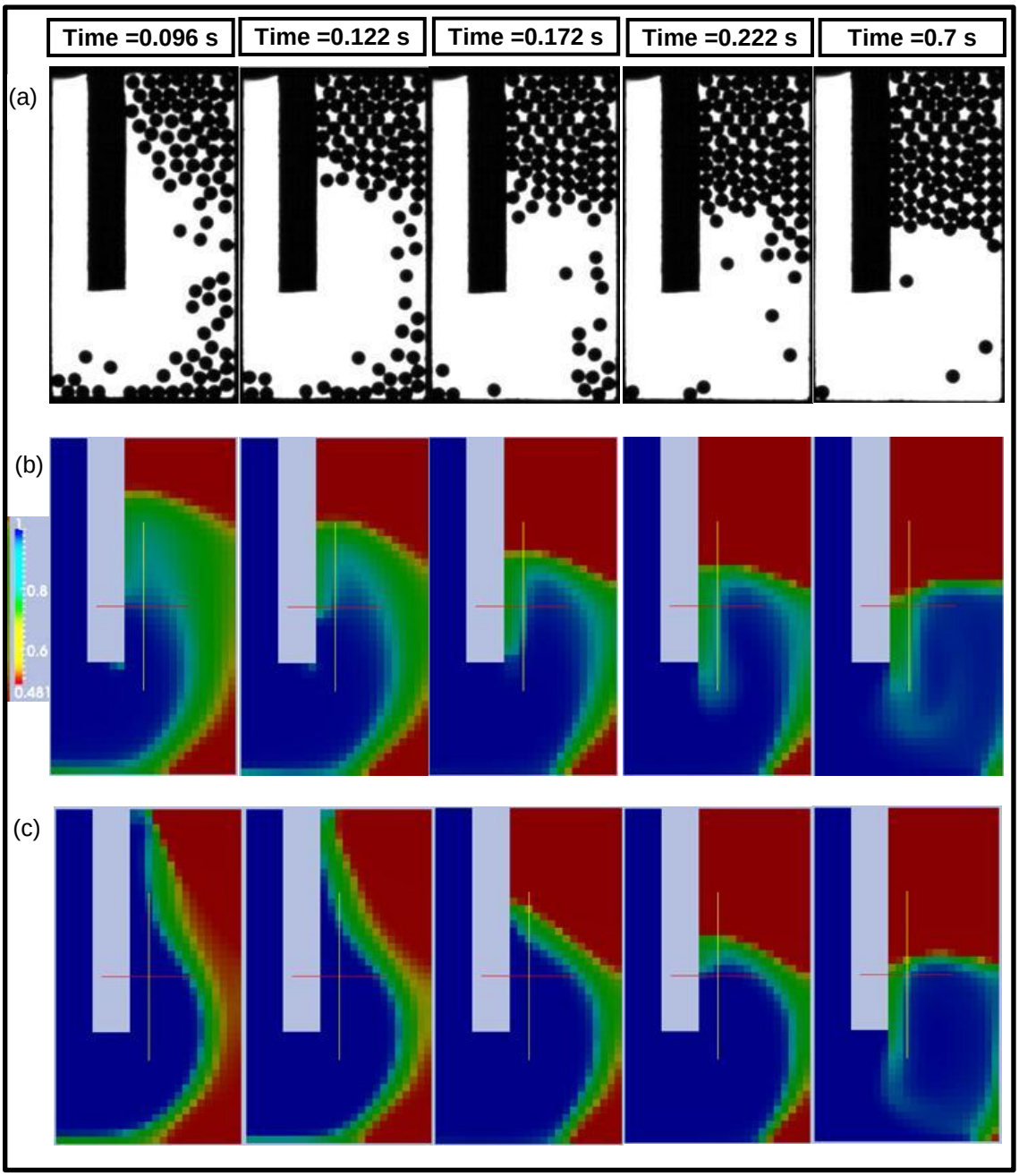

Figure 7-18: Comparison of experimental particles images at different instants in time with numerical void fraction predictions for kinetic theory models: (a) Experiments, (b) Lun, and (c) Garzo.

It is very difficult to trace quantitatively the exact mathematical terms in each kinetic model responsible for this discrepancy. The equations of both models have very complicated mathematical terms. However, one might provide a qualitative explanation for this qualitative discrepancy. In order to draw a picture for all variables, we need to compare the Mach number profiles between the two models: Lun and Garzo. This is shown in Figure 7-19. It is clear that the

Mach number predictions of the Lun model are much lower than that of the Garzo model throughout the simulation time. As the FSW simulation (section 7.2.2.), the aggregate fluidisation and the lack of dispersion in Garzo model predictions is also due to the lower granular temperature generated by this model. However, the main cause of this lower granular temperature is different from that of the FSW simulation. The increased significance of particle elasticity (restitution coefficient) increases the dissipation and hence reduces the diffusion with relative to convection. This relatively low diffusion manifests itself in higher convection and hence less dispersion compared to Lun model.

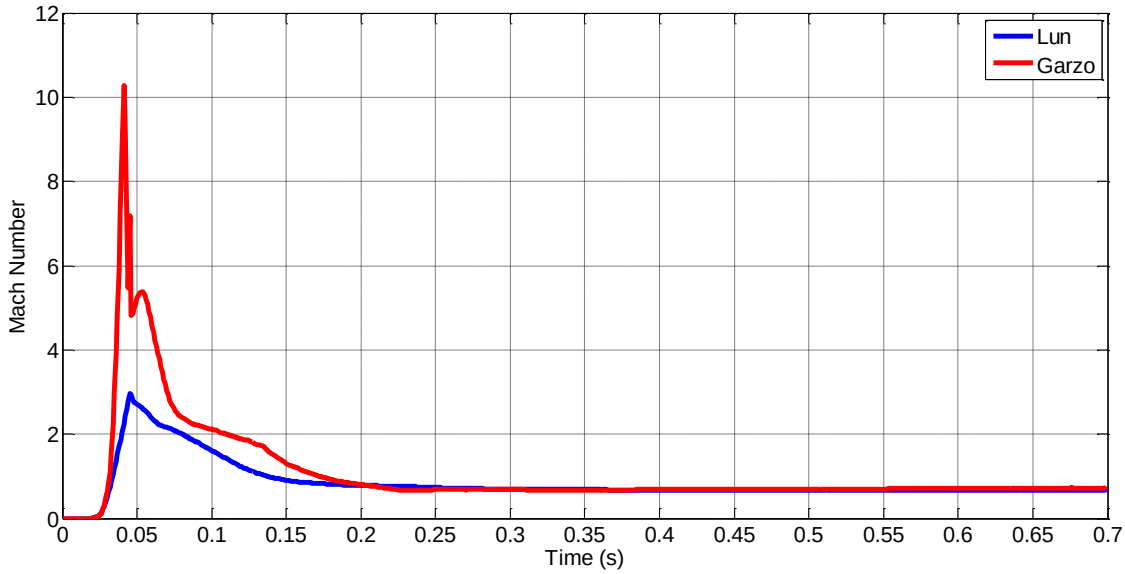

Figure 7-19: Comparison of the freeboard average Mach number for the kinetic theory models.

Figure 7-20, Figure 7-21 and Figure 7-22 show the comparison between the two kinetic models and the experimental results for the average void fraction and solid phase total velocity components over the freeboard region. In Figure 7-20 the void fraction predictions for both theories are nearly identical. This suggests that the effects of the kinetic theory models are negligible in predicting the average void fraction profiles for the freeboard region. The effect of dispersive fluidisation in 'Lun' model versus aggregative in Garzo's is smeared due to the averaging process.

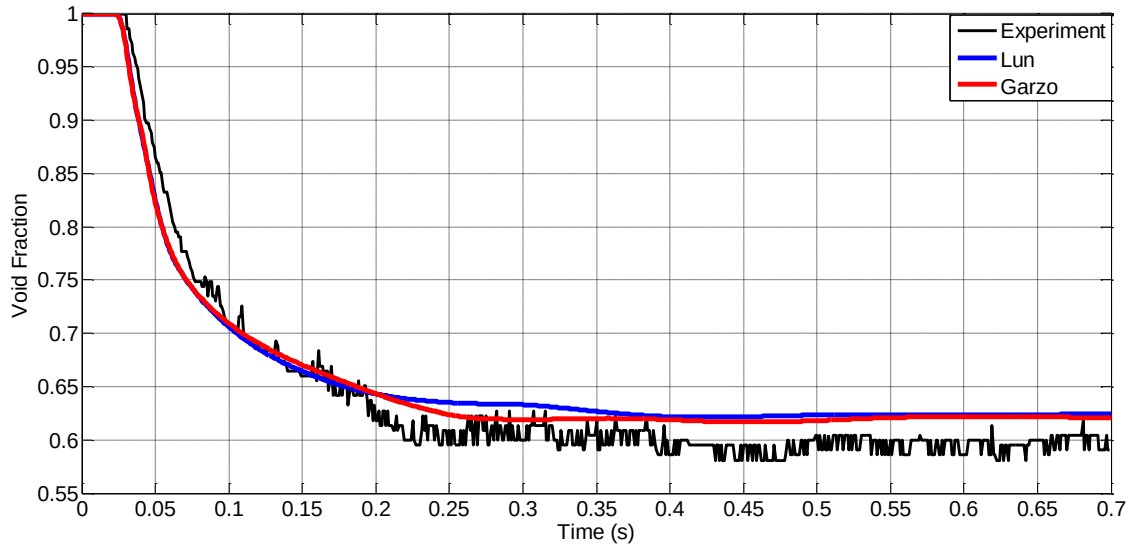

Figure 7-20: Comparison between experiments and numerical prediction of the freeboard average void fraction for the kinetic theory models.

Figure 7-21 shows the total horizontal velocity with time. It is clear that the two kinetic models have the same trend with some quantitative discrepancies (minor differences). Figure 7-22 shows the vertical velocity with time. It is clear that the predictions of both models are similar.

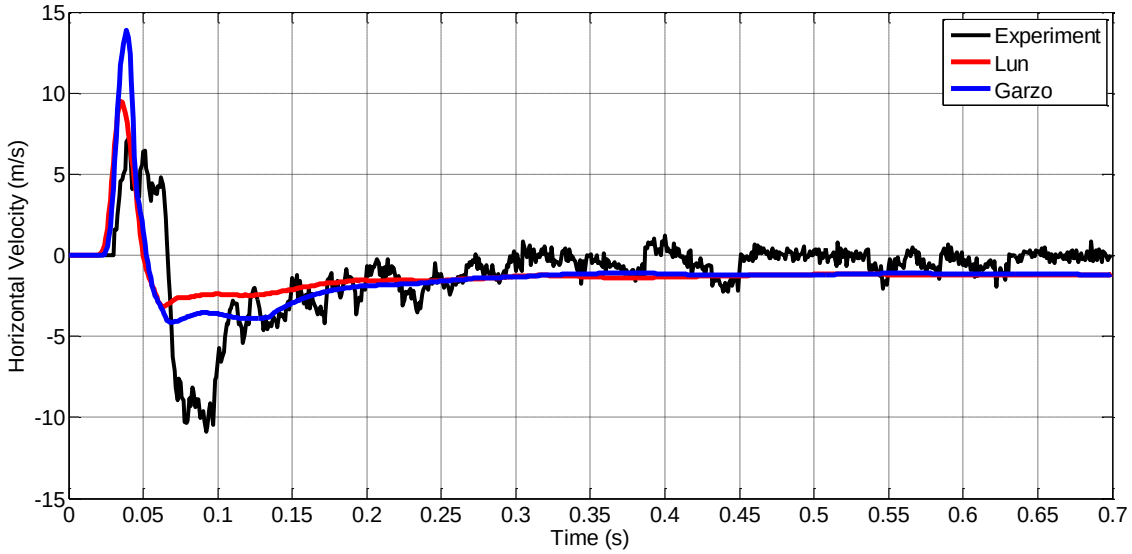

Figure 7-21: Comparison between experiments and numerical predictions of the freeboard total horizontal velocity for the kinetic theory models.

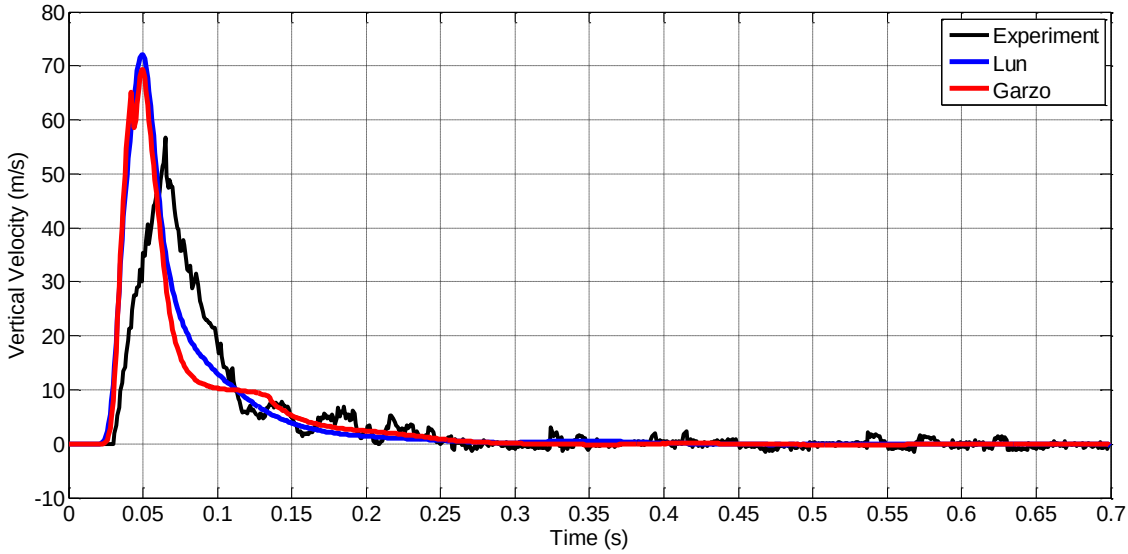

Figure 7-22: Comparison between experiments and numerical predictions of the freeboard total vertical velocity for the kinetic theory models.

The previous comparison between the predictions of the two kinetic theories shows that they nearly predict the same average void fraction and total vertical velocity. It has been shown that there are minor differences in the predictions of the total horizontal velocity. The differences between the two models are in the dispersive fluidisation in Lun versus the aggregate fluidisation of Garzo. This is mainly due to the increased significance of the particle restitution coefficient. In order to test the consistency of this argument (elasticity), a comparison between the predictions of the two models is needed where the effect of elasticity of particles is excluded. In other words, if the two models predict the same behaviour for fully elastic particles, the argument of the effect of elasticity on particle dispersion is valid. This comparison is shown in Figure 7-23. The simulation conditions are similar to that of Figure 7-18 with one exception. The particle elasticity in colliding with each other and with the enclosing walls (restitution coefficients) is set to unity. The comparison for elastic particles shows that the predictions are identical for the two models. Furthermore, the particles are dispersed throughout the whole test section due to their high elasticity. This diffusive behaviour is due to the fact that the particles are totally elastic and hence, there is no dissipation of the granular temperature.

The results of the fully elastic particles suggest that the inelasticity has an important effect on the predictions. As a matter of fact, the inelasticity is the

main cause for good agreement with the experiments. This is because it decreases the diffusion and increases the convection resulting in less dispersive fluidisation as the experiments.

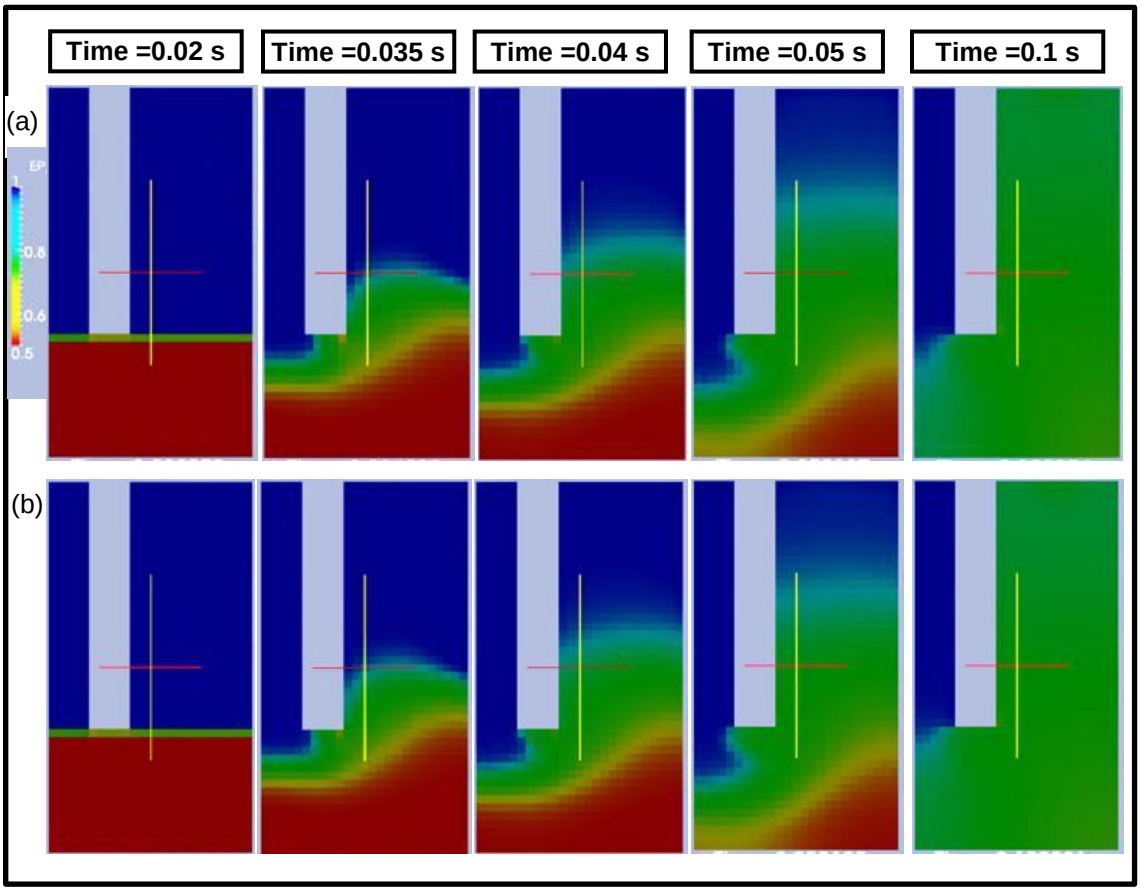

Figure 7-23: Comparison of the effect of kinetic theory models on the predicted void fraction profiles for fully elastic particles: (a) Lun and (b) Garzo.

7.5 Effect of Drag Sub-models

In this section, the effect of drag models described in Chapter 6 is investigated. Figure 7-24, Figure 7-25 and Figure 7-26 show the void fraction, horizontal and vertical total velocities of the freeboard region for different drag models.

The time dependent void fraction in Figure 7-24 shows the behaviour of the drag models. All the drag models have similar behaviour and are very close to the measurements for an experimental time up to 0.08 s. However, 'Hill-Koch-Ladd' model predicts the void fraction for the experiments slightly better for the rest of the experimental time.

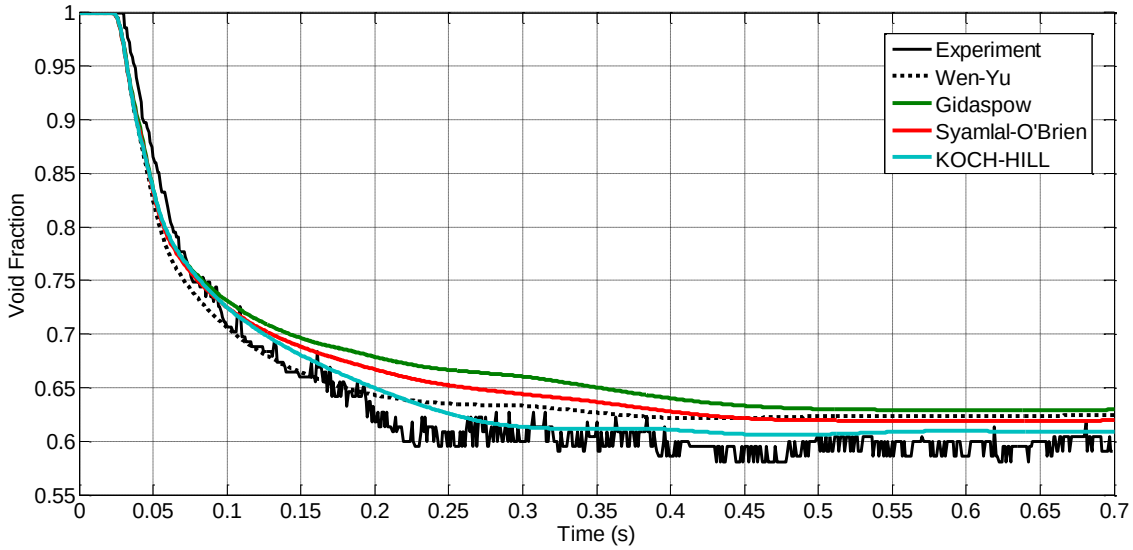

Figure 7-24: Comparison between experiments and numerical predictions of the freeboard average void fraction for the drag models.

The prediction of the total horizontal velocity is nearly similar for all the drag models as shown in Figure 7-25. The total vertical velocity profiles presented in Figure 7-26 show a small discrepancy in the maximum velocity between 'Wen-Yu' and 'Hill-Koch-Ladd'. This discrepancy is around 5 m/s between the two models.

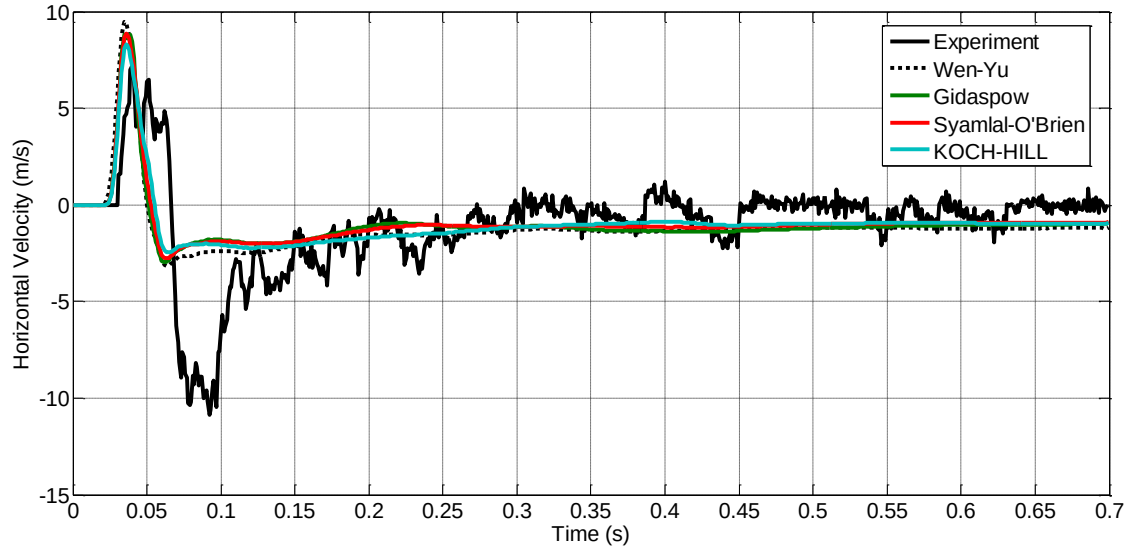

Figure 7-25: Comparison between experiments and numerical predictions of the freeboard total horizontal velocity for the drag models.

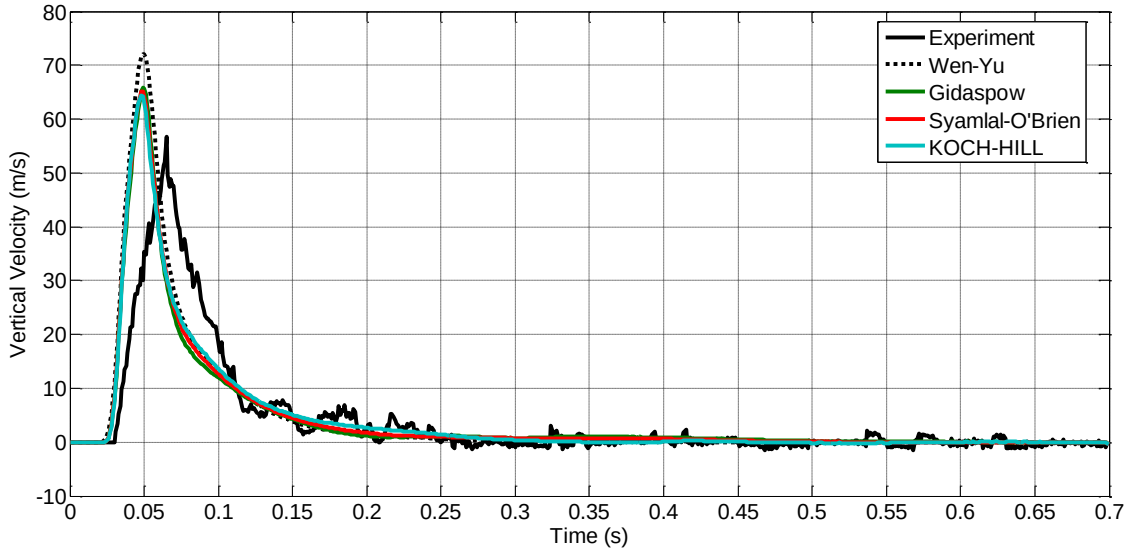

Figure 7-26: Comparison between experiments and numerical predictions of the freeboard total vertical velocity for the drag models.

It is noticed that the drag models are mostly similar, but Hill-Koch-Ladd model gives slightly better prediction for the void fraction profiles. The drag models used here are based on empirical formulas which makes it difficult to draw a conclusion about their validity. However, 'Hill-Koch-Ladd' model is based on lattice-Boltzmann predictions. This predicts more details of the flow, which might produce more precise results. However, using this kind of detailed flow brings some assumptions, which make it difficult to draw conclusions on the best model for calculating the drag.

To get more details of the effect of drag models, Figure 7-27 and Figure 7-28 show comparison between the void predictions of Hill-Koch-Ladd model and Wen-Yu model with experimental images showing the flow of the particles. These two models are chosen because Wen-Yu model is widely used and Hill-Koch-Ladd model represents another approach for computing the drag. It is clear that void fraction images are the same except that the flow supports the particles neighbouring the internal wall and hence prevents them from falling down when using 'Hill-Koch-Ladd' model. This is clear in the last frame at 0.7s. This difference is not significant and consequently, we will use Wen-Yu model as it is widely employed in solid-gas flows.

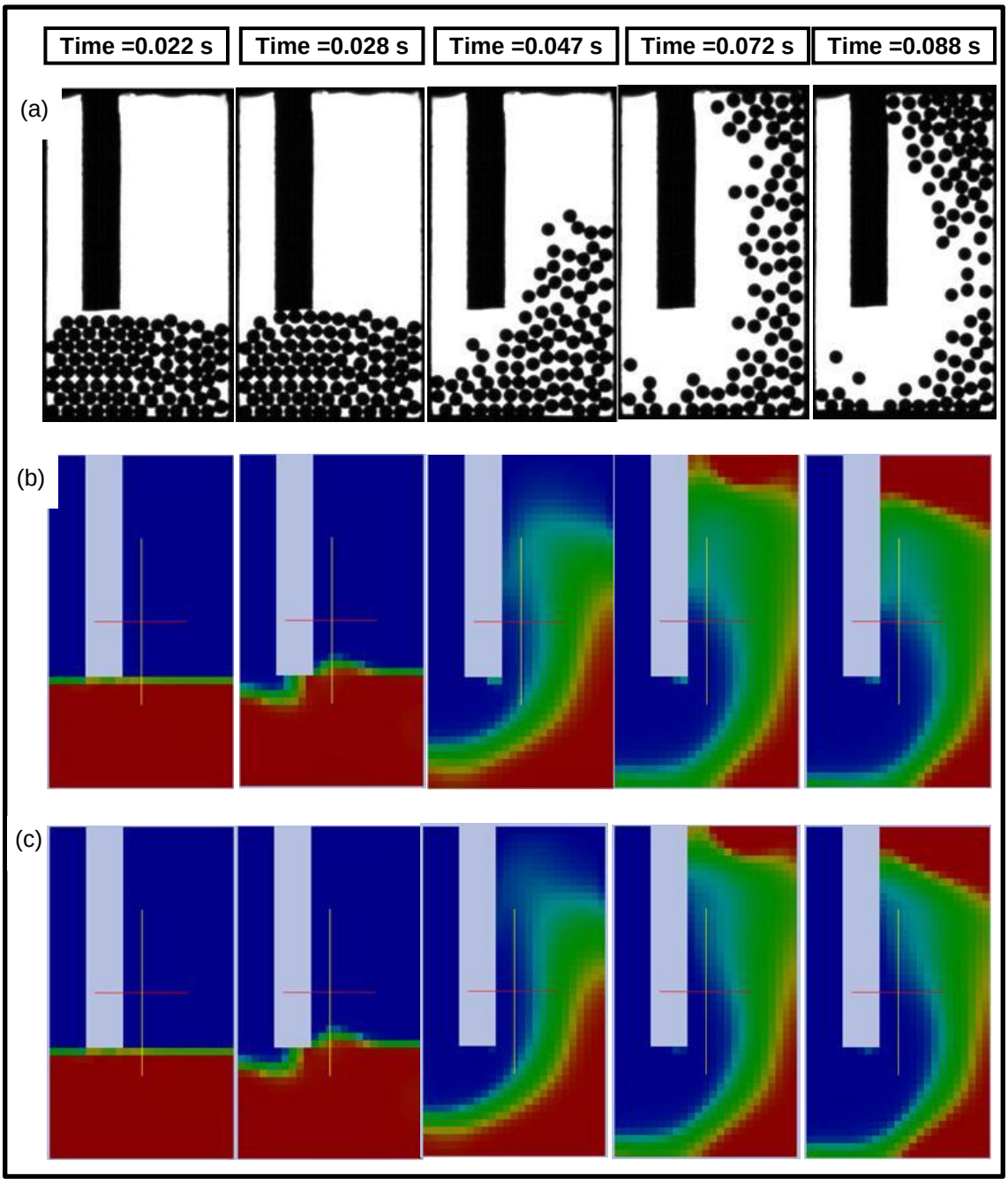

Figure 7-27: Comparison of experimental particles images at early time instants with numerical void fraction predictions for the drag models: (a) Experiments, (b) Wen-Yu, and (c) Hill-Koch-Ladd.

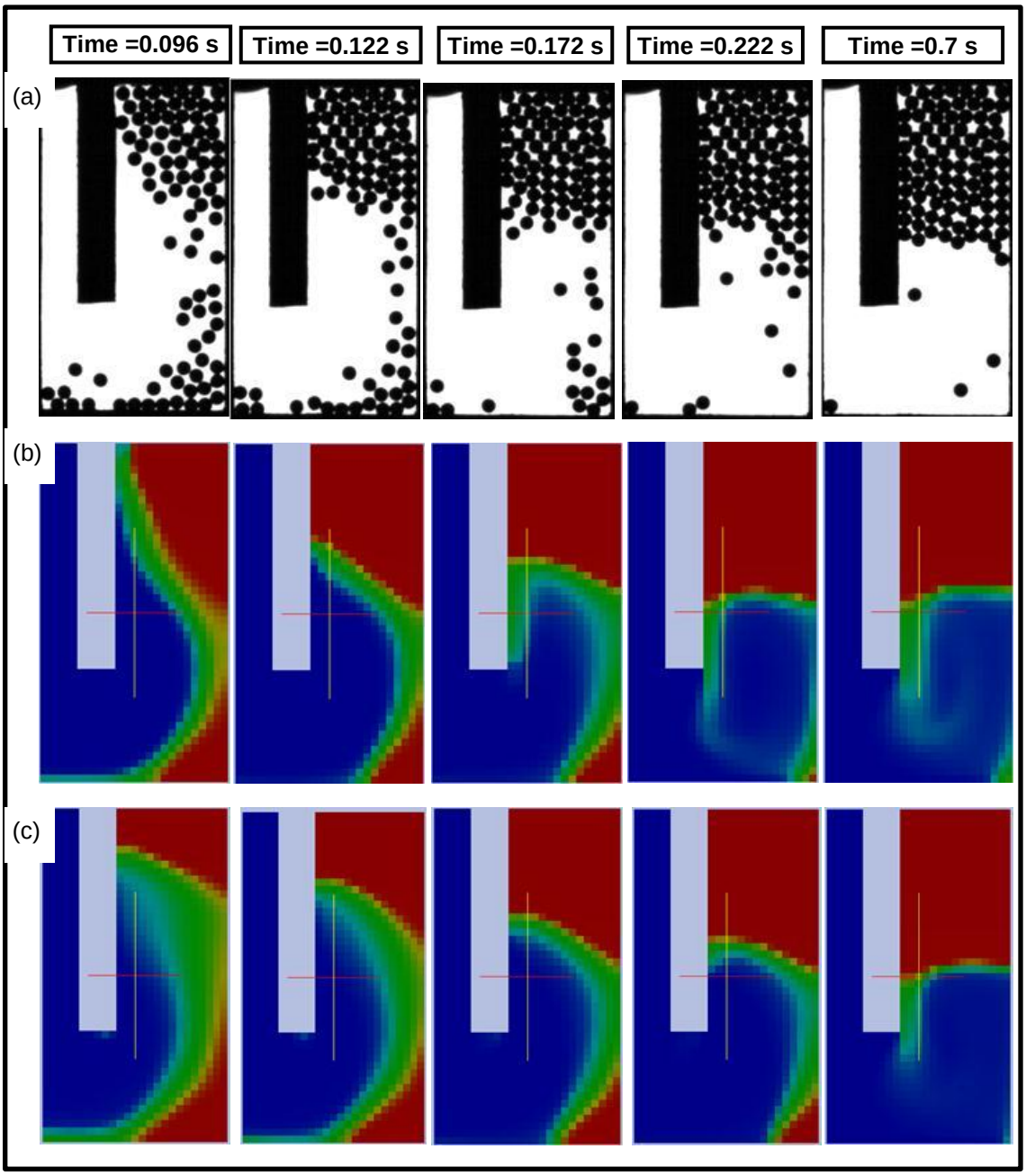

Figure 7-28: Comparison of experimental particles images at late time instants with numerical void fraction predictions for the drag models: (a) Experiments, (b) Wen-Yu, and (c) Hill-Koch-Ladd.

7.6 Discussion

In this chapter, the hydrodynamic model presented in Chapter 6 has been compared to the experimental results. The effect of various sub-models has been investigated. The computational mesh used was uniform with mesh size of 2 mm (25×45). The study of the drag models showed that they nearly

behave in a similar way. The main sub-models which gave physical insight in the behaviour of the hydrodynamic model are the wall boundary conditions models and the kinetic theory models. These models account for the particle-wall and particle-particle interactions respectively.

Three wall boundary conditions have been investigated. They are the no-slip wall (NSW), free-slip wall (FSW) and Johnson and Jackson (J&J) partial slip wall (PSW). It has been shown that NSW is unsuitable for modelling the flow. This is because it under-predicts the bed fluidisation with less mass being entrained from the bed region to the freeboard. This is due to the very high shear stress exerted on the granular phase. The FSW over-predicts the fluidisation timing. The particles are fluidised more quickly than the experiments. However, it can replicate the aggregate fluidisation of the particles. Using J&J PSW with a specularity coefficient 0.1 enhances the predictions of the fluidisation and the average void fraction in the freeboard especially for the initial stage. This is because particle-wall friction is included in the boundary condition. However, the prediction of the qualitative bed fluidisation behaviour deteriorates. The bed disperses during fluidisation in contrast to the aggregative fluidisation seen in the experiments. This dispersion has been traced to the higher diffusion in PSW compared to FSW. This diffusion is a direct result of the higher granular temperature due to higher viscous dissipation. This has been further confirmed by Mach number and granular temperature profiles. Increasing the specularity coefficient from 0.1 to 0.2 and 0.3 leads to more dispersion in the void fraction though 0.2 predicts better average vertical velocity. We suggest a form of wall boundary, which can compromise between the two effects: dispersion and fluidisation time. The granular-wall interactions need friction terms to delay the movement of the granular phase. However, these friction terms should not invoke granular heating in order to avoid extra dispersion. Consequently, a wall boundary condition which uses the friction as a sink term in the momentum equations without a source term in the granular temperature transport equation might enhance the predictions.

Two kinetic theory sub-models have been investigated: Lun model and Garzo model. Their predictions are similar in the average void fraction and total

vertical velocity with some minor quantitative discrepancies in the total horizontal velocity. However, their predictions of the qualitative fluidisation of the granular bed are different. Garzo model predicts less dispersive fluidisation due to the increased dissipation. Mach number profiles confirm that the diffusion in Garzo model is less than Lun model which leads to a more aggregative fluidisation in Garzo model predictions. The differences in the predictions of the two models disappear when the particles are fully elastic with a value of restitution coefficient of unity. This confirms that the way each model deals with the elasticity is responsible for the difference. In the fully elastic predictions, the granular bed diffuses as soon as the air strikes the bed. The convection of particles is much less than the previous case. This suggests that the inelasticity is responsible for driving the simulations towards better agreement with the experiments.

Based on the effects of the wall boundary conditions and kinetic theory models, one can spot common behaviour. Increasing the diffusion in the simulations increases the discrepancy with the experiments. This is because the particles showed strong convective behaviour in the experiments leading to aggregate fluidisation. The diffusion might be increased using two approaches: the wall boundary conditions models and the kinetic theory models. Both approaches result in the same mechanism of granular heating due to viscous dissipation for the J&J PSW, or the lower granular temperature dissipation in Lun model. Consequently, one might think that removing particle-particle and particle-wall interactions will lead to better agreement. MFIX code gives this option of removing all these interactions from the granular flow model. The void fraction profiles with time of this simulation are shown in Figure 7-30. It is clear that the lack of inter-particle interactions leads to circulating behaviour of the bed and the final stage of the experiment is not predicted. This stage happens when the particles are packed at the top of the freeboard. Removing the interactions with the walls and other particles does not allow the particles to hold each other, because the forces and stresses are not transmitted within the granular assembly, and the drag force cannot hold the weight of the particles in some regions of the freeboard. The circulating behaviour is clear in the fluctuating

trends of the void fraction and total vertical and horizontal velocities as shown in Figure 7-30, Figure 7-31 and Figure 7-32 respectively.

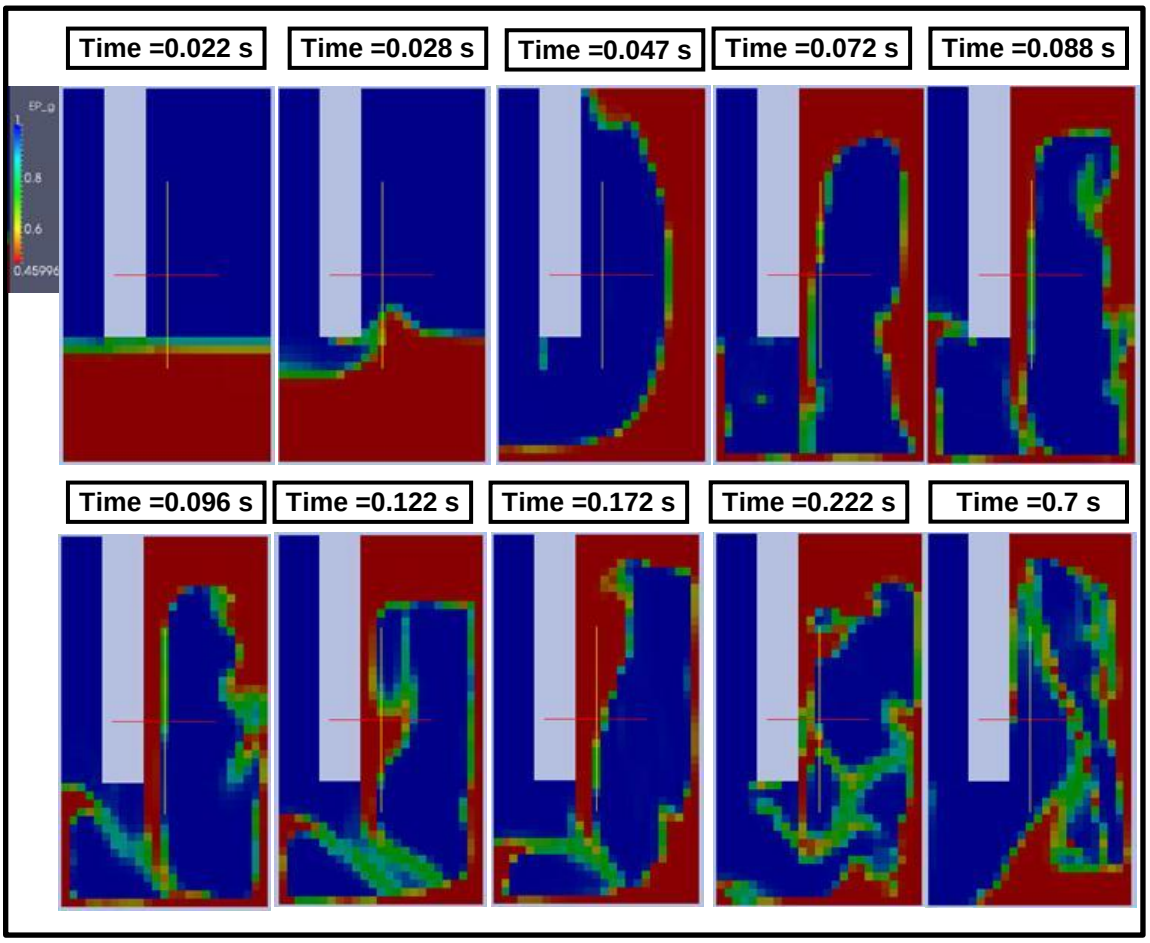

Figure 7-29: Void fraction profiles for a simulation without inter-particle interactions.

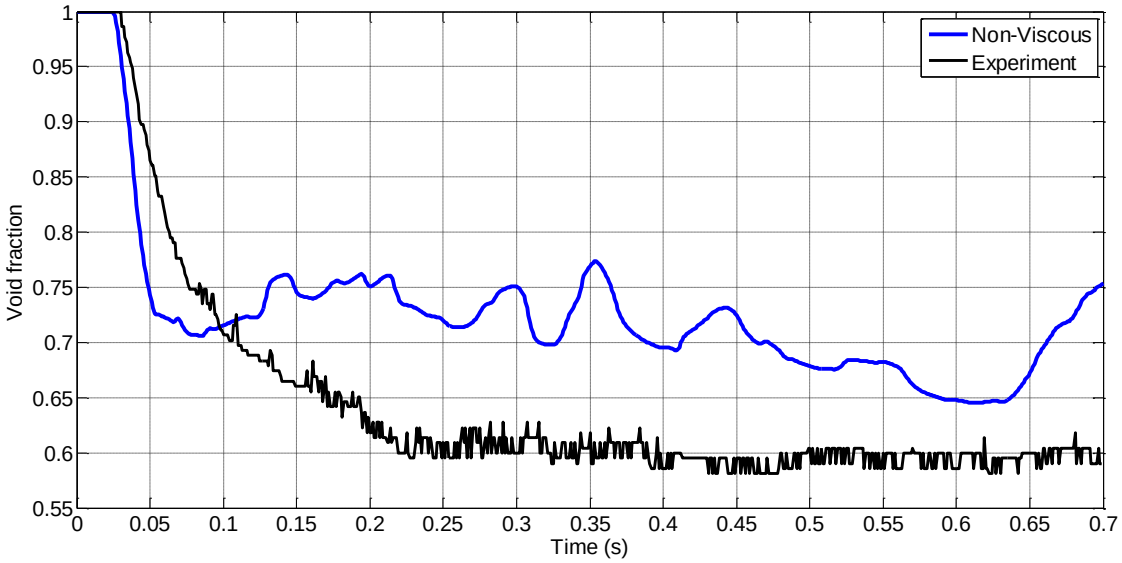

Figure 7-30: Comparison between the experiments and numerical predictions of the freeboard average void fraction for the non-viscous granular model.

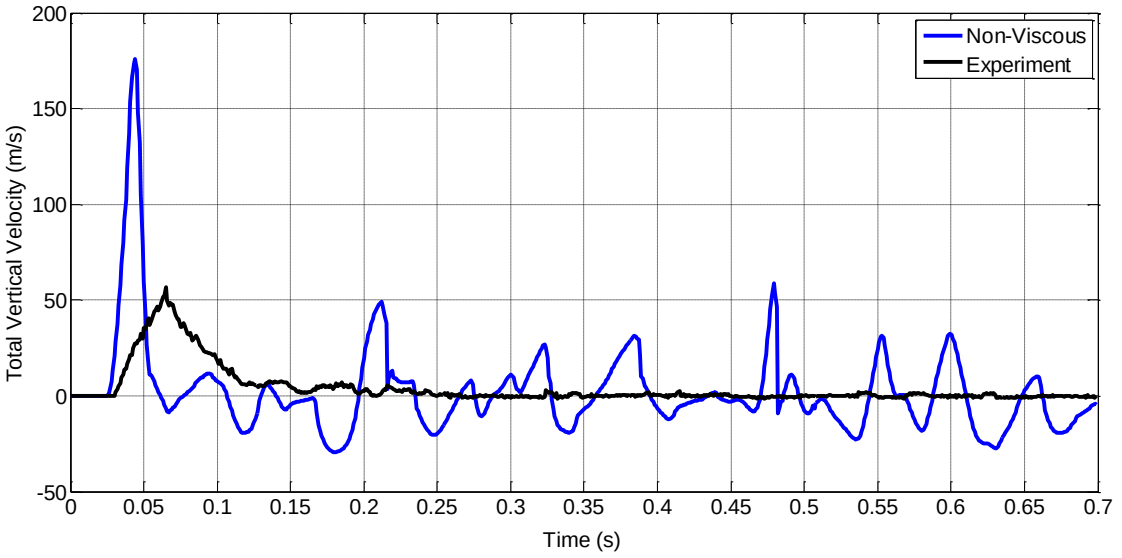

Figure 7-31: Comparison between the experiments and numerical predictions of the freeboard total vertical velocity for the non-viscous granular model.

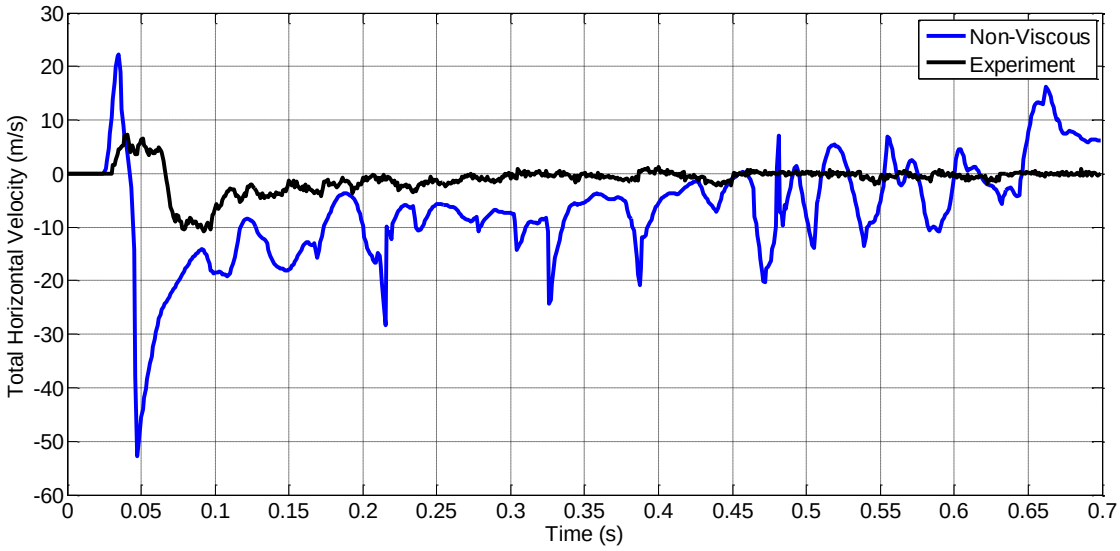

Figure 7-32: Comparison between the experiments and numerical predictions of the freeboard total horizontal velocity for the non-viscous granular model.

7.7 Summary and Conclusions

In this chapter, the TFM predictions have been compared to the experiments for the first flow case with high pressure difference of 16 kPa. The study shows that the model can predict the results of the experiments using certain sub-models and parameters. In order to replicate the predictions with the experimental results, TFM sub-models and parameters should be chosen to minimise diffusion and promote convection. The sub-models which contribute to the convection-diffusion ratio are the boundary walls and kinetic-theory, while the parameters are the particle-wall friction (via specularity coefficient in J&J PSW), and the particle restitution coefficient (via kinetic theory sub-models). The wall boundary conditions models should include wall-friction but without invoking granular heating due to viscous dissipation. None of the wall boundary conditions studied includes both physics and hence a form of boundary condition which includes friction as a sink term in the momentum equations without further implications on the granular temperature might be appropriate. Kinetic theory models which include higher granular temperature dissipation (Garzo) enhanced the qualitative predictions. However, the restitution coefficient should be the same order of magnitude as the experiments to avoid strong dispersion encountered in fully elastic particle predictions. Inter-particle

sub-models are important for predicting the re-packing of the granular phase in the freeboard region.

Chapter 8 : Computational Study of Particle Bed Fluidisation Using Weak Impinging Air Jet

8.1 Introduction

In this chapter, the numerical predictions corresponding to cases two and three, defined in Chapter 3, are presented and validated with the experiments. The experimental results of those cases, with low pressure difference between the inlet and outlet, were shown in Chapter 5. The low air pressure difference resulted in partial fluidisation of the particle bed. As seen in Chapter 5, the flow behaviour for those cases is different to that of the high pressure difference. The high pressure difference case (Chapter 4) is characterised by strong fluidisation of particles and convection dominated flow throughout the fluidisation event. On the other hand, the partial fluidisation cases have an initial fluidisation stage (up to 0.3 s) which is dominated by convection in a similar fashion to the high pressure (full fluidisation). However, fluctuations are noticed in the freeboard region for the partial fluidisation regime at later times. These fluctuations result from the complicated motion of the particles where collisional and convective motions take place. Furthermore, the particles end up clustering at the top of the freeboard. It was shown that applying the continuum and kinetic theory approaches to this fluctuating part might be problematic; the particle motion lacks a clear separation of macro and micro scales. This non-continuum behaviour challenges the ability of continuum models based on the KTGF to predict the flow of this regime in the later time range. However, the way these continuum models will deviate from the experiments is unclear. One of the aims of this chapter is to investigate this issue.

It was shown in Chapter 5 that the two cases of low pressure differences behave in a similar way. Accordingly, we present in detail the results of case two only. Then the results for case three are presented with the most important issues in a separate section. When analysing case two, we study the effects of the wall boundary conditions and kinetic theory models. The effects of drag models and mesh are not considered, because they were investigated in

Chapter 7 and they did not affect the simulations. Furthermore, an investigation for the present cases yielded the same conclusion. Accordingly, we use Wen-Yu drag model and a 2 mm uniform computational mesh size for all the predictions presented in this chapter.

8.2 Effect of Granular Phase Wall Boundary Conditions

In this section three types of boundary conditions are investigated: FSW, NSW and J&J partial slip wall. As in Chapter 7 the effect of specularity coefficient in the J&J PSW is studied.

8.2.1 Effect of Wall Boundary Conditions

In this section, Lun kinetic theory model is used. Following section 7.2.1., the specularity coefficient of J&J PSW is 0.1. Other simulation parameters are constant as reported in Table 6-1. Figure 8-1 and Figure 8-2 show void fraction predictions for the three types of wall boundary conditions (NSW, FSW and J&J PSW) and the experimental particle flow field. The NSW under-predicts the movement of particles due to the high shear stress exerted by the walls. The predicted mass of solid phase in the freeboard is much lower than the experiments. This is clear at time 0.07 s, 0.1 s, 0.2 s and 0.3 s. The FSW boundary condition over-predicts the fluidisation process during the initial fluidisation: i.e. the mass of solid phase in the freeboard region is higher than the experiments at 0.07 s, 0.1 s and 0.2 s. This is due to the neglected effect of wall friction. However, the particles are predicted to fall down from the freeboard region at time 0.3 s. This means that the external forces cannot hold the particles upwards and the net forces have downwards direction. Since the direction of the drag force is upwards and the weight is downwards, this means that the drag force is lower than the weight. J&J PSW gives the best results for the initial fluidisation up to 0.2 s. However, some particles are predicted to fall downward as shown at 0.3 s. The mass of falling particles in J&J PSW is much less than that of FSW. By comparing all the models and the experiments, one can state that the clustering which happens towards the end of the experiments (time 1.9 s) is not predicted by any of the boundary conditions.

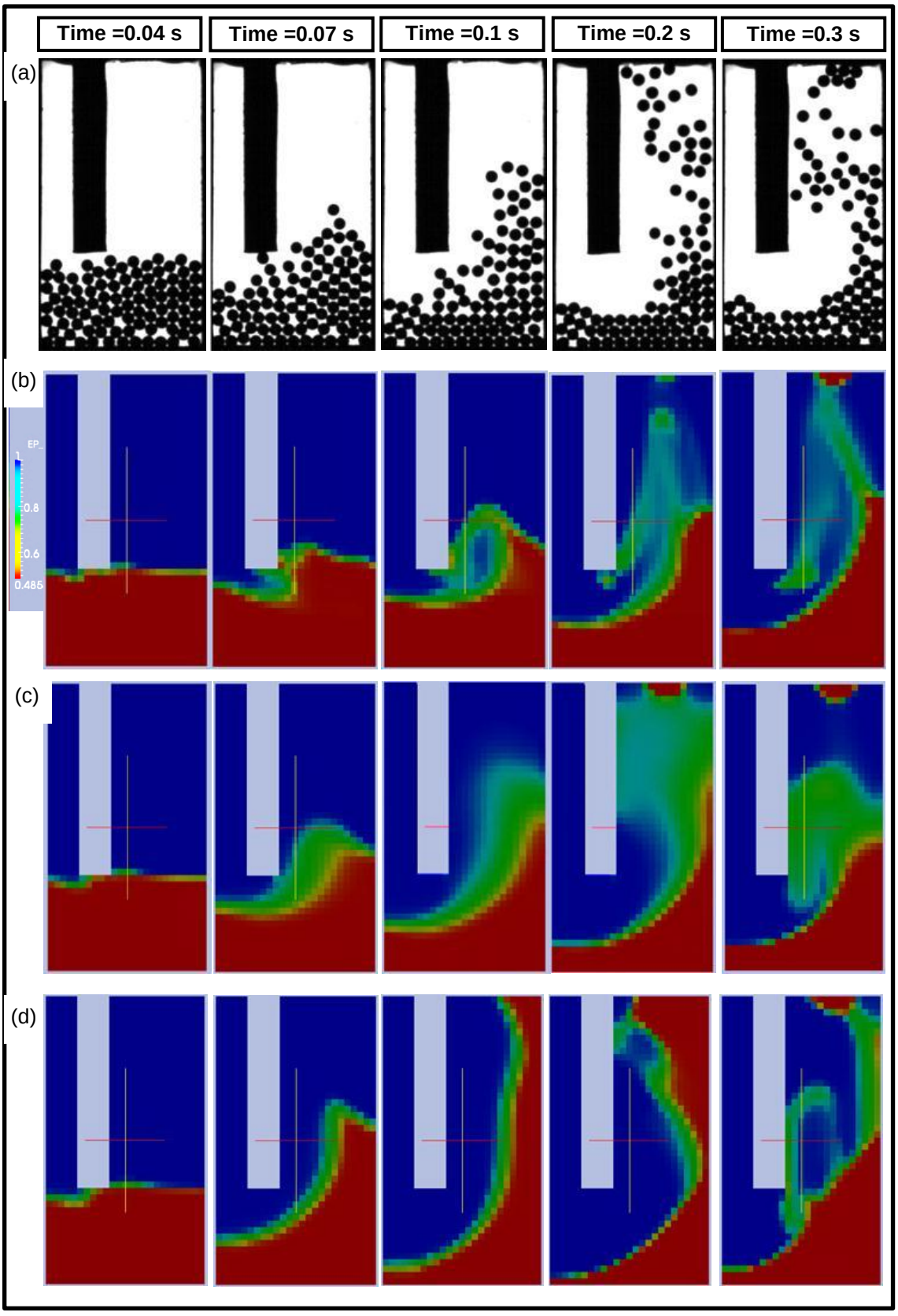

Figure 8-1: Comparison of experimental particles images at early instants in time with numerical void fraction predictions for the wall boundary conditions: (a) Experiments (b) NSW, (c) J&J PSW with ϕ' = 0.1, and (d) FSW.

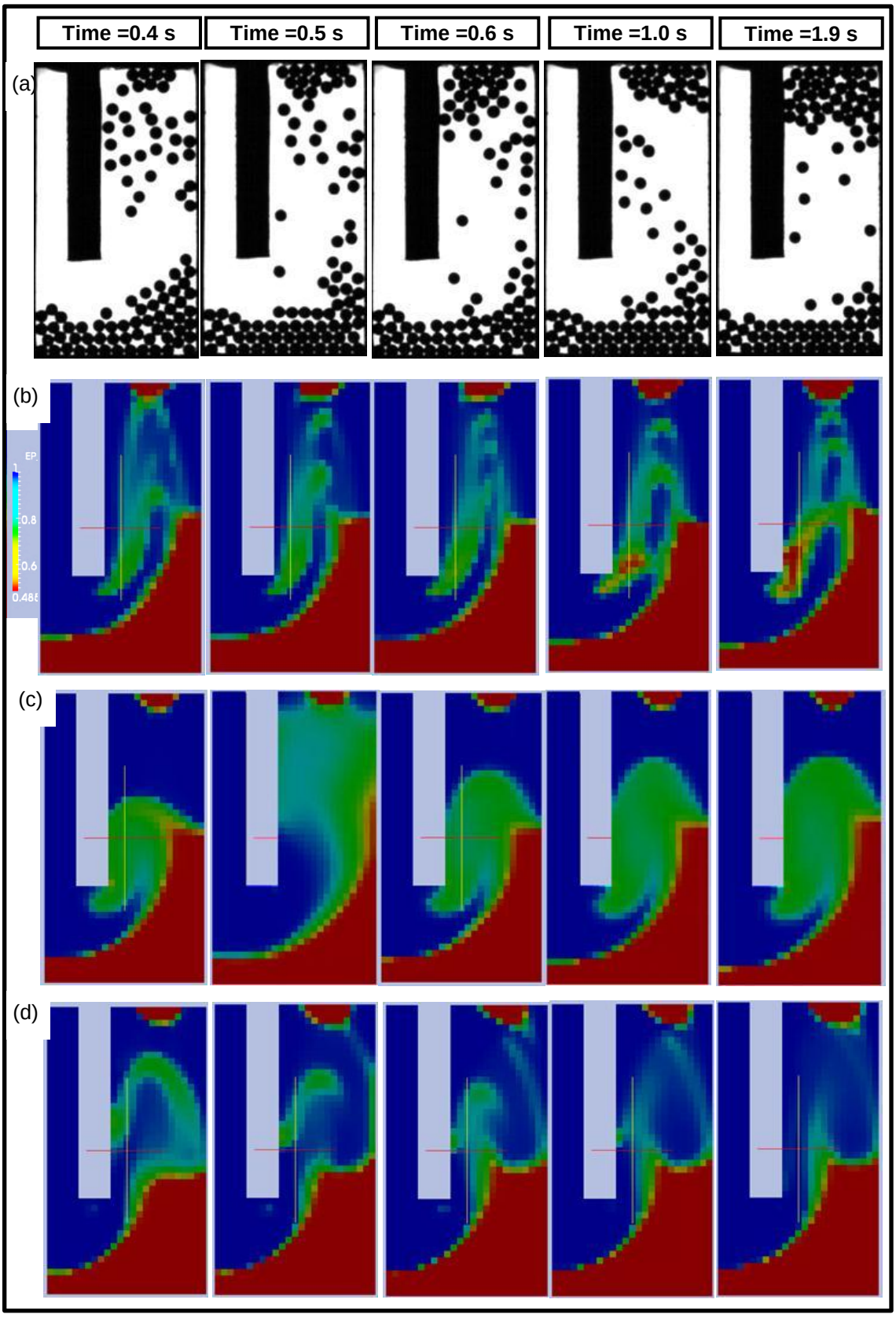

Figure 8-2: Comparison of experimental particles images at late instants in time with numerical void fraction predictions for the wall boundary conditions: (a) Experiments (b) NSW, (c) J&J PSW with $\phi' = 0.1$, and (d) FSW.

It is clear that the predicted void fraction profiles using FSW exhibit less dispersive fluidisation behaviour when compared to the PSW. This replicates the behaviour seen in Chapter 7. For example at time 0.5 s, 1.0 s and 1.9 s more particles are dispersed in the simulations using the PSW boundary condition compared with the FSW. However, it is difficult to state whether the fluidisation in the experiments is dispersive or not. This is because the dilute flow in this case combined with the large particle size constraints the length scale of comparison between the experimental and computational approaches. Consequently, we cannot say which boundary condition is better in this issue.

Figure 8-3 shows a comparison between the measured and the predicted average void fraction for the three types (NSW, FSW and J&J PSW) of wall boundary conditions. It is clear that the NSW under-predicts the movement of particles in the initial fluidisation. Consequently, this model is far from the experiments and it is not appropriate. For the FSW, the movement of particles in the initial fluidisation is over predicted due to the neglected effect of friction. At time 0.18 s, the predicted void fraction of the FSW is around 0.755 while the measured is 0.85. However, at this time (0.18 s) the FSW prediction of void fraction reaches a local minimum. The void fraction increases at this point until it reaches a value of 0.87 at time 0.3 s. This value is higher than the experimental value at the same time (0.3 s). The minimum occurs because the drag is not able to hold the particles (Figure 8-1). The FSW void fraction stays constant from 0.3 s until the end of the experiment.

The discrepancies in the void fraction are reduced significantly in J&J PSW predictions. The values of void fraction in the freeboard region are much closer to the experiments for time up to 0.2 s (the first stage of initial fluidisation). A minimum or under-shoot in the void fraction is also seen in the PSW predictions at time 0.2 s, but the magnitude of the under-shoot is much smaller than that of FSW. The overshoot which happens in void fraction at time 0.35 is smaller in PSW than FSW. From time 0.4 s until the end of the experiment, J&J PSW follows the same decreasing trend of the experiment, whereas the predictions with FSW yield a nearly constant void fraction after 0.4 s.

It is clear that J&J PSW gives the best agreement; however, the fluctuations in the void fraction seen in experiments between 0.3 s and 2.0 s are not predicted by any wall boundary condition model.

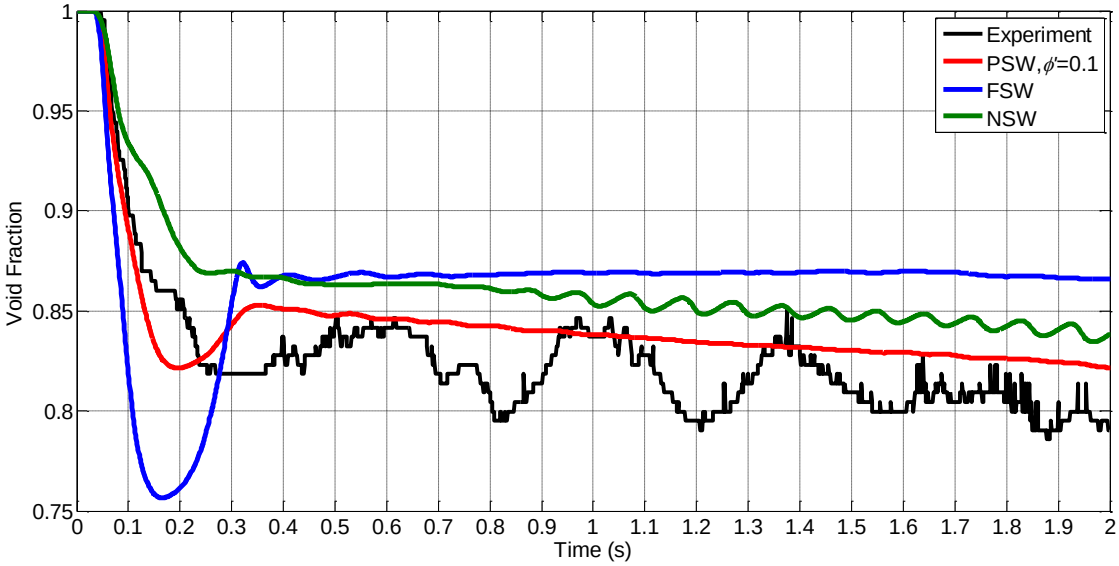

Figure 8-3: Comparison between experiments and numerical predictions of the freeboard average void fraction for the wall boundary conditions.

Figure 8-4 and Figure 8-5 show comparisons between the measured and the predicted total horizontal and vertical velocities over the freeboard region, respectively. It is clear that the PSW gives the best agreement among the other boundary conditions. However, the fluctuations in the velocities seen in experiments between 0.3 s and 2.0 s are not predicted by any wall boundary conditions model. Only some fluctuations in the horizontal velocity using FSW are present. Moreover, the under-shoot and over-shoot noticed in the average void fraction for the FSW case are clear in the total velocity profiles.

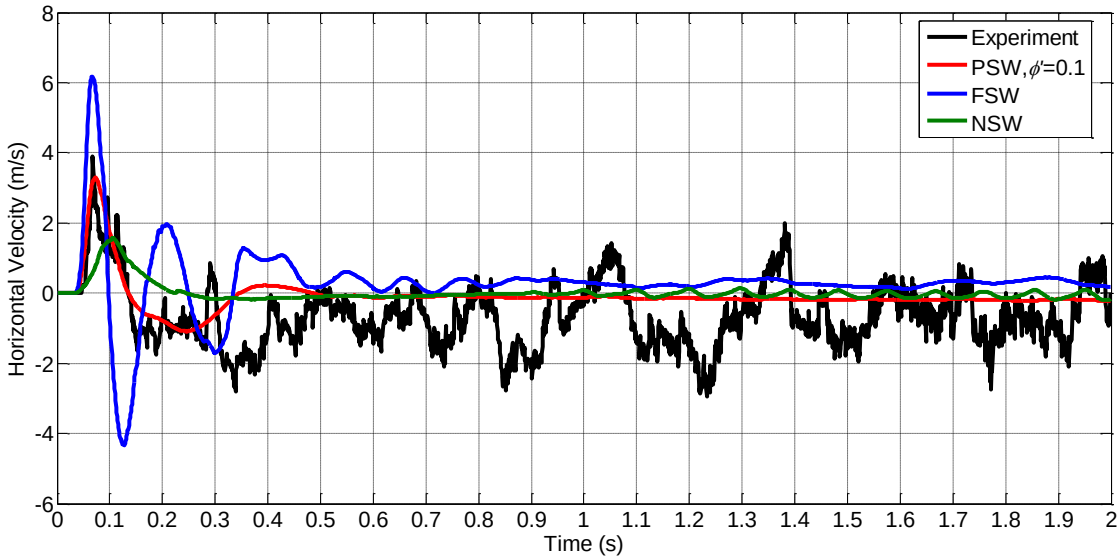

Figure 8-4: Comparison between experiments and numerical predictions of the freeboard total horizontal velocity for the wall boundary conditions.

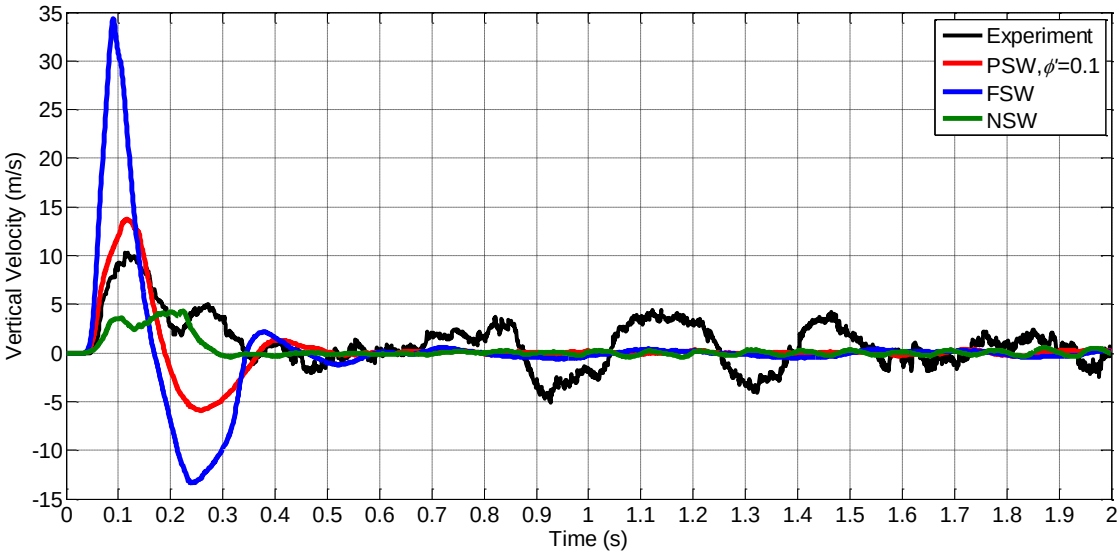

Figure 8-5: Comparison between experiments and numerical predictions of the freeboard total vertical velocity for the wall boundary conditions.

The air and granular phase are coupled together through the source term in the momentum equation. Consequently, checking the inlet air velocity might provide insight into the under-shoot and over-shoot of particles. Figure 8-6 shows a comparison between the inlet air velocity for the two boundary walls: FSW and J&J PSW. It is clear that the two predictions have the same trend. The velocity increases rapidly at the beginning until it reaches a maximum value of around 40 m/s. Then it decreases rapidly until it reaches a value of

around 20 m/s and retains this value until the end of the experiment. However, the differences between the two predictions are quantitative. The FSW prediction decreases rapidly at time 0.1 s. The PSW prediction decreases at later time of 0.12 s and the decrease is less rapid, reaching 15 m/s at time 0.2 s. At time 0.17 s, the air velocity has nearly the same value (15 m/s) for both predictions. However, the mass of the solid particles in the FSW is higher around 0.2 s as shown in Figure 8-1 and Figure 8-3. Since the PSW prediction which have less mass in the freeboard region cannot prevent the particles from falling down. Therefore, the FSW prediction will not hold the higher mass as well. This justifies the falling of the particles in the FSW. Generally speaking, the friction and viscous effects tend to stabilise the simulation. This is because they prevent excessive fluidisation of particles at the initial phase and consequently prevent their falling down back.

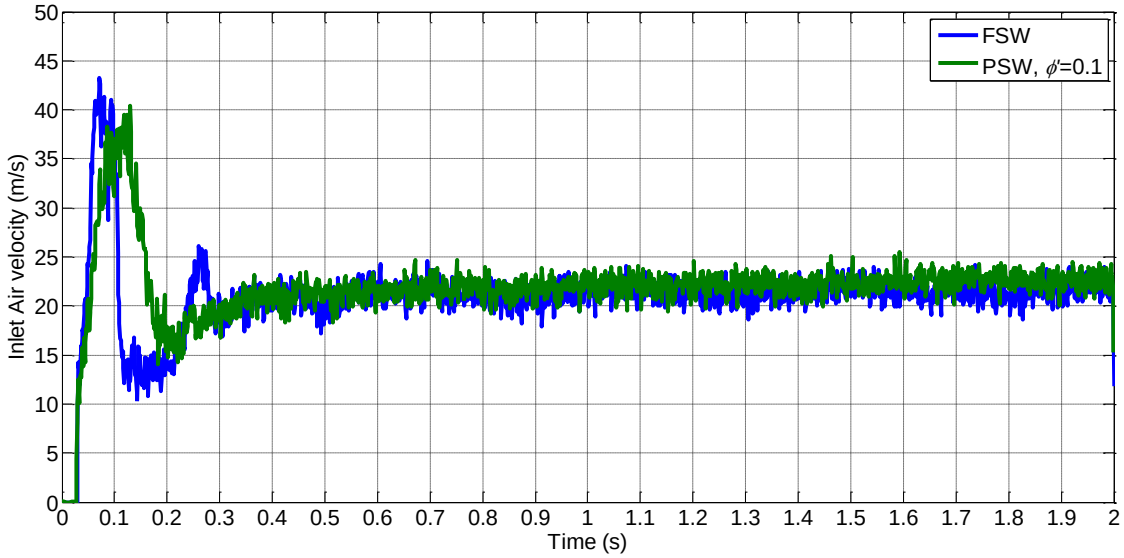

Figure 8-6: Comparison of the inlet air velocity for the wall boundary conditions.

Figure 8-7 shows the Mach number for the two wall boundary conditions: FSW and J&J PSW. It is clear that the Mach number of the FSW is much higher than that of the J&J PSW. This confirms that the diffusion plays a more prominent role in simulations with the J&J PSW boundary condition than with the FSW boundary condition.

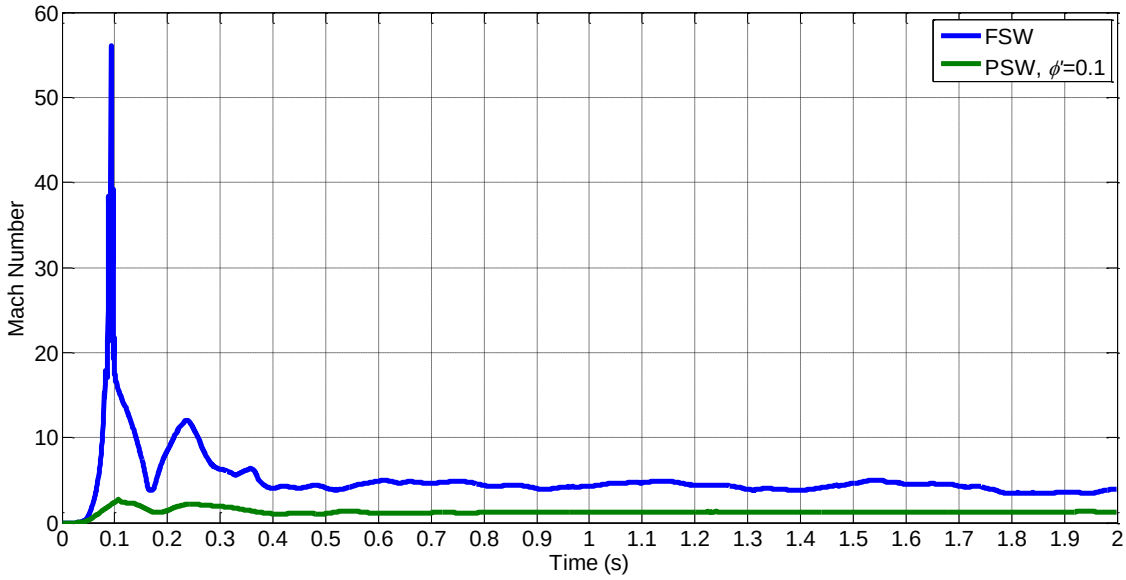

Figure 8-7: Comparison of the freeboard average Mach number for the wall boundary conditions.

Both quantitative and qualitative results for the effect of the wall boundary conditions confirm that the J&J PSW gives the best agreement with the experiments. The discrepancy noticed between all the predictions and the measurements is the lack of fluctuations in the simulations and the failure of the model to predict the clustering of particles, which happens towards the end of the experiment. In the next section, we will study the effect of specularity coefficient in order to know which value is in better agreement with the experiments.

8.2.2 Effect of Specularity Coefficient

In this section we examine the effect of the value of specularity coefficient on the predictions. Following Chapter 7 selections, we will use three values of this coefficient(ϕ'): 0.1, 0.2 and 0.3.

Figure 8-8 shows a comparison between the particle images obtained from the experiments and the void fraction predictions for different values of specularity coefficient. We use Wen-Yu drag model and Lun kinetic theory model (Chapter 6). Other simulation parameters are constant as in Table (6-1). The predicted mass of the solid phase in the freeboard region decreases slightly as the

specularity coefficient increases. This is clear at time 0.2 s. Again, this is due to the effect of increasing the friction between the granular phase and the wall. It is also clear that the dispersion increases slightly as the specularity coefficient increases. This is an effect of the increased granular temperature due to the increased shear stress and viscous dissipation. It is clear that none of the specularity coefficient values can predict the clustering of particles in the experiments.

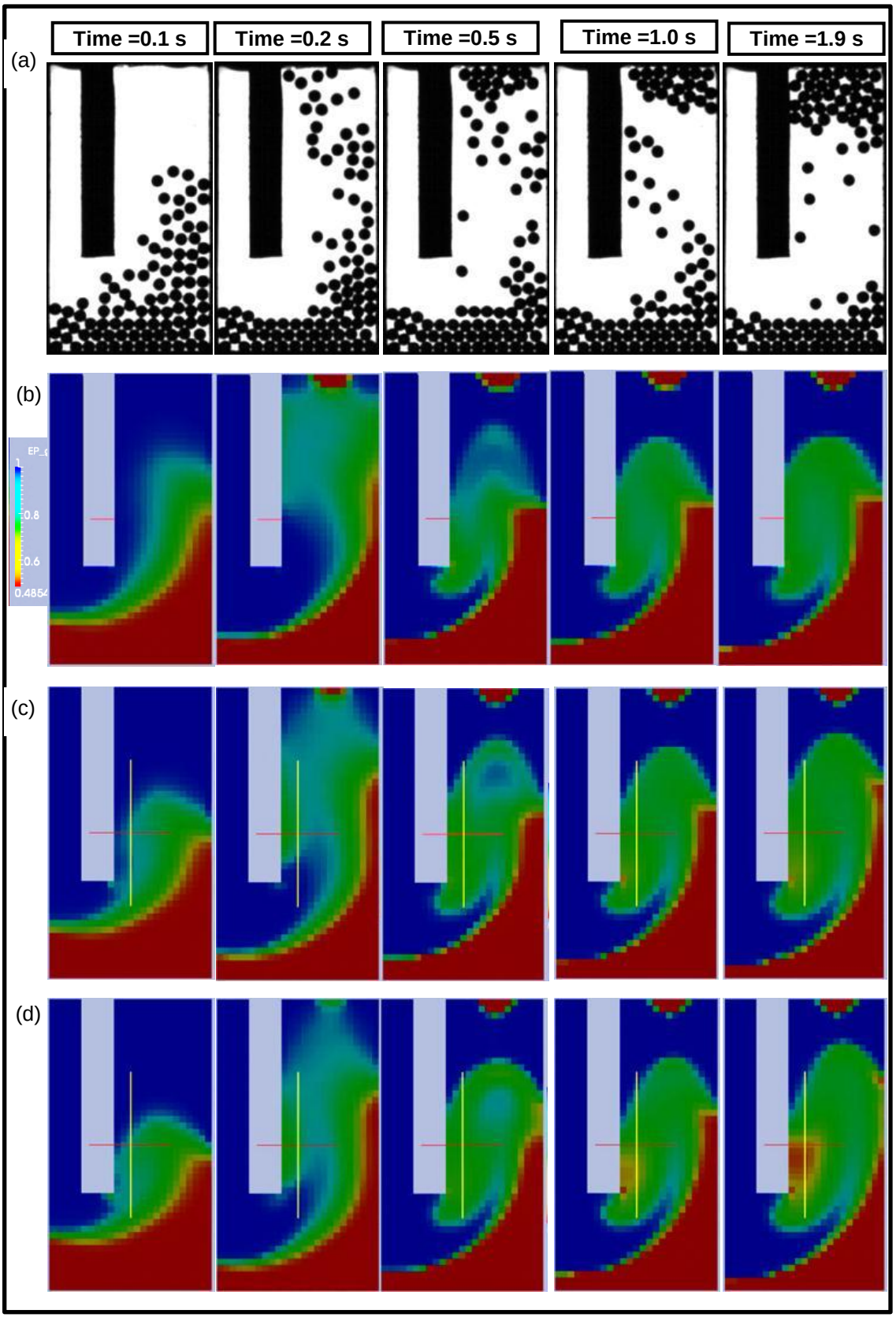

Figure 8-8: Comparison of experimental particles images at different instants in time with numerical void fraction predictions for the specularity coefficient: (a) Experiments, (b) $\phi' = 0.1$, (c) $\phi' = 0.2$, and (d) $\phi' = 0.3$.

Figure 8-9 shows a comparison between the predicted and the measured freeboard void fraction. The predictions follow the same trend of the experiments for a time up to 0.2 s. This corresponds to the initial fluidisation, which is dominated by convection. During this time interval, the void fraction decreases rapidly for the lowest specularity coefficient (0.1), and slightly more slowly for the highest (0.3). The falling of particles from the freeboard region decreases as the specularity coefficient increases. This is clear at time between 0.3-0.35 s where the over-shoot in void fraction curve occurs. This part even becomes negligible at a value of specularity coefficient of 0.3. For the rest of the experimental time (0.4 s to 2.0 s), the predicted void fraction decreases smoothly and follows the average trend of the measured void fraction. However, the measured void fraction oscillates around this average trend, whereas the predicted void fraction decreases monotonically. None of the predictions simulate the fluctuating part in the experiments. It is clear that the specularity coefficient values of 0.2 and 0.3 are slightly better than that of 0.1.

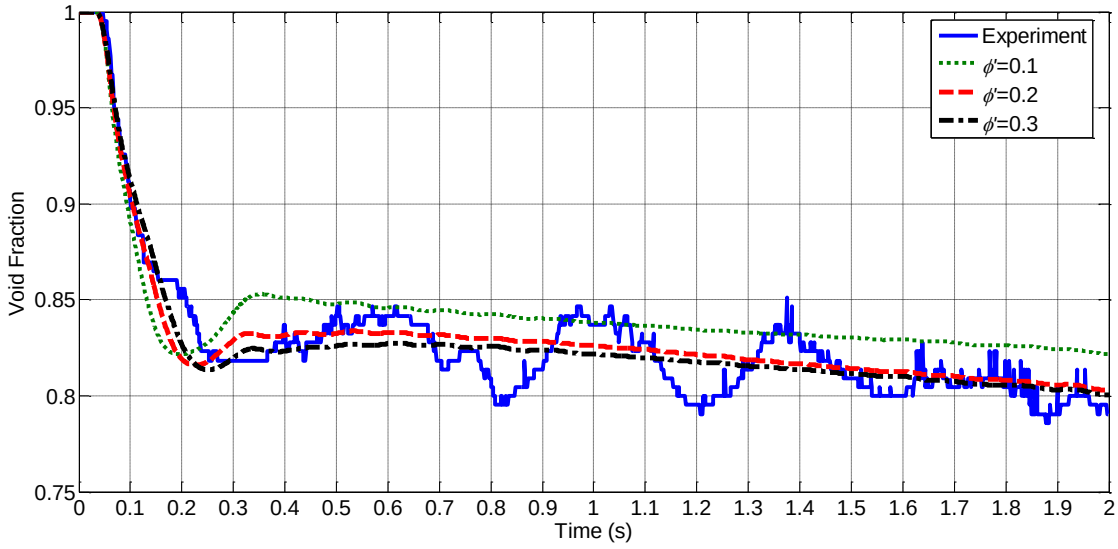

Figure 8-9: Comparison between experiments and numerical predictions of the freeboard average void fraction for the specularity coefficient.

Figure 8-10 and Figure 8-11 show comparisons of the measured and the predicted total vertical and horizontal velocity, respectively. The total vertical velocity shown in Figure 8-10 explains the void fraction profile. For the initial stage of fluidisation, the higher the specularity coefficient the lower the particles

peak velocity (at time around 0.1). This is due to the effect of viscous dissipation at the wall due to the higher friction. The predicted vertical velocity undershoots (at time around 0.25 s) and the magnitudes of this undershoot increases with decreasing specularity coefficient. This undershoot happens because the air cannot support the particles weight. These trends can also be observed in the horizontal velocity shown in Figure 8-11. The fluctuating behaviour noticed in the time range between 0.4 s and 2.0 s is not replicated in any of the predictions.

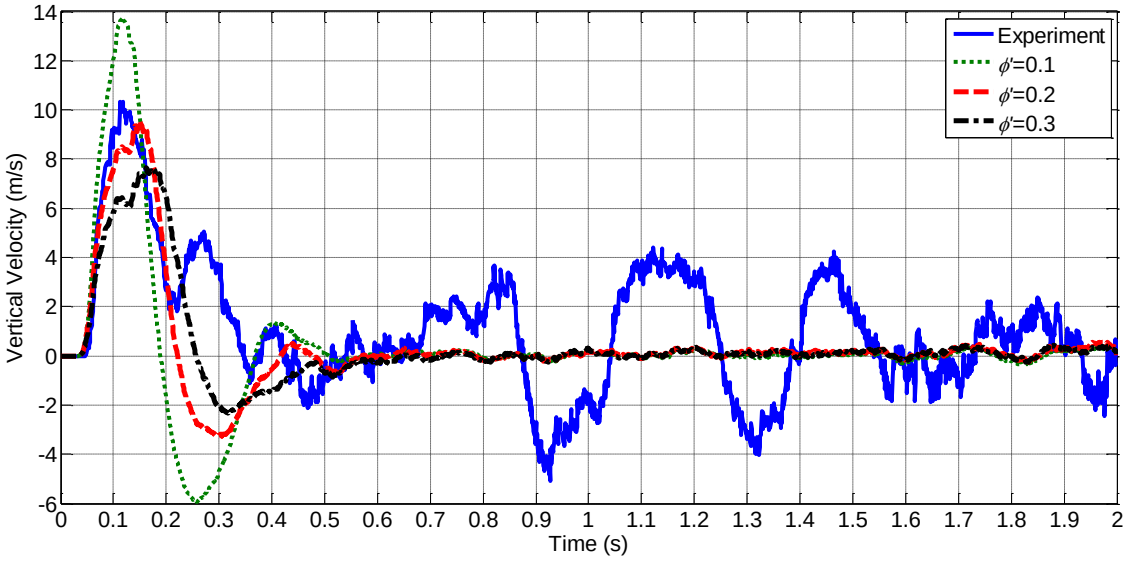

Figure 8-10: Comparison between experiments and numerical predictions of the freeboard total vertical velocity for the specularity coefficient.

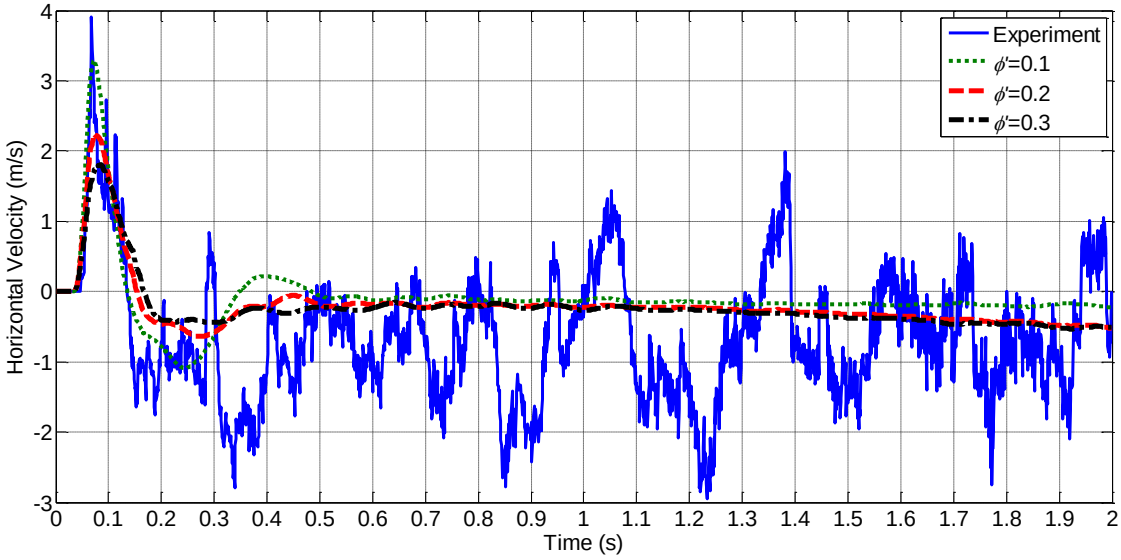

Figure 8-11: Comparison between experiments and numerical predictions of the freeboard total vertical velocity for the specularity coefficient.

Following section 8.2.1, the falling of particles from the freeboard might be understood by looking at Figure 8-12, which shows the inlet air velocity. The trend of the curves is similar for all values of specularity coefficient. The velocity increases from zero until it reaches a peak value of around 40 m/s then it decreases to a value of around 20 m/s. Then the velocity remains constant until the end of the experiment. The main difference between the curves is the duration of the initial peak of the curve. As the specularity coefficient is increased, the predicted inlet velocity maintains its peak for a longer time. This is mainly because fewer particles are entrained to the freeboard when the specularity coefficient is high. Consequently, the exit is not fully blocked with particles in this case, so the pressure losses are lower and the air flow rate remains higher for longer time.

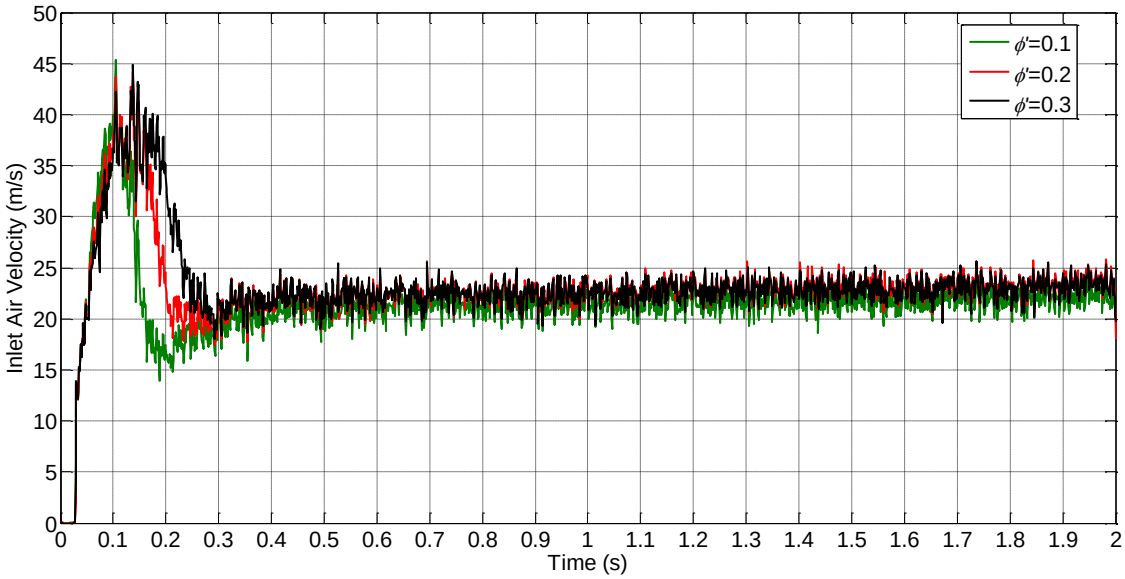

Figure 8-12: Effect of specularity coefficient on inlet air velocity.

It is not very clear which value of specularity coefficient might be considered as the best fit. The predictions using the three values are not very different. However, a value of 0.2 gives slightly better overall agreement especially for the fluidisation behaviour as seen in Figure 8-8. This value will be used in the simulations investigating the effect of other sub-models.

8.2.3 Summary

In this section, the effect of boundary conditions for case two (3 kPa pressure difference) has been studied. Following Chapter 7 results, the NSW under-predicts the particle fluidisation while the FSW over-predicts the particle fluidisation. Using J&J PSW with specularity coefficient of 0.2 gives the best results for the fluidisation process. However, none of the boundary conditions was able to predict the particle clustering at the top of the freeboard region. The fluctuations in granular phase velocity and void fraction in the second stage of flow (from time 0.3 s) were not predicted as well. However, the void fraction results for the FSW and J&J PSW with 0.1 specularity coefficient showed that the particles fall from the freeboard region when the air drag cannot hold them. This behaviour might be regarded as a qualitative replication to the fluctuations noticed in the experiments.

8.3 Effect of Kinetic Theory Sub-models

In this section, the effect of kinetic theory models is investigated. Figure 8-13 shows the comparison between the experimental particle flow images and the void fraction predictions based on 'Lun' model and 'Garzo' model. It is clear that the main qualitative behaviour is similar with some minor differences. Both models do not predict the clustering of particles towards the end of the experiment.

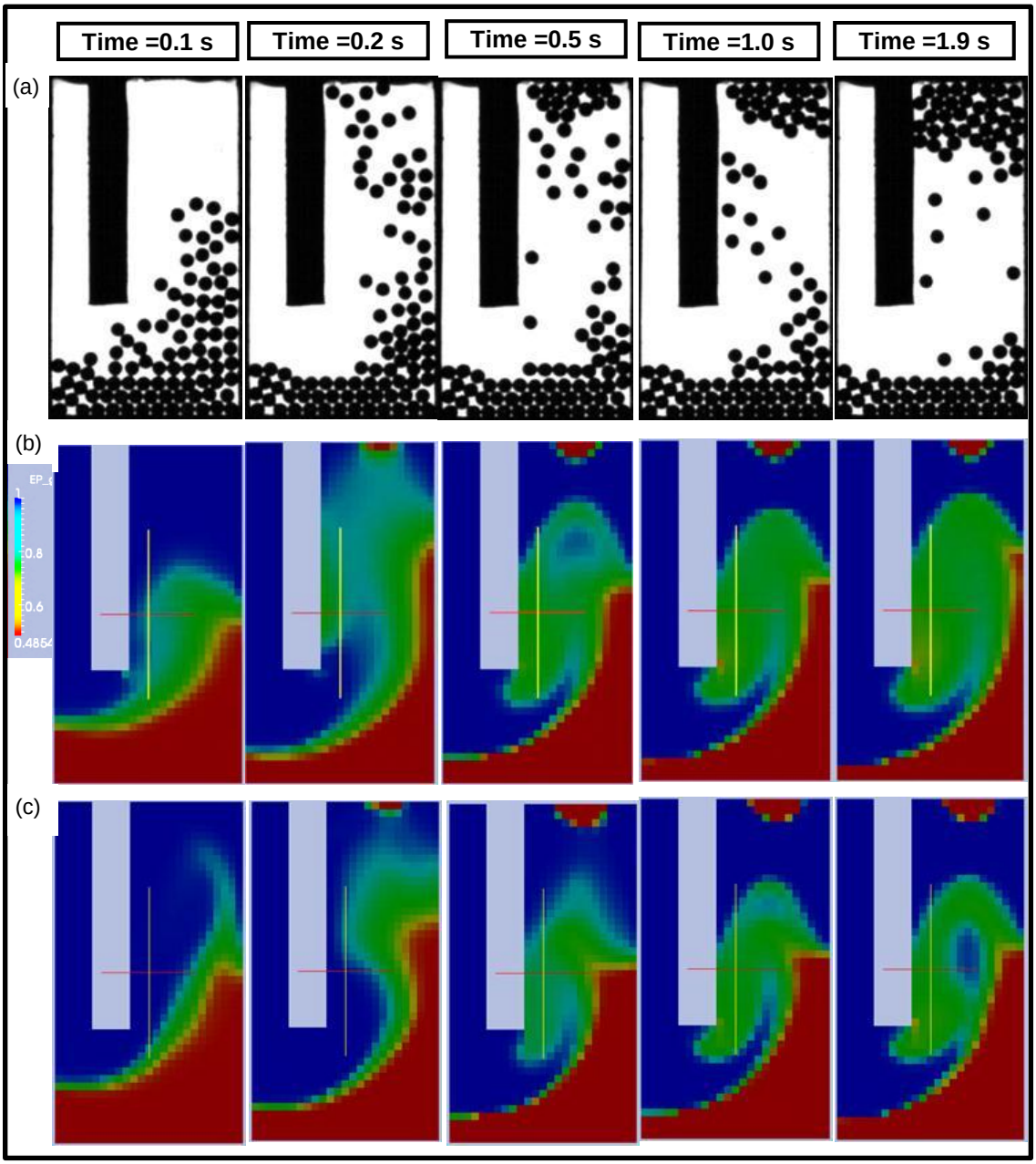

Figure 8-13: Comparison of experimental particles images at different instants in time with numerical void fraction predictions for kinetic theory models: (a) Experiments, (b) Lun, and (c) Garzo.

Figure 8-14, Figure 8-15 and Figure 8-16 show the average void fraction, total vertical and horizontal velocities, respectively. There are some minor discrepancies between the two models. Lun model predicts the void fraction slightly better. However, the two models cannot predict the fluctuation in the average void fraction and total velocities.

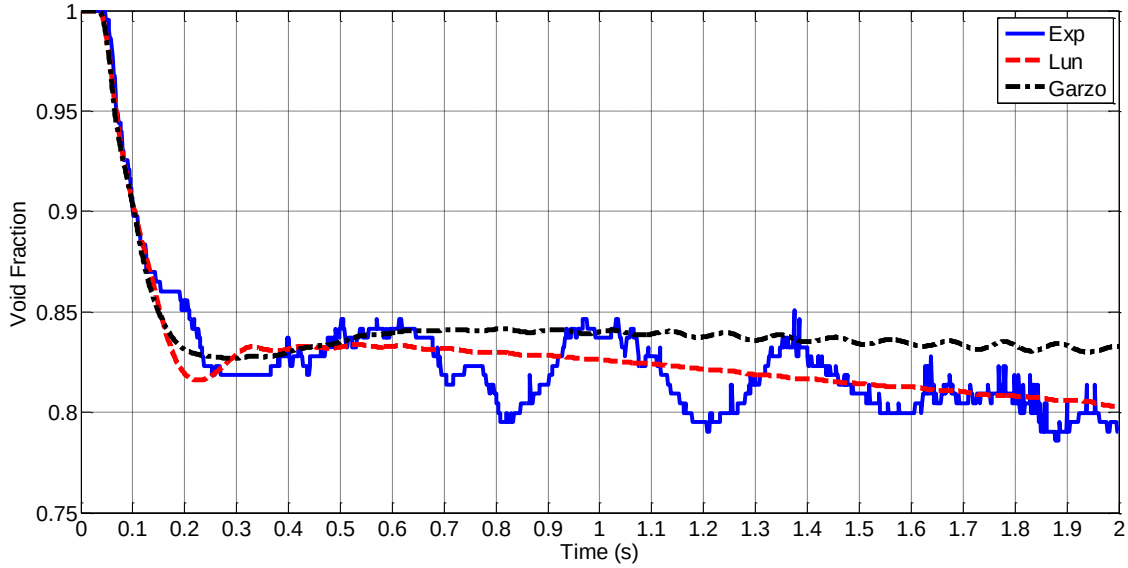

Figure 8-14: Comparison between experiments and numerical prediction of the freeboard average void fraction for the kinetic theory models.

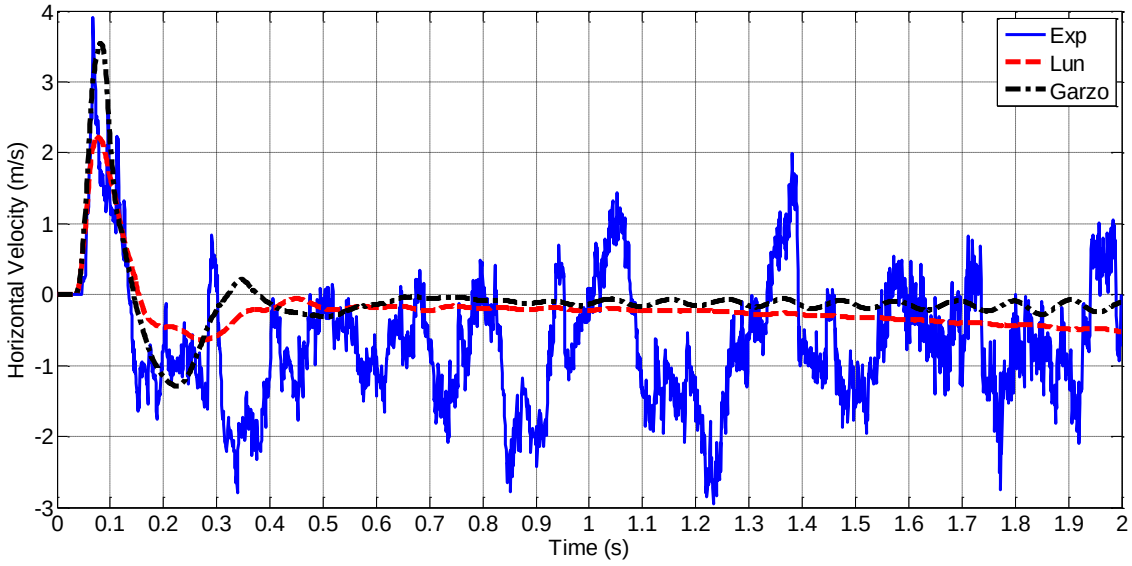

Figure 8-15: Comparison between experiments and numerical prediction of the freeboard total horizontal velocity for the kinetic theory models.

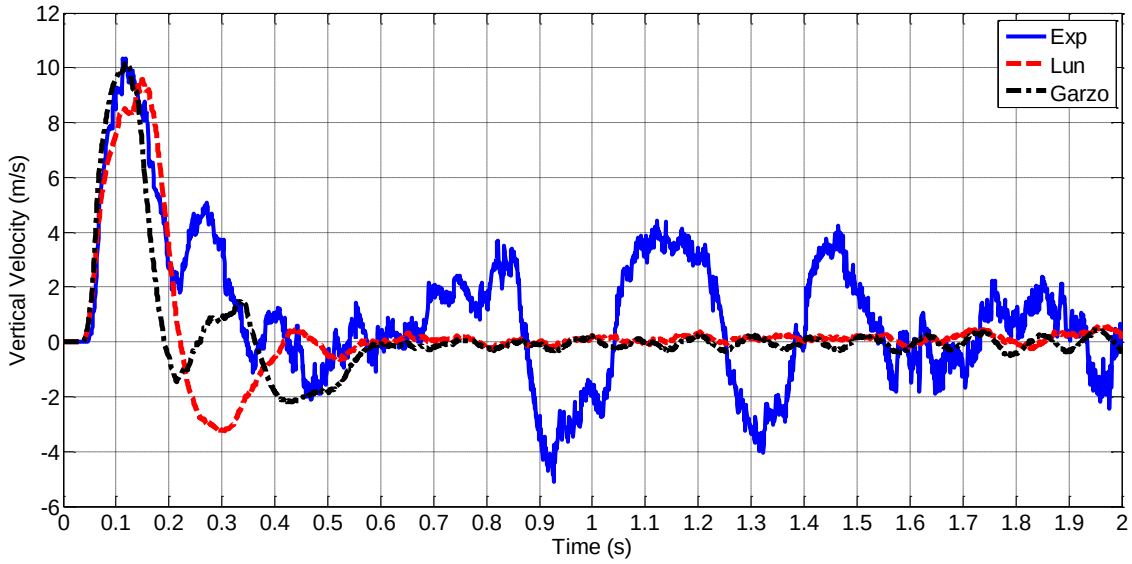

Figure 8-16: Comparison between experiments and numerical prediction of the freeboard total vertical velocity for the kinetic theory models.

8.4 Discussion

The comparison between the predictions and the measurements shows that the model is capable of predicting the particle flow for the early part of the fluidisation, but the model fails to predict the particle flow behaviour at later times. The experiments show fluctuating behaviour of the void fraction and total velocities, while the predictions show smooth trends. Furthermore, the particles in the experiments tend to cluster at the top of the freeboard region at the end of the experiment. This behaviour also does not happen in the simulations. Now we aim to discuss those two types of discrepancies: fluctuations and clustering.

One of the main findings of Chapter 5, where the experiments for this flow case were analysed, is that there is a lack of separation between the micro and macro scales. The inter-particle collisions happen on a similar time scale as that of the convective motion. This means that the continuum description based on the kinetic theory is problematic. Consequently, the simulations based on the kinetic theory might predict different behaviour. This lack of scale separation mainly results in other mechanisms of inter-particle interactions compared to those assumed by the kinetic theory. These inter-particle interactions are described using the viscosity and pressure. The particle

velocity vectors showed that collisions do not happen in all the images though they are important in some frames. On the other hand, the kinetic theory predictions shown in the previous sections assume an extreme case. The assumption of the kinetic theory is that many collisions happen on a very short time scale. In other words, the collisions that occur in the experiments are less than those assumed by the kinetic theory. This might lead to the over-prediction of the diffusion and pressure terms. Accordingly, it would be useful to compare the experiments with another extreme case of no inter-particle interactions. This is done in MFIX by setting the granular pressure and the granular viscous terms to zero. Comparisons between the experiments and non-viscous interactions are shown in Figure 8-17 for the void fraction distribution. The average void fraction of the freeboard region is shown in Figure 8-18, while the total horizontal and the vertical velocities over the freeboard region are shown in Figure 8-19 and Figure 8-20, respectively.

The void fraction distribution in Figure 8-17 shows that the clustering present in the experiment is not predicted by the model. In Figure 8-18, the predicted average void fraction in the freeboard shows fluctuating behaviour which replicates the experiments qualitatively. This indicates that the particles keep circulating in the domain in the non-viscous predictions. This is further confirmed by the total horizontal and vertical velocities shown in Figure 8-19 and Figure 8-20, respectively. However, there is no quantitative matching between the experiments and the simulations for both the void fraction and total velocity components. The predicted fluctuations in the void fraction and total velocity have much higher amplitude when compared to the experiments. The main cause for this relatively high amplitude of fluctuation is the removal of friction forces in the non-viscous model. The friction forces between the particles and the walls exert a dissipative force, whose direction is opposite to the solid phase motion, and hence reduces the upward acceleration of the particles. The over-prediction of total velocities when the wall friction is not taken into account appears in the FSW prediction (sections 7.2.1. and 8.2.1) as well.

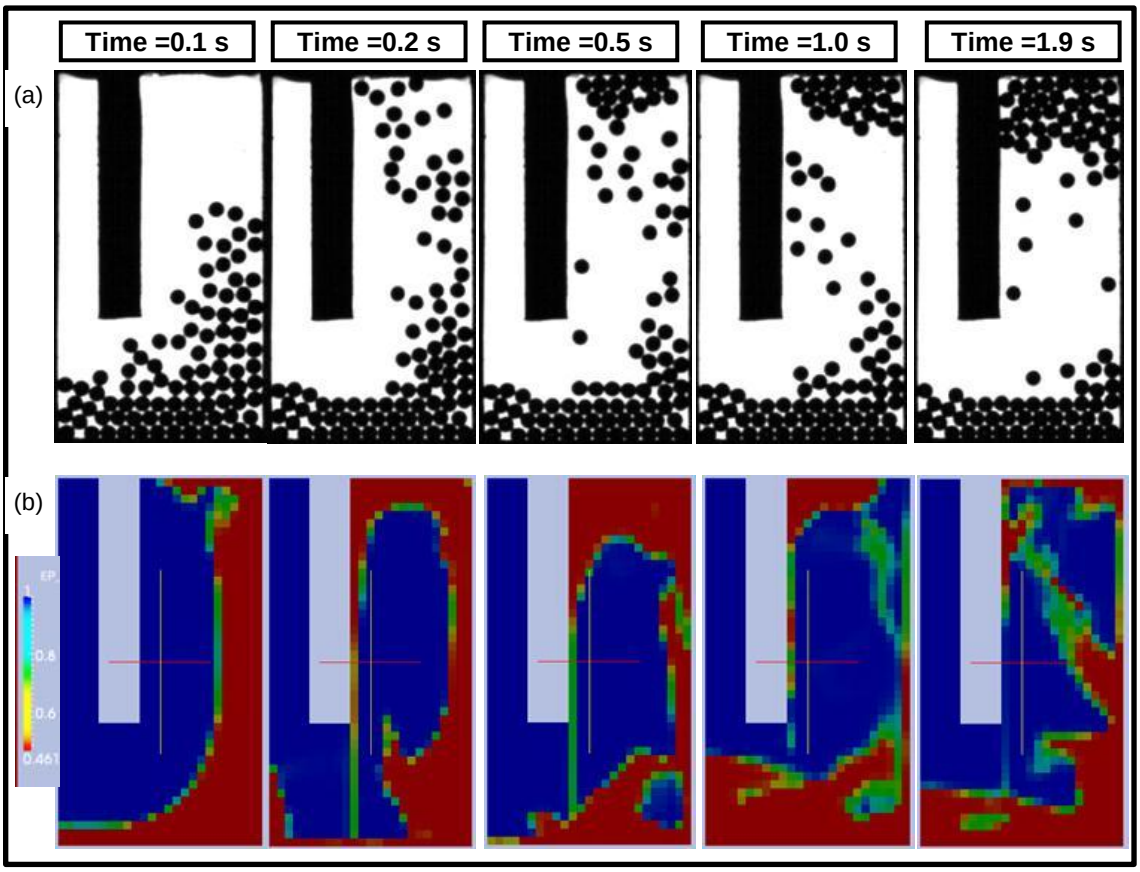

Figure 8-17: Comparison of experimental particles images at different instants in time with numerical void fraction predictions: (a) Experiments and (b) Non-viscous predictions.

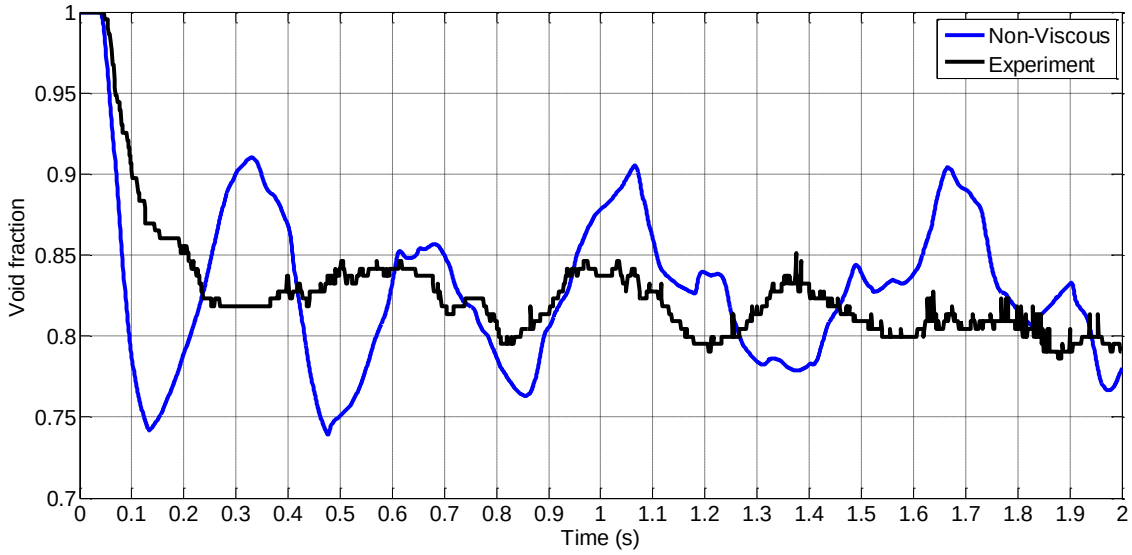

Figure 8-18: Comparison between experiments and non-viscous numerical predictions for the freeboard average void fraction.

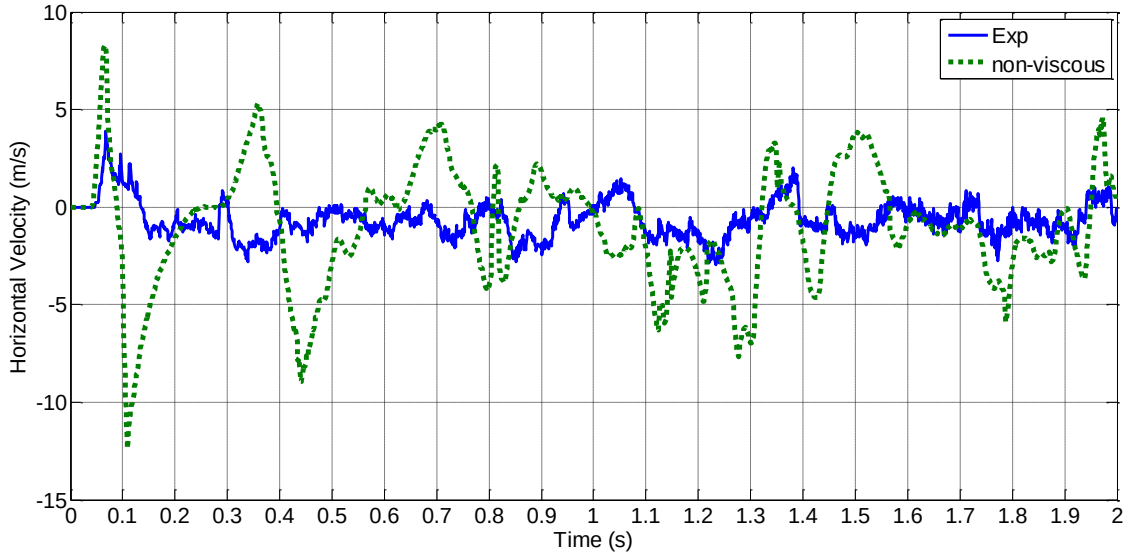

Figure 8-19: Comparison between experiments and non-viscous numerical predictions for the freeboard total horizontal velocity.

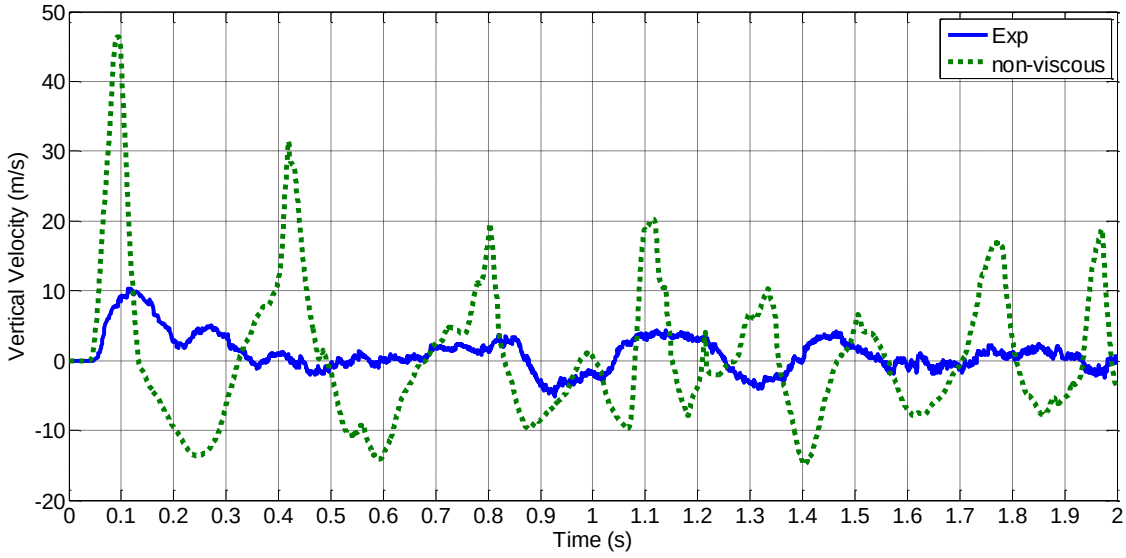

Figure 8-20: Comparison between experiments and non-viscous numerical predictions for the freeboard total vertical velocity.

Qualitatively, the fluctuating behaviour seen in the non-viscous simulations compared to the viscous simulations (sections 8.2. and 8.3.) is expected. This behaviour was seen in Chapter 7 for the high pressure difference case. It is traced to the lack of viscous forces which means that the bulk velocity is not dissipated or damped. The lack of viscous (inter-particle) forces prevents the particles from holding each other because the stresses are not transmitted

within the granular assembly and hence promotes their fluctuating behaviour when the ratio between the weight and the drag keeps changing.

The failure of the non-viscous model to predict clustering may be traced to the lack of clustering promoting dissipative mechanisms in that model. Due to the removal of friction and inter-particle forces from the non-viscous model, the bulk velocity is neither transformed to granular temperature (fluctuating velocity of individual particles in rapid regime) nor dissipated due to friction (in slow regime or due to friction with walls). Consequently, the particle will keep moving and circulating in the domain for infinite time. These dissipative mechanisms (such as friction and inelastic collisions) are responsible for clustering in the experiments (Chapter 5).

The results of non-viscous simulations can help in providing a reasonable explanation for the discrepancy between the viscous simulations and the experiments. The discrepancy emerges from the failure of the viscous model to predict the fluctuations and the clustering in the experiments. The lack of fluctuations in the total velocity and void fraction noticed in the viscous model predictions (sections 8.2 and 8.3) is probably due to over-predicting the diffusion or viscous forces. The high viscous forces prevent the emergence of fluctuations in the total velocity by damping or dissipating these fluctuations very quickly. These fluctuations are damped by viscous forces quicker than the experiments because of the scale separation issue. In the viscous simulations (KTGF based), the inter-particle collisions happen on a very small time scale compared to the macroscopic bulk velocity. In the experiments, this scale separation does not exist and inter-particle collisions happen on a similar time scale compared to the bulk motion of particles. Consequently, the fluctuations in the total velocity take more time to be transformed into granular temperature via inter-particle collisions in the experiments.

The scale separation and lack of fluctuating motion are responsible for not predicting the clustering in the viscous simulations. The fluctuations induced by the lack of scale separation in the experiments do not exist in the viscous simulations. The particles are stagnant and there are no moving particles to be clustered.

Based on the discussion presented in this section, one can state that both viscous and non-viscous models do not capture all the features of the experiments. There are some improvements of the continuum model that can be proposed. Including wall friction in the non-viscous model will help in reducing the amplitude of the fluctuations in the void fraction and total velocities. As suggested in Chapter 7, the wall friction should be implemented as a sink term in the momentum equations of the solid phase. This will make sure that the fluctuating motion of the solid phase seen in the experiments will be replicated with less quantitative discrepancy compared to the non-viscous simulations. However, it is not clear whether these friction terms will help in promoting particle clustering in the experiments. Wall friction is one dissipative mechanism for promoting clustering and there are other inter-particle dissipative interactions, such as inelastic collisions and inter-particle friction. Consequently, inter-particle interaction models need to be implemented in the model. Slow flow regime or higher order (Burnett) viscous models might help in this direction.

8.5 Validation of Case Three

In this section, the model predictions are compared for the third and the final case. This case has the smallest pressure difference between inlet and outlet (1.6 kPa).

Figure 8-21 and Figure 8-22 show the comparison between the predicted void fraction profiles and the particle flow images. The simulations presented were carried out with J&J PSW with two values of specularity coefficient (0.1 and 0.2) and a FSW. The simulation uses the Wen-Yu drag model and Lun kinetic theory model and other simulation parameters are shown in Table 6-1. The effect of friction on the fluidisation is clear in Figure 8-21 with FSW over-predicting the initial phase. Using specularity coefficient of 0.2 gives the best results for the initial phase of fluidisation up to 0.3 s as confirmed by Figure 8-21 .It is clear that there are some discrepancies in the flow between the predictions and the experiment at later time frames shown in Figure 8-22.

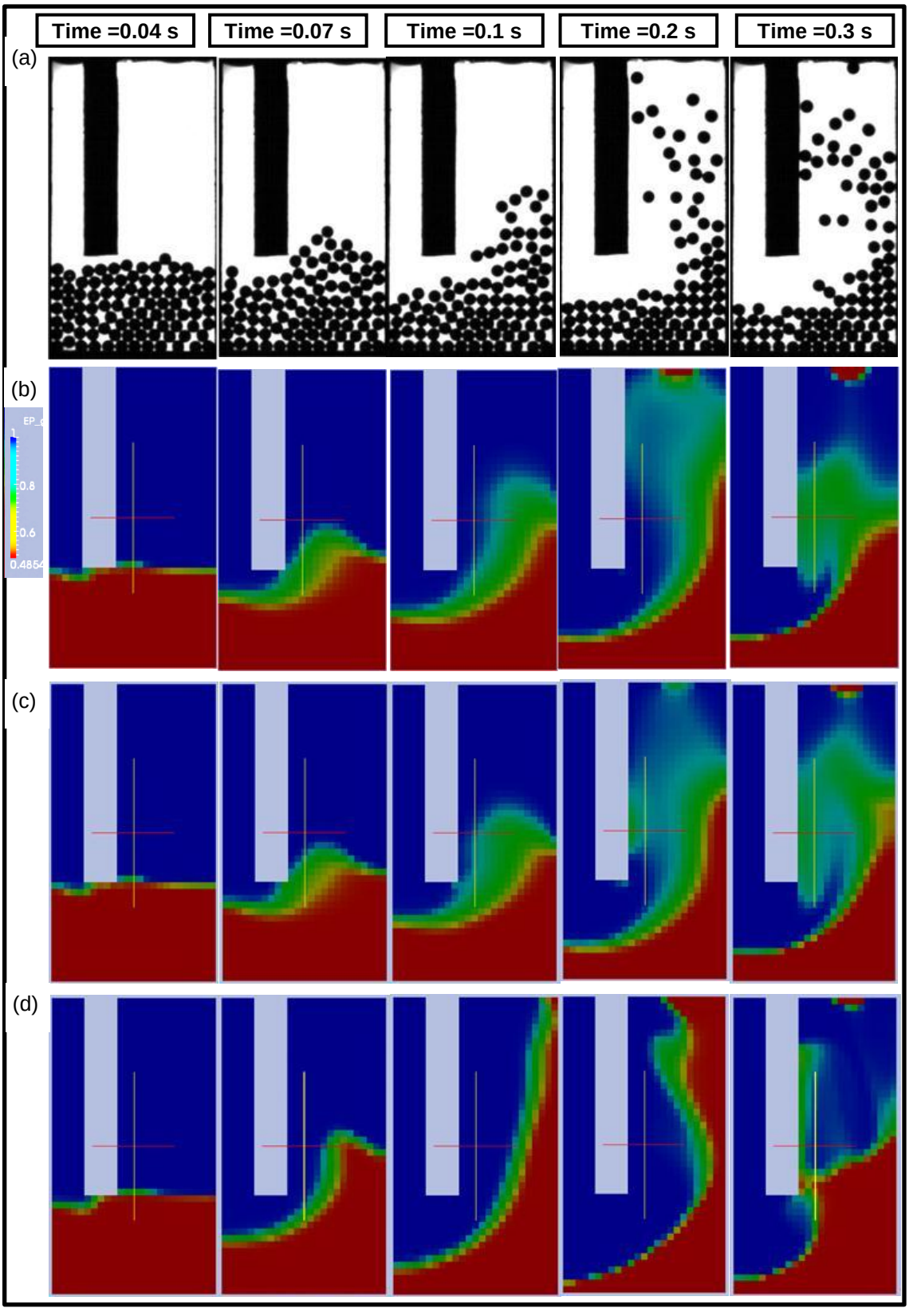

Figure 8-21: Comparison of experimental particles images at early instants in time with numerical void fraction predictions for the wall boundary conditions and the specularity coefficient. (a) Experiments, (b) J&J PSW with ϕ'=0.1, (c) J&J PSW with ϕ'=0.2, and (d) FSW.

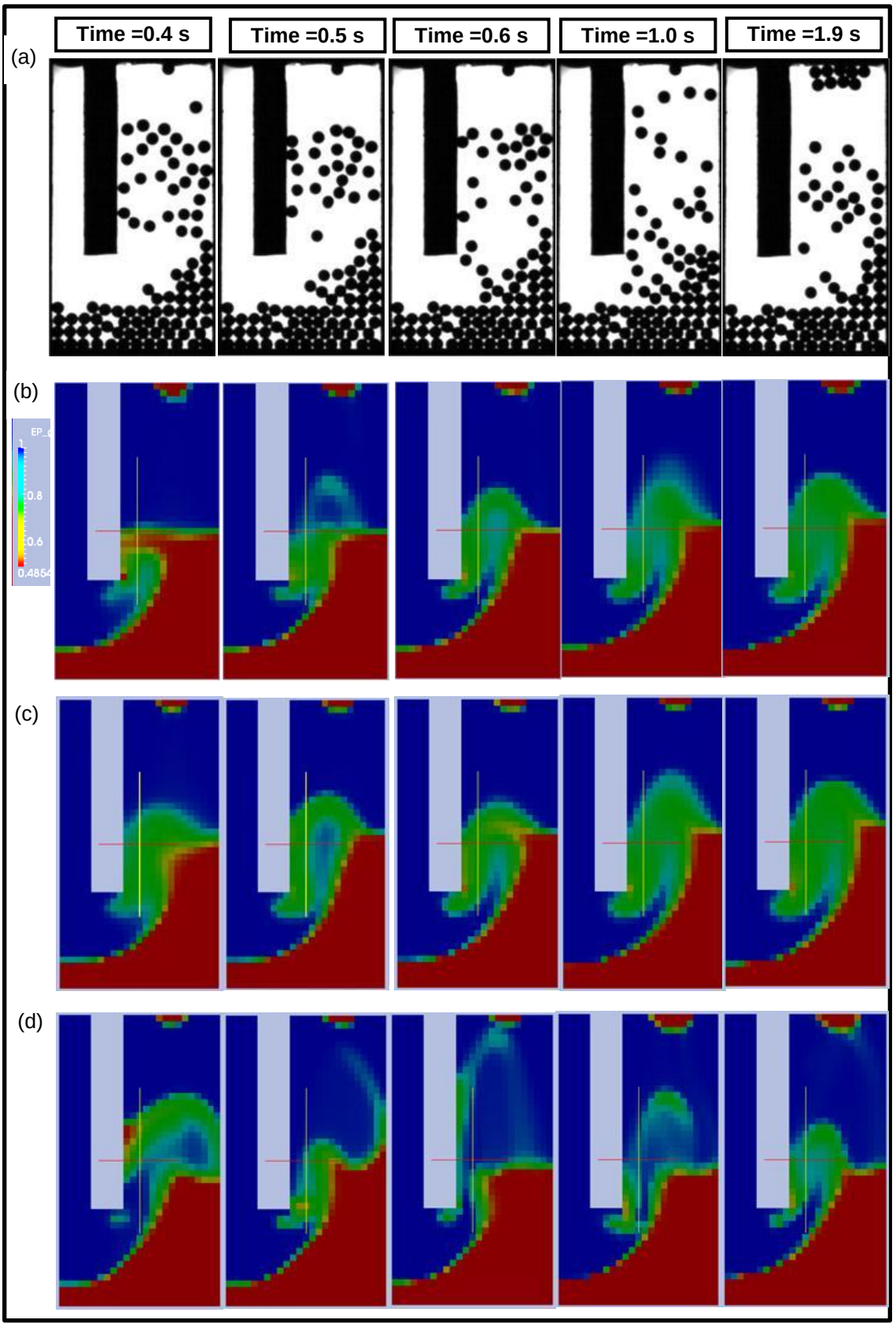

Figure 8-22: Comparison of experimental particles images at late instants in time with numerical void fraction predictions for the wall boundary conditions and the specularity coefficient. (a) Experiments, (b) J&J PSW with ϕ'=0.1, (c) J&J PSW with ϕ'=0.2, and (d) FSW.

Figure 8-23, Figure 8-24 and Figure 8-25 show the void fraction, total vertical and horizontal velocity, respectively. An interesting behaviour noticed is that the FSW replicates qualitatively the fluctuations in the experiments from time 0.3 s. This confirms that lower diffusion drives the simulation to replicate the experiments in the second part. However, reducing the diffusion in this case, where there is no scale separation, will not result in exact replication of the experiments. For example, it has been reported that the shear stress is over-predicted using continuum simulations compared to direct simulations Monte Carlo (DSMC) for rarefied flows (Reese, Gallis and Lockerby, 2003). This is because the continuum simulations based on kinetic theory over-predict collisions and its subsequent diffusion terms.

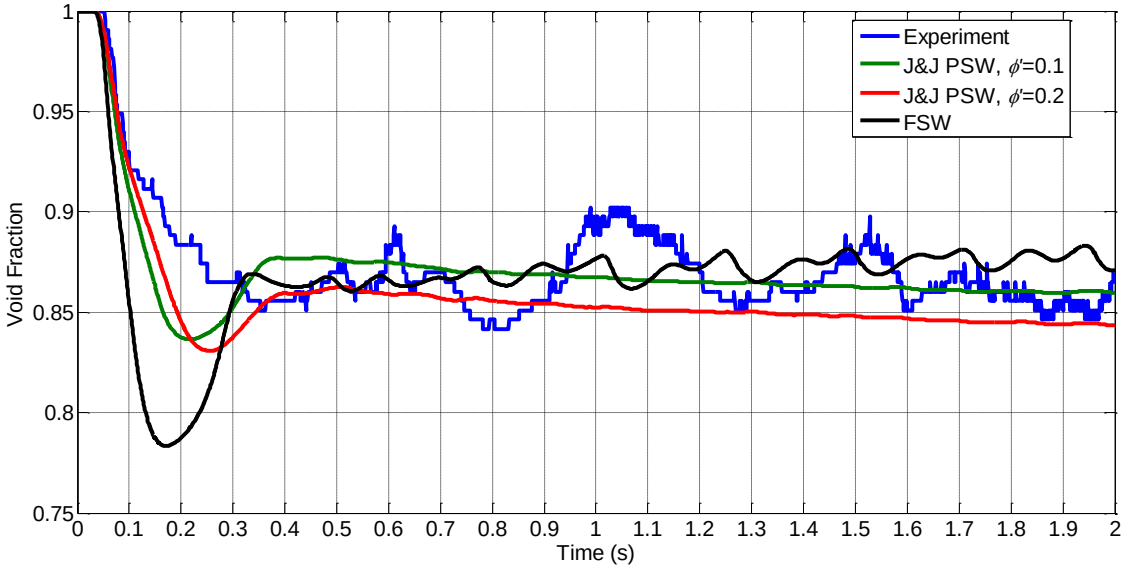

Figure 8-23: Comparison between experiments and numerical predictions of the freeboard average void fraction for the wall boundary conditions and specularity coefficient.

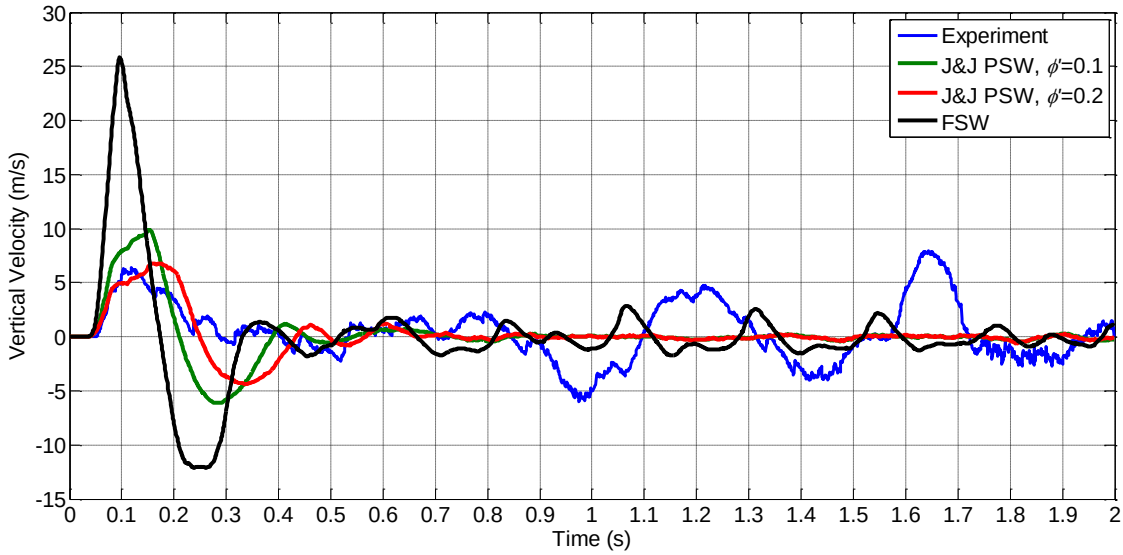

Figure 8-24: Comparison between experiments and numerical predictions of the freeboard total vertical velocity for the wall boundary conditions and specularity coefficient.

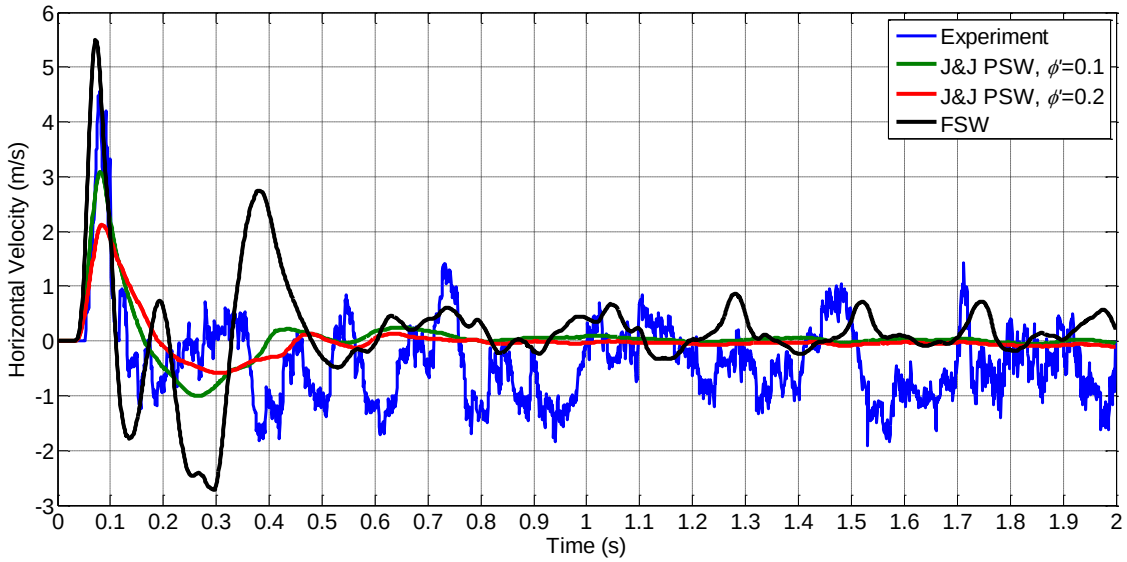

Figure 8-25: Comparison between experiments and numerical predictions of the freeboard total horizontal velocity for the wall boundary conditions and specularity coefficient.

8.6 Summary and Conclusions

In this chapter, the TFM predictions have been compared to the experiments for the second and third flow cases with low pressure differences of 3 kPa and 1.6 kPa, respectively. Both cases showed similar flow behaviour of partial fluidisation regime. The first stage of flow in the second case (3 kPa), which

corresponds to the initial fluidisation and lasts up to 0.2-0.3 s, was predicted by the model. In this stage, the particle flow is dominated by convection. In order to replicate the experiments, the model needs to minimise the diffusion and include the appropriate value of wall friction. This was achieved using J&J PSW boundary condition with specularity coefficient of 0.2. The second stage of flow from 0.3 s onwards was not predicted by the viscous model. The experiments showed fluctuating behaviour of the velocity and the void fraction while the predictions showed smooth trends. Furthermore, the clustering of particles, which happens towards the end of the experiment, was not replicated in the simulations. The lack of fluctuations in the viscous model is due to the over-prediction of the diffusion terms by the kinetic theory. Non-viscous simulations showed that the fluctuations appear due to the removal of diffusion terms. However the fluctuations in void fraction and total velocity, predicted by the non-viscous model, were not in quantitative agreement with the experiments. Furthermore, the clustering which happens towards the end of the experiment was not predicted by the non-viscous model. This suggests that neither the viscous nor the non-viscous model can fully capture the granular flow physics in the second stage of flow. This is mainly due to the lack of separation between the micro and macro particle scales in the experiments. The collision rates are higher in the viscous models than the experiments, while those collisions are completely neglected in the non-viscous model. Furthermore, the dissipative mechanisms are strong in the viscous models which lead to early dissipation of fluctuations and the clustering is not fully predicted. While in the non-viscous model, the dissipation is not present which leads to no clustering.

Chapter 9 : Conclusions and Recommendations for Future Work

9.1 Summary of Conclusions

The main aim of this thesis was to develop an understanding of the multiphase flow in DPI. Experimental and computational approaches were employed to study the fluidisation and the dense multiphase flow of solid particles using an impinging air jet. The experimental approach was based on high speed photography, while the computational approach was based on the continuum TFM. The inter-particle interactions in the TFM are described using two regimes: rapid and slow. The former is based on the kinetic theory of granular flow models, while the latter is based on the phenomenological models of soil mechanics.

The experimental technique involved a two-dimensional test section to detect and track 3.85 mm granular particles. This technique generates micro or particle scale results, thus allowing detailed description of particulate phase flow and detailed validation of numerical models. Three cases of flow were studied experimentally resulting into two fluidisation regimes. The main independent variable was the air pressure difference. Consequently, the inlet air flow rate was different between the three cases.

The first case (chapter 4), whose pressure difference was 16 kPa, resulted in full fluidisation of the particle bed. The fluidisation pattern was characterised by strong convective flow with no evidence of diffusion triggered by inter-particle collisions. This aggregate fluidisation happened very quickly and the whole bed was picked up after 0.25 s of the experiment. The strong drag force caused this behaviour and packed the particles at the top of the flow domain. Particle velocity vectors showed that the particle diffusive behaviour associated with Brownian or vibrating motion does not exist. This suggests that the kinetic theory based models might not capture the mechanics of inter-particle interactions. However, the particles convective motion, which results from the

air drag, is captured in the continuum models, and hence the TFM should reduce the diffusion contribution in order to replicate the experiments.

In order to investigate the repeatability of the experiments, the experiment was performed five times with nearly similar initial and boundary conditions. The ensemble average of the void fraction showed good repeatability with maximum standard deviation of around 3%. However, the total particle velocity showed higher standard deviation up to 30%. This was traced to the differences in the velocities of the individual experiments within the ensemble. Variations of particle and wall surface properties and initial and boundary conditions within the ensemble are the main causes of these differences within the ensemble.

The second flow case (Chapter 5) used an air pressure difference of around 3 kPa with an experimental time of 2 s. This low pressure difference caused a weak air jet. This jet was not able to fluidise the whole bed and around half of the particles moved to the freeboard region above the initial particle bed. The study of this partial fluidisation regime revealed that the movement of the particles undergoes through two stages. The first stage is the initial fluidisation of the bed which is dominated by convection in a similar fashion to case one. There was no evidence that diffusive motion occurs during this phase which ends at time between 0.2 s and 0.3 s. The second stage of flow occurs when the fluidised particles move in the freeboard region randomly. In this stage, different types of particle motion took place; the particles exhibited both convective and collisional motion. Particle velocity vectors showed that the collisional motion interacts with the convective motion and the time scale of collisions is of the same order of magnitude as the convective motion. This suggests that the flow lacks the separation between the micro and macro scales, which means that the kinetic theory based description of this regime is problematic. During the second phase of the flow, the particles exhibited fluctuating motion which appeared in the average void fraction and total velocity of the freeboard region. This means that the net forces on the granular phase keep changing during this stage. Furthermore, particles cluster at the top of the freeboard increases with time due to some dissipative mechanisms such as particle-wall, particle-particle friction and inelastic collisions.

Despite exhibiting the same qualitative fluctuating motion, the experiments within the ensemble were not replicated exactly with relatively high standard deviation up to 40% for the total velocity. A third case with pressure difference around 1.6 kPa was studied. The results of this case showed partial fluidisation and similar flow regimes and behaviour as the 3 kPa case.

The Two Fluid Model used in this thesis requires the specification of different sub-models. They include the drag models, the kinetic theory models and wall boundary conditions models. The computational study considered these sub-models in detail. The flow cases studied in the experiments were studied computationally using the same initial and boundary conditions.

For case one with high pressure difference (Chapter 7), the level of agreement between the computational predictions and the measurements depends on the sub-models used, but it is generally good. For the wall boundary condition, NSW under-predicted the particle fluidisation due to the high shear stress exerted by the wall on the granular bed. The FSW over-predicted the fluidisation timing because of the zero shear stress exerted by the walls. Using J&J PSW adjusted the predictions of average void fraction depending on the value of specularity coefficient. The best agreement with the experiments was obtained using a specularity coefficient whose value is 0.1. However, the dispersion of the solid particles increases as the specularity coefficient increases. This behaviour results in more homogenous fluidisation in the predictions in contrast to the aggregative fluidisation noticed in the experiments and FSW predictions. This qualitative discrepancy in the fluidisation profiles was traced to the granular heating caused by the viscous dissipation. The shear stress exerted by the wall on the granular phase increases the granular temperature resulting in higher diffusion-convection ratio, as confirmed by average Mach number profiles. A boundary condition, which is capable of including the friction without invoking granular heating, might cure both types of discrepancies: dispersion in PSW and over-prediction of the fluidisation in FSW. The study of the kinetic theory models confirmed that the diffusion should be minimised in order to replicate the aggregative fluidisation. Garzo model, which predicted more dissipation of the granular temperature, was in better qualitative

agreement than Lun model. The study of the drag models showed that their predictions were nearly identical.

For case two of low pressure difference (3 kPa), the predictions of the model were not as good as case one. Although the model predicted the initial fluidisation fairly well, its prediction for the second stage was worse. The first stage is dominated by convection which is similar to case one. On the other hand, the particle flow in the second stage is more complicated with both collisional and convective motion taking place on the same time and length scales. The fluctuations in the void fraction and granular velocity were not predicted using kinetic theory based models. However, the results of TFM without including inter-particle collisions replicated the fluctuations qualitatively. This showed that the kinetic theory based models over-predict the diffusion which damps the fluctuations. Neither the viscous nor the non-viscous model predicted the particle clustering noticed at the end of the experiments. This is due to the difference in both the dissipation and inter-particle collision mechanisms between the continuum model and the experimental approach. The computational results of case three with lower pressure difference of 1.6 kPa confirmed that the diffusion damps the fluctuations. The FSW predicted fluctuations in the void fraction and granular velocity profiles, because the FSW induces less shear stress on the granular phase resulting in less diffusion.

The results presented in this thesis showed that the continuum based approach can predict the high speed particle flow relevant to particle flow in DPIs and this approach is promising for modelling real DPIs. Regarding the fundamentals of multiphase flow modelling, the continuum approach predicted some of the flow situations while failing at others. Furthermore, within one flow situation the hydrodynamic model predicted the flow correctly for certain spatial or temporal range and failed at others. This shows that continuum granular models need further development in order to capture general multiphase flows.

9.2 Recommendations for Future Work

The findings of this thesis suggest possible future work for both the applications related to DPIs modelling and the fundamentals concerning the hydrodynamic modelling of granular and multiphase solid-gas flow.

9.2.1 DPIs Hydrodynamic Modelling

In this thesis, the multiphase flow system, used as a prototype for the inhaler, deviates from the real inhalers. Real DPIs have smaller size and the particles used are smaller with different physical properties. The powder type used in real inhalers has higher inter-particle cohesive and friction forces. However, the TFM results of the present study are promising and present a good starting point towards modelling real inhalers.

In order to predict the high speed particle flow in real DPIs, some modifications of the TFM are needed. The high speed flow of granular phase showed that convection is the main flow mechanism with lower effects of diffusion. Moreover, it is likely that the kinetic theory effects will be further reduced when the cohesive forces are taken into account and the inter-particle friction is higher. Consequently, the kinetic theory relations describing the viscous and pressure terms should be removed from the equations. However, the terms for the slow or quasi static regime need to be included in order simulate the powder flow beyond the critical packing fraction. Further terms describing the cohesive forces should be added to the granular pressure and viscous components. For the powder contact with the wall, there is a need for wall boundary condition which includes friction. This boundary condition should be implemented as a sink term in the momentum equations. Further developments include exporting the exact air flow profile in the inhaler to be used as a boundary condition.

9.2.2 Fundamentals of Granular Multiphase Flow

Despite studying the multiphase flow in an impinging air jet configuration, the methodology and the analysis used in this thesis can be extended to other multiphase solid-gas flow devices or processes. Using TFM for real applications requires fundamental understanding of particle-particle and particle-wall interactions. For the collisional regime, KTGF has been employed for this task so far. However, there are fundamental challenges regarding the validity of applying KTGF to some flow situations. The main challenge is the validity of the assumption of micro and macro scale separation. If this assumption is not satisfied, the model will not be consistent. However, this potential physical

inconsistency in the continuum model does not mean that the numerical results are wrong for all flow situations. For example, if the convection is very high compared to the diffusion, the value of the kinetic theory terms will not be significant. Consequently, direct computations of individual terms in the transport equations, such as the viscous, drag and weight terms; will show the relative importance of the inter-particle collisions for a certain flow configuration. Another assumption which is incorporated in the continuum granular models is the division of the granular flow regimes into rapid and slow. This assumption needs rigorous testing for better understanding of the physics of granular flow.

In order to test the validity of continuum granular flow theories or models, the TFM predictions need to be compared with particle scale flow data. There are some complexities associated with experimental measurements of practical granular flow on the particle scale as described in this thesis. Using simple experiments to avoid those complexities might change the flow behaviour. One example of the simplifications is using large particles and two-dimensional test section as done in this thesis. The two-dimensional test section increases the particle wall friction though it is not a significant problem when incorporating appropriate wall-friction models in the simulations. The large particles compared to the domain size increases the statistical fluctuations within the experiments. Consequently, smaller particles might be used in the two-dimensional optical technique. The repeatability of the experiments needs improvements in order to perform quantitative comparison with the predictions. This includes total control over both the initial and boundary condition such as inlet and outlet air pressure and initial particle configuration. In general, innovative experimental approaches are needed to measure the behaviour of granular flow on the particle scale. This includes avoiding the opaque nature in the three-dimensional granular flow, and accurate algorithms for particle detection and tracking.

Due to the complexities associated with particle scale measurements, particle scale computational approaches, such as DEM or molecular dynamics simulations, can be used to validate the continuum models. One advantage of using DEM is that the validity of continuum models can be investigated, while using similar sub-models and particle properties. For example, the values of

both restitution and friction coefficients will be the same in both models: TFM and DEM. Consequently, inherent uncertainties in measuring those coefficients experimentally will be avoided. Moreover, using the hard sphere model in conjunction with DEM ensures that particle-particle interactions are resolved with the same approach as the kinetic theory models.

Particle scale measurements or simulations produce huge amount of data describing temporal and spatial variations of individual particles. On the other hand, continuum models describe collective granular behaviour over averaged spatial and temporal increments. Consequently, data analysis techniques are crucial to link the two scales: particle or micro scale, and collective or macro scale. The obvious example of the analysis techniques is the one employed in the kinetic theory to distinguish between the convective and diffusive motions for a collection of particles. However, this approach implies that the assumptions of the kinetic theory are satisfied; the averaging length scale is larger than the mean free path and smaller than the spatial variations in the flow variables, and the averaging time scale is larger than the mean free time and smaller than the temporal variations of the flow variables. The temporal and spatial averaging implies that the micro and macro scales of particle flow are fully separated, which might not happen in many flow situations especially in transient or unsteady flow. Some field variables such as granular temperature, generated by the previous averaging process, might be irrelevant.

The findings of this thesis suggest that current continuum models are by no means complete; they can predict the particle flow in certain cases while failing in others. Consequently, DEM might be used for predicting the flow situation or regions in which the continuum approach fails. The development of hybrid models including both DEM and hydrodynamic approaches can address the two requirements for applying CFD in industrial setting: accuracy and computational time. However, those models need efficient and robust computational methods and algorithms which is a potential area of research. In this context, granular and multiphase flow can either benefit from, or contribute to, other multi-scale flow applications such as turbulent, non-equilibrium and micro flows.

Appendix A: CAD Drawings for the Experimental Test Section

The test section used in Chapter 3 consists of:

1- Aluminium main body (Figure A-1, A-2)
2- Front covering Perspex sheet which contains the pressure transducer holes (Figure A-3)
3- Rear covering Perspex sheet (Figure A-4)
4- Adapter for the transducer (Figure A-5)
5- Two sealing gaskets (Figure A-6)

The following are the drawing of each of those components:

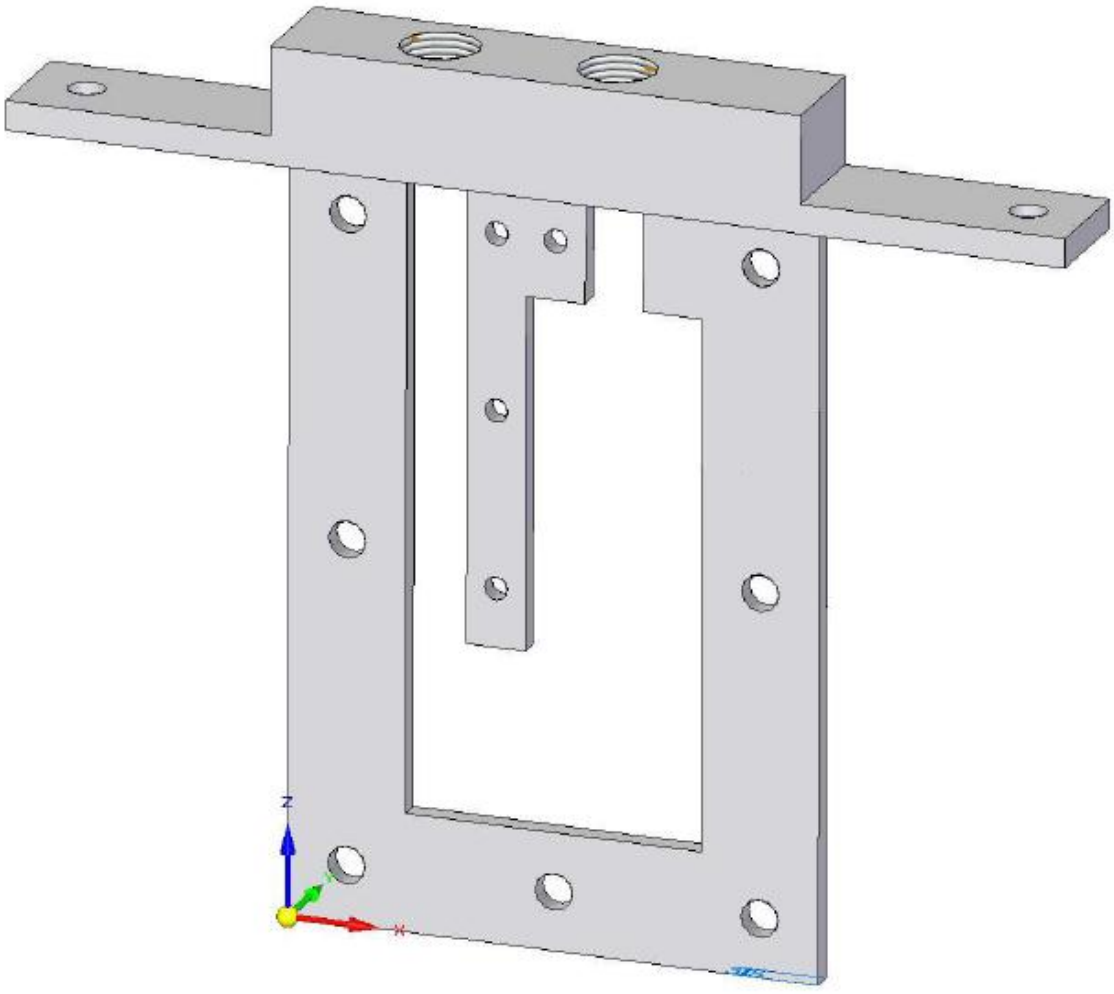

Figure A-1: 3D drawing of the main aluminium body.

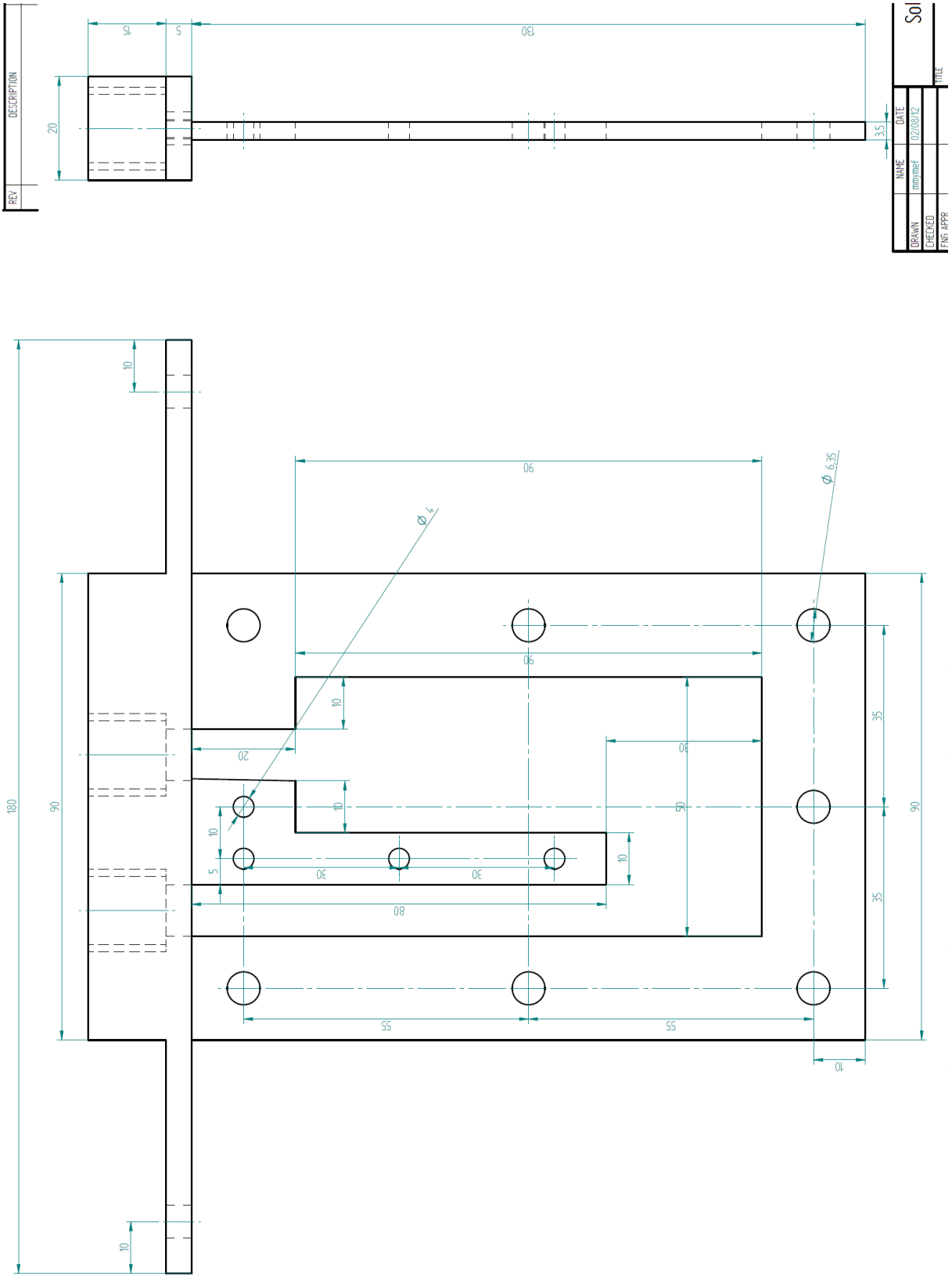

Figure A-2: CAD drawing of the main aluminium body.

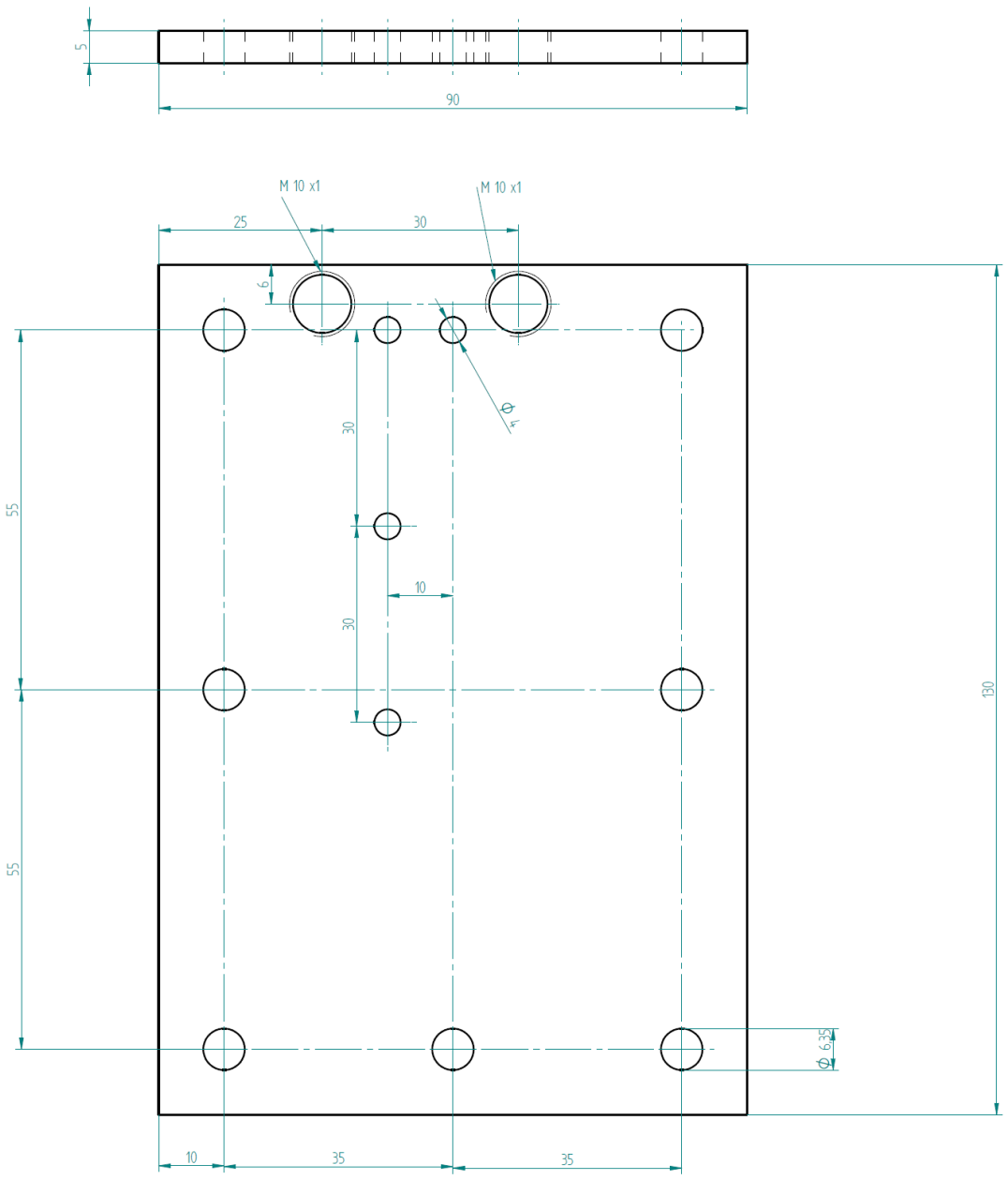

Figure A-3: CAD drawing of the front Perspex sheet.

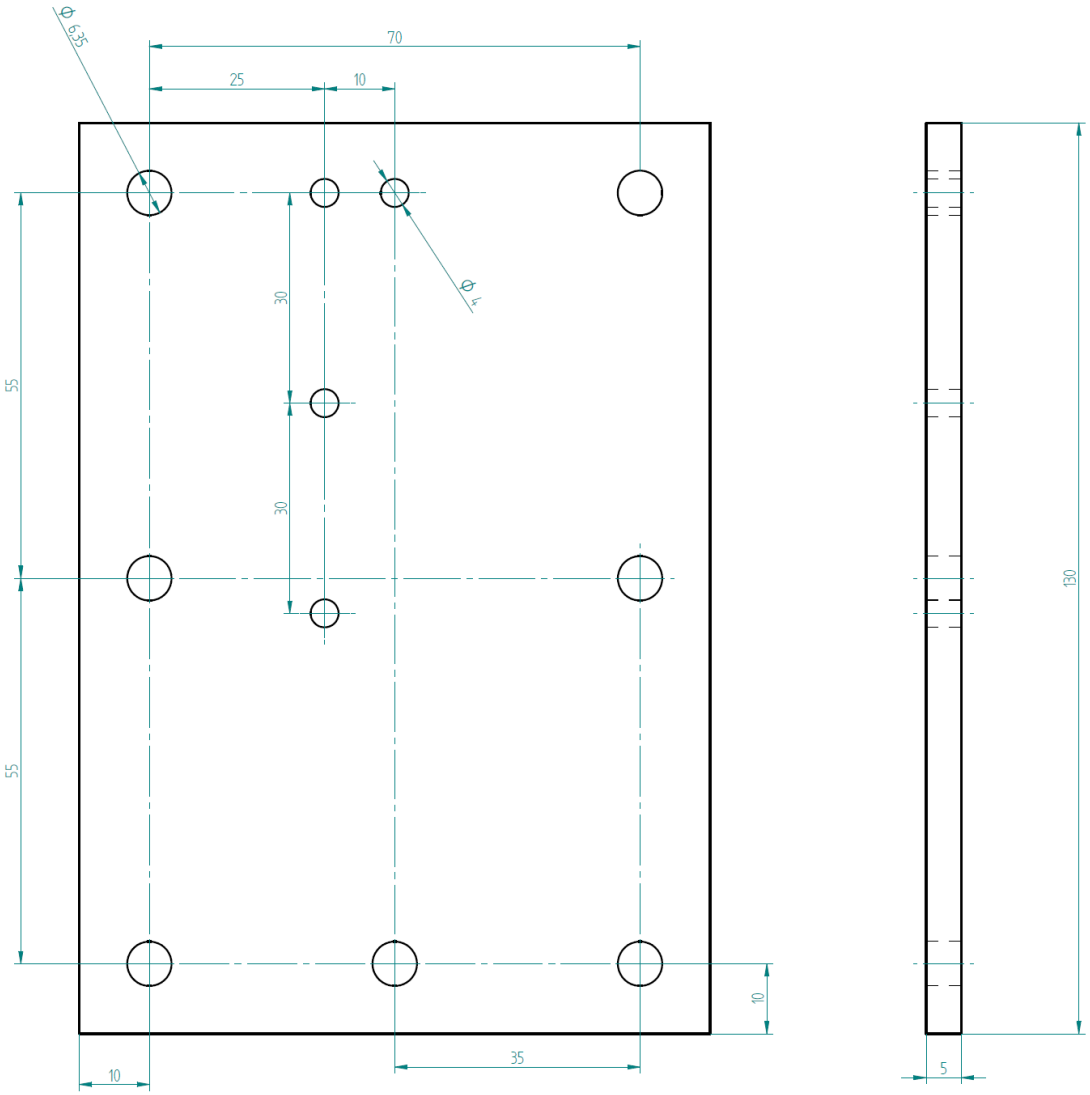

Figure A-4: CAD drawing of the rear Perspex sheet.

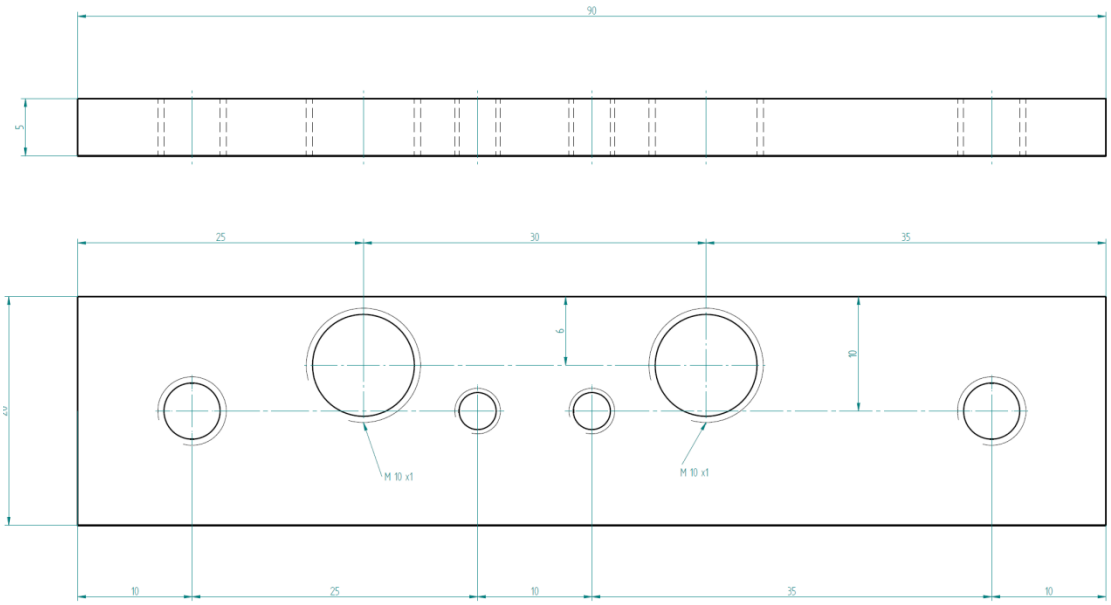

Figure A-5: CAD drawing of transducer adapter.

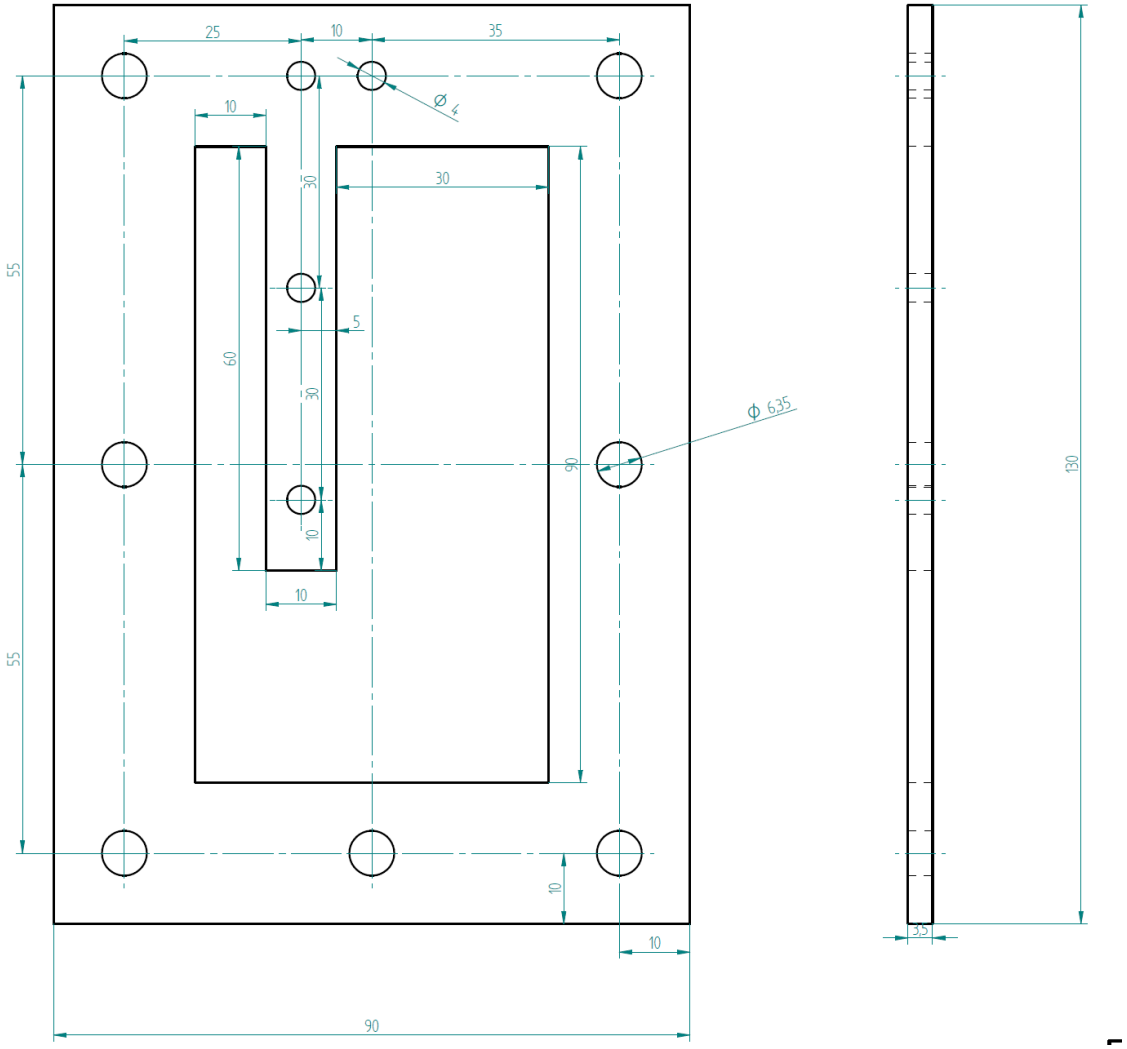

Figure A-6: CAD drawing of the sealing gaskets.

Appendix B: Matlab Code for Particle Tracking

```
% Particle Tracking Developed by YMF on 21/2/2013
close all;
file1 =
fopen('C:\First_Draft_PhD_Thesis\Chapter_5_Experiments\march_2013_low_
images\coords\1\1.dat');
file2 =
fopen('C:\First_Draft_PhD_Thesis\Chapter_5_Experiments\march_2013_low_
images\coords2\1\1.dat');
%filenamer =
('C:\First_Draft_PhD_Thesis\Chapter_5_Experiments\march_2013_high_imag
es\dist2.xlsx');
%fid
=fopen('C:\First_Draft_PhD_Thesis\Chapter_5_Experiments\march_2013_hig
h_images\dist5','w');

%file1 =
fopen('C:\First_Draft_PhD_Thesis\Chapter_5_Experiments\feb_2013_images
\coords\6\5.dat');
%file2 =
fopen('C:\First_Draft_PhD_Thesis\Chapter_5_Experiments\feb_2013_images
\coords2\6\6.dat');
% Read everything (first vector position, second vector position
%image_numb =[493,495,497,499];
image_numb =[400,500,600,1000,1900];
n = 100;
r = 18.0/2.0;
X1 = zeros(1,100);
XX1 = zeros(1,100);
X2 = zeros(1,100);
XX2 = zeros(1,100);
Y1 = zeros(1,100);
YY1 = zeros(1,100);
YY2 = zeros(1,100);
Y2 = zeros(1,100);
X11= zeros (1,100);
XX11=zeros (1,100);
Y11= zeros (1,100);
YY11=zeros (1,100);
VX = zeros (1,100);
VY = zeros (1,100);
VVX = zeros (1,100);
VVY = zeros (1,100);
momx = zeros(1,100);
momy = zeros(1,100);
KE1 = zeros (1,100);
KE2 = zeros (1,100);
DX = zeros (1,1);
DY = zeros (1,1);
DD = zeros (1,1);
MX  = zeros (1,2000);
MY  = zeros (1,2000);
MTO  = zeros (1,2000);
KE3 = zeros (1,2000);
KIN = zeros (1,2000);
%n1= zeros (1,1);
number1= zeros (1,1);
number2= zeros (1,1);
```

```
numberb1= zeros (1,1);
numberb2= zeros (1,1);
%number = zeros (1,1);

XPOS =zeros(1,200);
YPOS =zeros(1,200);
XVEL =zeros(1,200);
YVEL =zeros(1,200);

tx = zeros (1,700);
ty = zeros (1,700);

% we need to read the data here

% Read the first interrogation region

% Read the number of the first frame
f1 = fscanf (file1,'%d',1)
%read the number of the last frame
f2 = fscanf (file1,'%d',1)

% Read the coordinates of the first frame
% read the particle number
number = fscanf (file1,'%d',1);
for k=1:100;
    if k>number
      X1 (1,k)=0.0;
      Y1 (1,k)=0.0;
      continue
    end
    X1 (1,k)= fscanf (file1,'%*d%f',1);
    Y1 (1,k) = fscanf (file1,'%f',1);
    aha = fscanf (file1,'%*d%d',1);

end

n1 =number;

% end of reading first interrogation region

% Read the second interrogation region

% Read the number of the first frame
ff1 = fscanf (file2,'%d',1);
%read the number of the last frame
ff2 = fscanf (file2,'%d',1);

% Read the coordinates of the first frame
% read the particle number
numberb = fscanf (file2,'%d',1);
for kk=1:100;
    if kk>numberb
      XX1 (1,kk)=0.0;
      YY1 (1,kk)=0.0;
      continue
    end
    XX1 (1,kk)= fscanf (file2,'%*d%f',1);
    YY1 (1,kk) = fscanf (file2,'%f',1);
    ahaaha = fscanf (file2,'%*d%d',1);
```

```
end

nn1 =numberb;

% end of second interrogation region


% We will start the loop for frames here
for kk3 =1:(f2-1);
 %   for kk3 =1:400;
% Read the coordinates of the second frame
% read the particles number(count)
% first interrogation region
number2  = fscanf (file1,'%d',1);
% second interrogation region
numberb2  = fscanf (file2,'%d',1);

% read the coordinates of the second frame
%_____________________________________%
% first interrogation region
%_____________________________________%

for k2=1:100;
    if k2>number2
      X2 (1,k2)=0.0;
      Y2 (1,k2)=0.0;
      continue
    end

    X2 (1,k2) = fscanf (file1,'%*d%f',1);
    Y2 (1,k2) =  fscanf (file1,'%f',1);
    aha = fscanf (file1,'%*d%d',1);
end

%_____________________________________%
% second interrogation region
%_____________________________________%

for kk2=1:100;
    if kk2>numberb2
      XX2 (1,kk2)=0.0;
      YY2 (1,kk2)=0.0;
      continue
    end

    XX2 (1,kk2) = fscanf (file2,'%*d%f',1);
    YY2 (1,kk2) =  fscanf (file2,'%f',1);
    aha2 = fscanf (file2,'%*d%d',1);
end

%_____________________________________________________________________%
% End of reading second frame for both interrogation regions
%_____________________________________________________________________%


%_____________________________________________________________________%
% Detecting the velocity of each particle
```

```
%_____________________________________________________________%

%_____________________________________________________________%
% First interrogation region
%_____________________________________________________________%

%
% Outer loop for the first frame

for I=1:n1;
    DX = 0.0;
    DY = 0.0;
    DD = 0.0;
% Inner loop for the consecutive frame
    for J=1:number2;
        DX = -(X1(1,I)-X2(1,J));
        DY = -(Y1(1,I)-Y2(1,J));
        DD = sqrt(DX*DX+DY*DY);
        % do we need to set these variables to zero at the end???
        X11 (1,I)= (X1(1,I)/(1e-03*4.5*1000));
        Y11 (1,I)= (Y1(1,I)/(1e-03*4.5*1000));

        if DD<=1.0*r;
      %if abs(DX)<r || abs (DY)<r;
        %  DD = sqrt(DX*DX+DY*DY);
            VX(1,I) = (DX)/(1e-03*4.5*1000);
            VY(1,I) = (DY)/(1e-03*4.5*1000);
           % VX(1,I) = abs(DX)/(1e-03*4.5*1000);
           % VY(1,I) = abs(DY)/(1e-03*4.5*1000);
            % Kinetic energy
            KE1 (1,I) = sqrt (VX(1,I)^2+VY(1,I)^2);
            break;
       % else
            % No Matching, set velocities by zero
         end
        if J == number2;
           % no matching, set velocities to zero
           VX(1,I)=0.0;
           VY(1,I)=0.0;
          %  ss = 0.0;
        end
    end
end

%_____________________________________________________________%
% End of first interrogation region
%_____________________________________________________________%

%_____________________________________________________________%
% Second interrogation region
%_____________________________________________________________%

%
% Outer loop for the first frame

for II=1:nn1;
    DDX = 0.0;
    DDY = 0.0;
    DDD = 0.0;
% Inner loop for the consecutive frame
```

```
    for JJ=1:numberb2;
        DDX = -(XX1(1,II)-XX2(1,JJ));
        DDY = -(YY1(1,II)-YY2(1,JJ));
        DDD = sqrt(DDX*DDX+DDY*DDY);
     % do we need to set these variables to zero at the end???
     % Is this the right place?????
        XX11 (1,II)= 30.0 +(XX1(1,II)/(1e-03*4.5*1000));
        YY11 (1,II)= 20.0+(YY1(1,II)/(1e-03*4.5*1000));

        if DDD<=1.0*r;
      %if abs(DX)<r || abs (DY)<r;
        %  DD = sqrt(DX*DX+DY*DY);
            VVX(1,II) = (DDX)/(1e-03*4.5*1000);
            VVY(1,II) = (DDY)/(1e-03*4.5*1000);

            % Kinetic energy
            %KE1 (1,I) = sqrt (VX(1,I)^2+VY(1,I)^2);
            break;
       % else
            % No Matching, set velocities by zero
        end

       if JJ == numberb2;
           % no matching, set velocities to zero
           VVX(1,II)=0.0;
           VVY(1,II)=0.0;
         %  ss = 0.0;
       end
    end
end

%_____________________________________________%
% End of second interrogation region
%_____________________________________________%

%_____________________________________________%
% End of interrogation regions
%_____________________________________________%

% Now we have the velocities of each particle
% The velocities of unmatched particles are set to zero
% Make the required operation
%momx = zeros (1,100);
%momy = zeros (1,100);
%momx = (VX)*2500*1e-09*22*(4^3)/(6*7);
%momy = (VY)*2500*1e-09*22*(4^3)/(6*7);

%momx = abs(VX)/number2;
%momy = abs(VY)/number2;
%_____________________________________________________%
% we might need to add the two regions here
%_____________________________________________________%

%
for Iaha=1:n1;
    XPOS(1,Iaha)= X11(1,Iaha);
    YPOS(1,Iaha)= Y11(1,Iaha);
    XVEL(1,Iaha)= VX (1,Iaha);
    YVEL(1,Iaha)= VY (1,Iaha);
end
```

```
%}
%
for Iaha2=1:nn1;
    XPOS(1,(Iaha2+n1))=XX11(1,Iaha2);
    YPOS(1,(Iaha2+n1))=YY11(1,Iaha2);
    XVEL(1,(Iaha2+n1))=VVX(1,Iaha2);
    YVEL(1,(Iaha2+n1))=VVY(1,Iaha2);
end

for Iaha10=1:n1+nn1;
%GT(1,kk3) = GT(1,kk3)+0.5*((abs(momx(1,Iaha10)-
abs(MY(1,kk3)/n1)).^2)+(abs(momy(1,Iaha10)-abs(MX(1,kk3)/n1))).^2);
%GT(1,kk3) = GT(1,kk3)+0.5*(((momx(1,Iaha10)-
MY(1,kk3)/n1).^2)+((momy(1,Iaha10)-MX(1,kk3)/n1).^2));
KIN(1,kk3) = KIN(1,kk3)+0.5*((XVEL(1,Iaha10)).^2+(YVEL(1,Iaha10)).^2);
end

% we make this part for scaling (we should add n1 in the argument)
%
    XPOS(1,(nn1+n1+1))=85.0;
    YPOS(1,(nn1+n1+1))=5.0;
    XVEL(1,(nn1+n1+1))=0.0;
    YVEL(1,(nn1+n1+1))=1.0;
%}

%
% here we might compute the granular temperature for different regions
cvx = 0.0;
cvy = 0.0;
np1 = 0.0;
for kyaya1=1:100;

if (YPOS(1,kyaya1)>=15.0)&&(YPOS(1,kyaya1)<=30);
   np1 = np1 + 1;
   cvx =cvx + XVEL(1,kyaya1);
   cvy =cvy + YVEL(1,kyaya1);
end
end

cvxa = cvx/np1;
cvya = cvy/np1;

tx(1,kk3)=0.0;
ty(1,kk3)=0.0;

for kyaya2=1:100
    if (YPOS(1,kyaya2)>=15.0)&&(YPOS(1,kyaya2)<=30);
        tx(1,kk3) = tx(1,kk3) + (XVEL(1,kyaya2)-cvxa)^2.0;
        ty(1,kk3) = ty(1,kk3) + (YVEL(1,kyaya2)-cvya)^2.0;
    end
end

%}
% end of granular regions
%{
% velocity vectors
% get velocity distributions

i5=1;
```

```
for i5 = 1:(nn1+n1)
   fprintf(fid,'\n%3i %10.4f %10.4f %10.4f %10.4f',
kk3,XPOS(1,i5),YPOS(1,i5),XVEL(1,i5),YVEL(1,i5));
end

%}
%{
arg_remove = (nn1+n1):200;
XPOS(arg_remove) = [];
YPOS(arg_remove) = [];
XVEL(arg_remove) = [];
YVEL(arg_remove) = [];

xlRangey = sprintf('A%i',kk3);
sheet1 ='time';
%xlRange1 = 'A1';
xlswrite(filenamer,kk3,sheet1,xlRangey);
sheet2 ='X-Position';
%xlRange2 = 'A1';
xlswrite(filenamer,XPOS,sheet2,xlRangey);
sheet3 ='Y-Position';
%xlRange3 = 'A1';
xlswrite(filenamer,YPOS,sheet3,xlRangey);

sheet4 ='X-Velocity';
%xlRange4 = 'A1';
xlswrite(filenamer,XVEL,sheet4,xlRangey);
sheet5 ='Y-Velocity';
%xlRange5 = 'A1';
xlswrite(filenamer,YVEL,sheet5,xlRangey);

%}

%
if any (ismember(kk3,image_numb));
%if kk3 == 72;

    figure;
    daspect([1 1 1]);
    axis([0.0 50.0 0.0 90.0])
    quiver
(YPOS,XPOS,10.0*YVEL,10.0*XVEL,'autoscale','off','Color','k','linewidt
h',1.6,'MaxHeadSize',1.5);
   % quiver
(YPOS,XPOS,3.75*YVEL,3.75*XVEL,'autoscale','off','Color','k','linewidt
h',1.6,'MaxHeadSize',1.5);
    %quiver (YPOS,XPOS,YVEL,XVEL,'Color','black');
    daspect([1 1 1]);
    axis([0.0 50.0 0.0 90.0])
   % hold on
  % quiver(10,60, 1, 0,'autoscale','off');
   text(5, 85-2 , '1 m/s');

end
%}
momx = (VX);
momy = (VY);
% Kinetic energy
%KE  = 0.5*KE1*2500*1e-09*22*(4^3)/(6*7);
```

```
KE  = 0.5*KE1;

MY (1,kk3) = sum (momx,2);
MX (1,kk3) = sum (momy,2);
MTO (1,kk3)= sqrt(MY (1,kk3)*MY (1,kk3)+ MX (1,kk3)*MX (1,kk3));
% Kinetic energy
KE3 (1,kk3) = sum (KE,2);
%X1 = zeros (1,100);
X1=X2;
%X2=zeros (1,100);

%Y1 = zeros (1,100);
Y1=Y2;
%Y2=zeros (1,100);

n1=number2;
nn1=numberb2;
%}
VX = zeros(1,100);
VY = zeros(1,100);

momx = zeros(1,100);
momy = zeros(1,100);
% Kinetic energy
KE1 = zeros(1,100);
KE = zeros(1,100);

% remember to update the values of the second interrogation region
here
XX1=XX2;
YY1=YY2;
VVX = zeros(1,100);
VVY = zeros(1,100);
% not very sure of the following
%
X11= zeros (1,100);
XX11=zeros (1,100);
Y11= zeros (1,100);
YY11=zeros (1,100);
%}
% update the final positions and velocities
XPOS =zeros(1,200);
YPOS =zeros(1,200);
XVEL =zeros(1,200);
YVEL =zeros(1,200);
end
KEaha = sqrt(KE3);
%figure;
%plot (MX);
%figure;
%plot (MY);

%figure;
%plot(tx);
%figure;
%plot (ty);
%fclose(fid);

%figure;
%plot (KE3);
```

```
%figure;
%plot (KEaha);
%figure;
%plot (MTO);
%hold all;
%figure;
%plot (KIN);

%{
% This part is for excel sheets
MX1=transpose(MX);
MY1=transpose(MY);
filenamer =
'C:\First_Draft_PhD_Thesis\Chapter_5_Experiments\initial_real_results\
velocity2Yahia\vel2.xlsx';
sheet1 ='X-mom';
xlRange1 = 'F1';
xlswrite(filenamer,MX1,sheet1,xlRange1);
sheet2 ='Y-mom';
xlRange2 = 'F1';
xlswrite(filenamer,MY1,sheet2,xlRange2);

%}
%}

%{
% This part is for excel sheets
KIN1=transpose(KIN);
filenamer =
'C:\First_Draft_PhD_Thesis\Chapter_5_Experiments\initial_real_results\
Granular\KE_Tot.xlsx';
sheet1 ='Kinetic_Energy_Total';
xlRange1 = 'F1';
xlswrite(filenamer,KIN1,sheet1,xlRange1);


%}
```

References

Agrawal, K., Loezos, P.N., Syamlal, M. and Sundaresan, S. 2001, "The role of meso-scale structures in rapid gas–solid flows", *Journal of Fluid Mechanics,* vol. 445, pp. 151-185.

Allen, M.P. and Tildesley, D.J. 1989, *Computer simulation of liquids,* Oxford University Press.

Almendros-Ibáñez, J.A., Pallares, D., Johnsson, F. and Santana, D. 2010, "Voidage distribution around bubbles in a fluidized bed: Influence on throughflow", *Powder Technology,* vol. 197, no. 1, pp. 73-82.

Almuttahar, A. and Taghipour, F. 2008, "Computational fluid dynamics of a circulating fluidized bed under various fluidization conditions", *Chemical Engineering Science,* vol. 63, no. 6, pp. 1696-1709.

Armstrong, L.M., Luo, K.H. and Gu, S. 2010, "Two-dimensional and three-dimensional computational studies of hydrodynamics in the transition from bubbling to circulating fluidised bed", *Chemical Engineering Journal,* vol. 160, no. 1, pp. 239-248.

Bagnold, R.A. 1954, "Experiments on a gravity-free dispersion of large solid spheres in a Newtonian fluid under shear", *Proceedings of the Royal Society of London, Series A (Mathematical and Physical Sciences),* vol. 225, no. 1160, pp. 49-63.

Benyahia, S., Syamlal, M. and O'Brien, T.J. 2012, "Summary of MFIX Equations 2012-1", *https://mfix.netl.doe.gov/documentation/MFIXEquations2012-1.pdf.*

Benyahia, S., Syamlal, M. and O'Brien, T.J. 2007, "Study of the ability of multiphase continuum models to predict core-annulus flow", *AIChE Journal,* vol. 53, no. 10, pp. 2549-2568.

Benyahia, S., Syamlal, M. and O'Brien, T.J. 2006, "Extension of Hill–Koch–Ladd drag correlation over all ranges of Reynolds number and solids volume fraction", *Powder Technology,* vol. 162, no. 2, pp. 166-174.

Boyalakuntla, D.S. 2003, "Simulation of granular and gas-solid flows using discrete element method", Doctoral Dissertation, Carnegie Mellon University.

Brey, J.J., Dufty, J.W., Kim, C.S. and Santos, A. 1998, "Hydrodynamics for granular flow at low density", *Physical Review E,* vol. 58, no. 4, pp. 4638.

Brey, J.J., Dufty, J.W. and Santos, A. 1999, "Kinetic models for granular flow", *Journal of statistical physics,* vol. 97, no. 1-2, pp. 281-322.

Brey, J.J., Dufty, J.W. and Santos, A. 1997, "Dissipative dynamics for hard spheres", *Journal of statistical physics,* vol. 87, no. 5-6, pp. 1051-1066.

Brilliantov, N.V. and Pöschel, T. 2010, *Kinetic theory of granular gases,* Oxford University Press.

Campbell, C.S. 2006, "Granular material flows–An overview", *Powder Technology,* vol. 162, no. 3, pp. 208-229.

Candela, D., Huan, C., Facto, K., Wang, R., Mair, R.W. and Walsworth, R.L. 2007, "NMR measurements of grain and gas motion in a gas-fluidized granular bed", *Granular Matter,* vol. 9, no. 5, pp. 331-335.

Chan, H.K. 2006, "Dry powder aerosol drug delivery—Opportunities for colloid and surface scientists", *Colloids and Surfaces A: Physicochemical and Engineering Aspects,* vol. 284–285, pp. 50-55.

Chapman, S. and Cowling, T.G. 1970, *The mathematical theory of non-uniform gases: an account of the kinetic theory of viscosity, thermal conduction and diffusion in gases,* Cambridge university press.

Coates, M.S., Chan, H.K., Fletcher, D.F. and Chiou, H. 2007, "Influence of mouthpiece geometry on the aerosol delivery performance of a dry powder inhaler", *Pharmaceutical research,* vol. 24, no. 8, pp. 1450-1456.

Coates, M.S., Chan, H.K., Fletcher, D.F. and Raper, J.A. 2005a, "Influence of air flow on the performance of a dry powder inhaler using computational and experimental analyses", *Pharmaceutical research,* vol. 22, no. 9, pp. 1445-1453.

Coates, M.S., Fletcher, D.F., Chan, H.K. and Raper, J.A. 2004, "Effect of design on the performance of a dry powder inhaler using computational fluid dynamics. Part 1: grid structure and mouthpiece length", *Journal of pharmaceutical sciences,* vol. 93, no. 11, pp. 2863-2876.

Coates, M.S., Fletcher, D.F., Chan, H.K. and Raper, J.A. 2005b, "The role of capsule on the performance of a dry powder inhaler using computational and experimental analyses", *Pharmaceutical research,* vol. 22, no. 6, pp. 923-932.

Cundall, P.A. and Strack, O.D. 1979, "A discrete numerical model for granular assemblies", *Geotechnique,* vol. 29, no. 1, pp. 47-65.

Danby, M. 2010, "Towards the prediction of agglomerate behaviour in dry powder inhaler devices", Ph.D. thesis, University of Southampton.

Daniher, D.I. and Zhu, J. 2008, "Dry powder platform for pulmonary drug delivery", *Particuology,* vol. 6, no. 4, pp. 225-238.

Davidson, J. F. 1961, Symposium on Fluidization-discussion. *Transactions of the Institute of Chemical Engineers,* vol. 39, pp. 223-240.

Ding, J. and Gidaspow, D. 1990, "A bubbling fluidization model using kinetic theory of granular flow", *AIChE Journal,* vol. 36, no. 4, pp. 523-538.

Drake, T.G. 1991, "Granular flow: physical experiments and their implications for microstructural theories", *Journal of Fluid Mechanics,* vol. 225, pp. 121-152.

Ergun, S. 1952, "Fluid flow through packed columns", *Chemical Engineering Progress,* vol. 48, pp. 89-94.

Fan, R. 2006, "Computational fluid dynamics simulation of fluidized bed polymerization reactors", PhD Thesis, Iowa State University.

Fennell, P.S., Davidson, J.F., Dennis, J.S., Gladden, L.F., Hayhurst, A.N., Mantle, M.D., Müller, C.R., Rees, A.C., Scott, S.A. and Sederman, A.J. 2005, "A study of the mixing of solids in gas-fluidized beds, using ultra-fast MRI", *Chemical engineering science,* vol. 60, no. 7, pp. 2085-2088.

Finlay, W.H. 2001, *The Mechanics of Inhaled Pharmaceutical Aerosols (An Introduction)*, Academic Press.

Foerster, S.F., Louge, M.Y., Chang, H. and Allia, K. 1994, "Measurements of the collision properties of small spheres", *Physics of Fluids,* vol. 6, pp. 1108.

Gad-el-Hak, M. 1999, "The fluid mechanics of microdevices—the Freeman scholar lecture", *Journal of Fluids Engineering,* vol. 121, no. 1, pp. 5-33.

Garzó, V. and Dufty, J.W. 1999, "Dense fluid transport for inelastic hard spheres", *Physical Review E,* vol. 59, no. 5, pp. 5895.

Gidaspow, D. 1994, *Multiphase flow and fluidization: continuum and kinetic theory descriptions,* Academic press.

Goldschmidt, M.J.V., Beetstra, R. and Kuipers, J.A.M. 2004, "Hydrodynamic modelling of dense gas-fluidised beds: comparison and validation of 3D discrete particle and continuum models", *Powder Technology,* vol. 142, no. 1, pp. 23-47.

Goldschmidt, M.J.V, Kuipers, J.A.M. and Van Swaaij, W.P.M. 2001, "Hydrodynamic modelling of dense gas-fluidised beds using the kinetic

theory of granular flow: effect of coefficient of restitution on bed dynamics", *Chemical Engineering Science,* vol. 56, no. 2, pp. 571-578.

Goldschmidt, M.J.V., Link, J.M., Mellema, S. and Kuipers, J.A.M. 2003, "Digital image analysis measurements of bed expansion and segregation dynamics in dense gas-fluidised beds", *Powder Technology,* vol. 138, no. 2, pp. 135-159.

Guenther, C. and Syamlal, M. 2001, "The effect of numerical diffusion on simulation of isolated bubbles in a gas–solid fluidized bed", *Powder Technology,* vol. 116, no. 2, pp. 142-154.

Haehnel, R.B., Dade, W.B. and Cushman-Roisin, B. 2008, "Crater evolution due to a jet impinging on a bed of loose particles", *11th ASCE Earth & Space Conference,* pp. 3.

Haughney, J., Price, D., Barnes, N.C., Virchow, J.C., Roche, N. and Chrystyn, H. 2010, "Choosing inhaler devices for people with asthma: current knowledge and outstanding research needs", *Respiratory Medicine CME,* vol. 3, no. 3, pp. 125-131.

He, Y., Ngoc Cong, T. and Ding, Y. 2006, "Gas-solid Two-phase Mixtures Flowing Upward through a Confined Packed Bed", *Particle & Particle Systems Characterization,* vol. 23, no. 3-4, pp. 279-288.

Hill, R.J., Koch, D.L. and Ladd, A.J. 2001a, "The first effects of fluid inertia on flows in ordered and random arrays of spheres", *Journal of Fluid Mechanics,* vol. 448, no. 2, pp. 213-241.

Hill, R.J., Koch, D.L. and Ladd, A.J. 2001b, "Moderate-Reynolds-number flows in ordered and random arrays of spheres", *Journal of Fluid Mechanics,* vol. 448, no. 2, pp. 243-278.

Holland, D.J., Müller, C.R., Davidson, J.F., Dennis, J.S., Gladden, L.F., Hayhurst, A.N., Mantle, M.D. and Sederman, A.J. 2007, "Time-of-flight

variant to image mixing of granular media in a 3D fluidized bed", *Journal of Magnetic Resonance,* vol. 187, no. 2, pp. 199-204.

Hoomans, B.P.B., Kuipers, J.A.M., Briels, W.J. and Van Swaaij, W.P.M. 1996, "Discrete particle simulation of bubble and slug formation in a two-dimensional gas-fluidised bed: a hard-sphere approach", *Chemical Engineering Science,* vol. 51, no. 1, pp. 99-118.

Hopkins, M.A. and Louge, M.Y. 1991, "Inelastic microstructure in rapid granular flows of smooth disks", *Physics of Fluids A: Fluid Dynamics,* vol. 3, pp. 47.

Islam, N. and Gladki, E. 2008, "Dry powder inhalers (DPIs)—A review of device reliability and innovation", *International journal of pharmaceutics,* vol. 360, no. 1–2, pp. 1-11.

Jackson, R. 1983, "Some mathematical and physical aspects of continuum models for the motion of the granular materials", in R. E. Meyer (ed.), *Theory of Dispersed Multiphase Flow*, Academic Press, New York, pp. 291–337.

Jackson, R. 2000, *The dynamics of fluidized particles,* Cambridge University Press.

Jaeger, H.M., Nagel, S.R. and Behringer, R.P. 1996, "Granular solids, liquids, and gases", *Reviews of Modern Physics,* vol. 68, no. 4, pp. 1259-1273.

Jenkins, J.T. and Savage, S.B. 1983, "A theory for the rapid flow of identical, smooth, nearly elastic, spherical particles", *Journal of Fluid Mechanics,* vol. 130, no. 1, pp. 187-202.

Johnson, K.L. 1987, *Contact mechanics,* Cambridge University Press.

Johnson, P.C. and Jackson, R. 1987, "Frictional-collisional constitutive relations for granular materials, with application to plane shearing", *Journal of Fluid Mechanics,* vol. 176, pp. 67-93.

Jung, J., Gidaspow, D. and Gamwo, I.K. 2005, "Measurement of two kinds of granular temperatures, stresses, and dispersion in bubbling beds", *Industrial & Engineering Chemistry Research,* vol. 44, no. 5, pp. 1329-1341.

Jyotsna, R. 1993, "Frictional-kinetic models for steady cohesionless granular flow through a wedgeshaped hopper", Ph.D. Dissertation, Indian Institute of Science, Bangalore.

Jyotsna, R. and Rao, K.K. 1991, "Steady incompressible flow of cohesionless granular materials through a wedge-shaped hopper: Frictional-kinetic solution to the smooth wall, radial gravity problem", *Chemical Engineering Science,* vol. 46, no. 8, pp. 1951-1967.

Kawaguchi, T. 2010, "MRI measurement of granular flows and fluid-particle flows", *Advanced Powder Technology,* vol. 21, no. 3, pp. 235-241.

Kharaz, A.H., Gorham, D.A. and Salman, A.D. 1999, "Accurate measurement of particle impact parameters", *Measurement Science and Technology,* vol. 10, no. 1, pp. 31.

Larhrib, H., Martin, G.P., Prime, D. and Marriott, C. 2003, "Characterisation and deposition studies of engineered lactose crystals with potential for use as a carrier for aerosolised salbutamol sulfate from dry powder inhalers", *European journal of pharmaceutical sciences,* vol. 19, no. 4, pp. 211-221.

Li, T., Grace, J. and Bi, X. 2010, "Study of wall boundary condition in numerical simulations of bubbling fluidized beds", *Powder Technology,* vol. 203, no. 3, pp. 447-457.

Li, T. and Benyahia, S. 2012, "Revisiting Johnson and Jackson boundary conditions for granular flows", *AIChE Journal,* vol. 58, no. 7, pp. 2058-2068.

Li, T. and Benyahia, S. 2013, "Evaluation of wall boundary condition parameters for gas-solids fluidized bed simulations", *AIChE Journal,* vol. 59, no. 10, pp. 3624-3632.

Link, J., Zeilstra, C., Deen, N. and Kuipers, H. 2004, "Validation of a Discrete Particle Model in a 2D Spout-Fluid Bed Using Non-Intrusive Optical Measuring Techniques", *The Canadian Journal of Chemical Engineering,* vol. 82, no. 1, pp. 30-36.

Liu, J. 2001, "Particle and gas dynamics of high density circulating fluidized beds", Ph.D. Thesis, The University of British Columbia.

Lun, C.K.K., Savage, S.B., Jeffrey, D.J. and Chepurniy, N. 1984, "Kinetic theories for granular flow: inelastic particles in Couette flow and slightly inelastic particles in a general flowfield", *Journal of Fluid Mechanics,* vol. 140, no. 1, pp. 223-256.

Mantle, M.D., Sederman, A.J., Gladden, L.F., Huntley, J.M., Martin, T.W., Wildman, R.D. and Shattuck, M.D. 2008, "MRI investigations of particle motion within a three-dimensional vibro-fluidized granular bed", *Powder Technology,* vol. 179, no. 3, pp. 164-169.

Martin, T.W., Huntley, J.M. and Wildman, R.D. 2005, "Hydrodynamic model for a vibrofluidized granular bed", *Journal of Fluid Mechanics,* vol. 535, pp. 325-345.

Martin, T.W., Wildman, R.D., Hargrave, G.K., Huntley, J.M. and Halliwell, N. 2005, "Capturing gas and particle motion in an idealised gas-granular flow", *Powder Technology,* vol. 155, no. 3, pp. 175-180.

Metzger, P.T., Latta III, R.C., Schuler, J.M. and Immer, C.D. 2009, "Craters formed in granular beds by impinging jets of gas", *Powders and Grains 2009: Proceedings of the 6th international conference on micromechanics of granular media, AIP conference Proceedings,* vol. 1145, pp. 767-770.

Mitrano, P.P., Zenk, J.R., Benyahia, S., Galvin, J.E., Dahl, S.R. and Hrenya, C.M. 2014, "Kinetic-theory predictions of clustering instabilities in granular flows: beyond the small-Knudsen-number regime", *Journal of Fluid Mechanics,* vol. 738, pp. R2.

Müller, C.R., Davidson, J.S., Dennis, J.S., Fennell, P.S., Gladden, L.F., Hayhurst, A.L., Mantle, M.D., Rees, A.C. and Sederman, A.J. 2006, "Real-time measurement of bubbling phenomena in a three-dimensional gas-fluidized bed using ultrafast magnetic resonance imaging", *Physical Review Letters,* vol. 96, no. 15, pp. 154504.

Müller, C.R., Holland, D.J., Sederman, A.J., Scott, S.A., Dennis, J.S. and Gladden, L.F. 2008, "Granular temperature: comparison of magnetic resonance measurements with discrete element model simulations", *Powder Technology,* vol. 184, no. 2, pp. 241-253.

Newman, S.P. and Busse, W.W. 2002, "Evolution of dry powder inhaler design, formulation, and performance", *Respiratory medicine,* vol. 96, no. 5, pp. 293-304.

Ogawa, S., Umemura, A. and Oshima, N. 1980, "On the equations of fully fluidized granular materials", *Journal of Applied Mathematics and Physics (ZAMP),* vol. 31, no. 4, pp. 483-493.

Patankar, S.V. 1980, *Numerical heat transfer and fluid flow,* Hemisphere Publishing Corporation, New York.

Prime, D., Atkins, P.J., Slater, A. and Sumby, B. 1997, "Review of dry powder inhalers", *Advanced Drug Delivery Reviews,* vol. 26, no. 1, pp. 51-58.

Reese, J.M., Gallis, M.A. and Lockerby, D.A. 2003, "New directions in fluid dynamics: non-equilibrium aerodynamic and microsystem flows", *Philosophical transactions of the Royal Society, Series A (Mathematical, physical, and engineering sciences),* vol. 361, no. 1813, pp. 2967-2988.

Reuge, N., Cadoret, L., Coufort-Saudejaud, C., Pannala, S., Syamlal, M. and Caussat, B. 2008, "Multifluid Eulerian modeling of dense gas–solids fluidized bed hydrodynamics: influence of the dissipation parameters", *Chemical Engineering Science,* vol. 63, no. 22, pp. 5540-5551.

Savage, S.B. 1998, "Analyses of slow high-concentration flows of granular materials", *Journal of Fluid Mechanics,* vol. 377, pp. 1-26.

Savage, S.B. and Jeffrey, D.J. 1981, "The stress tensor in a granular flow at high shear rates", *Journal of Fluid Mechanics,* vol. 110, no. 1, pp. 255-272.

Schaeffer, D.G. 1987, "Instability in the evolution equations describing incompressible granular flow", *Journal of differential equations,* vol. 66, no. 1, pp. 19-50.

Seville, J.P.K., Willett, C.D. and Knight, P.C. 2000, "Interparticle forces in fluidisation: a review", *Powder Technology,* vol. 113, no. 3, pp. 261-268.

Sheikh, N.A. 2011, "Comparison of constitutive relationships based on kinetic theory of granular gas for three dimensional vibrofluidized beds", PhD thesis, Loughborough University.

Spalding, D.B. 1980, "Numerical computation of multi-phase fluid flow and heat transfer", in Taylor C. and Morgan K. (eds.), *Recent advances in numerical methods in fluids,* Pineridge Press, vol. 1, pp. 139-167.

Srivastava, A. and Sundaresan, S. 2003, "Analysis of a frictional–kinetic model for gas–particle flow", *Powder Technology,* vol. 129, no. 1, pp. 72-85.

Stein, M., Ding, Y.L., Seville, J.P.K. and Parker, D.J. 2000, "Solids motion in bubbling gas fluidised beds", *Chemical Engineering Science,* vol. 55, no. 22, pp. 5291-5300.

Stevens, N.E. 2006, "Multiphase modelling methods for dry powder inhaler flow", PhD thesis, Imperial College London.

Syamlal, M. 1998, "MFIX documentation: Numerical technique DOE/MC-31346-5824. NTIS/DE98002029. National Technical Information Service, Springfield, VA

Syamlal, M., Rogers, W. and O'Brien, T.J. 1993, "MFIX documentation: Theory guide", Technical Note, DOE/METC-94/1004, NTIS/DE94000087, National Technical Information Service, Springfield, VA.

Tardos, G.I. 1997, "A fluid mechanistic approach to slow, frictional flow of powders", *Powder Technology,* vol. 92, no. 1, pp. 61-74.

Thornton, C. and Yin, K.K. 1991, "Impact of elastic spheres with and without adhesion", *Powder Technology,* vol. 65, no. 1, pp. 153-166.

Tsuji, Y., Kawaguchi, T. and Tanaka, T. 1993, "Discrete particle simulation of two-dimensional fluidized bed", *Powder Technology,* vol. 77, no. 1, pp. 79-87.

Tuley, R., Shrimpton, J., Jones, M.D., Price, R., Palmer, M. and Prime, D. 2008, "Experimental observations of dry powder inhaler dose fluidisation", *International journal of pharmaceutics,* vol. 358, no. 1, pp. 238-247.

Tuley, R.J. 2007, "Modelling dry powder inhaler operation with the discrete element method", Ph D thesis, Imperial College London.

Tüzün, U., Houlsby, G.T., Nedderman, R.M. and Savage, S.B. 1982, "The flow of granular materials—II Velocity distributions in slow flow", *Chemical Engineering Science,* vol. 37, no. 12, pp. 1691-1709.

Van Beijeren, H. and Ernst, M.H. 1973, "The modified Enskog equation for mixtures", *Physica,* vol. 70, no. 2, pp. 225-242.

Versteeg, H.K. and Wildman, R.D. 2004, "An Optical Method for the Study of Aerosol Generation in Dry Powder Inhalers", *ASME 7th Biennial Conference on Engineering Systems Design and Analysis,* American Society of Mechanical Engineers, vol. 3, pp. 415-420.

Versteeg, H.K., Hargrave, G.K. and Hind, R.J.A. 2005, "An optical study of aerosol generation in dry powder inhalers", *Drug Delivery to the Lungs,* vol. 16, pp. 3-6.

Viswanathan, H., Sheikh, N.A., Wildman, R.D. and Huntley, J.M. 2011, "Convection in three-dimensional vibrofluidized granular beds", *Journal of Fluid Mechanics,* vol. 682, pp. 185.

Warr, S., Jacques, G.T.H. and Huntley, J.M. 1994, "Tracking the translational and rotational motion of granular particles: use of high-speed photography and image processing", *Powder Technology,* vol. 81, no. 1, pp. 41-56.

Wen, C.Y. and Yu, Y.H. 1966, "A generalized method for predicting the minimum fluidization velocity", *AIChE Journal,* vol. 12, no. 3, pp. 610-612.

Wildman, R.D. 2002, "Measurement of the first and second moments of the velocity distribution in two-dimensional vibro-fluidised granular beds", *Powder Technology,* vol. 127, no. 3, pp. 203-211.

Wildman, R.D. and Huntley, J.M. 2008, "Experimental measurements and modelling of rapid granular flows", *Powder Technology,* vol. 182, no. 2, pp. 182-191.

Wildman, R.D. and Huntley, J.M. 2000, "Novel method for measurement of granular temperature distributions in two-dimensional vibro-fluidised beds", *Powder Technology,* vol. 113, no. 1, pp. 14-22.

Wildman, R.D., Martin, T.W., Huntley, J.M., Jenkins, J.T., Viswanathan, H., Fen, X. and Parker, D.J. 2008, "Experimental investigation and kinetic-theory-based model of a rapid granular shear flow", *Journal of Fluid Mechanics,* vol. 602, pp. 63-79.

Wong, W., Fletcher, D.F., Traini, D., Chan, H.K., Crapper, J. and Young, P.M. 2011, "Particle aerosolisation and break-up in dry powder inhalers: Evaluation and modelling of impaction effects for agglomerated systems", *Journal of pharmaceutical sciences,* vol. 100, no. 7, pp. 2744-2754.

Xie, N., Battaglia, F. and Pannala, S. 2008, "Effects of using two-versus three-dimensional computational modeling of fluidized beds: part I, hydrodynamics", *Powder Technology,* vol. 182, no. 1, pp. 1-13.

Yu, A.B. and Xu, B.H. 2003, "Particle-scale modelling of gas–solid flow in fluidisation", *Journal of Chemical Technology and Biotechnology,* vol. 78, no. 2-3, pp. 111-121.

Zhou, Y.C., Wright, B.D., Yang, R.Y., Xu, B.H. and Yu, A.B. 1999, "Rolling friction in the dynamic simulation of sandpile formation", *Physica A: Statistical Mechanics and its Applications,* vol. 269, no. 2, pp. 536-553.